AD/A-006 108

MINIATURIZED HIGH SPEED CONTROLS FOR TURBINE ENGINES (FABRICATION AND TEST)

D. G. Burnell, et al

Colt Industries, Incorporated

Prepared for:

Air Force Aero Propulsion Laboratory

August 1974

DISTRIBUTED BY:

NTIS

National Technical Information Service
U. S. DEPARTMENT OF COMMERCE
5285 Port Royal Road, Springfield Va. 22151

REPORT DOCUMENTATION PAGE

READ INSTRUCTIONS BEFORE COMPLETING FORM

1. REPORT NUMBER AFAPL-TR-74-93	2. GOVT ACCESSION NO.	3. RECIPIENT'S CATALOG NUMBER AD/A006108
4. TITLE (and Subtitle) Miniaturized High Speed Controls for Turbine Engines (Fabrication and Test)		5. TYPE OF REPORT & PERIOD COVERED Final May 1973 - Aug 1974
		6. PERFORMING ORG. REPORT NUMBER N/A
7. AUTHOR(s) D.G. Burnell A.H. White M.A. Cole R.D. Zagranski T.B. Morrison		8. CONTRACT OR GRANT NUMBER(s) F33615-73-C-2040
9. PERFORMING ORGANIZATION NAME AND ADDRESS Colt Industries Chandler Evans Controls Division West Hartford, Conn. 06101		10. PROGRAM ELEMENT, PROJECT, TASK AREA & WORK UNIT NUMBERS 30661507
11. CONTROLLING OFFICE NAME AND ADDRESS Air Force Aero Propulsion Laboratory (TBP) Wright-Patterson AFB, Ohio 45433		12. REPORT DATE August 1974
		13. NUMBER OF PAGES 185
14. MONITORING AGENCY NAME & ADDRESS (if different from Controlling Office) N/A		15. SECURITY CLASS. (of this report) Unclassified
		15a. DECLASSIFICATION/DOWNGRADING SCHEDULE N/A

16. DISTRIBUTION STATEMENT (of this Report)

Approved for public release; Distribution Unlimited

17. DISTRIBUTION STATEMENT (of the abstract entered in Block 20, if different from Report)

N/A

18. SUPPLEMENTARY NOTES

N/A

19. KEY WORDS (Continue on reverse side if necessary and identify by block number)

Turbine Engine Fuel Control
Fuel Pumps
Radiation Pyrometer
Pressure Sensors

20. ABSTRACT (Continue on reverse side if necessary and identify by block number)

This report summarizes the design and development of control components and high speed fuel pump technology for future drone, missile and RPV gas turbine engines. The hardware was designed for installation on an existing engine to provide a vehicle for control mode demonstration and evaluation testing. The developed hardware includes a fluidic/LVDT $\Delta P/P$ airflow sensor, a

(CONTINUED ON REVERSE SIDE)

NOTICES

When Government drawings, specifications, or other data are used for any purpose other than in connection with a definitely related Government procurement operation, the United States Government thereby incurs no responsibility nor any obligation whatsoever; and the fact that the government may have formulated, furnished, or in any way supplied the said drawings, specifications, or other data, is not to be regarded by implication or otherwise as in any manner licensing the holder or any other person or corporation, or conveying any rights or permission to manufacture, use, or sell any patented invention that may in any way be related thereto.

This report has been reviewed and cleared for open publication and/or public release by the appropriate Office of Information (OI) in accordance with AFR 190-17 and DODD 5230.9. There is no objection to unlimited distribution of this report to the public at large, or by DDC to the National Technical Information Service (NTIS).

This technical report has been reviewed and is approved for publication.

Elmer E. Buchanan

Elmer E. Buchanan
Project Engineer

Ernest C. Simpson

Ernest C. Simpson
Director, Turbine Engine Division
Air Force Propulsion Laboratory

Copies of this report should not be returned unless return is required by security considerations, contractual obligations, or notice on a specific document.

AIR FORCE/56780/7 February 1975 — 50

20. ABSTRACT (Cont'd)

radiation pyrometer for sensing turbine blade temperature, three pressure transducers for sensing burner pressure (variable capacitance, strain gage, and potentiometric types), a 70,000 rpm centrifugal pump and proportional solenoid-operated fuel metering system, a magnetic clutch-driven 12,000 rpm gear pump for fuel metering and fuel pressurization, and an electronic unit for interfacing these components with an engine test cell digital computer. The results of component steady-state, environmental, and dynamic performance testing, and closed-loop system testing using a computer model to provide control functions are included herein.

FOREWORD

This is the final report covering work completed under Contract Number F33615-73-C-2040 titled "Miniaturized High Speed Controls for Turbine Engines". The program was conducted for the Air Force Aero Propulsion Laboratory, Wright-Patterson Air Force Base, during the period May 1973 through August 1974, under the direction of Mr. E. E. Buchanan.

The program work was conducted by Colt Industries, Inc., Chandler Evans Control Systems Division, under the cognizance of Mr. J. M. Maljanian, Manager, Engine Controls. Mr. A. H. White was the Program Manager, and Messrs. M. A. Cole, D. G. Burnell, T. B. Morrison and R. D. Zagranski the principal investigators. Acknowledgment is given to the following organizations their contributions to this program.

American Optical Corporation
Delevan Division, American Precision Industries
Electro Optical Industries
Fluidics Operation, General Electric Company
Rosemount Incorporated
Statham Instruments Inc.
Williams Research Corporation

CONTENTS

CONTENTS (Cont)

ILLUSTRATIONS

ILLUSTRATIONS (Cont)

ILLUSTRATIONS (Cont)

ILLUSTRATIONS (Cont)

ILLUSTRATIONS (Cont.)

ILLUSTRATIONS (Cont)

ILLUSTRATIONS (Cont)

TABLES

LIST OF SYMBOLS

a	fuel transportation lag
A	orifice area
A/D	analog to digital
B_{pR}	burner pressure ratio
C_p	specific heat
CPU	central processing unit
D/A	digital to analog
EMI	electro magnetic interference
f	frequency
F	engine gross thrust, lbs
F/B	feedback
g	gravitational acceleration, 32.2 ft/sec^2
GPC	general purpose computer
HC	hybrid computer
IC	integrated circuit
I/O	input/output
i	current, amps
i(c)	magnetic clutch current, amps
i(p)	proportional solenoid current, amps

LIST OF SYMBOLS (Cont)

i(s)	shutoff solenoid current, amps
IGV	inlet guide vanes
J	mechanical equivalent of heat, 778 ft-lb/BTU
J_g	gas generator turbine inertia
K	flow coefficient, °R/sec
K_B	temperature control gain, pph/°F
K_i	control integral gain
K_i'	Mach No. control integral gain
K_p	control proportional gain
K_p'	Mach No. proportional gain
K_s	starting fuel flow gain, pph/sec
K_T	throttle control gain
LSI	large scale integration
MMV	main metering valve
m sec	milli seconds
MSI	medium scale integration
N_1	low pressure rotor speed, rpm
N_2	high pressure rotor speed, rpm
N_2^*	speed demand signal

LIST OF SYMBOLS (Cont)

N_p	pump speed, rpm
N_p^*	pump set speed, rpm
P_a	ambient total pressure, psia
P_o	standard day atmospheric pressure, psia
P_r	intermediate pressure between two orifices
P_{s4}	compressor discharge static pressure, psia
P_{T1}	ambient inlet total pressure, psia
P_{T2}	fan inlet total pressure, psia
P_{T3}	compressor inlet total pressure, psia
P_{T4}	compressor discharge total pressure, psia
P_{T5}	high pressure turbine inlet total pressure, psia
P_{T6}	low pressure turbine inlet total pressure, psia
P_{T7}	exhaust nozzle total pressure, psia
S	Laplace operator
SFC	specific fuel consumption
t	time, sec
T_{amb}	ambient temperature, °R
T_D	radiation detector temperature
TIT	turbine inlet temperature

LIST OF SYMBOLS (Cont)

T/L	throttle lever
T_o	standard day temperature, °R
T_{skin}	engine skin temperature, °R
T_{total}	total temperature, °R
T_{T1}	ambient temperature, °R
T_{T2}	fan inlet total temperature, °R
T_{T3}	compressor inlet total temperature, °R
T_{T4}	compressor discharge total temperature, °R
T_{T5}	high pressure turbine inlet total temperature, °R
T_{T6}	low pressure turbine inlet total temperature, °R
T_{T7}	exhaust nozzle gas total temperature, °R
T_{T8}	exhaust discharge total temperature, °R
T_B	high pressure turbine blade temperature, °F
V/L	vapor/liquid ratio
V(c)	magnetic clutch computer voltage, DC
V(p)	proportional solenoid computer voltage, DC
W_a	airflow, pps
W_F	fuel flow, pph
γ	ratio of specific heats, C_p/C_v

LIST OF SYMBOLS (Cont)

$\Delta P/P$	$(P_{T4}-P_{s4})/P_{T4}$
η	efficiency (isentropic)
θ	relative inlet temperature, T_{T2}/T_o
θ_B	bleed valve geometry angle, degrees
θ_v	guide vane geometry angle, degrees
τ	time constant, seconds
τ_B	turbine blade thermal time constant, seconds
τ_1, τ_2	thermocouple lead lag time constants, seconds
2-D	two dimensional
3-D	three dimensional

1

INTRODUCTION

Future drone, missile, and RPV systems will require small, low cost, high performance, high thrust/weight and high thrust/volume gas turbine engines. One area in which considerable progress toward these requirements appears possible is in the engine fuel pump and control system.

The majority of the past effort in these areas has been directed toward either large engines or shaft engines for helicopter applications requiring much longer life than missiles and drones. Although some of this technology is applicable to small turbofan engines, the controls and accessories continue to account for a substantial percentage of the overall propulsion system weight, volume and cost. Some significant accomplishments have been made in the areas of high speed pumps and controls; however, the overall utilization of these efforts has generally not kept pace with the reduction in engine size.

This program was undertaken to investigate and develop, for subsequent engine evaluation, control technology for 1976-1980 gas turbine engines in the 1000 pound thrust class.

During the first phase of the program, studies were conducted to evaluate, based on a weighted assessment criteria, various control concepts which offered potential for the desired improvement in fuel pumping and control systems. Trade-offs and surveys of airframe and engine manufacturers were conducted to gather information concerning drone and missile missions, the overall airframe fuel system, and the potential integration of the engine control and vehicle computer and/or flight control. The initial results of this study effort, as reported in Reference 1, indicated that the wide range of engine control and fuel pumping requirements covered by the various possible missions made it impossible to generate a general engine control specification. Therefore, three general classes of controls were specified to encompass the broad range of engine control functional requirements indicated by the various missions. These classes of control covered the very sophisticated requirements of a high performance, variable geometry engine to a simple fixed geometry engine requiring at most a simple on-off compressor bleed controller, a speed governor, and a time-scheduled engine transient control. The trade-off studies were directed to considered analog, hybrid and programmable digital electronic control and sensing, electrohydromechanical fuel metering, geometry actuation and fuel pumping. Quantitative trade-off studies were conducted based on the following weighted assessment criteria, which was established by surveying engineering personnel from airframe and engine manufacturers and in-house staffs.

Reliability	33
Cost	21
Performance	19
Weight and Volume	15
Maintainability	12

Based on the results of these studies, the decision was made to develop fuel metering and pumping components, various sensors, and the necessary electronic interface unit, and thereby provide for demonstrating several different engine control modes. The components were designed for mounting on an existing engine for future control mode demonstration testing. Control functional and logic requirements will be provided by a test cell digital computer. The components that were selected for development include:

1. A solenoid-operated fuel meter system with integral 70,000 rpm centrifugal pump and magnetic speed sensor.

2. A variable speed magnetic hysteresis clutch-driven gear pump (12,000 rpm) with magnetic speed sensors.

3. A $\Delta P/P$ fluidic sensor for closed loop engine transient control.

4. A radiation pyrometer for sensing turbine blade temperature for temperature limiting and engine transient control.

5. Variable capacitance and a strain gage pressure transducer for sensing compressor discharge pressure in a W_f/P_{cd} control, and for the same control mode, a potentiometric-type pressure sensor for application where some performance can be sacrificed for low cost.

6. Breadboard electronic unit for interfacing with the test cell computer.

An overview of the system which depicts the control mode demonstration test setup is included in Figure 1. This report gives a summary of the component designs and the results of the component and closed-loop bench testing that was conducted using an analog computer simulation, and a digital computer simulation of the control logic for the different control modes being investigated.

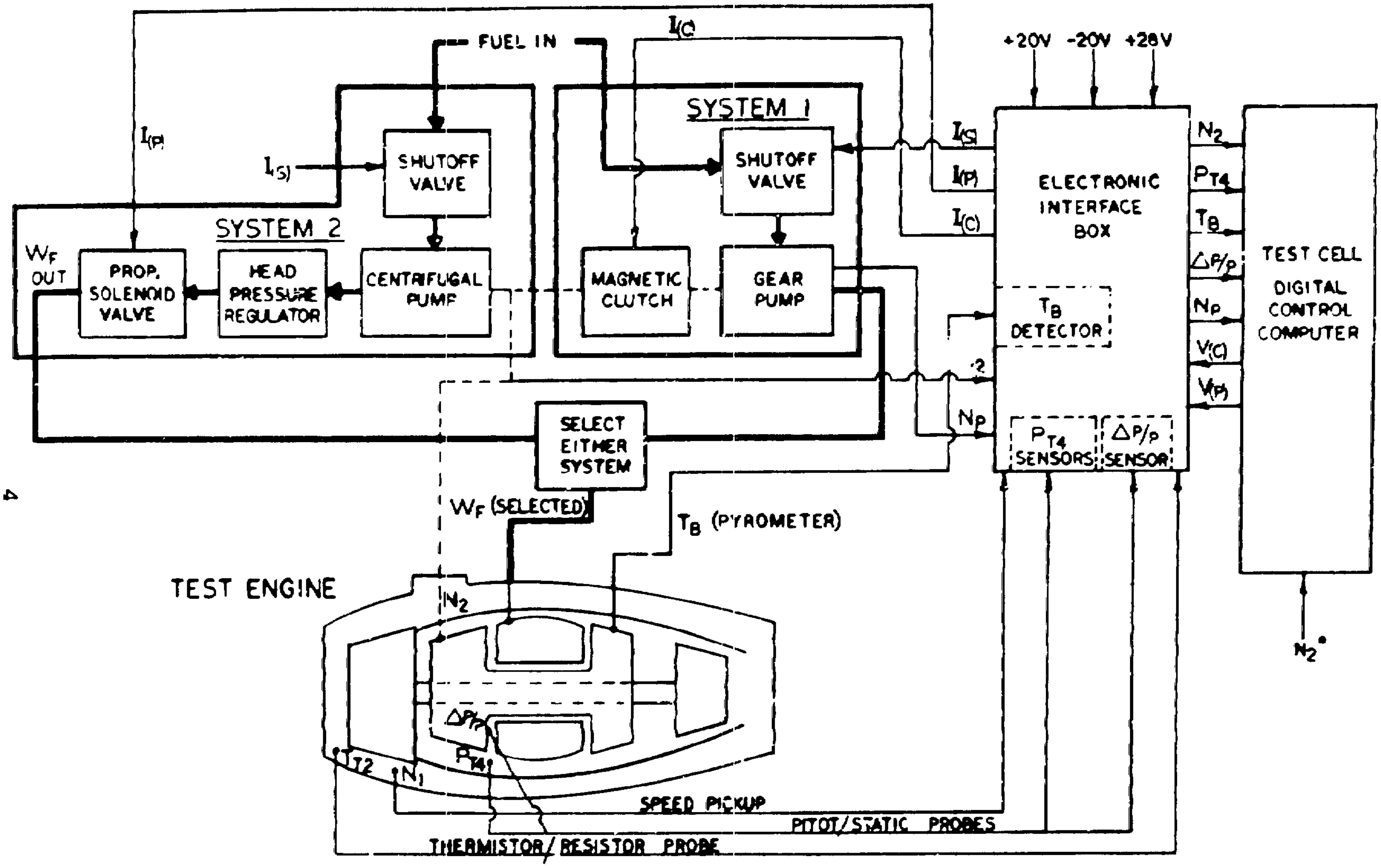

Figure 1. Engine Control Interface Block Diagram.

2

FUEL METERING AND PUMPING

1. CONCEPT TRADE-OFF STUDY

To select the optimum fuel metering and pumping concept for development, trade-off studies were performed to determine concepts which offer the greatest reduction in cost and size, and meet the requirements for reliability, maintainability and performance. The fuel metering and pumping concepts considered were designed to interface with an electronic control, for use with any of the control modes discussed in this report.

Six fuel metering and pumping concepts were considered and evaluated using the weighted assessment criteria. A summary of the evaluation and schematics of the six systems are shown in Figure 2 . Based on this information, and applying the weighted assessment criterion for each design factor, the results summarized in Table I were determined. This table gives the relative merits of each system, and designates the most promising systems for development. A brief description of each system is included in the following sections.

TABLE I . FUEL METERING & PUMP TRADE-OFF

System	Reliability Based on MTBF (33)	Cost (21)	* Performance (19)	Weight (15)	Maintainability (12)	Total (100)
1 with c/f Pump	22	9	19	14	9	73
2	17	16	10	3	4	50
3	32	11	14	15	12	84
4	33	21	10	13	12	89
5	23	10	19	14	9	75
6	19	19	12	13	4	67

* Open Loop Fuel Flow Accuracy

FUEL METERING & PUMP TRADE-OFF STUDY

SYSTEM SCHEMATIC	* NUMBER OF COMPONENTS	RELATIVE PERFORMANCE	MTBF / RELIABILITY	COST	WEIGHT LB	RELATIVE MAINTAINABILITY	COMMENTS
1 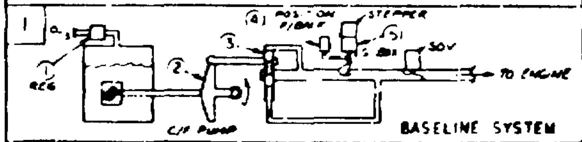 BASELINE SYSTEM	WITH CENTRIFUGAL PUMP 5 OR WITH GEAR PUMP 5	ACCURATE	6039 WITH CF PUMP 5393 WITH GR PUMP .9917 WITH CF PUMP .9902 WITH GR PUMP	WITH CENTRIFUGAL PUMP 2.1 / WITH GEAR PUMP 2.34	2.3	COMPLEX	FIXED DISPLACEMENT VANE PUMP MAY BE USED IN PLACE OF GEAR PUMP BUT [illegible] EXPENSIVE
2 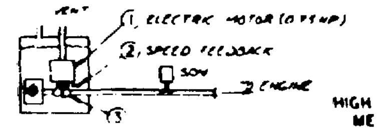 HIGH POWER MOTOR METERING PUMP	3	ACCEL SHIFTS WITH FUEL TEMP & FUEL TYPE GOOD S/L PERFORMANCE	4763 .9895	1.3	10.7	REQUIRES ACCESS TO FUEL TANK	IF 115 V AC MOTOR IS USED WEIGHT IS REDUCED TO 3.6 LB. BUT AC IS NOT AVAILABLE FOR START UP, HENCE OTHER PROVISIONS WOULD HAVE TO BE MADE
3 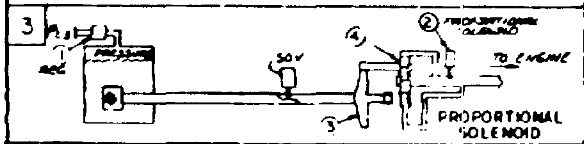 PROPORTIONAL SOLENOID	4		8950 .9974	1.84	2.2	SIMPLE	
4 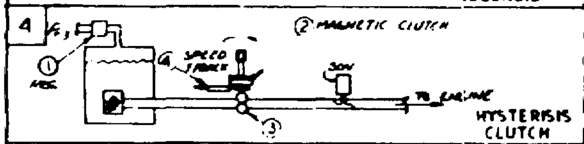 HYSTERISIS CLUTCH	4	ACCEL SHIFTS WITH FUEL TEMP & FUEL TYPE	9100 .9945	1.00	2.45	SIMPLE	
5 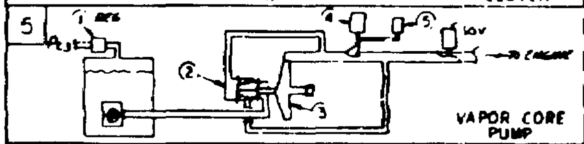 VAPOR CORE PUMP	5	ACCURATE	6252 .9920	2.11	2.3	COMPLEX	HIGHER ALTITUDE CAPABILITY THAN BASELINE SYSTEM
6 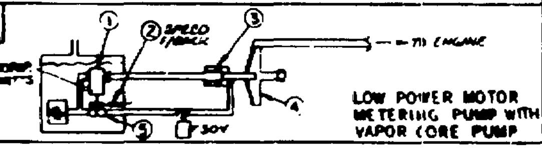 LOW POWER MOTOR METERING PUMP WITH VAPOR CORE PUMP	5	ACCEL SHIFTS WITH FUEL TEMP & FUEL TYPE	5251 .9905	1.03	2.6	REQUIRES ACCESS TO FUEL TANK	

* NOT INCLUDING COMMON COMPONENTS

Figure 2. Fuel Metering and Pump Trade-Off Study.

System 1 - Baseline System

This system uses an engine-driven pump and meters fuel flow to the engine with a rotating plate valve driven by a stepping motor. The pump may be a gear, vane, or a centrifugal type, depending on the engine requirements. The pressure drop across the fuel metering valve is held essentially constant by a fuel bypass valve when a gear or vane pump is used, or a throttling valve when a centrifugal pump is used. Fuel tank pressurization or a boost pump is needed for any of the systems to prevent pump cavitation.

System 2 - High Power Electric Motor Metering Pump

An electric motor (0.75 hp) is used to drive a gear pump. The gear pump provides the required engine fuel flow and pressure. The engine fuel flow is controlled by controlling the gear pump speed closed loop. This is done with the electronic computer by varying the power to the electric motor as a function of gear pump speed error. Feedback of gear pump speed is provided by a speed pickup. Fuel tank pressurization is not required if the motor/pump is mounted in the fuel tank.

System 3 - Proportional Solenoid System

High pressure fuel is supplied by an engine-driven high speed centrifugal pump. Fuel is metered to the engine by an unservo'd linear solenoid. The metering head is held essentially constant by a throttling regulator. The fuel tank is pressurized to prevent pump cavitation.

System 4 - Magnetic Clutch System

This system uses a magnetic clutch-driven gear pump to provide the required engine fuel flow and pressure. The magnetic clutch is the hysteresis-type which transmits torque by magnetic interaction, and is the equivalent of a variable speed drive but without mechanical contact between the input and output shafts. The current to the clutch is controlled by the electronic computer; feedback of gear pump speed is provided by a magnetic pickup. Fuel tank pressurization is required to prevent pump cavitation.

System 5 - Vapor Core Pump System

This system is similar to System 1 except that the throttling head regulator is in the inlet to the centrifugal pump and, therefore the pump operates in the vapor mode which improves overall efficiency. Fuel tank pressurization is required to allow fuel throttling at the inlet to the vapor core pump.

System 6 - Low Power Electric Motor Metering Pump

This system is similar to System 2 except that the functions of fuel metering and fuel pressurization are separated. Fuel pressure is provided by a vapor core pump and fuel metering is achieved by using an electric motor-driven gear pump. The pressure rise across the gear pump is held constant and to a low value to minimize the power required by the electric motor (100 watts). No fuel tank pressurization is necessary.

Based on the results of the trade-off study, the magnetic clutch system and the proportional solenoid system were selected for development.

2. SPECIFICATION FOR FUEL METERING & PUMPING

For demonstration purposes, the magnetic clutch system and centrifugal pump system were designed to meet the performance and installation requirements of an existing engine. The following are the basic design parameters:

Fuel Flow	25 lb/hr minimum to 500 lb/hr maximum
Fuel Pressure	458 psia*
Fuel Inlet Temperature	-65°F to +135°F
Pump Drive Speed (max)	12,000 rpm (gear pump magnetic clutch system)
	70000 rpm (centrifugal pump)
Required Accuracy	± 4% of fuel flow (during acceleration and deceleration)

---

* This is the fuel pressure required at the pump design point, 88% pump speed -65°F day acceleration fuel flow = 435 lb/hr

3. MAGNETIC CLUTCH SYSTEM

Description

A schematic of the magnetic clutch system is shown on Figure 3 . Fuel is received from a pressurized source and passes through the solenoid shutoff valve. From the shutoff valve the fuel flows to the metering gear pump and on to the engine. The speed of the pump is controlled by the magnetic hysteresis clutch. Feedback of gear pump speed to the electronic interface unit is provided from the magnetic pickup. The current to the clutch is proportional to gear pump speed error. Energizing the clutch coil sets up a magnetic flux between the input and output shafts. Rotation of the output shaft (gear pump drive) is caused by the torque created by the force generated by the magnetic flux.

Control of fuel flow is achieved by proportional control of pump speed. Accurate control of engine fuel flow by controlling pump speed is possible because the relationship between fuel flow, pump speed, and pump back pressure is predictable for different flight conditions and compressor inlet temperatures, as explained in the following discussion.

The fuel flow for a given pump speed is dependent on the back pressure and is defined by:

$$W_f = k_1 N_p - k_2 \Delta P \quad ①$$

where	W_f = engine fuel flow	lb/hr
	k_1 = pump flow per rpm	lb/hr/rpm
	N_p = pump speed	rpm
	k_2 = change in pump flow per psi	lb/hr/psid
	ΔP = back pressure - inlet pressure	psid

also

$$\Delta P = P_B + \Delta P_{noz} - P_1 \quad ②$$

where	P_B = burner pressure	psia
	ΔP_{noz} = burner nozzle pressure drop	psid
	P_1 = pump inlet pressure	psig

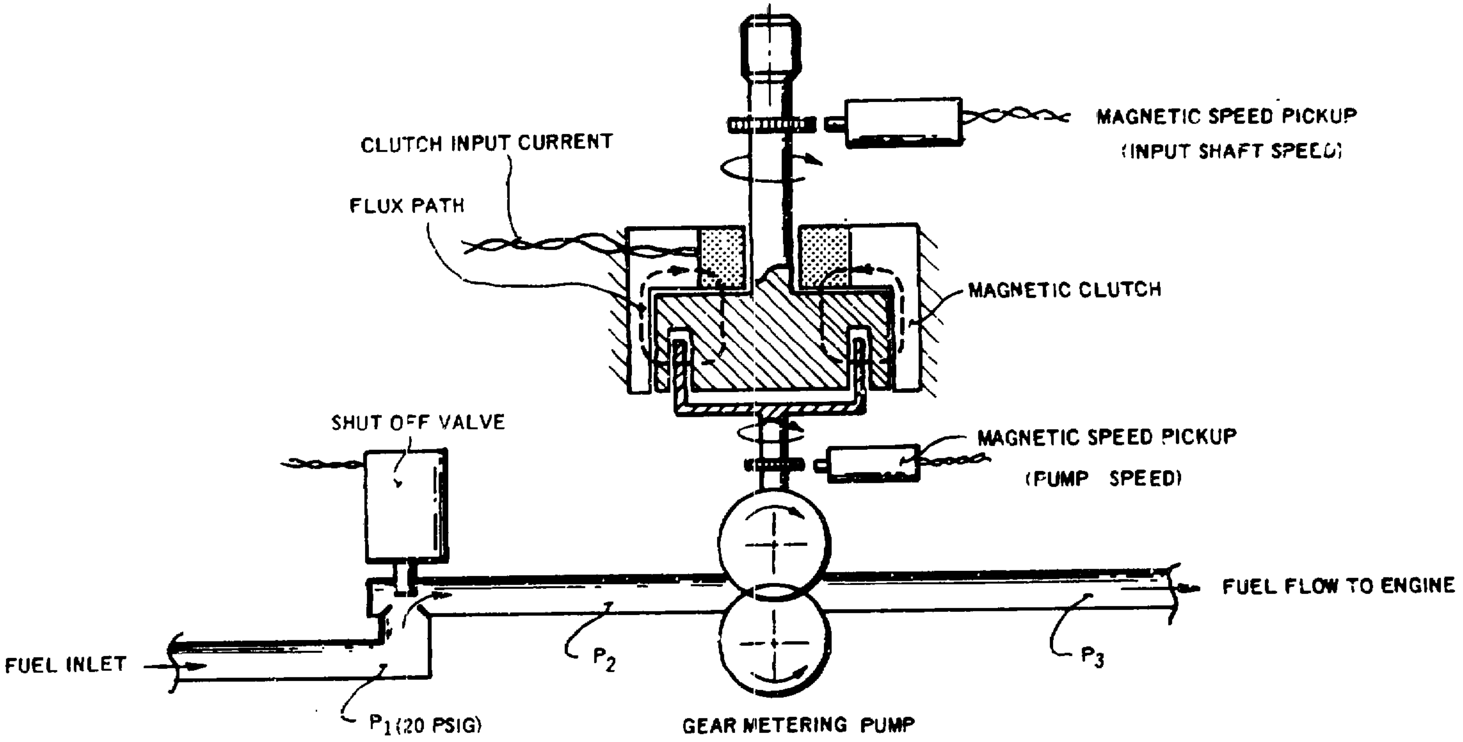

Figure 3. Schematic of Magnetic Clutch System.

P_B is defined during acceleration (and similarly during deceleration by

$$W_f = k_3 \ P_B\sqrt{\theta} \qquad ③$$

and $$\Delta P_{noz} = k_4 \ W_f^{\,2} \qquad ④$$

hence $$\Delta P = k_4 \ W_f^{\,2} + \frac{1}{k_3\sqrt{\theta}} \ W_f - P_1 \qquad ⑤$$

Substituting for ΔP into ① produces an engine working line of the form:

$$N_p = k_5 \ W_f^{\,2} + \frac{k_6}{\sqrt{\theta}} \ W_f - k_7 \qquad ⑥$$

where k_5, k_6, k_7 are burner nozzle, acceleration/deceleration, and inlet pressure constants, θ is the ambient temperature correction.

Equation ⑥ is superimposed on the gear pump map in Figure 4 for an engine acceleration line covering sea level to 20,000 ft conditions (60°F day). If the same plot is done for different ambient temperatures (-65°F to 135°F) and for engine deceleration, the error in required fuel flow for a given scheduled pump speed is within ± 2% of point. If required, fuel flow errors due to variations in ambient temperatures can be compensated for in the electronic control system.

Magnetic Clutch Design

A section drawing of the magnetic clutch is shown on Figure 5. This drawing also shows the gear pump and magnetic speed pickup.

The clutch input shaft is made of Stellite 6B. This material meets the mechanical requirements for a drive shaft and is non-magnetic to satisfy electrical requirements. The input shaft is supported between two ball bearings. The bearings are grease-packed with Mobil 28. The output shaft (drive shaft to the gear

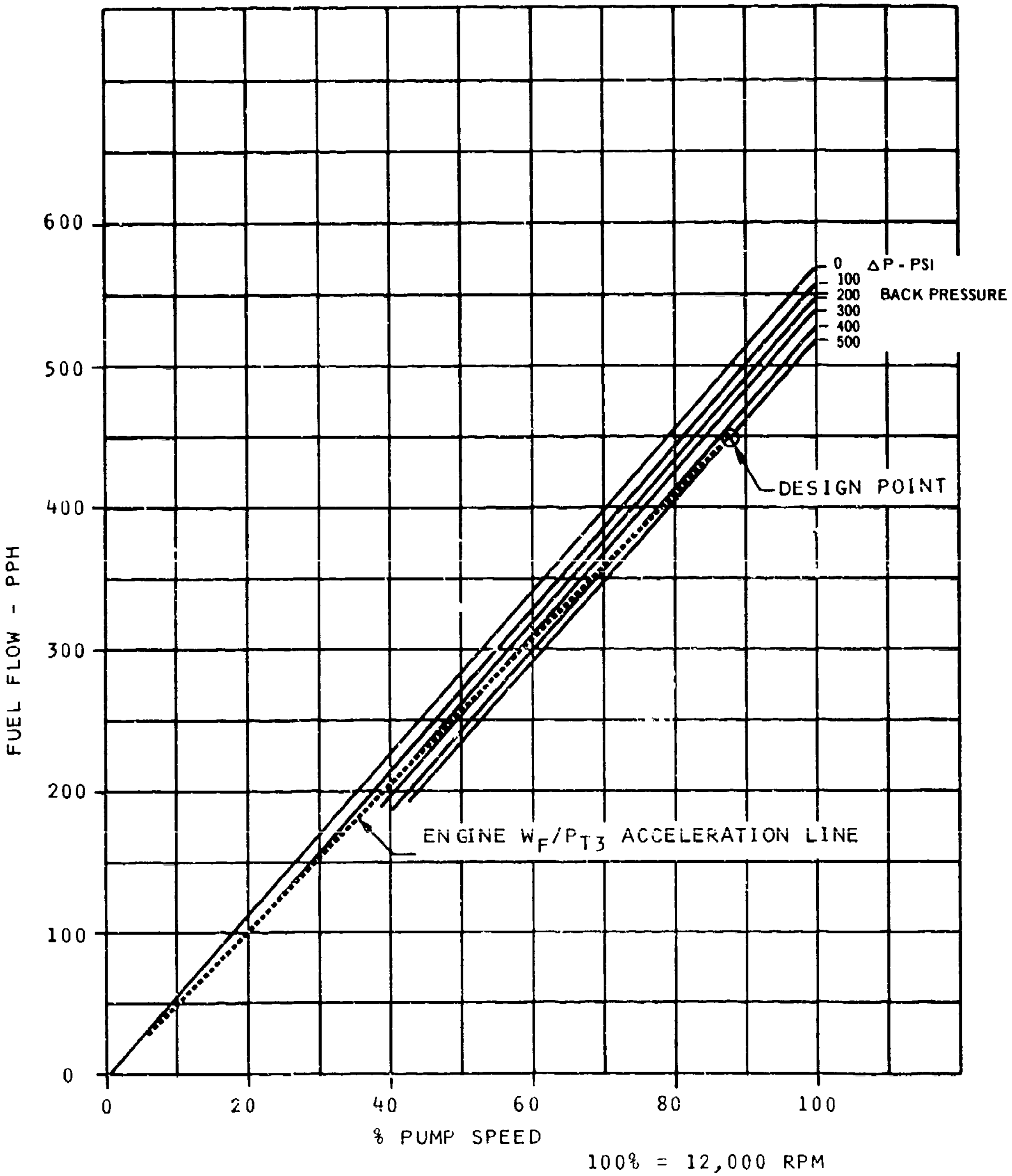

Figure 4. Predicted Gear Pump Characteristic.

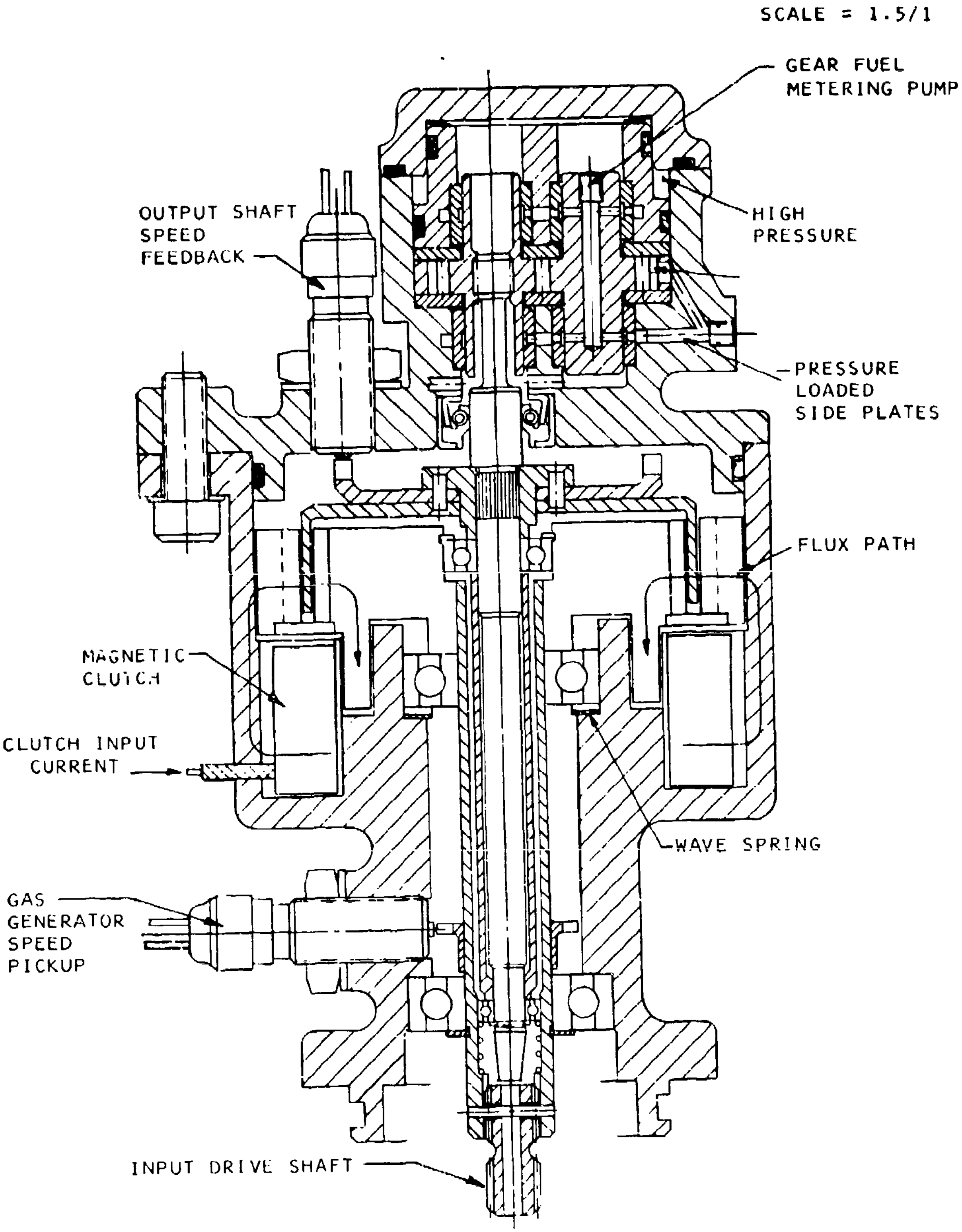

Figure 5. Magnetic Clutch System Layout.

pump) is concentric with the input shaft and is also supported by two grease-packed ball bearings mounted in the input shaft. The bearings for the input and output shafts are spring-preloaded.

The magnetic flux passes from the coil (1500 turns) through the outer part of the housing to a cylinder bonded to the input shaft and back through the inner part of the housing. The cylinder on the input shaft has an annular slot, into which fits a close clearance cup that is attached to the output shaft. Torque is transmitted to the pump by magnetic interaction between the input rotor and the output shaft cup.

The clutch was designed to provide a maximum of 67 in.-oz. torque at 250 milliamps.

Gear Pump Design

The pump is designed to provide high volumetric and overall efficiency to minimize power requirements and hence the size of the magnetic clutch. To provide high pump efficiency, the pump is designed with pressurized side plates and a pressurized tip seal at the pump discharge. The materials chosen to minimize wear and give high volumetric and overall efficiency are as follows:

Gears -	tool steel
Pressurized side plates and tip seal block -	tungsten carbide
Shaft seal -	lip type
Bearings -	lead bronze

The pump bearings are cooled and lubricated with fuel that is provided from the centrifugal head generated by the difference between the journal and gear tip diameters. This represents 4.6 psid at 100% speed (12,000 rpm).

The design of the gear pump does not involve any high risk development items such as high bearing loading, sliding velocities, or Hertz stresses. The basic design data is as follows:

Diametral Pitch	24.
Outside Diameter	0.666 inches
Number of Teeth	14
Gear Width	0.197 inches
Maximum Hertz Stress	47,263 psi
Maximum Tip Sliding Velocity	16.7 ft/sec
Journal Diameter	0.34 inches
Journal Length	0.34
Journal PV (19 x 8170)	156,000 psi ft/min

Shutoff Valve Design

The fuel shutoff valve is a fully developed solenoid operated poppet valve, supplied by G. W. Lisk, Clifton Springs, N. Y. and used in a production fuel control system. The valve is opened by applying 28 v to the coil, and closed by a spring. The shut off valve is installed by screwing it into the housing on the inlet side of the gear pump. The poppet valve has a polyurethane seal for positive fuel shutoff and has a nominal stroke of 0.03".

Magnetic Pickup Design

The magnetic speed pickups are supplied by Airpax, Fort Lauderdale, Florida. The pickups are screwed into the pump housing as shown on Figure 5. The pickup signal is generated by a toothed wheel with tooth spacing designed to provide a minimum peak to peak voltage to 1.8 v at 700 cps.

Magnetic Clutch System Testing

The magnetic clutch system is shown set up on the test stana on Figure 6, and a photograph of the disassembled hardware after 59 hours of testing is shown in Figure 7.

Magnetic Clutch Tests

The magnetic clutch was tested to determine the output torque for various slip speeds and input currents. A performance map of test results is shown on Figure 8. The clutch was also tested to ensure sufficient heat dissipation capacity. The tests show that the torque and heat capacity of the clutch are satisfactory to meet pump requirements.

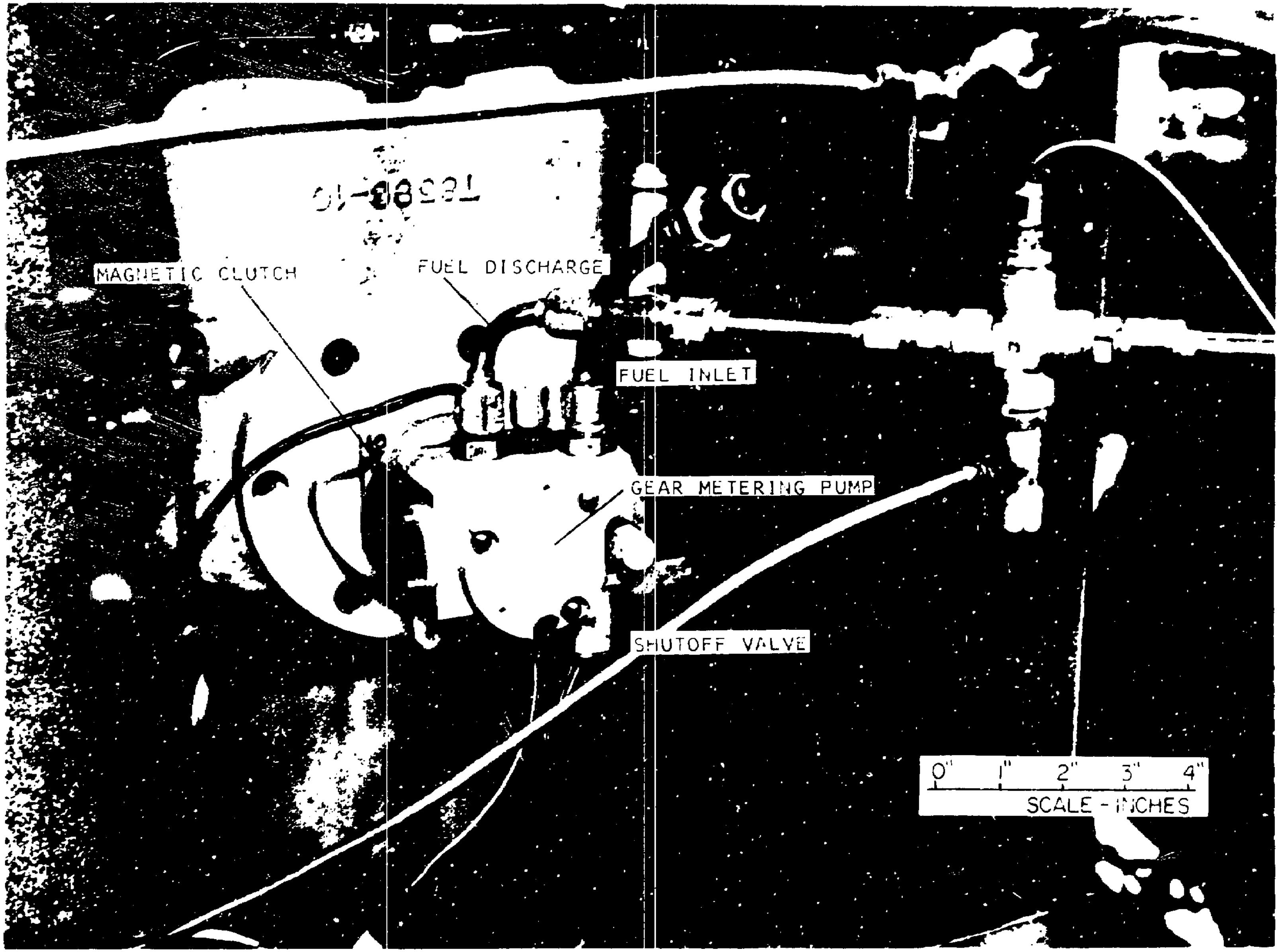

Figure 6. Magnetic Clutch System Test Setup.

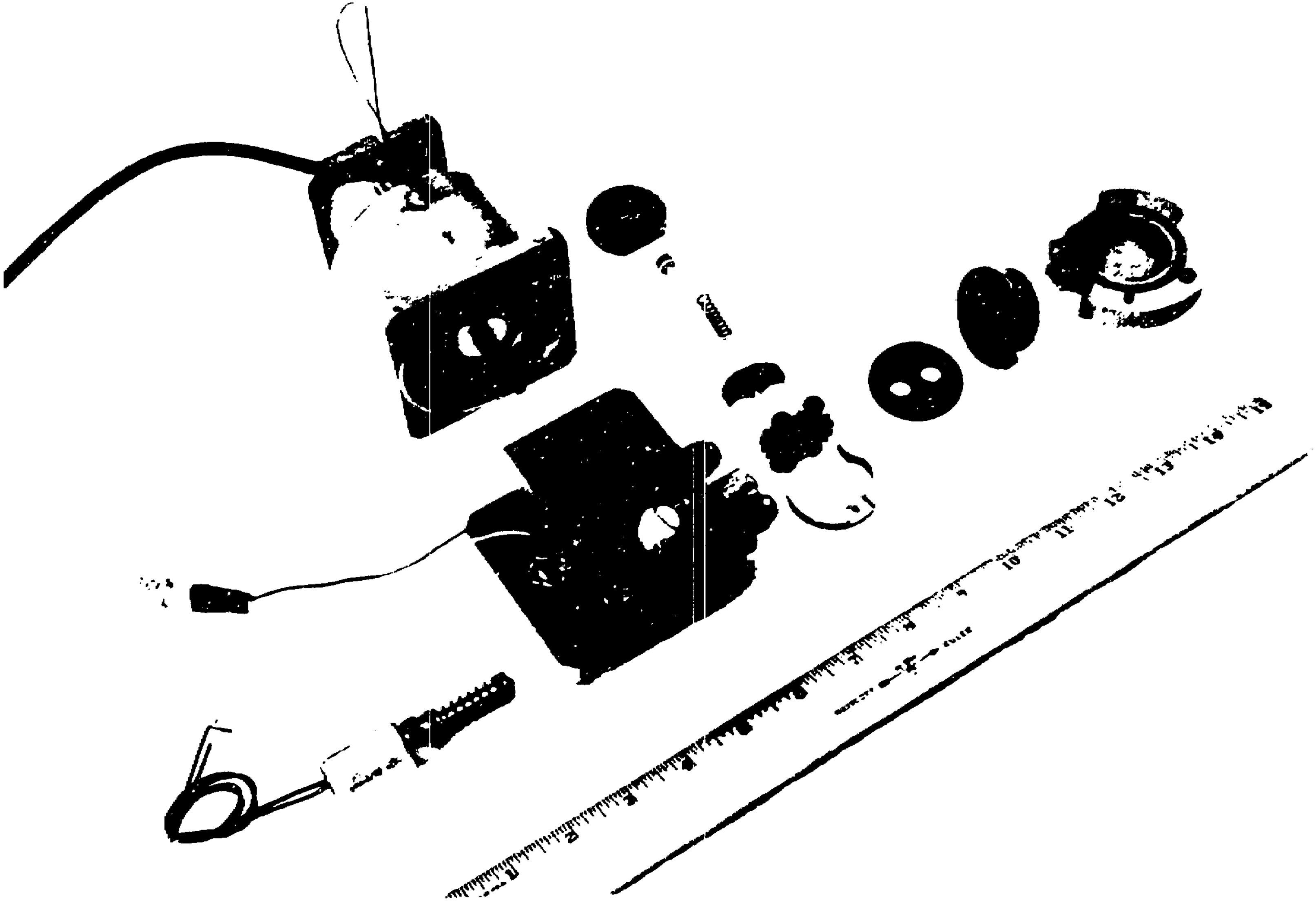

Figure 7. Magnetic Clutch System Components After Development Testing.

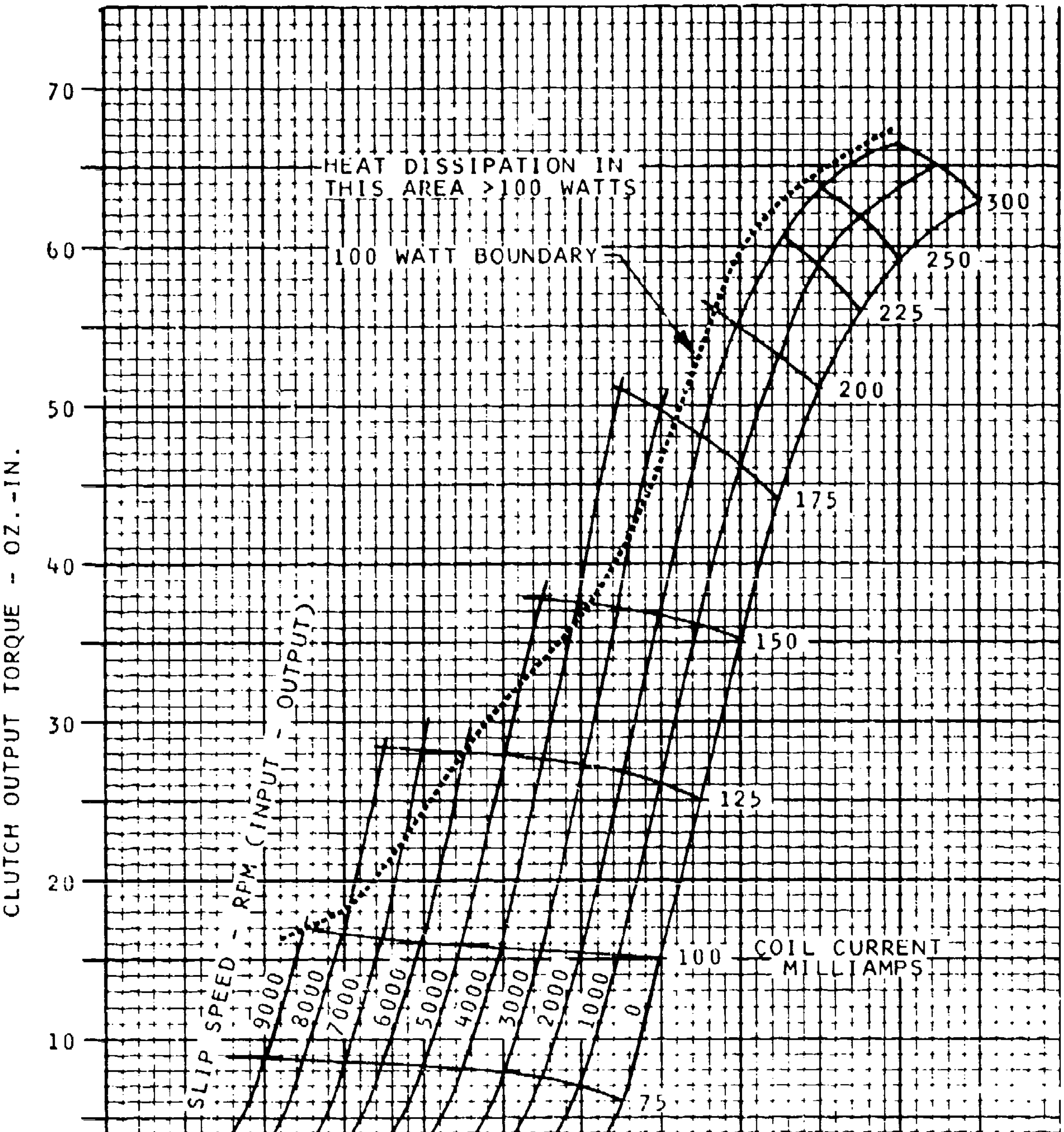

Figure 8. Magnetic Clutch Characteristic.

Gear Pump Tests

Performance of the gear pump is presented on Figures 9 and 10. The gear pump performed satisfactorily when driven by the magnetic clutch throughout the speed range tested. Starting (breakaway) torque was 17.0 oz.-in. which was slightly higher than anticipated. This value could be reduced by further development effort.

Figure 9 shows pump flow vs. rpm over the operating pressure range requirements. This figure, and Figure 10, show a volumetric efficiency of 90% at the design point of 88% rpm, 458 psia discharge pressure. Maximum pump overall efficiency demonstrated was 57% at 12,000 rpm and 480 psi pressure rise. Input power data was taken using the clutch characteristics relating torque, slip, and coil current in milliamps. This provides an accurate method of determining pump power requirements.

The pump demonstrated the ability to operate without loss of performance with 70°F JP-4 fuel and 0 psia inlet pressure. This is the equivalent of 13.7 NPSP at the inlet and meets the inlet requirements of 135°F JP-4 fuel at 20 psig.

A curve of temperature rise vs. pump speed based on estimated engine requirements has been plotted on Figure 11. A comparison study between the magnetic clutch-driven gear pump system and a conventional bypassing gear pump system is presented in this figure. The curves shown account for magnetic clutch losses and the increased flow and back pressure requirements of a conventional bypassing system. The magnetic clutch system demonstrated lower temperature rise (higher overall efficiency) than the bypassing system throughout the performance range.

A summary of the pump performance data is given below.

Input Power (maximum)	.70 hp
Input Torque (maximum)	59 in.oz.
Input Torque (breakaway)	17 in.oz.
Volumetric Efficiency 12,000 rpm 480 psid, 536 pph	92.5
Overall Efficiency 12,000 rpm 480 psid, 536 pph	57

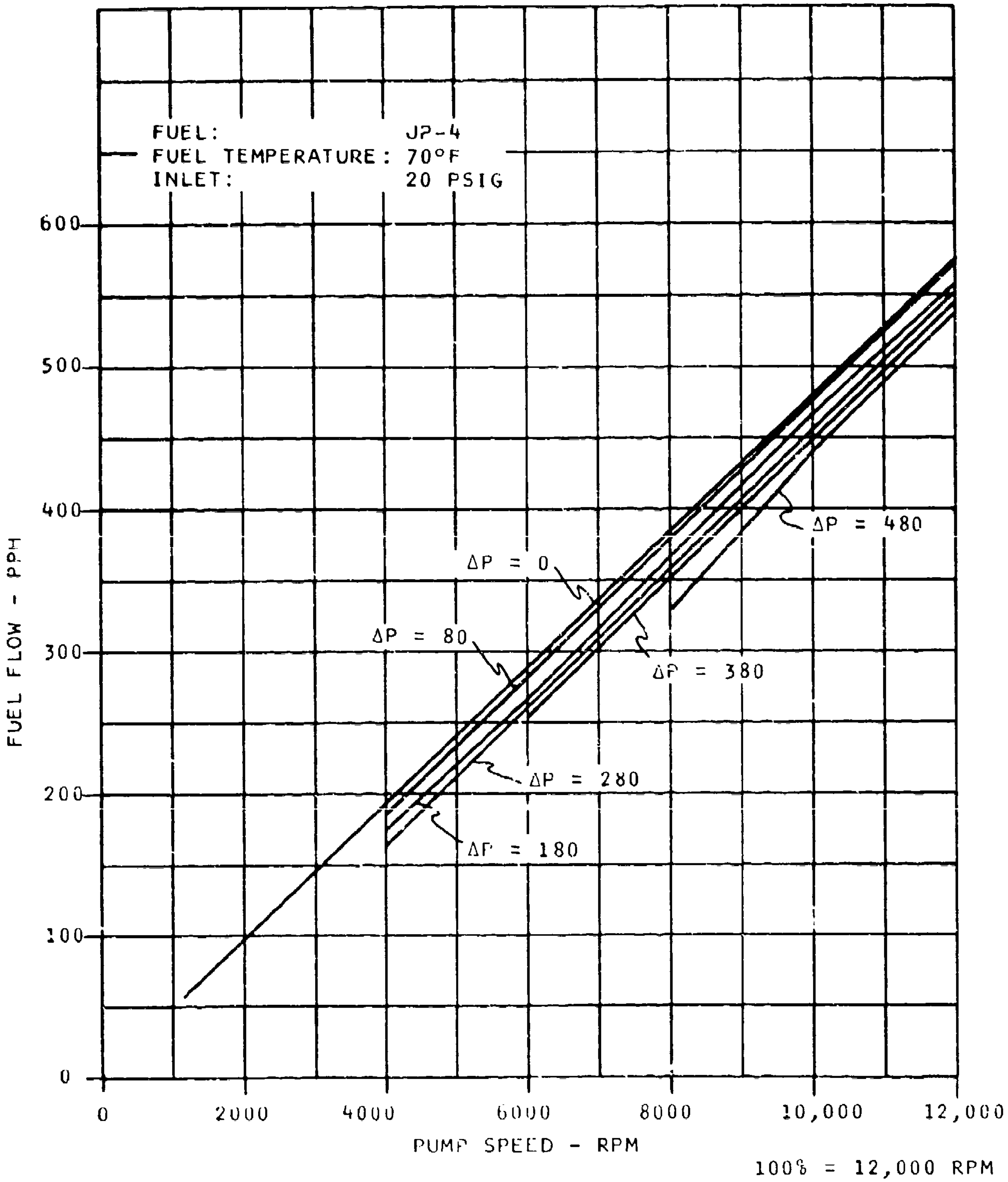

Figure 9. Gear Pump Flow vs. Speed.

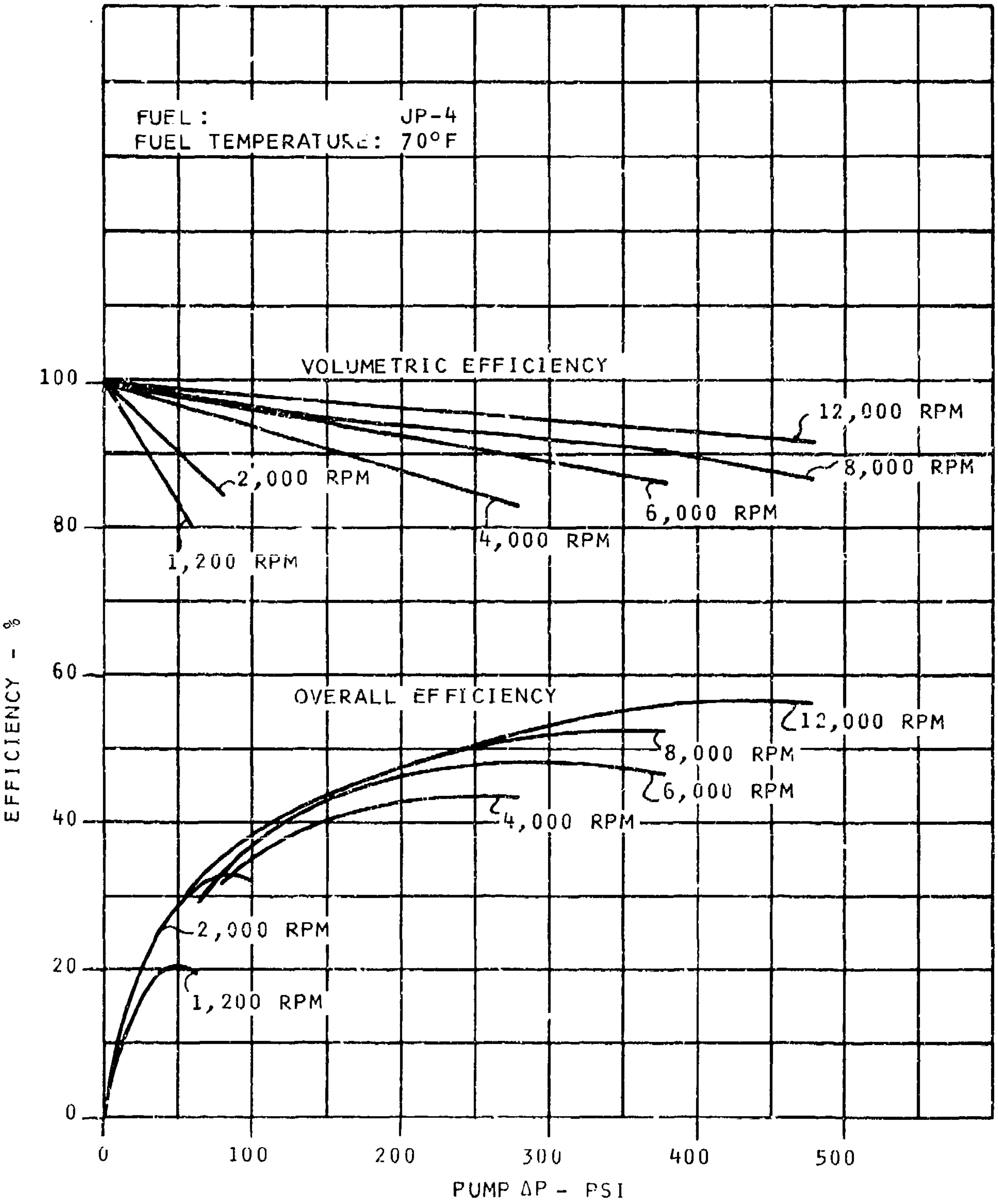

Figure 10. Efficiency vs. Gear Pump ΔP.

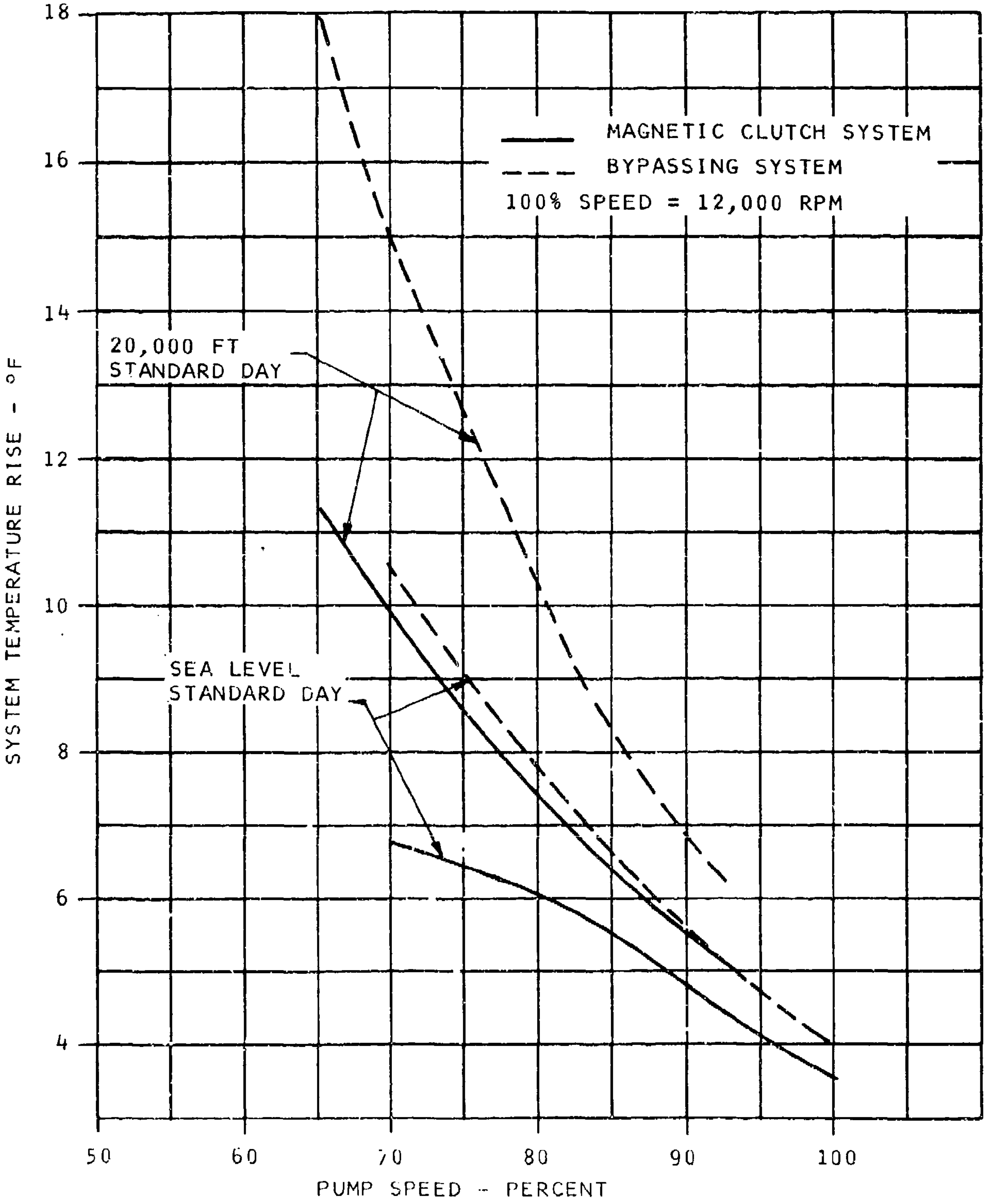

Figure 11. Maximum Fuel Temperature Rise Comparison.
Magnetic Clutch vs. Bypass Systems

Magnetic Speed Pickup Tests

The signal from the magnetic speed pickup was tested for form to verify that there was no magnetic interference from the clutch. The signal was found to be satisfactory in both form and signal strength.

Magnetic Clutch/Pump Dynamic Response

A closed-loop frequency response of the pump speed control loop was performed at two levels of fuel flow and is shown on Figures 12 and 13. The system has closed-loop natural frequency of about 20 rad/sec at low fuel flows and 35 rad/sec at high fuel flows. The calculated natural frequency is 32.5 rad/sec using nominal values of gain through the control loop, based on the linearized block diagram model of the system as shown below.

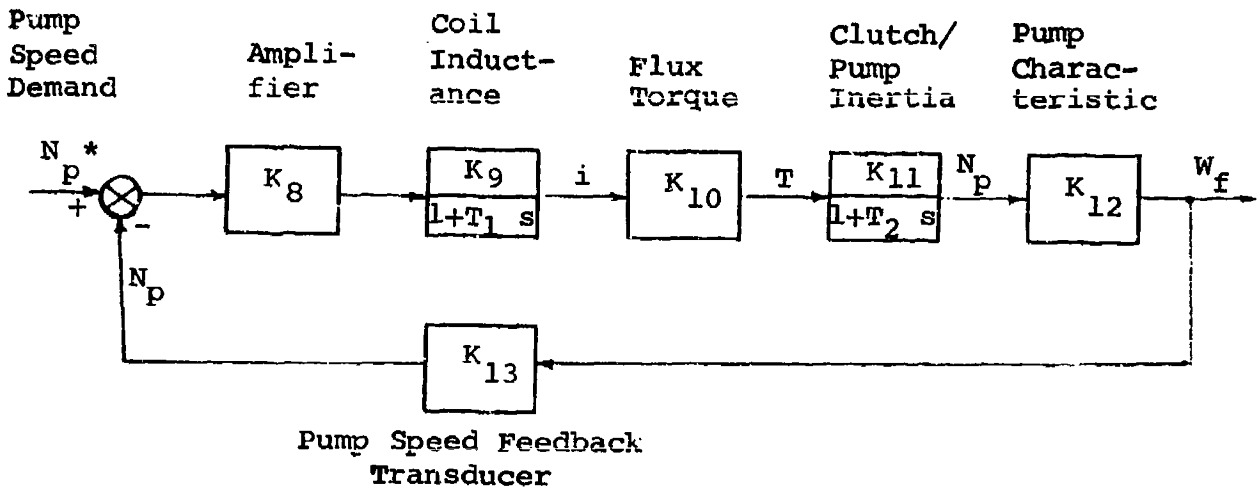

This gives a transfer function of pump speed to pump speed demand as:

$$\frac{N_p}{N_p^*} = \frac{\frac{1}{K_{13}}}{1 + \frac{\tau_1 + \tau_2}{K_8 K_9 K_{10} K_{11} K_{13}} s + \frac{\tau_1 \quad \tau_2}{K_8 K_9 K_{10} K_{11} K_{13}} s^2}$$

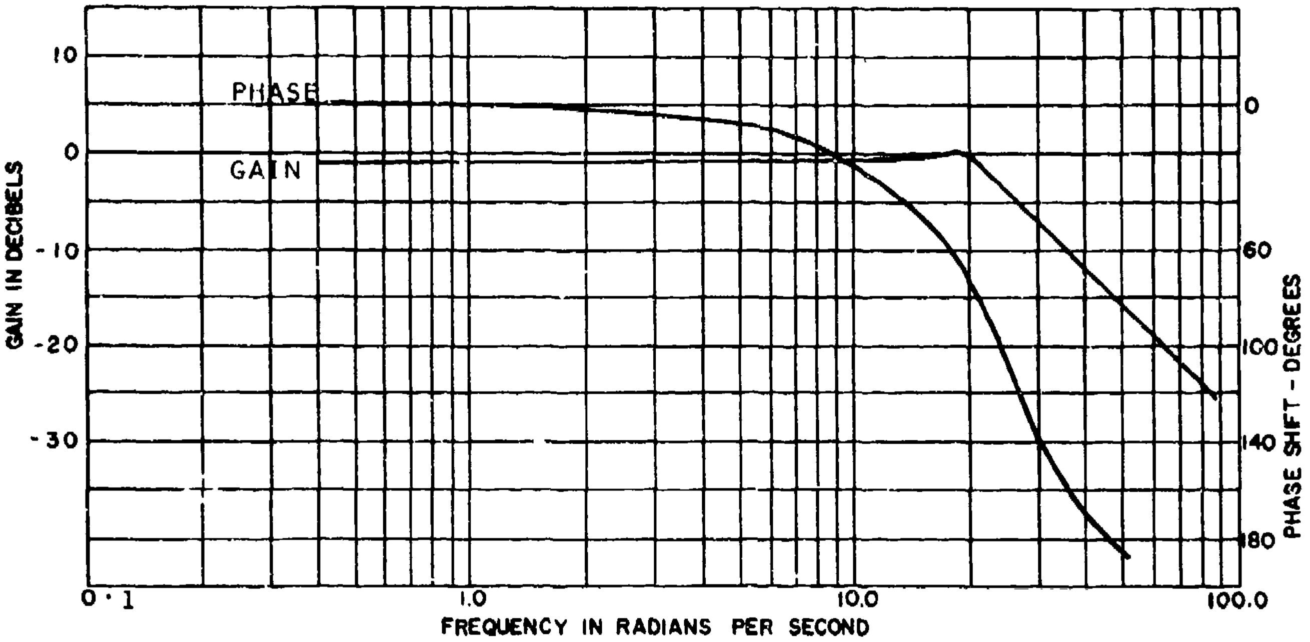

FIGURE 12. MAGNETIC CLUTCH CLOSED LOOP FREQUENCY RESPONSE AT PUMP SPEED 2000 RPM (W_F = 100 PPH)

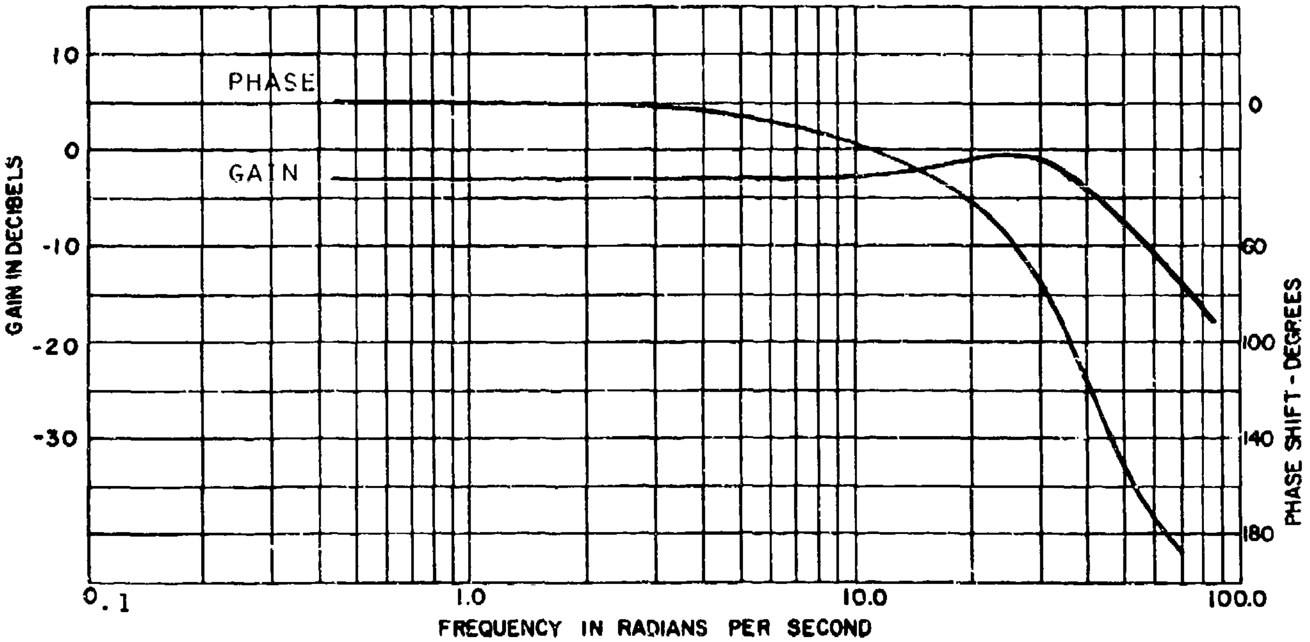

FIGURE 13. MAGNETIC CLUTCH CLOSED LOOP FREQUENCY RESPONSE AT PUMP SPEED 9000 RPM (W_F = 410 PPH)

The nominal design values for the above are:

τ_1 = 0.072 seconds (coil time constant

τ_2 = 0.032 seconds (output shaft inertia time constant)

$K_8K_9 = \frac{0.25}{5}$ amp/volt

K_{10} = 455 oz in/amp

K_{11} = 186 rpm/oz in.

$K_{13} = \frac{5}{12000}$ volts/rpm

The form of the transfer function is second order and the value of K_8 has been chosen to give a damping ratio of 0.7 and a natural frequency of 32.5 rad/sec. This corresponds favorably with test results and compares with the dynamic response of conventional fuel metering systems.

Conclusions and Recommendations

1. The magnetic hysteresis clutch and gear metering pump meet the performance requirements of this program.

2. Themagnetic clutch system produces a lower fuel temperature rise than a conventional gear pump and bypass-type fuel metering system. This is because with the conventional bypass system, the pump has to be oversized to provide starting flow and operates at a slightly higher back pressure because of pressure losses in the fuel metering system. As a consequence, the magnetic clutch system uses as much as 25% less power from the engine at a specific operating condition.

3. The pump starting torque and torque at low speeds is higher than anticipated. The system satisfactorily metered fuel flow down to 22 lb/hr. At 16 lb/hr, the fuel flow oscillated ± 5% due to high pump friction torque. Increasing the pump speed control loop gain would reduce the amplitude of this oscillation and increase the frequency; however, the loop gain was chosen to optimize the transient control of the engine. Therefore, a better solution is to improve the pump overall efficiency at low pump speeds through material selections and coatings for reduced friction.

4. The magnetic clutch provides an accurate method of determining the pump overall efficiency.

5. It is recommended that further effort be directed toward improving the gear pump overall efficiency to meter fuel flow down to 10 lb/hr.

6. It is recommended that work be conducted on the use of high density fuels to determine their effect on pump power consumption and volumetric efficiency.

4. CENTRIFUGAL PUMP SYSTEM

Description

A schematic of the centrifugal pump system is shown on Figure 14. Fuel is received from a pressurized source (20 psig) and passes through a solenoid shutoff valve. The fuel then enters the engine-driven, 70,000 rpm, high pressure centrifugal pump. The fuel is metered to the engine by a proportional solenoid-operated poppet-type metering valve which varies the flow area approximately linear to solenoid input current. The pressure drop across the solenoid metering valve (P_4-P_5) is held essentially constant by a throttling head regulator. The fuel from the output of the metering valve flows to the engine. The system also provides a gas generator speed signal from a magnetic speed pickup directed at a toothed wheel on the pump drive shaft.

Centrifugal Pump Design

A cross section drawing of the pump and drive shaft is shown on Figure 15. The centrifugal pump design is a single stage open impeller with straight radial vanes. The open impeller design reflects the requirement for a simple low cost pumping system. The collector is a constant area type and discharges into a 7.5° (included) diffuser.

The impeller is supported in a carbon journal bearing, which is lubricated by clean fuel from a 25μ absolute barrier filter. The drive shaft seal is a carbon face seal.

The basic design parameters for the pump are as follows:

Design Point - at 88% Speed: $\Delta P = 432$ psid

$W_f = 435$ lb/hr

at 100% Speed: $\Delta P = 560$ psid
(70,000 rpm) $W_f = 500$ lb/hr

Head Coefficient $\psi = \frac{\Delta H}{U_2^2} g = .65$

ΔH = Head (1690 ft), ft. head

g = conversion constant

U_2 = impeller tangential velocity, ft/sec

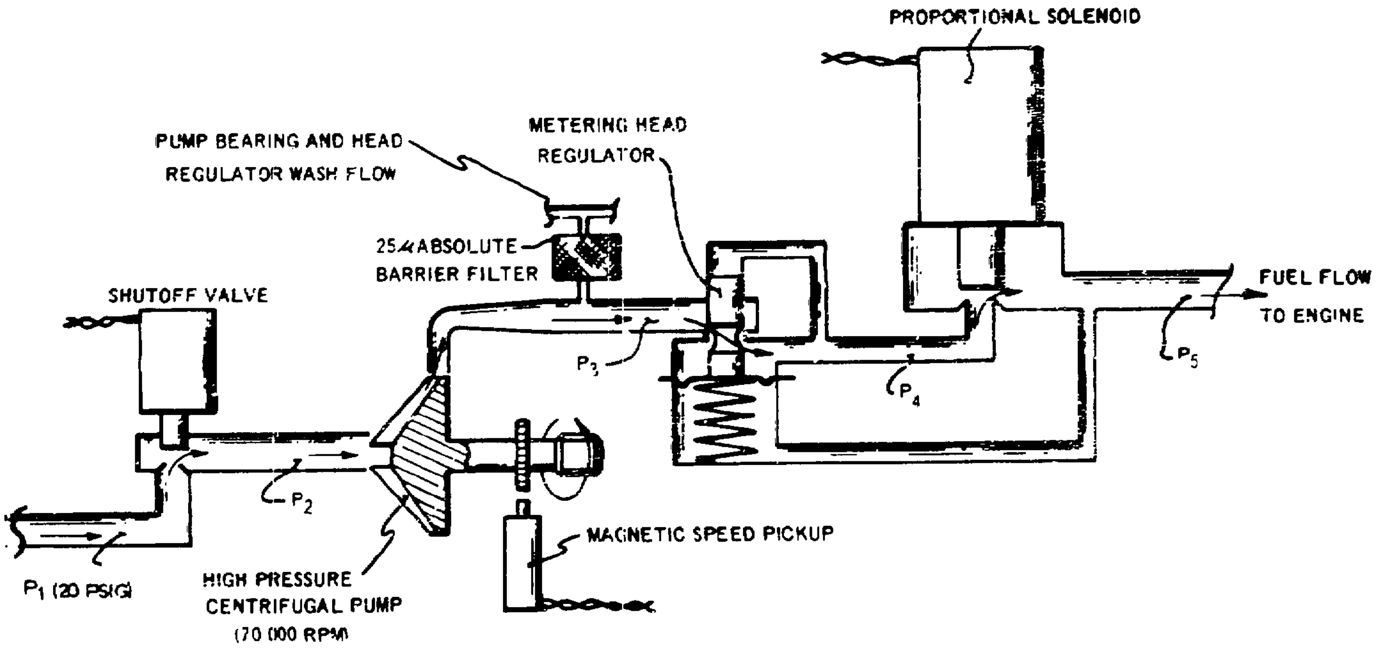

Figure 14. Schematic of Centrifugal Pump System.

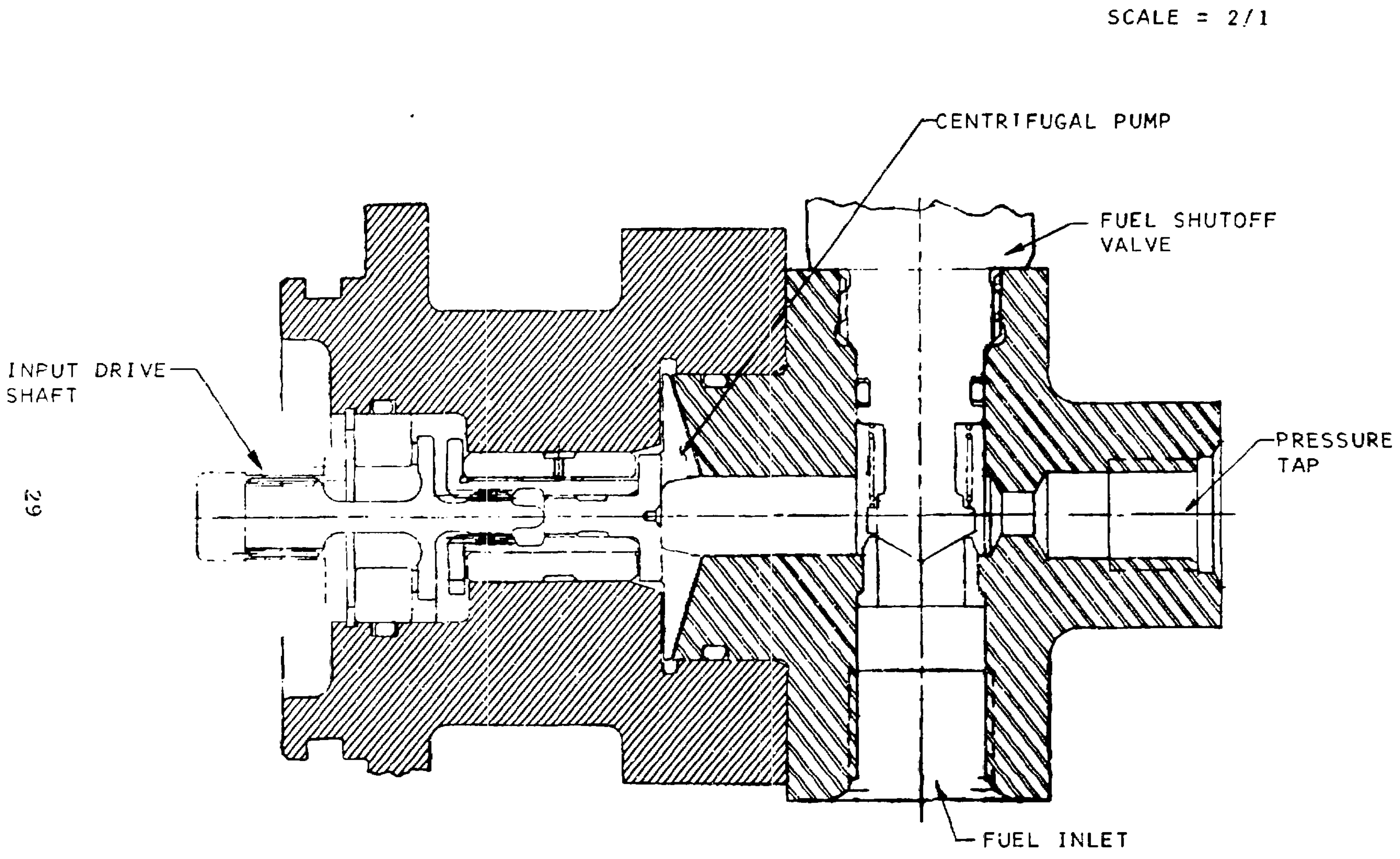

Figure 15. 70,000 RPM Centrifugal Pump Layout.

Impeller outside diameter = 1.015 inches

Impeller inlet diameter = 0.3 inches

Number of vanes = 14 (straight radial)

Specific Speed $= \dfrac{N_p\, Q^{0.5}}{H^{0.75}} = 300$

where Q = maximum flow, gpm

N_p = maximum impeller speed, rpm

H = head, ft.

The materials used in the pump are:

Impeller	Stainless Steel (AMS 5643)
Impeller Drive Shaft	Nitriding Steel (AMS 6470)
Journal Bearing	Silver Impregnated Carbon
Housings	Aluminum (AMS 4120)

Solenoid Metering Valve Design

The solenoid metering valve design is shown on Figure 16 The solenoid is provided by the Fema Corporation, Portage, Michigan. The input current to the coil comes from the electronic interface unit in the form of fuel flow demand. The magnitude of the signal is zero to 500 milliamps. The relationship between input current and plunger stroke or flow area is essentially linear. This is arranged by matching the characteristics of the coil, springs, and permanent magnet. A viscous damper is provided to dampen high frequency vibrations. The vibrations (150 cps) are produced by input disturbances from the fuel flow. An adjustable mechanical minimum fuel flow stop is provided.

Metering Head Regulator

The design of the metering head regulator is shown on Figure 17.

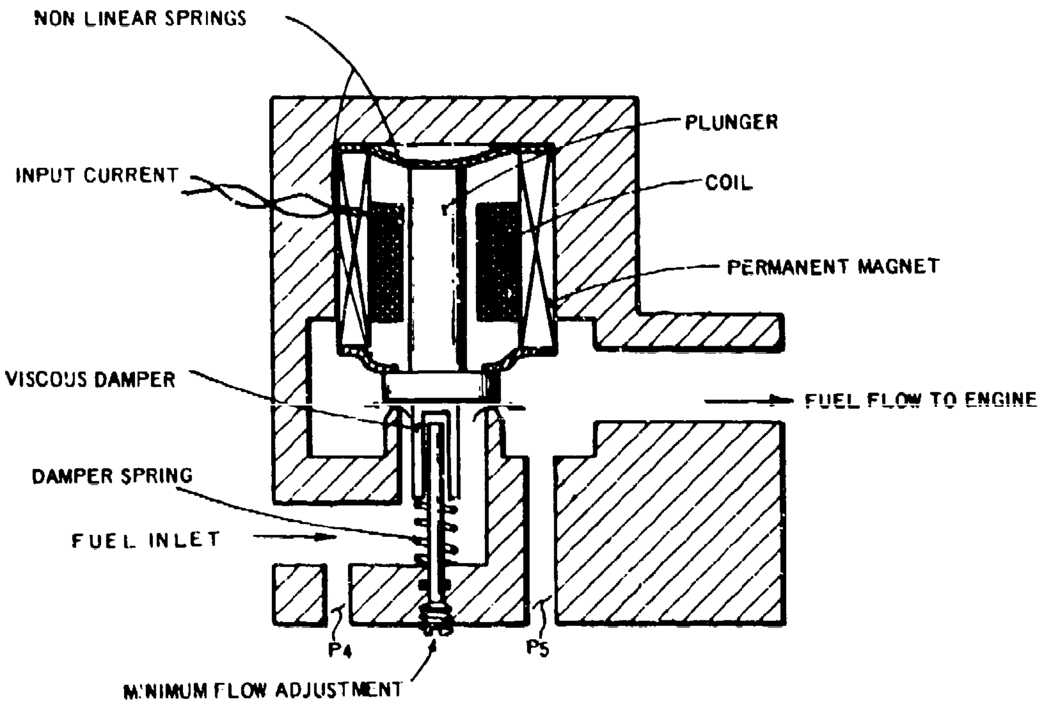

Figure 16. Proportion Solenoid Fuel Metering Valve.

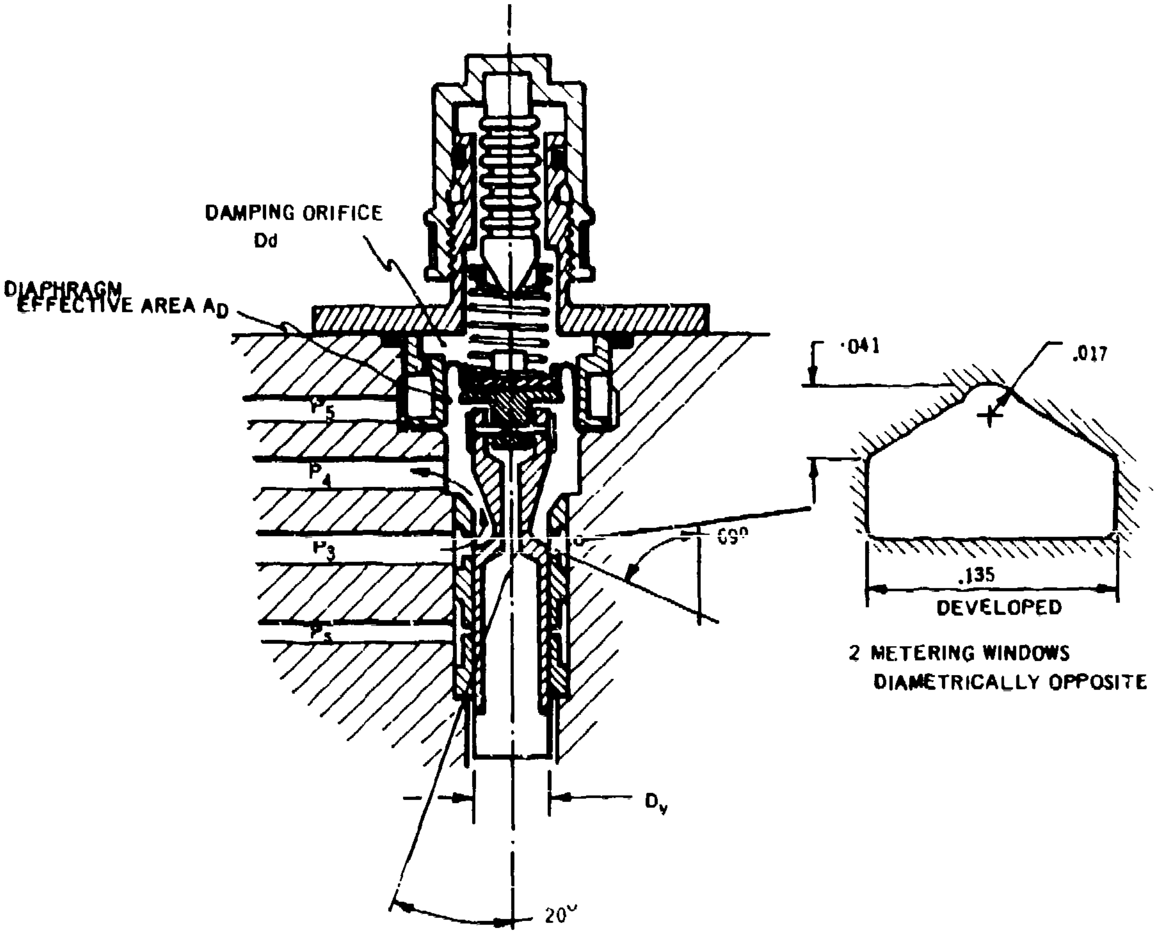

VALVE DIAMETER • D_v	0.375 IN
DIAPHRAGM EFFECTIVE AREA • A_D	0.287 in^2
DIAPHRAGM MATERIAL	LS • 53
SPRING PRELOAD	2.58 LB.
SPRING RATE	5 LB/IN
DAMPING ORIFICE • Dd	0.025 IN
FUEL TEMPERATURE COMPENSATION (TOLUENE FILLED)	-65°F TO 300°F
TIME CONSTANT (MEASURED)	0.025 SECONDS

Figure 17. Metering Head Regulator.

The metering head is sensed across a diaphragm such that if the head increases, the valve moves to throttle flow and reduce the head. Automatic fuel temperature compensation is provided. The regulator has an adjustment for fuel type. To minimize the valve friction, a wash flow of clean fuel is provided between the valve and sleeve. The clean fuel is supplied from a 25u absolute barrier filter.

Shutoff Valve

The same solenoid operated shutoff valve as the magnetic clutch system is used.

Gas Generator Speed Pickup

The same magnetic speed pickup is used as the magnetic clutch system, except that it is increased in fuel, and the body of the pickup is modified to allow an outside diameter fuel seal.

Centrifugal Pump System Testing

The centrifugal pump system is shown on the test stand on Figure 18. The system is also shown disassembled after 60 hours of testing, on Figure 19. There is no visible degradation of any of the components.

Centrifugal Pump Tests

Two centrifugal pump designs were manufactured for evaluation - one a shrouded design, and the other a fully open configuration. All other components in the system are identical. Sufficient testing was done to establish that the open impeller had better overall efficiency and head rise. A comparison of the open and shrouded impeller performance is shown on Figures 20 and 21. As a result of this evaluation, the open impeller design was selected for use in this program.

Open Impeller Performance

Performance of the centrifugal pump is presented by the head-flow curve shown in Figure 22. The data shows a rising head flow characteristic indicating a mismatch between the impeller and

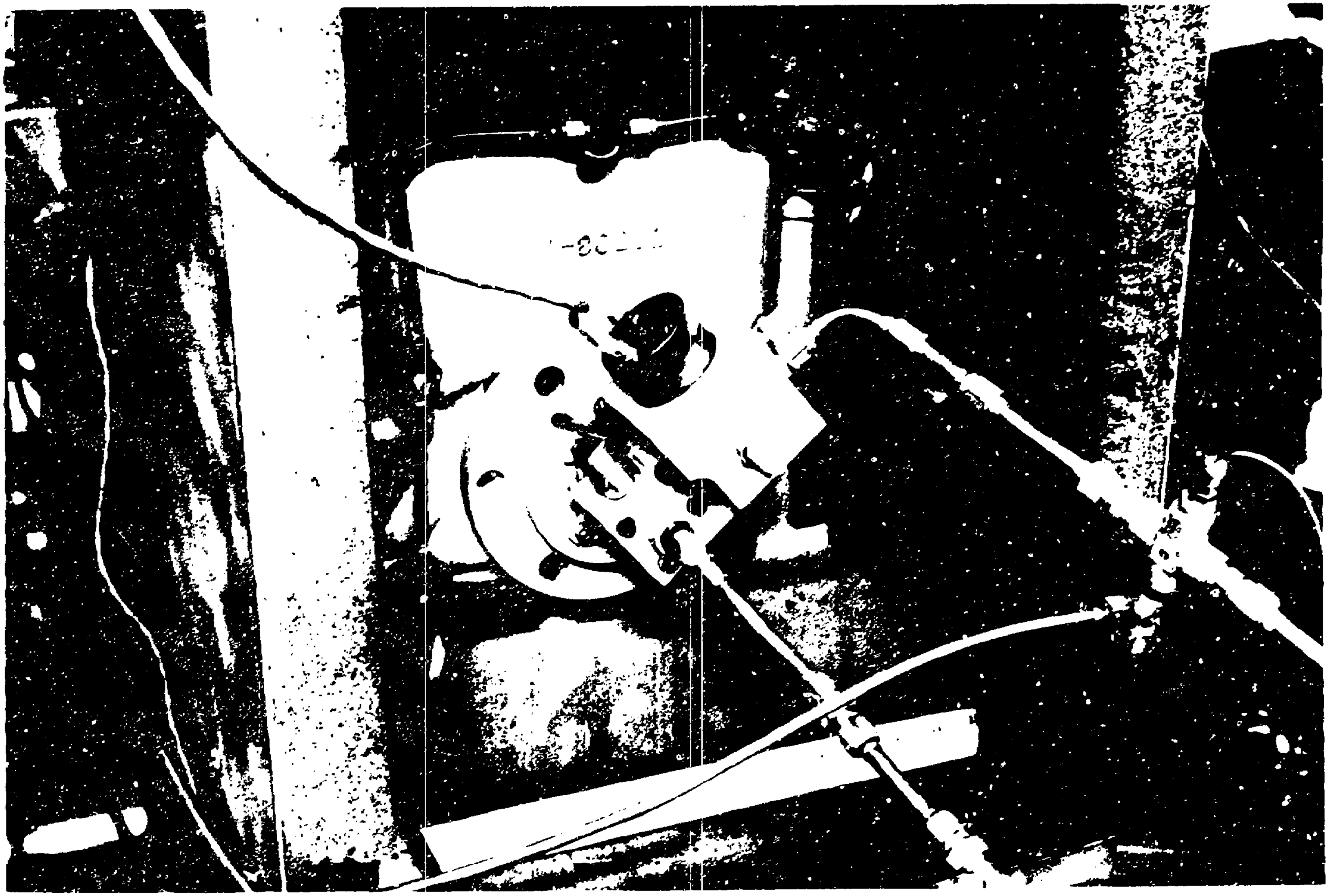

Figure 18. Centrifugal Pump System Test Setup.

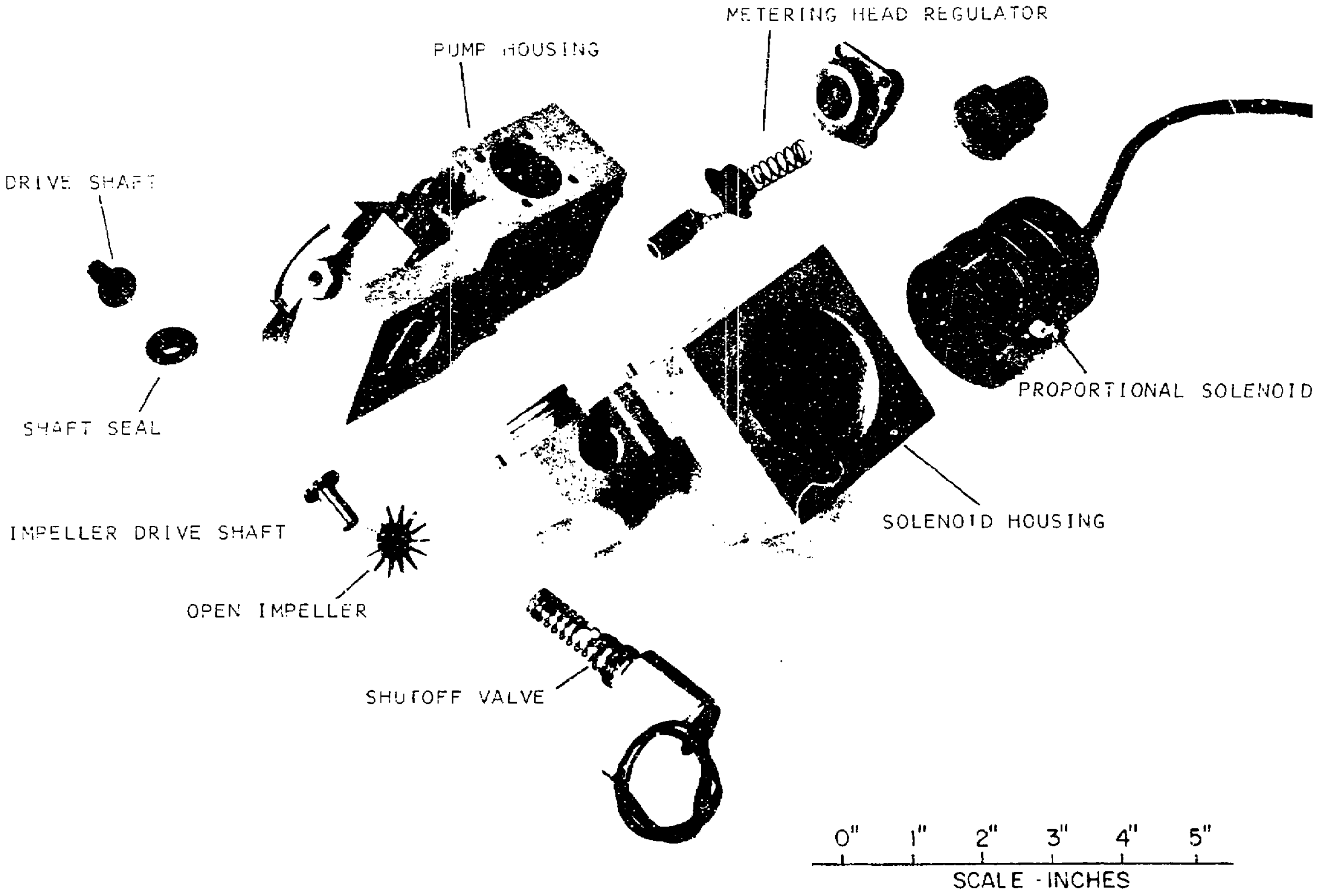

Figure 19. Centrifugal Pump System Components After Development Testing.

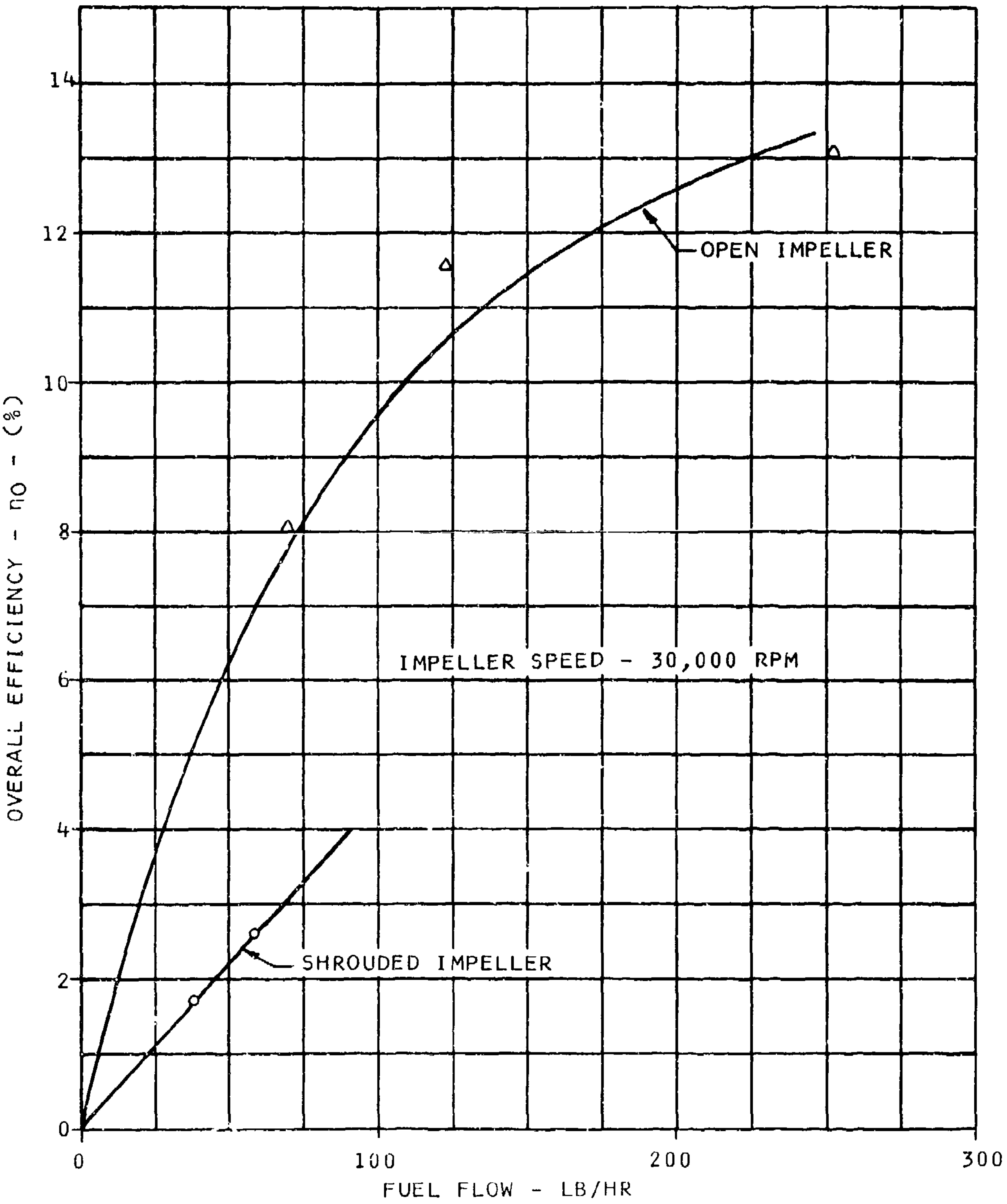

Figure 20. Open & Shrouded Impeller-Overall Efficiency Comparison.

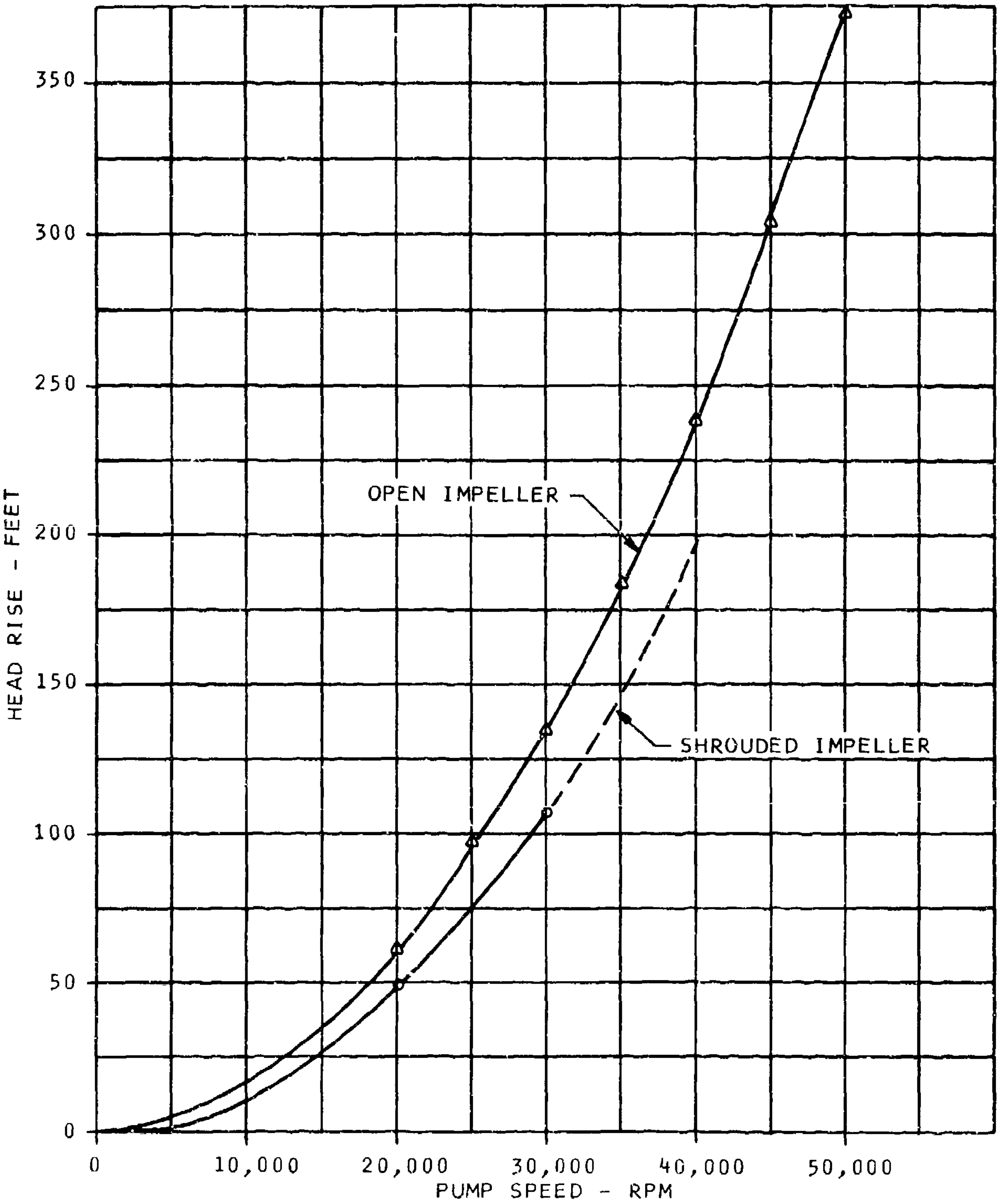

Figure 21. Open & Shrouded Impeller-Head Rise Comparison.

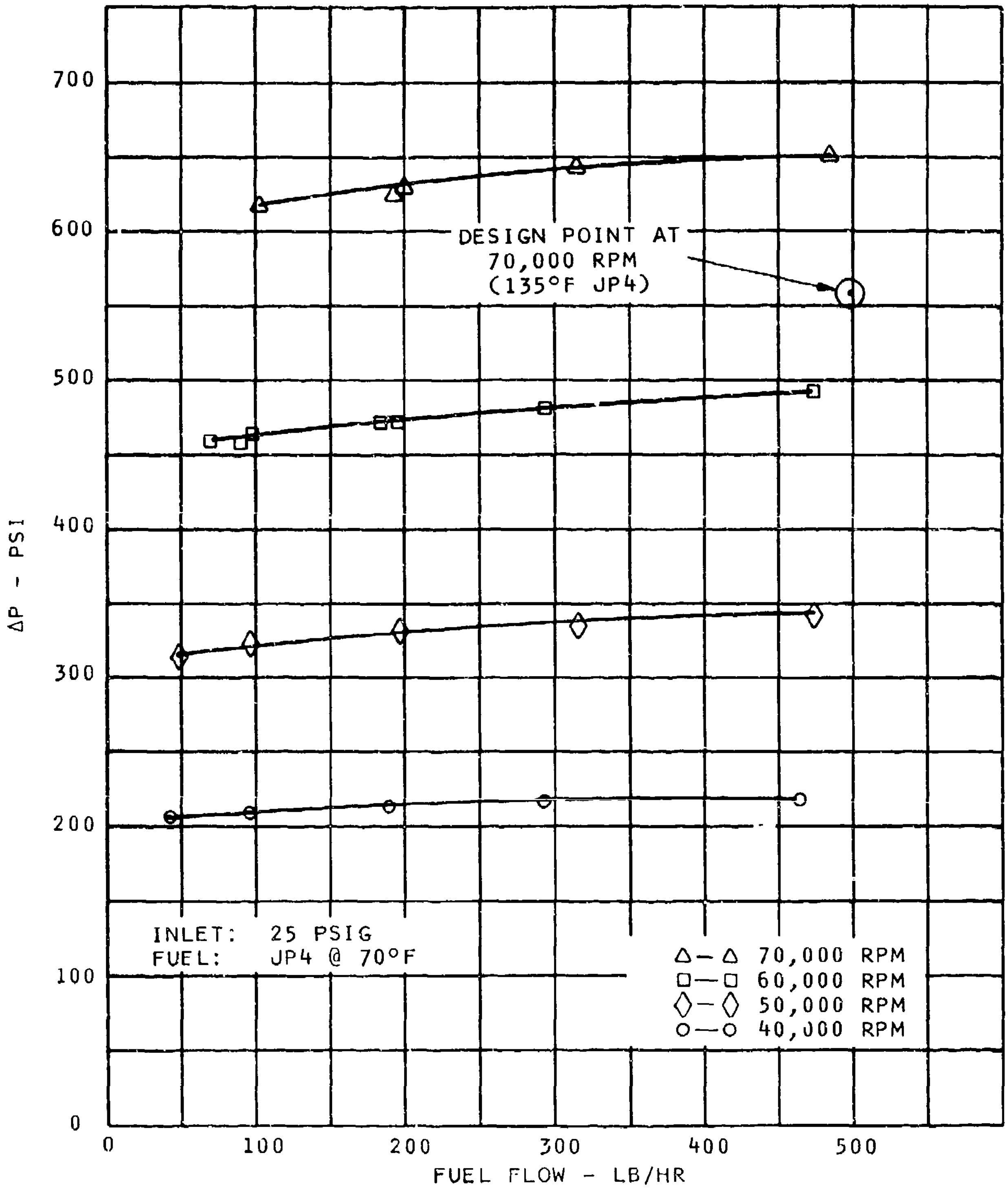

Figure 22. Centrifugal Pump Performance.

volute. This mismatch does not present a problem and is the result of reducing the original impeller OD because the unit was producing too much head rise. Reducing the impeller OD had a similar effect as enlarging the volute cross-sectional area.

A calculated pump efficiency curve is plotted on Figure 23. This curve was generated from the pump ΔT data which is presented on Figure 24.

Maximum Fuel Temperature

The maximum fuel temperature is at the outlet from the centrifugal pump, and occurs at conditions simulating an altitude of 45,000 ft., hot day with a fuel inlet temperature of 135°F. The maximum fuel temperature as a function of pump speed (or gas generator speed) is plotted on Figure 25. The highest fuel temperature is 277°F at a minimum flow of 50 lb/hr.

Since the highest fuel temperature is less than the fuel coking limit, the centrifugal pump system is satisfactory for operation throughout the flight envelope.

Performance of the unit operating at sea level inlet pressure and on 70°F JP-4 fuel demonstrated a minimum net positive suction pressure capability of 13.7 psi. This figure is adequate to insure satisfactory performance at inlet conditions of 20 psig and 135°F JP-4 fuel, and demonstrates a suction specific speed capability of 5000.

$$\text{suction specific speed} = \frac{\text{RPM}\sqrt{\text{GPM}}}{\text{NPSH}^{.75}}$$

A summary of pump performance data is given below.

head coefficient = .65

max OA efficiency = 13.5%

" flow = 486 pph
" rpm = 70,000
" Δp = 656.5
temp. rise 70,000 rpm 104 pph = 92°F
suction specific speed = 5,000

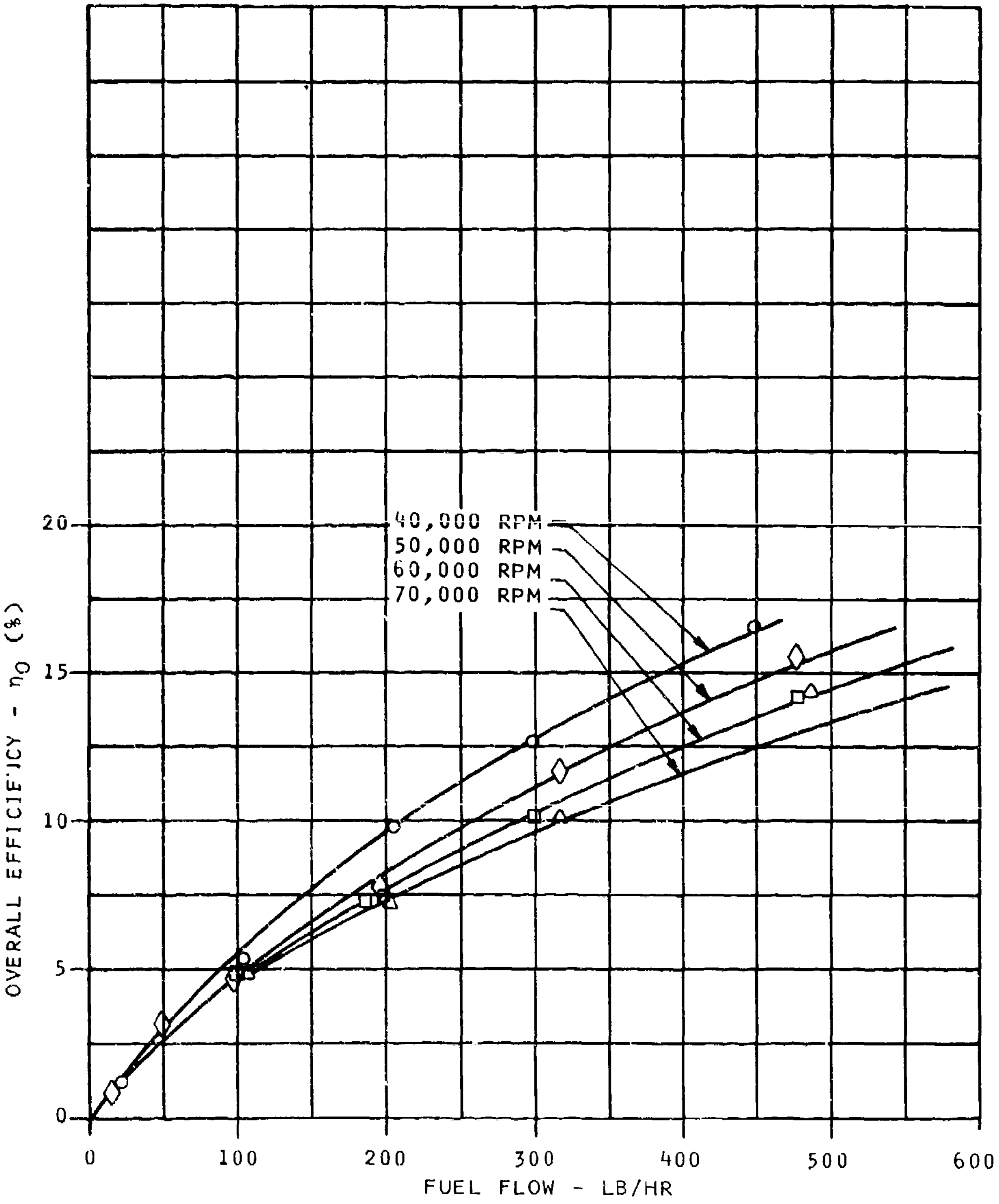

Figure 23. Centrifugal Pump Overall Efficiency.

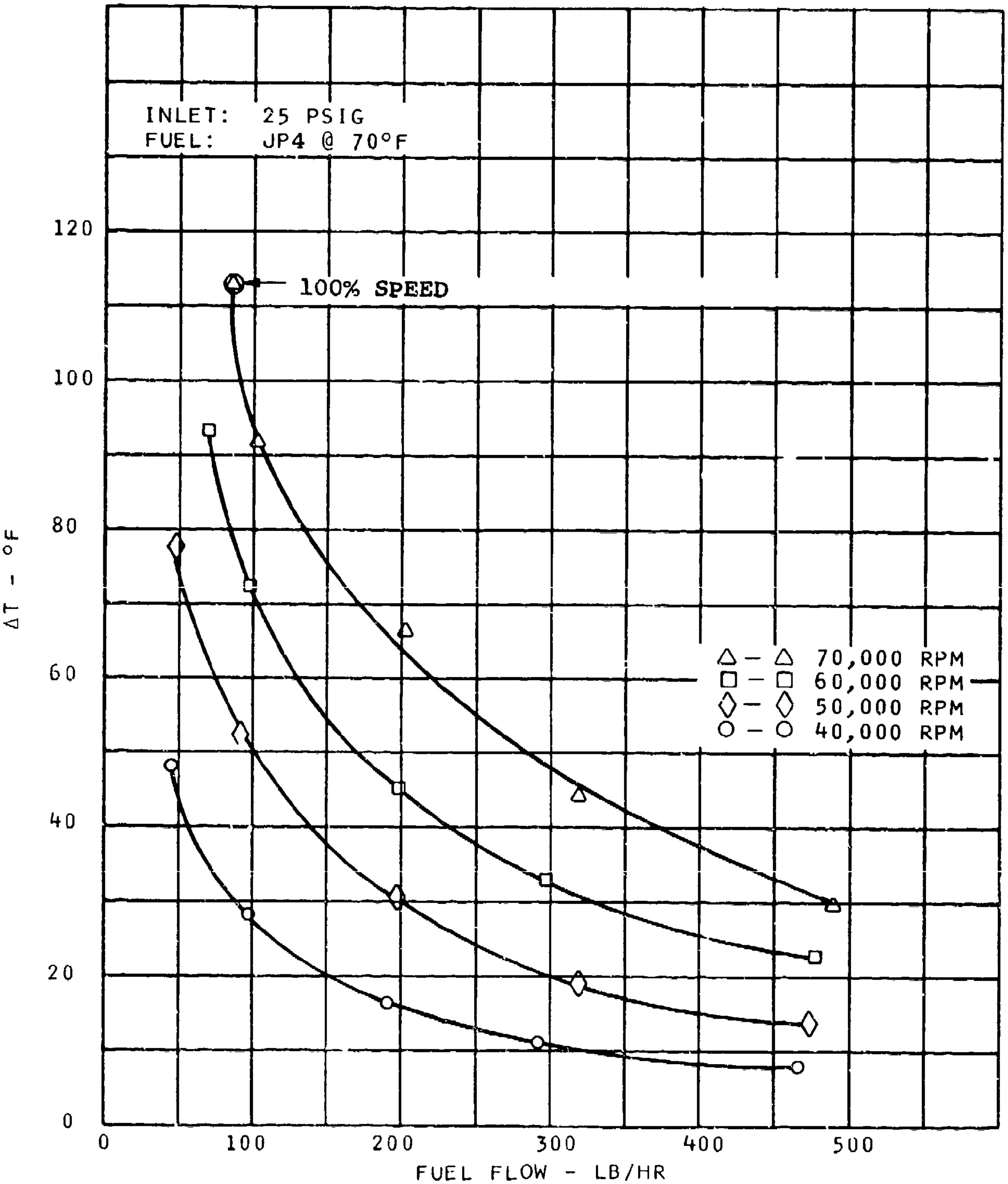

Figure 24. Centrifugal Pump Fuel Temperature Rise.

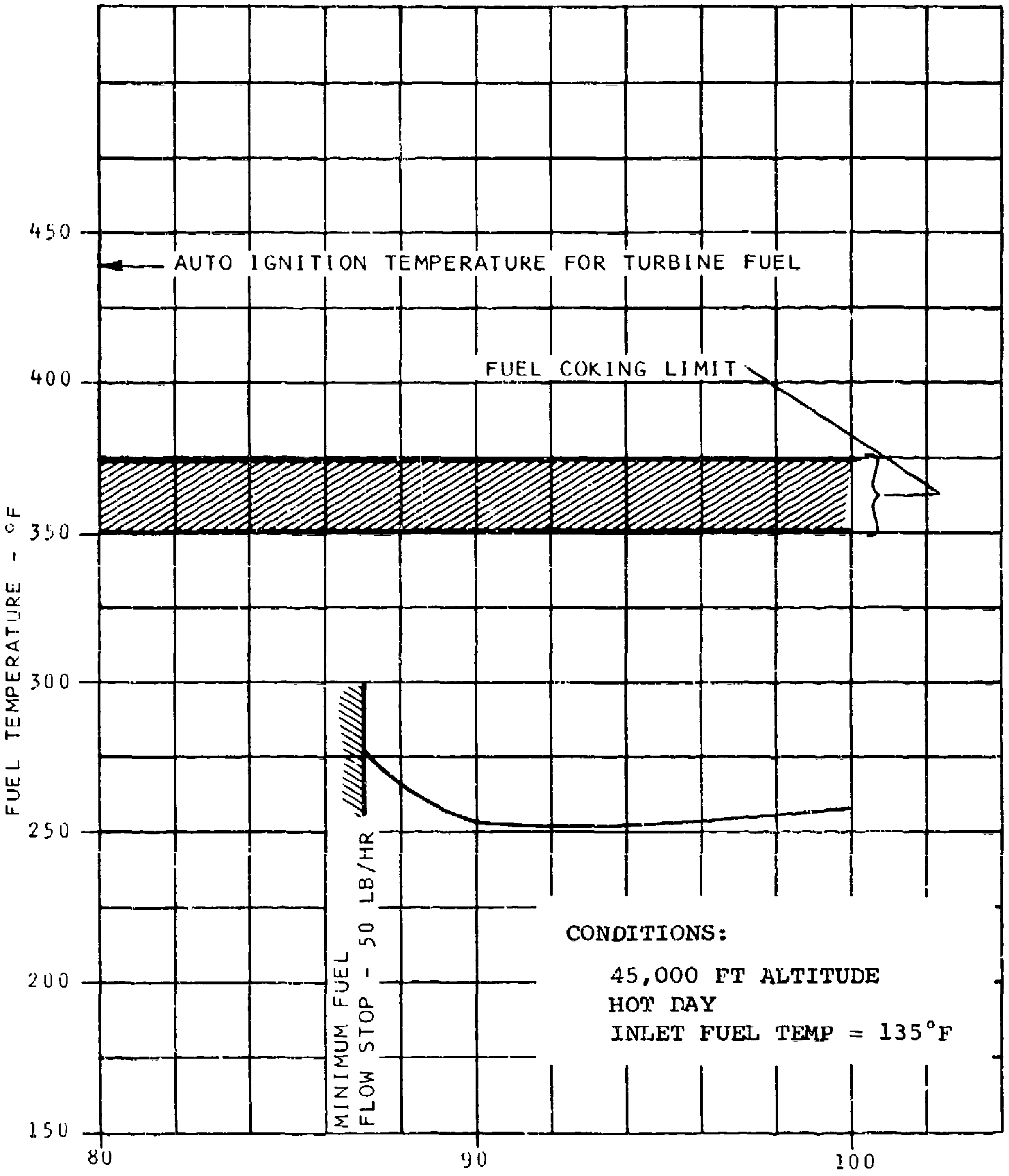

Figure 25. Maximum Steady State Fuel Temperature With Centrifugal Pump System.

Head Regulator Tests

The head regulator characteristics are shown on Figure 26 The performance of the regulator is satisfactory for meeting system requirements. The droop characteristic is a function of fuel flow and therefore can be compensated for if required in the electronic computer by modifying flow schedules. The variation in regulated pressure with the pressure levels is only .1 psi for a 100 psi change in pressure which also, if necessary, could be compensated for in the electronic computer. However, this should not be necessary for the type of fuel scheduling requirements specified for this program.

Solenoid Metering Valve Tests

The characteristic of the solenoid metering valve is shown on Figure 27. The solid line shows the predicted characteristic provided that all components in the proportional solenoid give nominal performance. The proportional solenoid characteristic relies on the summation of four nonlinear functions:

a) Coil force as a function of current

b) A nonlinear spring force as a function of displacement

c) Permanent magnetic force as a function of air gap

d) Orifice discharge flow coefficient

The variation in fuel flow for a given input current from the nominal characteristic shown on Figure 27 is expected for the relatively inexpensive device used, and can be allowed for by a gain change in the electronic computer.

Centrifugal Pump System Dynamic Performance

The frequency response of the system was determined by inducing a sinusoidal current input to the metering valve solenoid and analyzing the resulting fuel flow response. The linearized transfer function block diagram, together with the estimated values

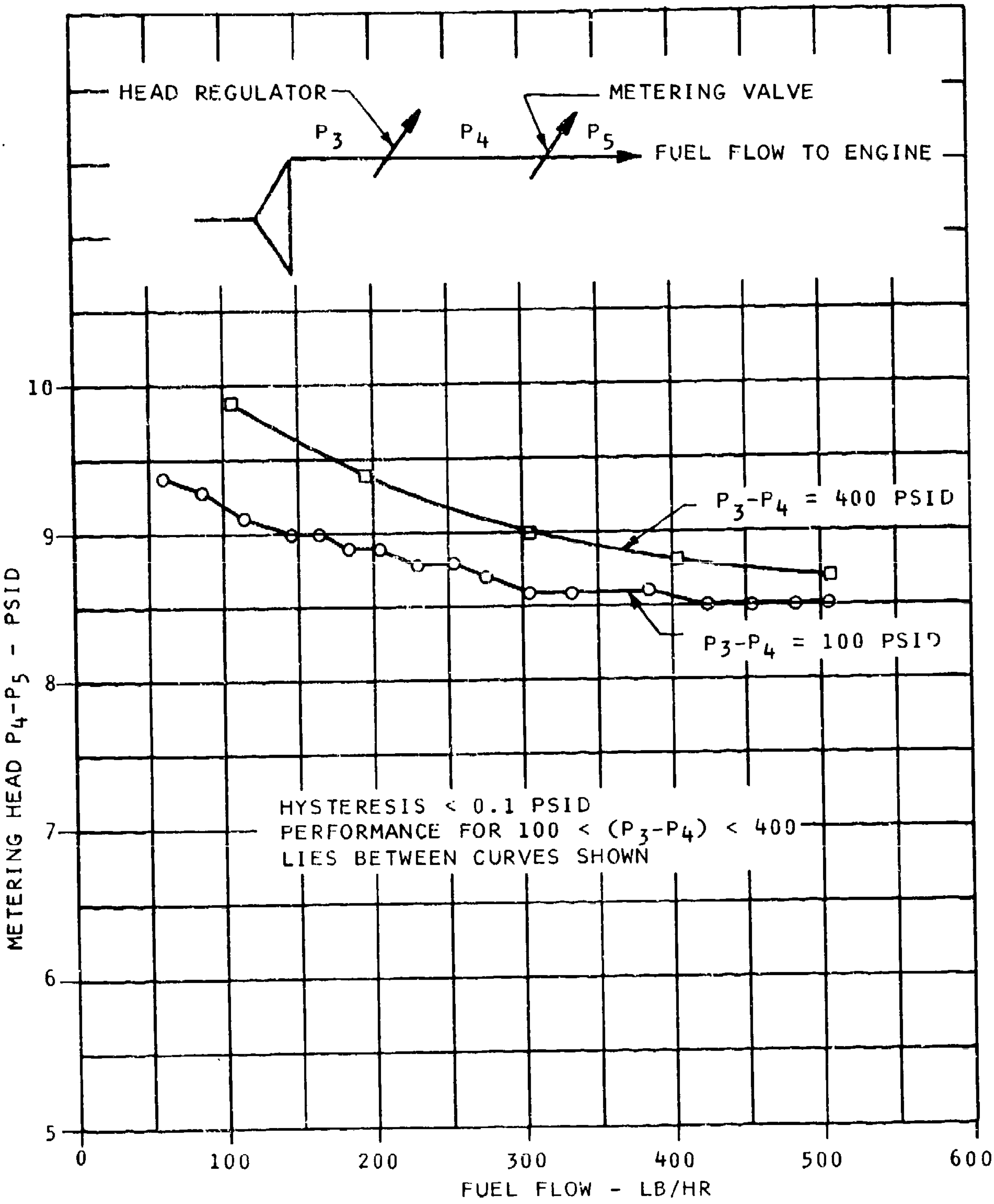

Figure 26. Metering Head Regulator Characteristic.

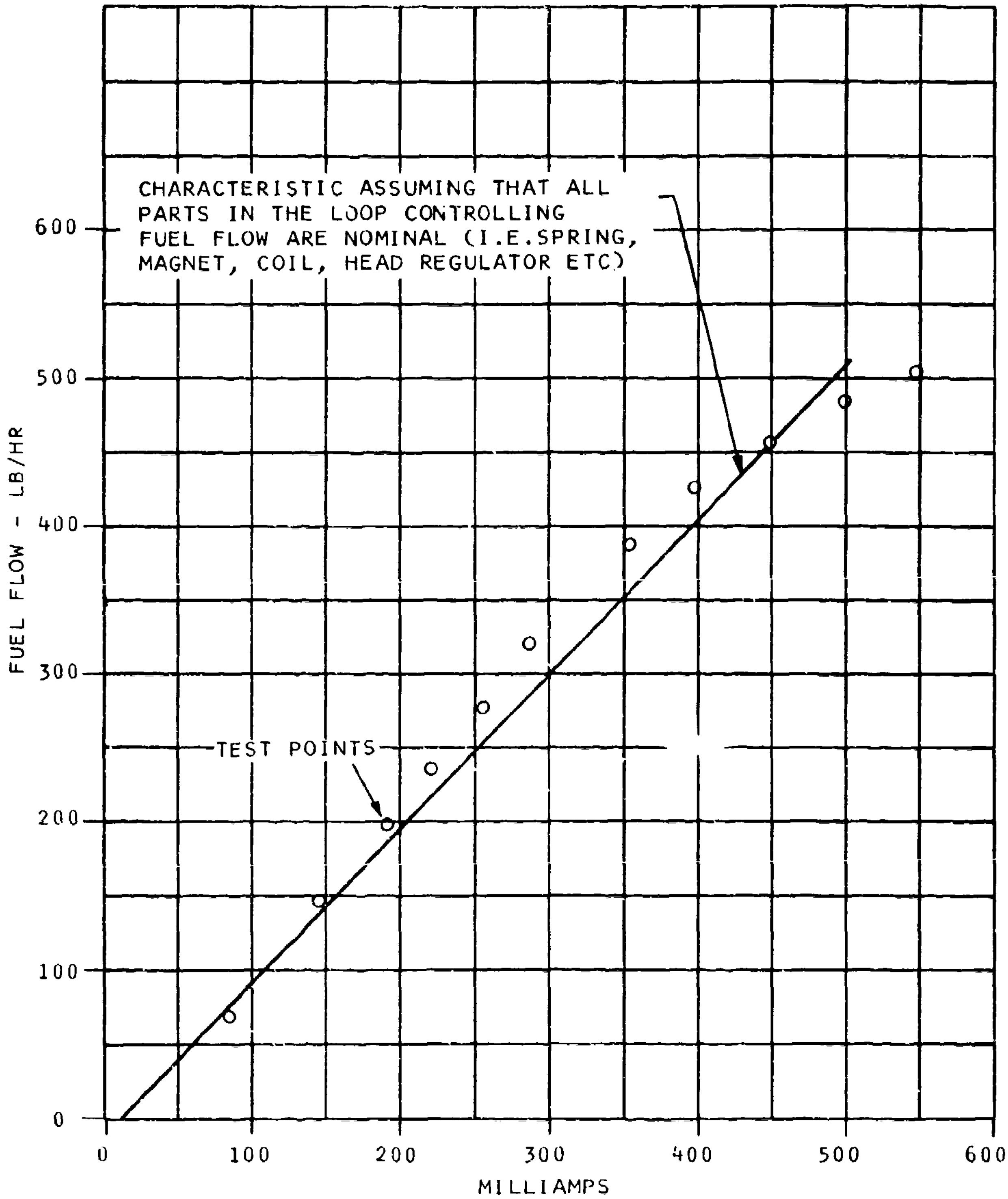

Figure 27. Proportional Solenoid Fuel Metering Characteristic.

of the parameters, is shown in Figure 28 . This includes the fuel flow sensor and signal conditioning circuit which is necessary for supplying the fuel flow signal, but which would not normally be part of the system. The bode plots of Figures 29 and 30 indicate the system to be responsive out to 20 rads/second. If allowance is made for the dynamics of the fuel flow sensor, the system can be approximated as a 30 millisecond lag for the head pressure regulator, and a 20 millisecond lag for the solenoid and its associated electronics. The figures also show close correlation indicating the system response is independent of the operating point (high or low fuel flow).

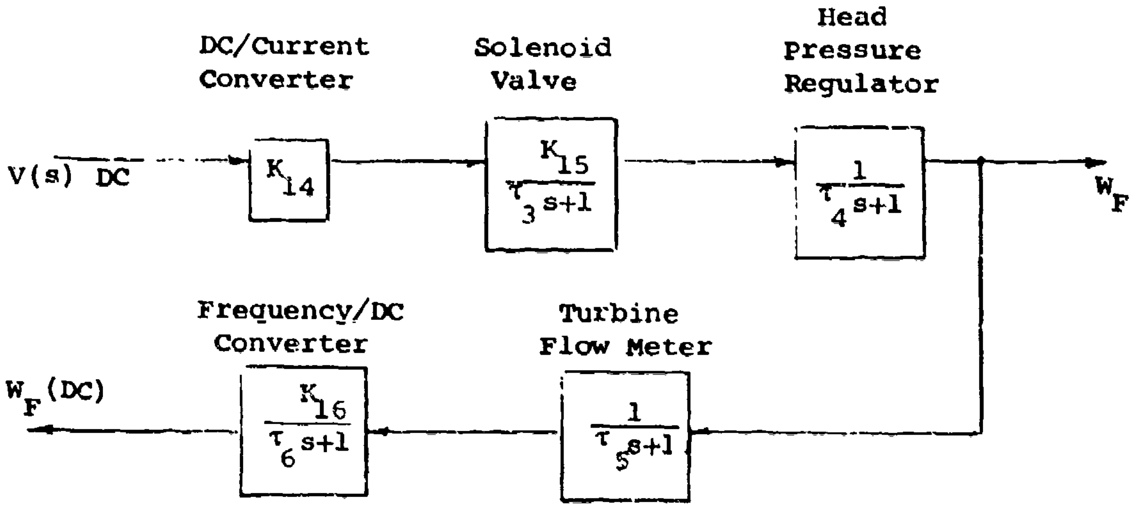

Parameters	Value
K_{14}	100 m amps/volt
K_{15}	1 pph/m amp
K_{16}	1 volt/pph
τ_3	20 m secs
τ_4	40 m secs
τ_5	10 m secs
τ_6	40-60 m secs

Figure 28 . Centrifugal Pump System Transfer Block Diagram

CENTRIFUGAL PUMP SYSTEM

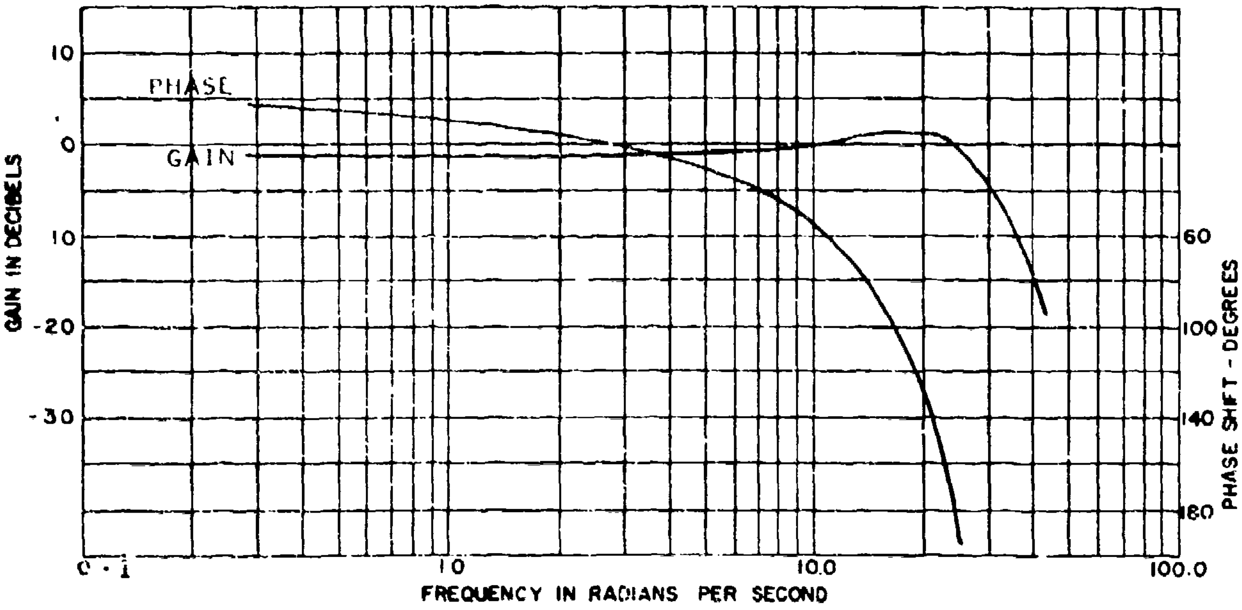

FIGURE 29. OPEN LOOP FREQUENCY RESPONSE FROM SOLENOID CURRENT TO FUEL FLOW AT LOW FLOW (W_F = 100 PPH)

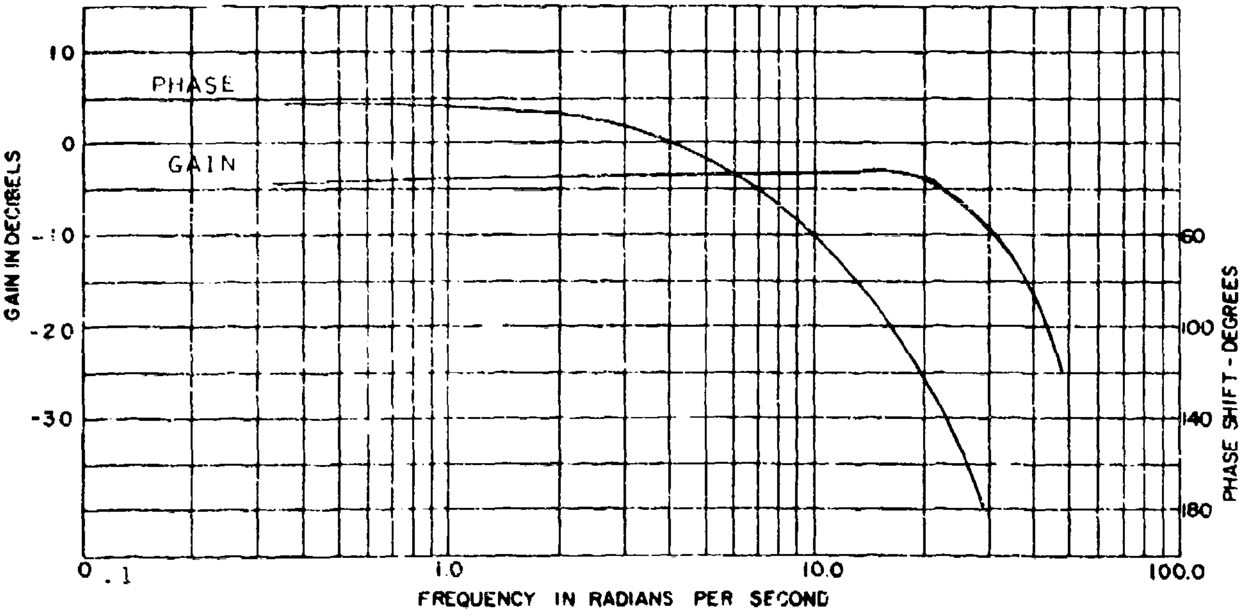

FIGURE 30. OPEN LOOP FREQUENCY RESPONSE FROM SOLENOID CURRENT TO FUEL FLOW AT HIGH FLOW (W_F = 400 PPH)

5. CONCLUSIONS AND RECOMMENDATIONS

1. The centrifugal pump and solenoid fuel metering system meet the requirements of this program.

2. The open impeller provided a 100% increase in overall efficiency compared to a shrouded impeller, throughout the operating range. This is based on test conducted during this program and high speed shrouded impeller tests done during previous development program (4).

3. Operation of the open impeller, carbon journal bearing, and face seal at 70,000 rpm disclosed no unexpected problem areas.

4. Evidence of a moderate amount of drive spline wear was observed after 60 hours of testing.

5. It is recommended that the open impeller design be used on any future high speed centrifugal pumps.

6. The heat generated by the centrifugal pump causes an estimated maximum fuel temperature of 277°F at 45,000' at the minimum fuel flow of 50 lb/hr hot day with an inlet fuel temperature of 135°F.

7. It is recommended that the centrifugal pump and proportional solenoid metering system be tested using high density fuels to determine the cold starting, and overall efficiency performance.

3

SENSORS

The sensors which were developed or procured during this program were selected based on providing engine control concepts which evolved from the surveys of engine and airframe manufacturers and the results of the control mode and trade studies that were conducted in-house. The sensors selected for development and evaluation include:

1. A pressure ratio sensor ($\Delta P/P$) to sense the compressor discharge airflow for a closed loop acceleration control (developed).
2. A radiation pyrometer-type turbine blade temperature sensor for use in turbine blade temperature limiting, and closed-loop turbine inlet temperature control (developed).
3. Three off-the-shelf compressor discharge pressure sensors.

   A capacitance-type high performance long life sensor.

   A strain-gage-type, high performance long life sensor.

   A lower cost potentiometric-type which is suitable for short life applications.
4. A thermistor/resistor temperature probe for measuring the engine compressor inlet temperature (designed but not fabricated).
5. An off-the-shelf magnetic speed pickup for sensing engine and fuel pump speeds.

1. PRESSURE RATIO SENSOR ($\Delta P/P$)

Recent analytical studies (3) have indicated the feasibility of using the compressor discharge corrected airflow as an engine acceleration control parameter. This control concept has emerged because for many engines the surge line is an almost constant corrected airflow in the idle to maximum speed range. The possibility of a simple constant acceleration limit to replace the complex bivariant functions presently being used is particularly attractive for meeting the low cost aspects of this program. However, the lack of an available corrected airflow sensor which would also meet these low cost objectives has given rise to the present development of a pressure ratio sensor. The pressure ratio of interest is the difference between the compressor discharge total and static pressures divided by the total pressure, and can be shown to have a fixed and unique relationship to the corrected engine airflow. This results in the pressure ratio being constant for a constant corrected airflow and, therefore, still pertains to a simple schedule.

A previous in-house development program produced a fluidic interface device which provides a mechanical motion in proportion to a control pressure differential. It consists of a two-segment, momentum interaction type fluidic amplifier and a diaphragm type actuator. The amplifier is segmented below the interaction area so that the lower half, splitter/receiver section can be moved relative to the upper half, power/control section by diaphragm action. Receiver pressures acting on the diaphragms force the splitter to center itself on the power jet. When the power jet is deflected by variations in control pressure differential, the splitter follows the power jet. Studies had shown that if the constant supply pressure is replaced by the total compressor discharge pressure and the control pressure by total and static compressor discharge pressure, then by the theory of momentum interaction summing of jets, the mechanical output would be proportional to the required ratio. The development of this theory into a workable pressure ratio sensor was conducted in two stages.

Stage I defined a specification for the sensor and included a detailed theoretical study to verify the earlier conclusions. This included defining the summing and discharge jet orifices and a preliminary design of the sensor.

Stage II was concerned with the detailed design, fabrication and testing of the sensor.

Design Requirements

The design goals established for the development of the sensor were to meet future small turbofan engine requirements. Accuracy requirements were determined by the idle to maximum acceleration requirements of typical engines.

The specification established as a guideline for the compressor airflow sensor are as follows:

Working Media:	Gas turbine compressor discharge air
Input Pressure Range:	Line pressure 375 psia maximum (Sea level) 40-250 psia at ambient 15 psia (40,000 ft.) 7.4-46 psia at ambient 2.76 psia
Input Temp. Range:	-65°F to 400°F
Ambient Temperature:	-65°F to 250°F
Input Lines:	Two (P_{T4}, P_{S4}) ten inch long lines
Input Flow:	Maximum flow rate 0.002 lb/second for P_{T4} and P_{S4}
Mechanical Stroke:	Goal: +0.040 inch range Acceptable: +0.030 inch range
Range:	0.0 to 0.25 pressure ratio units
Accuracy:	Nominally, the repeatability of any point should be within ± 1.5% of rated pressure ratio. This includes errors due to hysteresis temperature sensitivity acceleration and vibration. It does not include nonlinearity errors.
Response:	Less than 20 mseconds time constant at sea level standard day conditions.
Vibration:	See Figure 31
Size & Weight:	Minimized in accordance with engine sensor requirements.
Materials:	Compatible with environmental conditions and weight limitations.
Applicable MIL Spec:	MIL-E-8593A

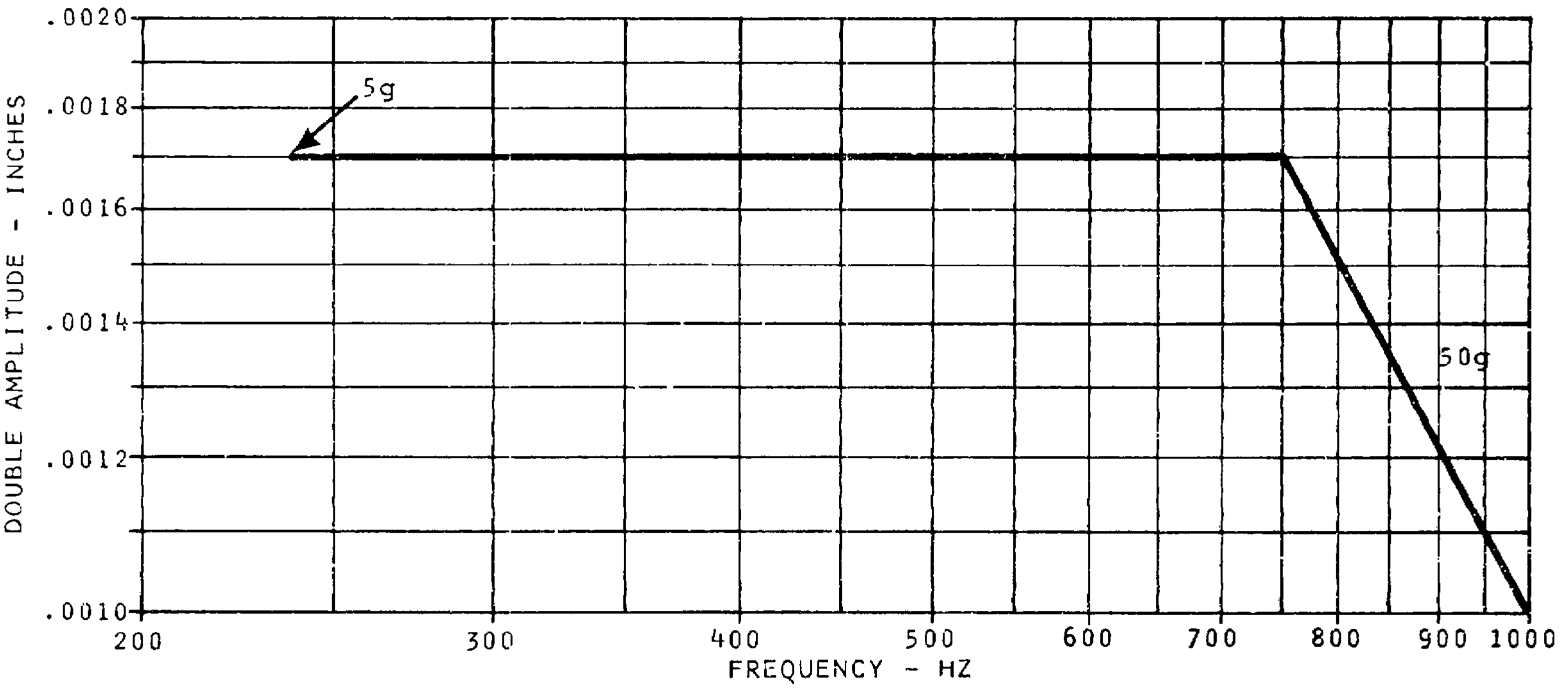

Figure 31. Vibration Requirement.

Design

General

The $\Delta P/P$ sensor is based on the momentum flux of a jet. If two jets are summed so that the momentum flux of one jet is perpendicular to the momentum of flux of the second, then the resultant jet angle is given by:

$$\theta = \mathrm{Tan}^{-1} \frac{(W_1 V_1)}{(W_2 V_2)} \qquad ①$$

Where W_1 and W_2 are the mass flows in the two jets and V_1 and V_2 are the jet velocities and θ is the angle measured relative to the axis of jet #2.

With incompressible flow WV is directly related to the pressure drop across the jet, hence

$$\theta = \mathrm{Tan}^{-1} \frac{A_1 P_1}{A_2 P_2} \qquad ②$$

Where A_1 and A_2 are the jet areas and P_1 and P_2 are the pressure drops across the jets. The angle is then a measure of the ratio of the pressure drops across the jets. It should be noted that even for the incompressible case the angle is not directly related to the ratio of absolute pressures which is generally the ratio of interest.

Implementation of the sensor to obtain $\Delta P/P$ can be done either with two jets and an initial angle offset or by a power jet and two opposing control jets. In the first case for small angles

$$\theta \approx \frac{A_1 P_1}{A_2 P_2} - \theta_o = \frac{A_1 P_1 - A_2 P_2 \theta_o}{A_2 P_2} \qquad ③$$

and for the latter case

$$\theta \approx \frac{A_1 P_1 - A_1 P_2}{A_2 P_2} = \frac{A_1}{A_2} \left(\frac{P_1 - P_2}{P_2} \right) \qquad ④$$

In either case, the fundamental relationship between angle and momentum vectors remain the same.

Compressible Flow

To determine the characteristics of the sensor under compressible flow the relationship between momentum flux and pressure must be established for compressible flow.

(Mass Flow) $$W = \frac{C_d A\ (.532) P_u}{\sqrt{T}}\ f\left(\frac{P_d}{P_u}\right) \qquad ⑤$$

(Velocity) $$V = M^* \sqrt{0.83\gamma RT} \qquad ⑥$$

where T = upstream stagnation temperature

P_u = upstream pressure, psia

P_d = discharge pressure, psia

C_d = nozzle discharge coefficient

A = nozzle area

γ = ratio of specific heats

R = gas constant

$f\left(\frac{P_d}{P_u}\right)$ and M^* are functions of the pressure ratio and are tabulated in gas tables for flow through nozzles and orifices.

It is apparent from the flow equation that a prime prerequisite of a $\Delta P/P$ sensor is maintaining a constant pressure ratio across the jets as P_{T4}/P_a is varied. If the pressure ratio is maintained constant, then both the flow function and velocity remain constant and the momentum flux becomes directly proportional to the pressure establishing the jet.

A technique for controlling the pressure ratio is to collect the flow from the jet interaction region and expel the flow to local ambient through an orifice. As P_{T4}/P_a approaches some lower limit the jet pressure ratio can be no longer maintained and the jet angle is no longer a true measure of $\Delta P/P$.

Equation of Operation

From the compressible flow equation ⑤ and the jet deflection equation ⑥ the following points are significant in selecting the design parameters for the sensor:

a) The angular deflection of the power jet depends on both the weight flows and the velocities of the jets.

b) Both the weight flow and the velocity of the jets are dependent on the pressure ratio across their orifices.

c) If the pressure ratio across the jets can be maintained constant for the range of input pressures corresponding to values of $\Delta P/P$, then the jet deflection will be proportional to $\Delta P/P$ and independent of the supply pressure.

d) It can be shown that if two orifices are in series and the downstream orifice is choked, then the pressure ratio across the upstream orifice is proportional to the ratio of their areas. Or if the areas are fixed, the ratio remains constant.

The discharge orifice is selected to yield a pressure ratio of 0.5 at the lowest input pressure ($P_{T4}/P_a = 2.65$ at idle speed), thus ensuring choked conditions throughout the operating range.

For a maximum jet deflection of 12° at maximum $\Delta P/P = 0.2$ the jet pressure ratio and orifice area ratios were determined as follows:

Since $$\frac{P_a}{P_d} = 0.5 \text{ and } \frac{P_{T4}}{P_a} = 2.65 \qquad ⑦$$

then the jet pressure ratios are

$$\frac{P_d}{P_4} = 0.75 \quad \frac{P_d}{P_{s4}} = 0.94 \qquad ⑧$$

Defining the control orifice area as A_c, the power jet orifice A_p and the discharge orifice A_d areas can be calculated

From equation 1 for the jet angular deflection

$$\operatorname{Tan}(12^\circ) = \frac{A_c\, P_{T4}\, f\left(\frac{P_d}{P_{T4}}\right) M^*\left(\frac{P_d}{P_{T4}}\right) - A_c\, P_{s4}\, f\left(\frac{P_d}{P_{s4}}\right) M^*\left(\frac{P_d}{P_{s4}}\right)}{A_p\, P_{T4}\, f\left(\frac{P_d}{P_{T4}}\right) M^*\left(\frac{P_d}{P_{T4}}\right)}$$

$$= \frac{A_c\, P_{4}\, f\,(0.75)\, M^*\,(0.75) - A_c\,(0.8\, P_{T4})\, f\,(0.94)\, M^*\,(0.94)}{A_p\, P_{T4}\, f\,(0.75)\, M^*\,(0.75)}$$

$$.212 = \frac{A_c}{A_p}\,(1 - 0.2)$$

$$\frac{A_c}{A_p} = 0.265$$

The area of the back pressure orifice is determined by the continuity of flow equation. That is, for steady state conditions the sum of the input weight flows are equal to the discharge flow.

Thus, from equation 5

$$1.265\, A_p\, P_{T4}\, f\left(\frac{P_d}{P_{T4}}\right) + 0.265\, A_p\, P_{s4}\, f\left(\frac{P_d}{P_{s4}}\right) = A_d\, P_d\, f\left(\frac{P_a}{P_d}\right)$$

where P_d is the absolute pressure in the jet interaction region, and A_d is the area of the back pressure orifice.

Solving the preceding equation yields

$$A_d = 1.6\, A_p$$

Using these area ratios the jet pressure ratio as a function of both P_{T4}/P_a and $\Delta P/P$ can be calculated by substitution into the mass flow equation. Because of the choked condition of the discharge orifice for $P_{T4}/P_a > 2.65$, there will be no error due to the vector summation of momentum flux. However, the error will increase rapidly for values < 2.65. The sensor output vs. $\Delta P/P$ is shown in Figure 32. For $P_{T4}/P_a > 2.65$ the output is linear, whereas the sensor output becomes a nonlinear function of P_{T4}/P_a for values smaller than 2.65. It should be noted that momentum flux is temperature independent. Temperature can affect sensor accuracy only by its influence on the pressure ratios across the jets. This can occur if the temperature of the fluid passing through the back pressure nozzles changes relative to the P_{T4} and P_{s4} air passing through the jet nozzles.

A temperature drop of 50°F as the fluid flows through the sensor will give an error of 0.25% at a nominal 400°F inlet temperature. This error is in a direction to give an indicated $\Delta P/P$ ratio smaller than the actual.

The predominant effect of temperature will be a change in sensor bandwidth. The bandwidth will be proportional to the square root of absolute temperature of the working fluid.

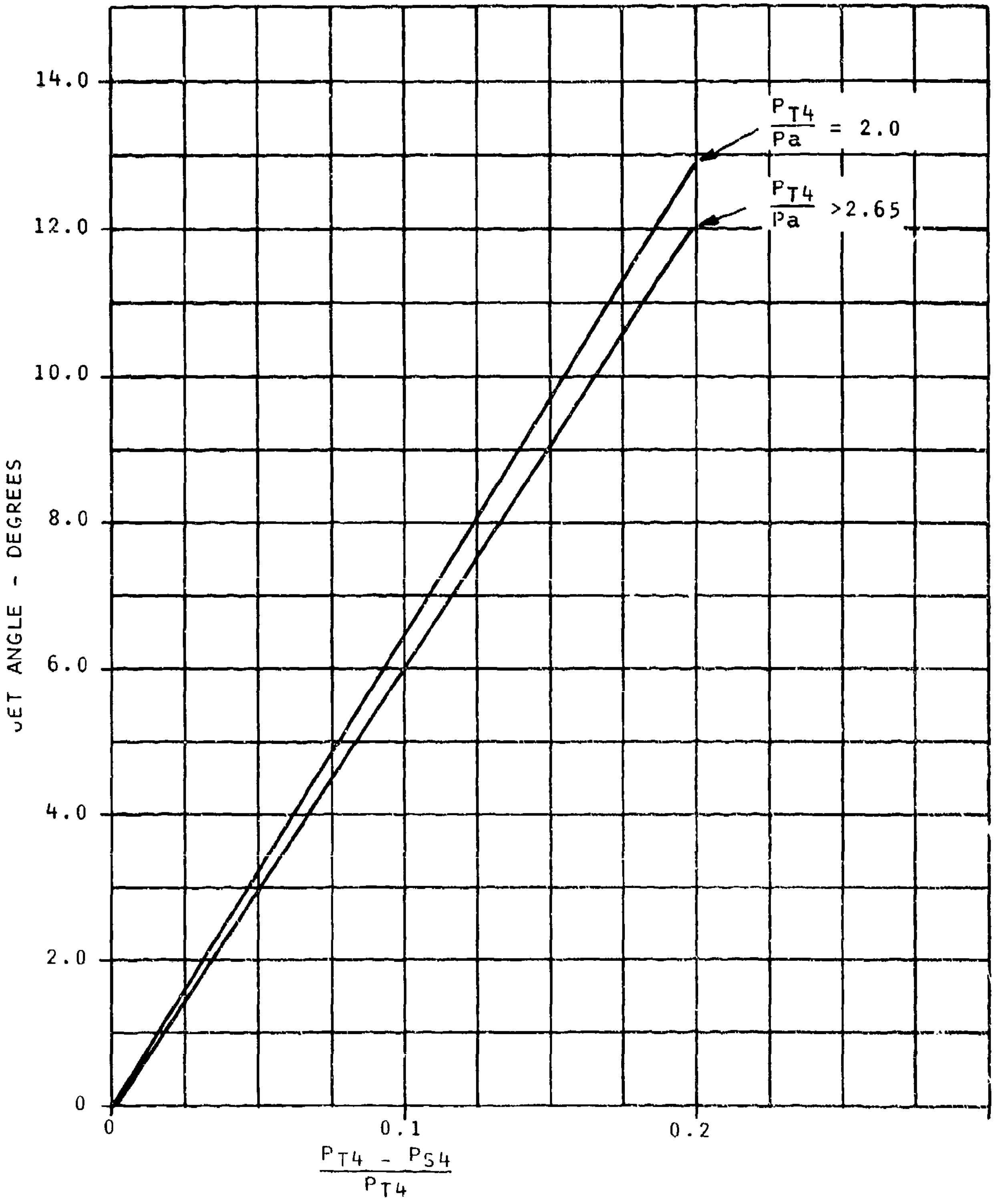

Figure 32. Estimated Performance of Fluidic ΔP/P Sensor.

Dynamic Performance

Figure 33 is a linearized block diagram of the sensor indicating the transfer functions of the various stages indicated in Figure 38.

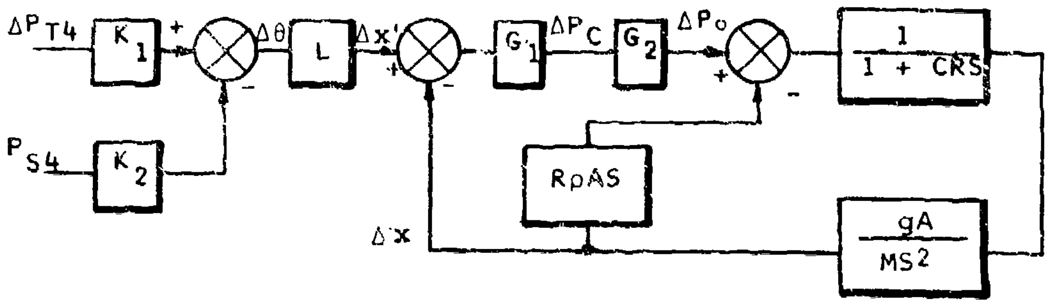

Figure 33. $\Delta P/P$ Linearized Block Diagram.

where g = gravitational acceleration ~ 32.2 ft/sec^2

G_1 = gain of splitter/receiver - psi/in

G_2 = gain of 2nd stage amplifier - psi/psi

A = area of piston - in^2

ρ = air density in piston - lb/in^3

C = capacitance of piston end volume - in^2

M = mass of suspended member - lb

L = length, control port to splitter - inches

S = Laplace operator

$\Delta x'$ = jet deflection from centerline - inches

Δx = piston displacement - inches

R = output impedance of 2nd stage amplifier - sec/in^2

$\Delta\theta$ = angular deflection of jet - radians

ΔP_c = pressure difference at control ports of amplifier

ΔP_o = pressure difference at output ports of amplifier

K_1, K_2 = constants

Incremental control pressure changes, ΔP_{T4} and ΔP_{S4}, cause a jet deflection $\Delta\theta$ which results in the jet being deflected a distance $\Delta x'$ at the input ports on the floating member. The pressure gain of this first stage receiver is G_1, while that of the follow-up fluidic amplifier is G_2. The output pressures will result from the pressure gain of the amplifier minus the pressure drop due to airflow through the output ports. As the diaphragms slew during dynamic changes, air will flow into or out of the diaphragm volume. If the second stage amplifier output is considered as the flow control orifice with an output impedance R, then the flow into the volume resulting from the velocity of the diaphragm can be correlated to a pressure drop.

i.e., $$\Delta P = R\Delta W$$

where the mass flow $$\Delta W = \rho A \frac{dx}{dt}$$

The pressure change into the volume will be lagged by the volume capacitance C. The resulting pressure change in the volume will act on the diaphragm area A to create a force to accelerate the floating member of mass M. This will result in a time change Δx in the position of the receiver ports.

The open loop transfer function of the sensor is given by

$$T_f = \frac{\Delta x}{\Delta x'} = \frac{G_1 \; G_2}{RA\rho S\left[\frac{CM}{gA^2\rho} S^2 + \frac{M}{gRA^2\rho} S + 1\right]}$$

The bandwidth in rad/sec is equal to

$$BW \approx \frac{G_1 G_2}{RA\rho}$$

The ratio G/ρ is relatively independent of the total working pressure and R can be maintained relatively constant providing the second stage amplifier is operated at a constant pressure ratio. The overall bandwidth can be made relatively insensitive to total operating pressure.

The maximum bandwidth of the sensor is determined by the characteristics of the quadratic in the open loop transfer function. The natural frequency of the quadratic is given by

$$A\left(\frac{\rho g}{CM}\right)^{\frac{1}{2}} \quad \text{and the damping ratio is} \quad \frac{1}{2AR}\left(\frac{M}{C\rho g}\right)^{\frac{1}{2}}$$

The overall bandwidth must be sufficiently low to maintain less than unity gain at resonance. Both the natural frequency and the peak amplitude are a function of density or total working pressure. Estimates indicate that the roots will vary from 150 Hz to 1000 Hz over the total pressure range and that the stability margin will remain constant over the range. The analysis indicates that a bandwidth of 8 Hz (required for specified time constant) will result in a high frequency instability.

A conventional technique for extending the bandwidth of this type of system is to include a controlled lag time constant at a frequency lower than the quadratic resonance. While this approach is not particularly attractive for this sensor, (the fluidic capacitors required to obtain the time constant have to be on the suspended member), it appears to be the only alternative. Two 0.1 $(\text{in})^3$ volumes are required; inclusion of these volumes increases the weight of the suspended member from 0.025 to 0.35 lbs and also increases the total length of the sensor by approximately 25%.

Figures 34 and 35 show the open loop frequency response of the sensor over the operating range of P_{T4}. As indicated, the stabilizing volume meets the stability requirements by attenuating the second order resonant frequency. The closed loop frequency responses shown in Figures 36 and 37 indicate bandwidths of 20 to 24 Hz over the range of P_{T4}.

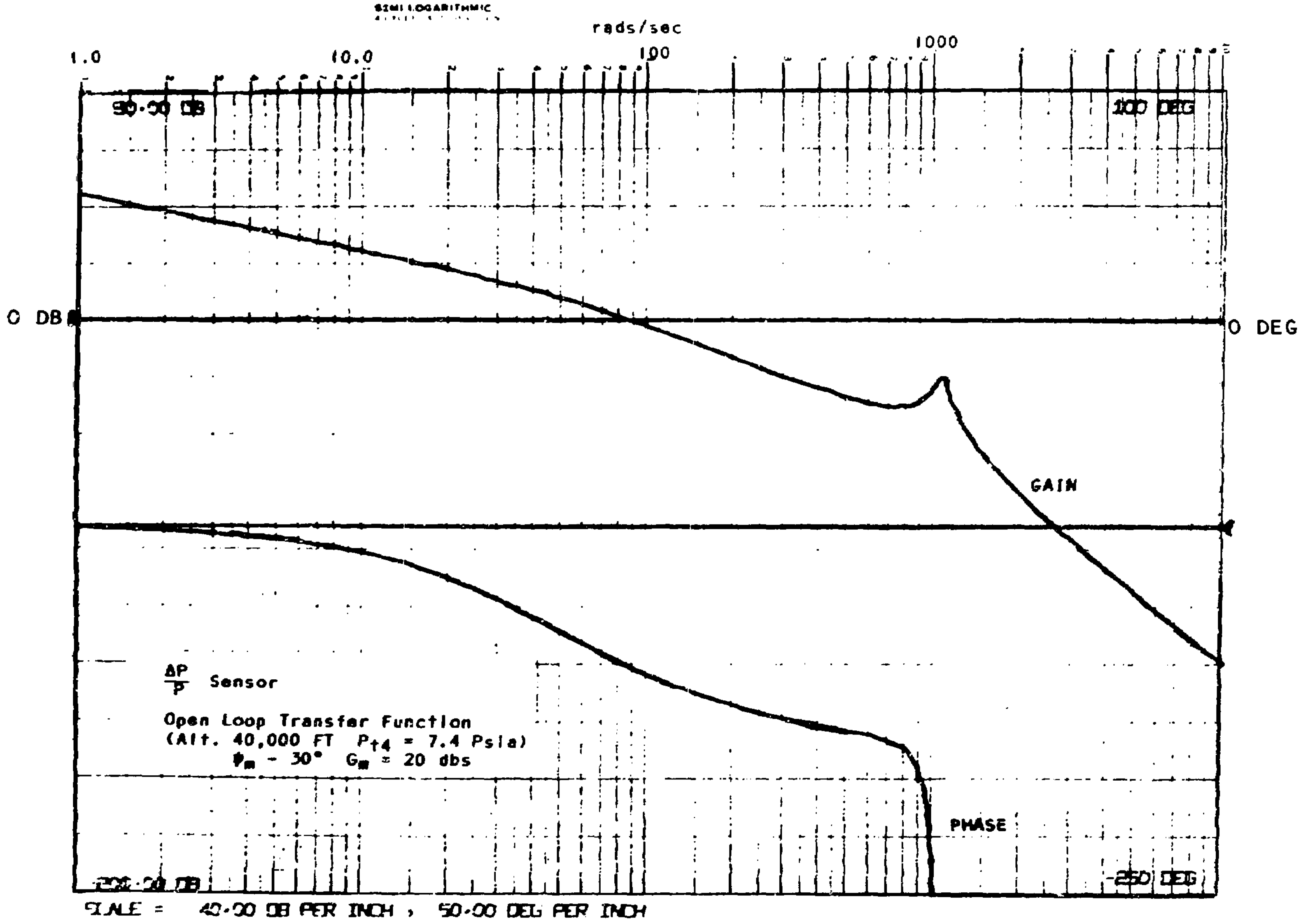

Figure 34. ΔP/P Open Loop Frequency Response at Low Compressor Pressure.

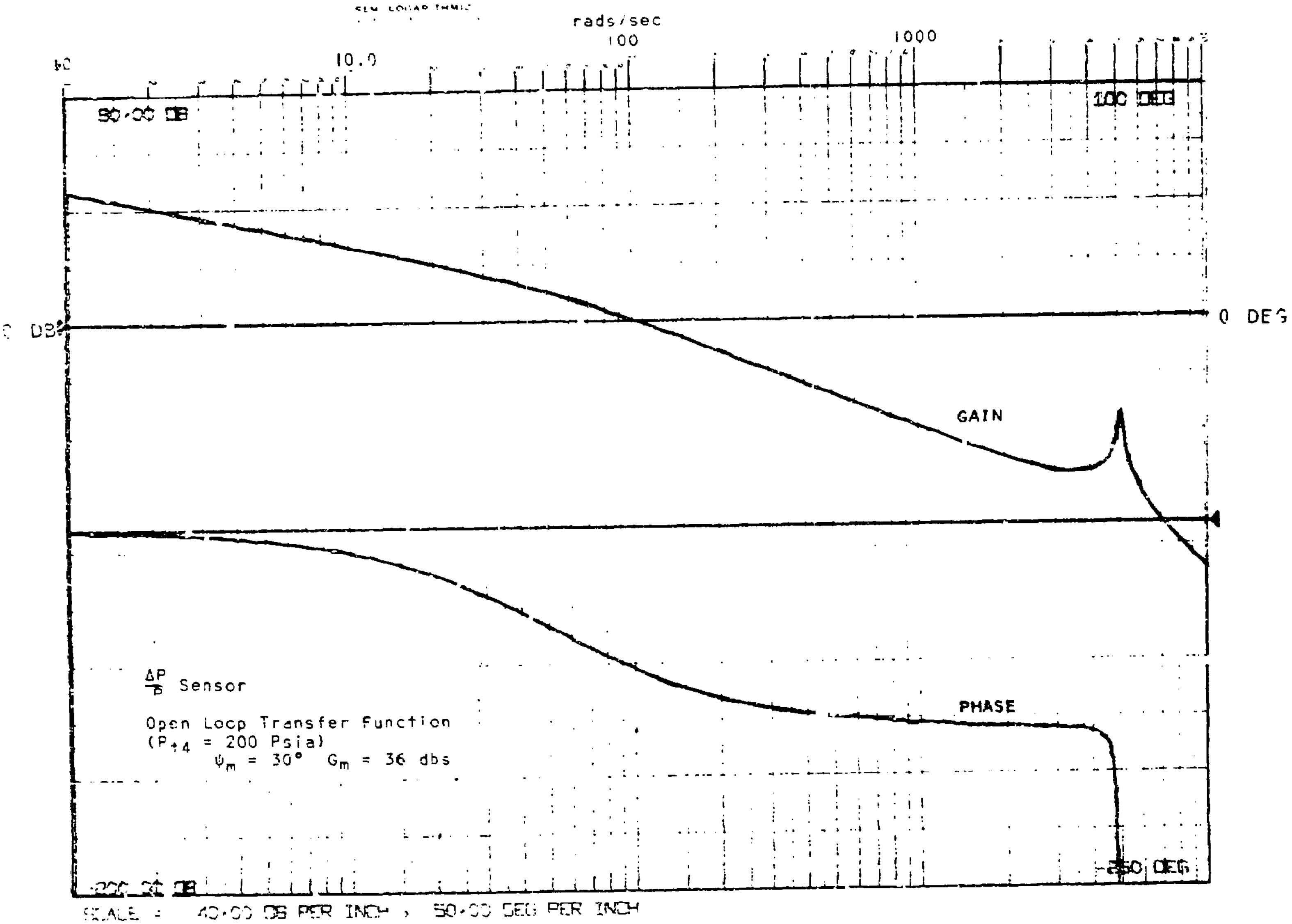

Figure 35. ΔP/P Open Loop Frequency Response at High Compressor Pressure.

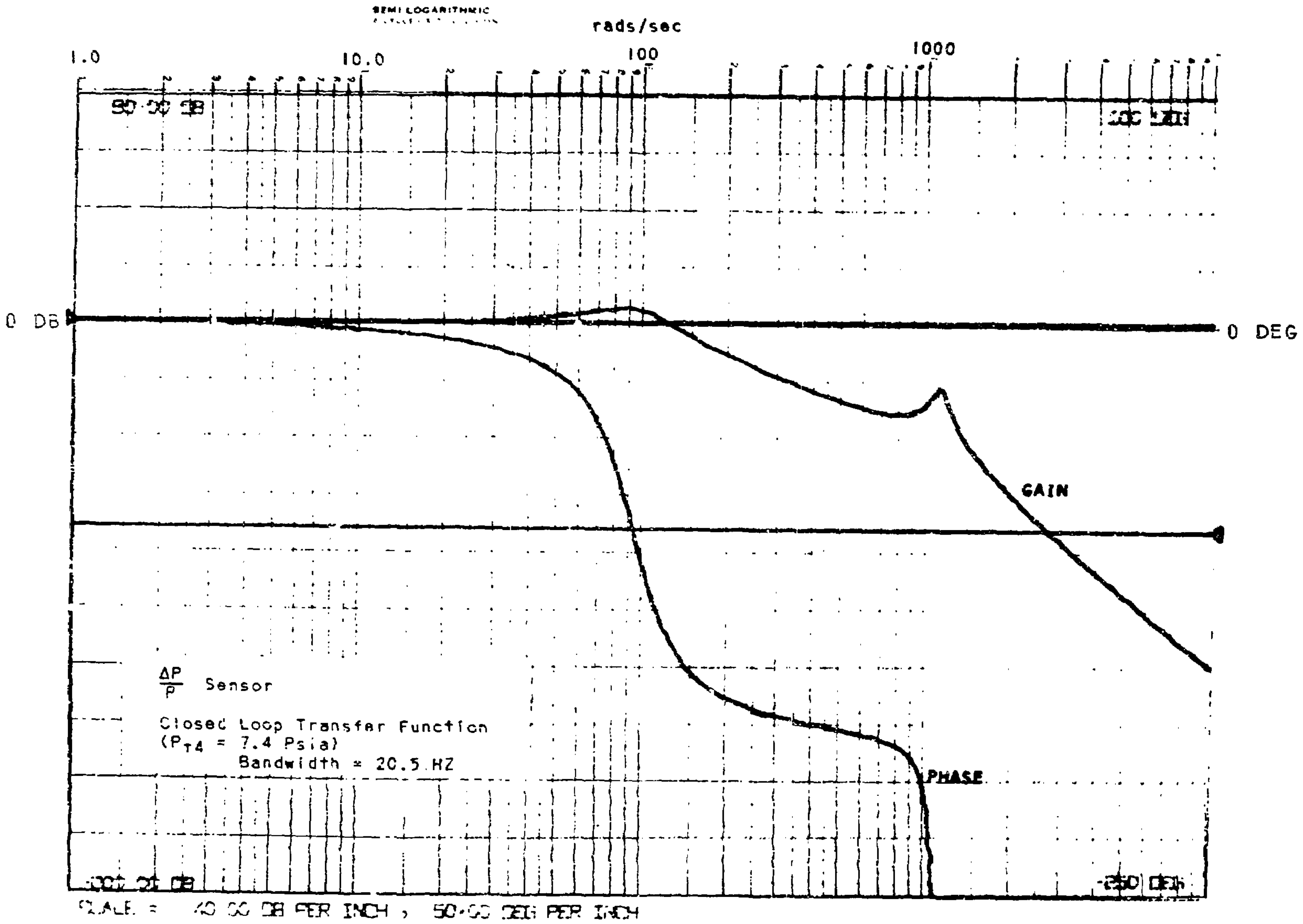

Figure 36. ΔP/P Closed Loop Frequency Response at Low Compressor Pressure.

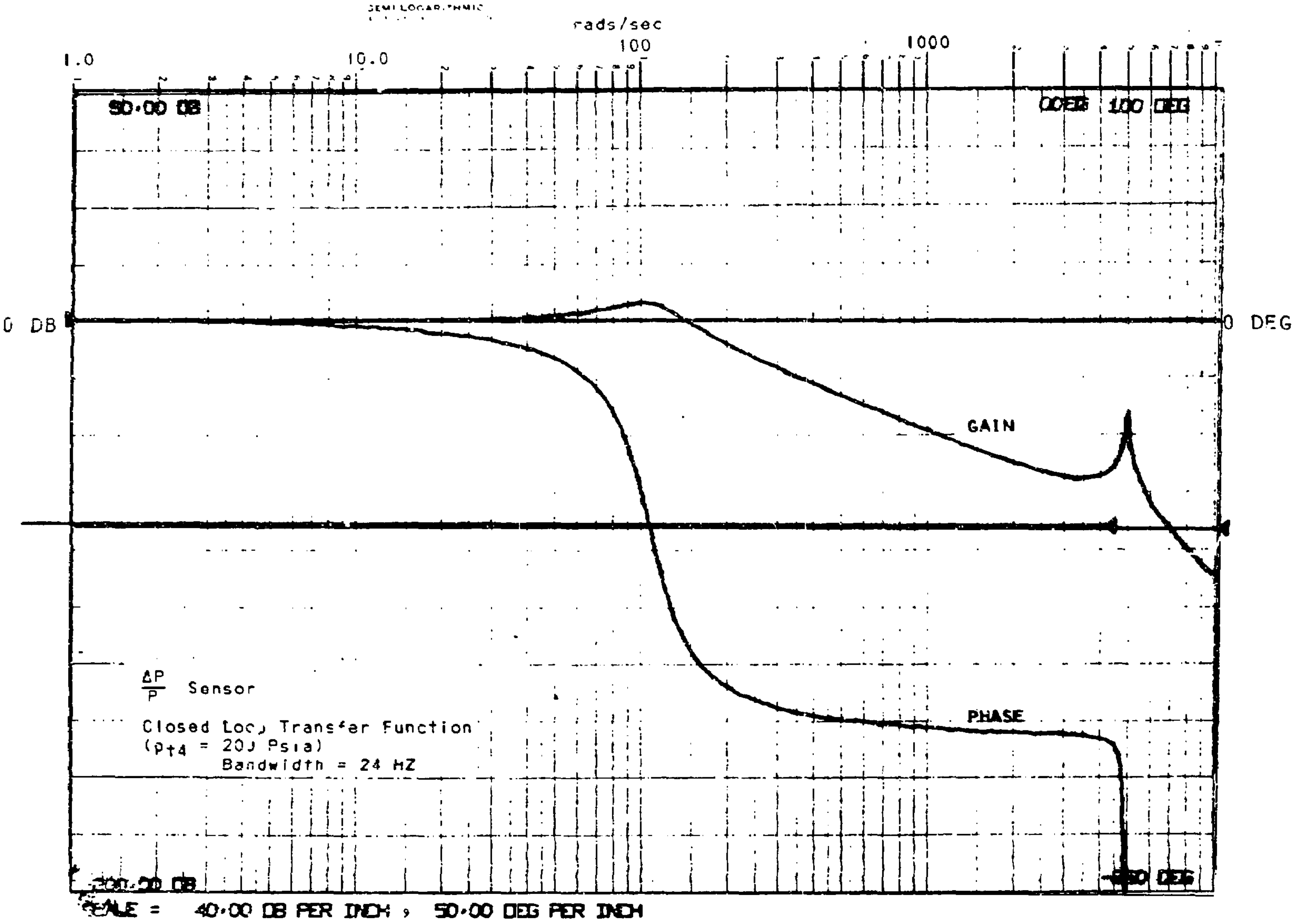

Figure 37. ΔP/P Closed Loop Frequency Response at High Compressor Pressure.

Steady State g Sensitivity

Acceleration along the sensitive axis of the sensor results in an extraneous force input which is counteracted by a displacement of the receivers relative to the jet.

The displacement is given by

$$D = \frac{Wg}{A\ Go}$$

where W = suspended weight
g = applied g's
A = effective actuator area
Go = sensor pressure gain - #/in^2/in

This error will be a maximum when Go is a minimum. At 7.4 psia total pressure and 2.76 ambient, the available differential for a supply to the fluid amplifier is 1.9 psi. Approximately 40% of this can be recovered as a ΔP across the centering diaphragms. The minimum Go based on two stages of amplification is then estimated at approximately 250 #/in^2/in.

The weight of suspended receivers is estimated at .035#. Assuming an effective centering diaphragm area of 1 in^2 yields a displacement of $1.4/10^4$ inches per g or 0.7% of full scale per g. This error is inversely proportional to P_{T4}. The error can be minimized by mounting the unit at right angle with respect to the engine centerline.

Vibration

Vibration frequencies falling within the sensor bandwidth will result in sinusoidal displacements approximately the same as for steady state applied g's. For frequencies higher than the sensor bandwidth the displacement will be inversely proportional to frequency. Also, because the sensor is mounted in the electronic package, additional vibration isolation is provided which will minimize potential vibration problems.

Description

The compressor discharge airflow sensor, (ΔP/P), is a two-part design consisting of a fluidic-to-mechanical pressure ratio sensing section and a mechanical-to-electrical transducer Linear Variable Differential Transformer (LVDT). The fluidic section is based on a redesign of a standard proportional fluidic element to provide a pure momentum interaction device required in this application. A schematic of the fluidic section is shown in Figure 38, while the exploded view of the sensor is included in Figure 39. The basic sensing element is a two-stage receiver and amplifier section suspended on two soft fabric diaphragms and two metallic springs. The two diaphragms form a leakless push-pull piston for applying the centering force on the receiver assembly. The metallic springs prevent twisting and cocking of the receiver section and also provide a stiff constraint along the axis perpendicular to the axis of the diaphragm piston. This particular spring is fabricated by chemical etching and has a spring gradient of 0.5 #/in. on the sensitive axis. This compares to an estimated pneumatic gradient of 350 #/in. at the minimum supply of 7.4 psia and 40,000 ft. altitude. This combination of diaphragms and springs results in a virtually frictionless suspension with no close fitting or sliding parts.

The momentum summing nozzles are a laminated diffusion bonded assembly operating directly off the compressor discharge pressure. The relative widths of the primary nozzle and cross axis nozzles are made to give a jet deflection of 0.04 inch at the receivers over the specified range of ΔP/P pressures. The total flow from the momentum summing jets is collected in the internal volume containing the receivers and expelled to ambient through a bleed orifice. The bleed orifice is sized to establish a pressure ratio of approximately 2:1 across the primary momentum nozzle. The constancy to which the pressure ratio can be held over the total pressure range, to a large extent determines the ultimate accuracy of the sensor.

The receiver section uses a standard miniature proportional amplifier configuration. The amplifier supply is derived from the high velocity flow around the primary jet centerline. Two receivers on either side of the centerline are located at the maximum gradient portion of the jet and form the first stage of amplification.

The maximum pressure recovery at the output of the second stage is estimated at 40% of the primary jet supply. This is somewhat less than could be achieved with a single stage (60%); however,

MECHANICAL SPRING

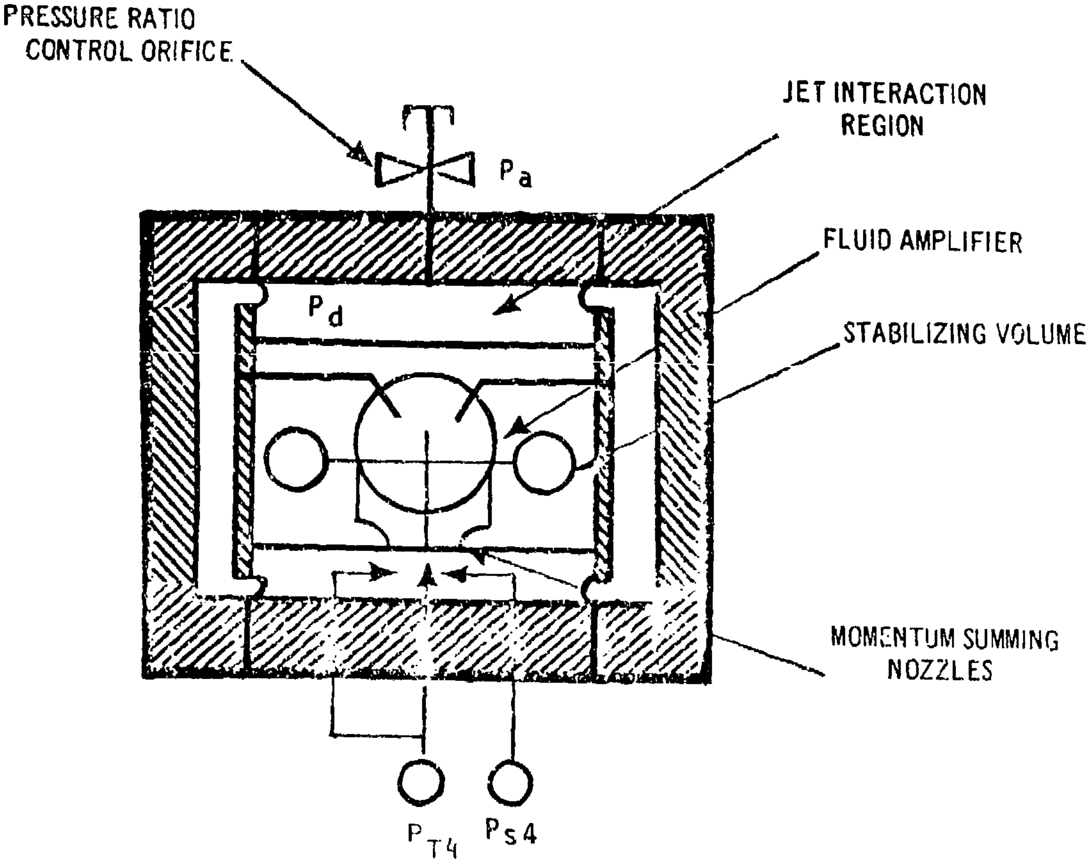

Figure 38. Fluidic ΔP/P Sensor Schematic.

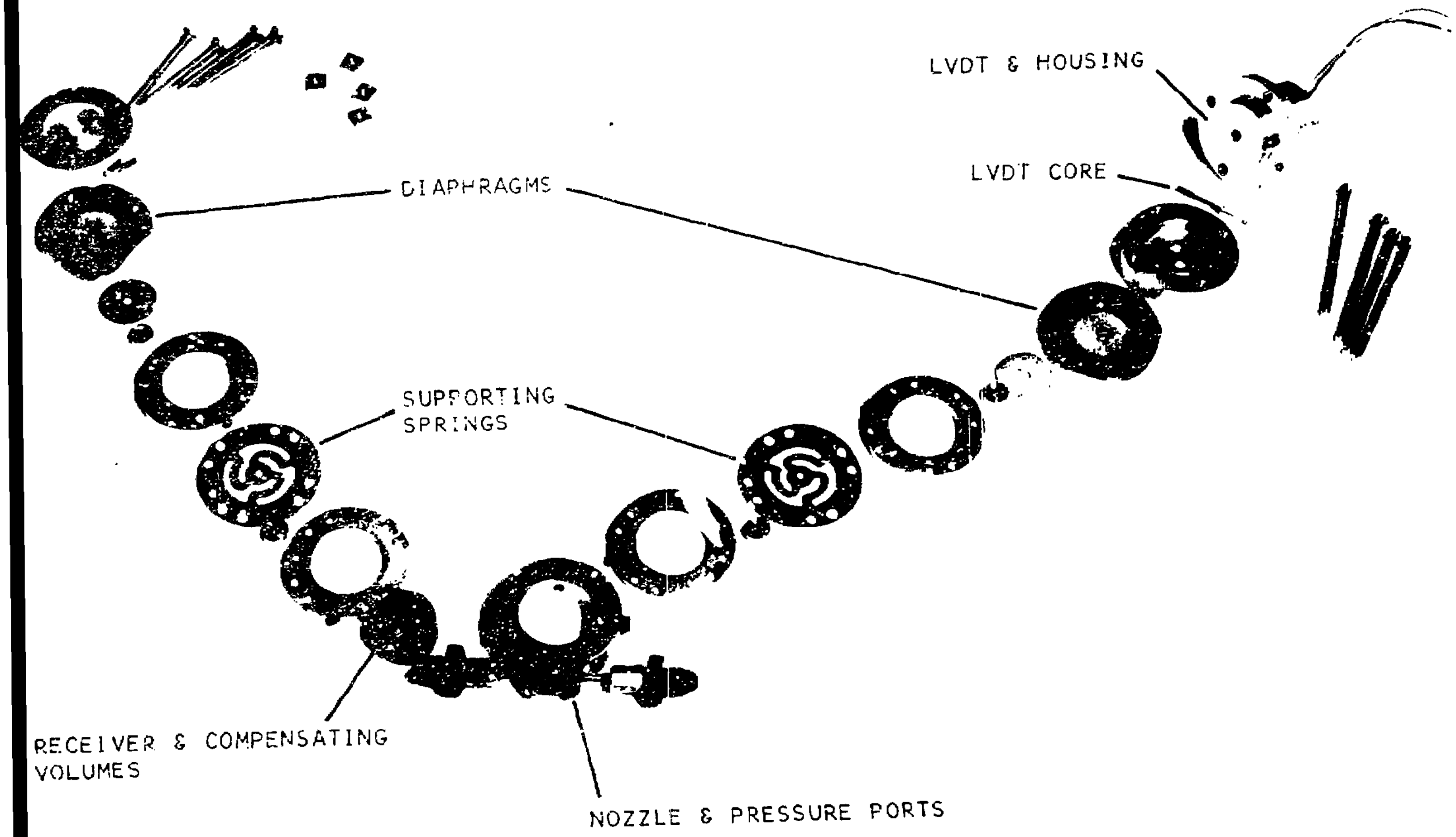

Figure 39. Exploded View of ΔP/P Sensor.

the two-stage amplifier does give approximately a 5:1 higher force gradient than could be obtained with a single stage. At the minimum specified total pressure at 40,000 feet, the estimated force gradient (based on a 1 in^2 piston area) is 350 #/in.

The receiver-amplifier and fluidic capacitors required for stability are diffusion-bonded to eliminate leakage and give the structural strength required to operate at the relatively high supply pressures associated with the specified maximum total pressures. Titanium is used for both the receiver-amplifier section and the diaphragm reaction plates. Titanium was selected because of the relative ease of bonding and low density compared to stainless steel. The weight of the suspended assembly is critical in that it determined the sensor's sensitivity to applied g's along the sensitive axis. Estimated sensitivity at minimum total pressure and altitude is 0.7%/g. This g sensitivity is the primary justification for using two stages of amplification in the receiver section.

The electrical transducer consists of a Pickering LVDT Model No. 7304Y with a linear range of ± 0.040 inch. The LVDT is bonded to a threaded housing with adjustable wrench flats at one end. The housing screws into the supporting assembly which is solidly attached, via 4 bolts, to the fluidic section containing the LVDT core. An approximate electrical zero is obtained by screw adjustment of the LVDT housing assembly. Fine adjustment is provided via a trim potentiometer in the LVDT electronic signal processor circuit. A ballscrew mechanism is used for locking the LVDT and its housing to the fluidic assembly.

Testing

The following tests were performed on the sensor:

Sensor output versus $\Delta P/P$ over the sea level standard day range of P_{T4}.

Measurement of pressure ratio across the summing jets versus P_{T4}/P_a.

Vibration scan through the resonant frequency range of the sensor.

Steady stage g sensitivity.

Time response

Results of tests are summarized in the table below.

Table II. $\Delta P/P$ SENSOR CHARACTERISTICS	
Time Response	0.015 seconds
Travel (0 to 0.2 $\Delta P/P$)	0.016 inches
Linear Range	0.1 to 0.3 $\Delta P/P$
Accuracy *	± 3.5%
Hysteresis	± 1.3%
g Sensitivity **	0.5%/g
Amplification Factor at Resonance	1

* Spread in all tests between engine idle to maximum speed pressure from 50 to 180 psia for $\Delta P/P$ 0.1-0.25.

** Measured at P_{T4} = 65 psia.

Static Calibration

The calibration of $\Delta P/P$ against supply pressure P_{T4} is shown in Figure 40 . Using the acceleration schedule indicated in Figure 81 for the idle to maximum acceleration range of $\Delta P/P$ (approximately 0.1 to 0.22), shows the sensor accuracy to be ± 3.5% of the maximum value for standard day conditions. For $\Delta P/P$ values below 0.1, the sensor output tends to become supply pressure dependent.

Figure 41 is the sensor hysteresis characteristics indicating a possible 3.5% hysteresis error. The preliminary design shows a four diaphragm configuration, two are used to form a push-pull piston for applying the centering force while the additional diaphragms are used to preclude the possibility of rapid pressure transients back pressuring the diaphragms. Since it is estimated that these transients will not occur on the engine, the additional two diaphragms are probably unnecessary. Results of a two-diaphragm configuration are shown in Figure 42 demonstrating a worst case hysteresis error of ± 1.3%. For the present control application, $\Delta P/P$ is used for closed loop control of acceleration only. This establishes a unidirectional operation (decreasing $\Delta P/P$) and means that the hysteresis error would not be relevant.

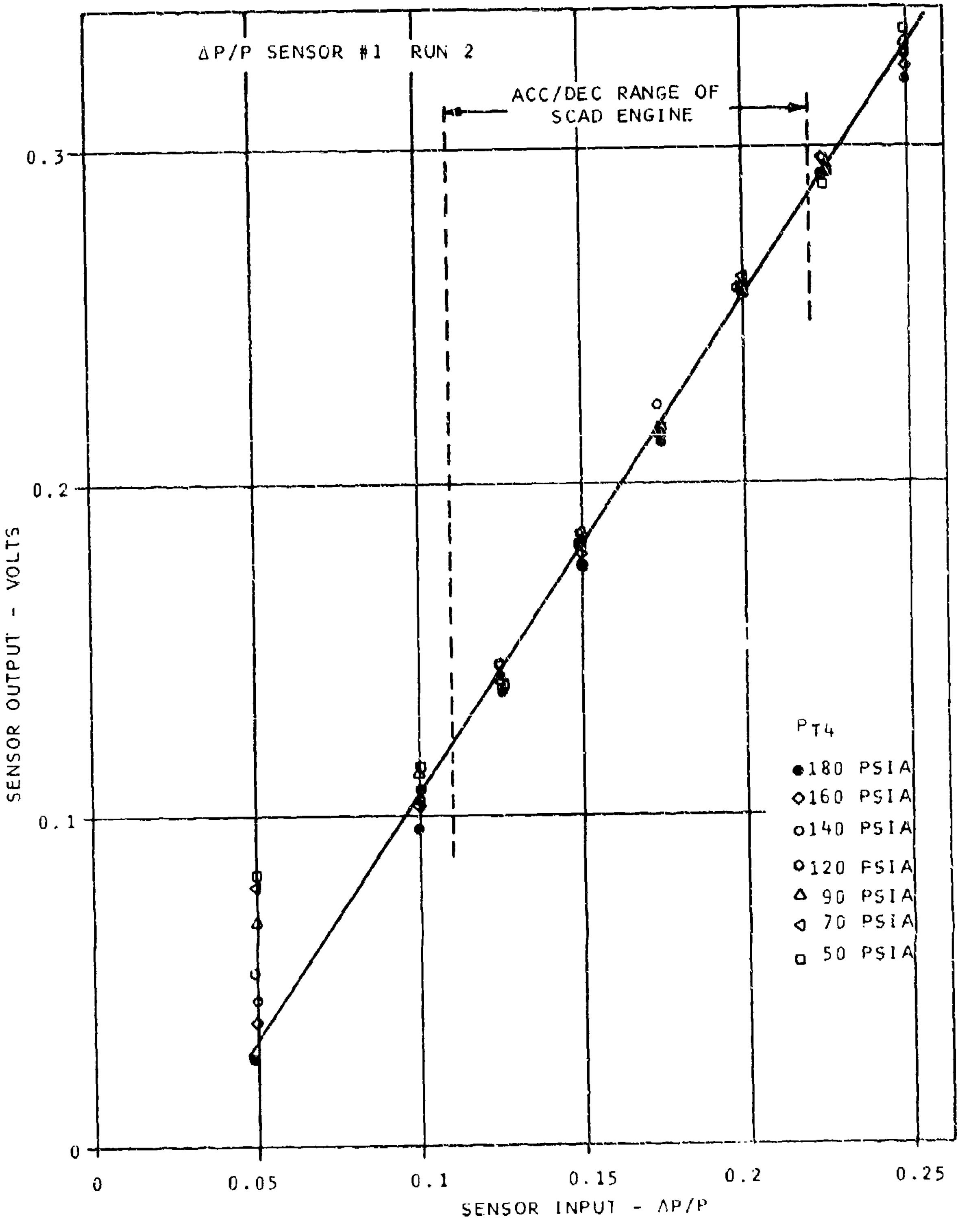

Figure 40. ΔP/P Sensor Performance.

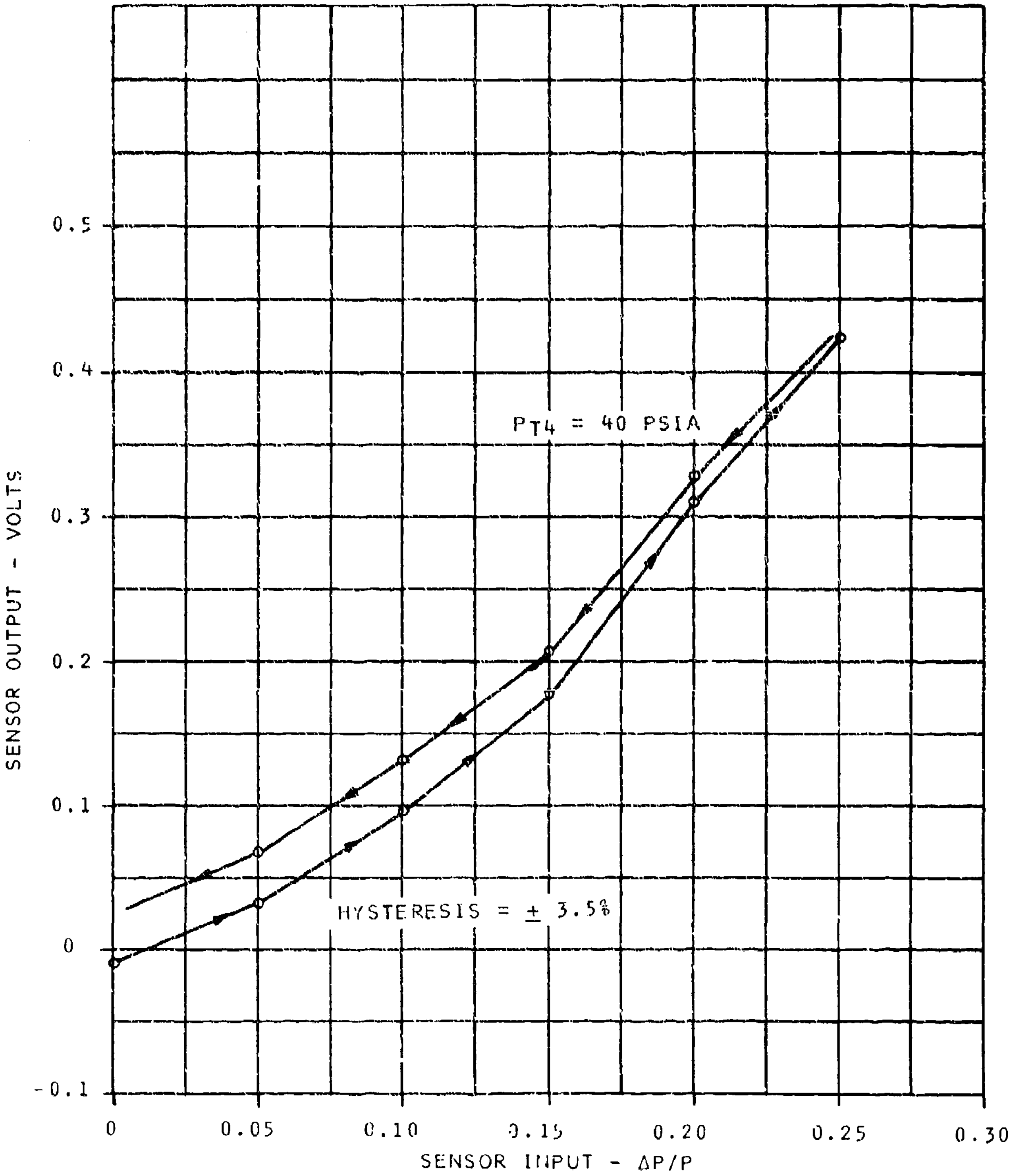

Figure 41. ΔP/P Sensor Hysteresis (4 Diaphragm Configuration).

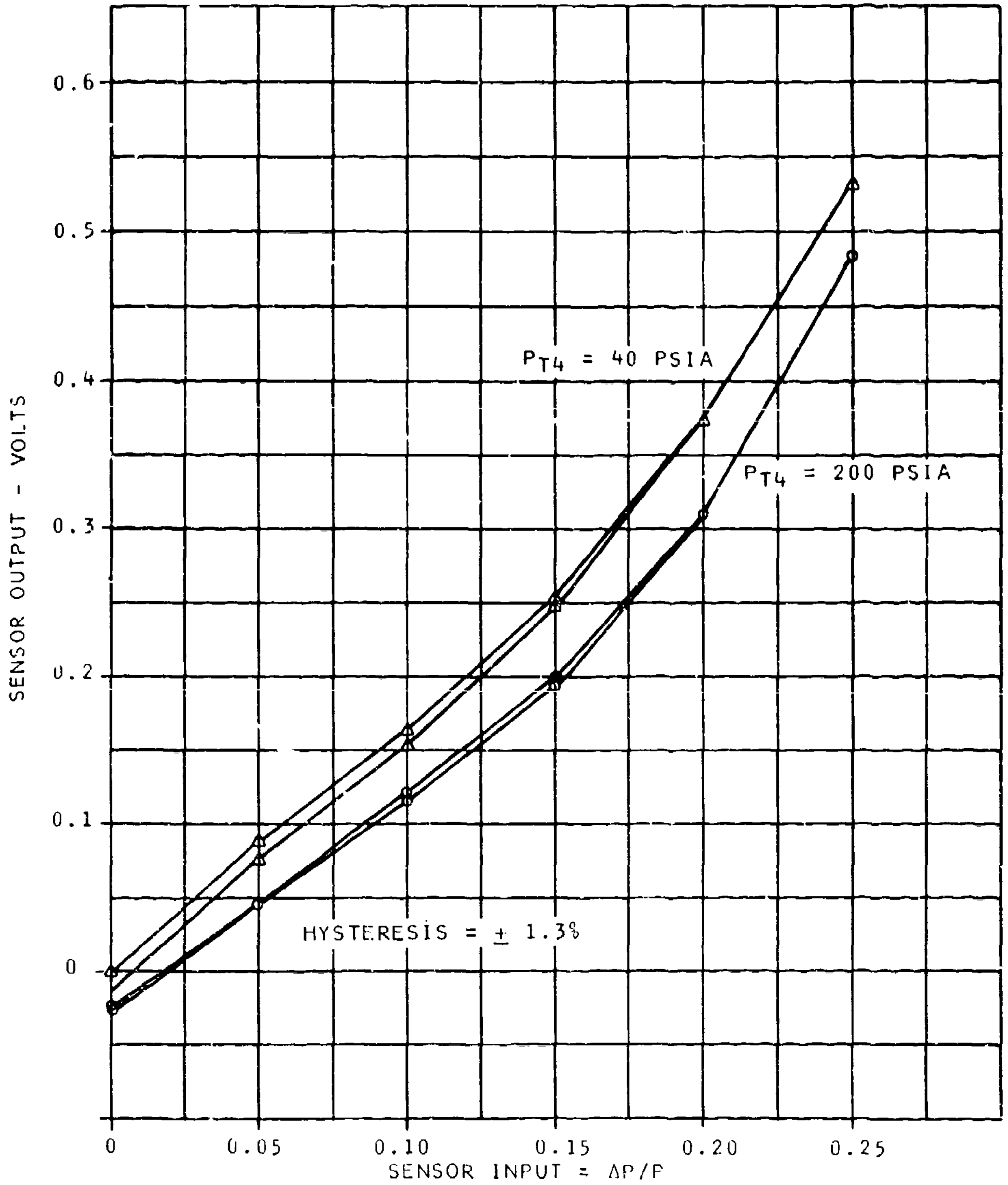

Figure 42. ΔP/P Sensor Hysteresis (2 Diaphragm Configuration).

Dynamic Performance

Figure 43 shows a typical time response obtained by applying a step pressure change to P_{S4}. Output of the linear voltage transducer was recorded on a Visicorder with a chart speed of 8 inches/second. There is no ringing apparent on the recording indicating that the sensor loop is adequately damped. The small sinusoidal perturbation on the recorder trace is caused by 60 cycle pickup on the recorder galvanometer. The measured time constant was 15 m secs which is considered adequate for these applications.

Vibration

The amplification factor at the sensor resonant frequency was observed by mounting the sensor on a vibration table. The applied vibration was scanned through 30 to 600 Hz. No amplification was apparent on these tests indicating that the rolling diaphragms are contributing significant damping between the sensor body and the sensor mass. This contribution was assumed to be negligible in the analysis.

Temperature

Presently, the device tends to be more temperature sensitive than anticipated for the following reasons:

a) The original specification was for a diaphragm stroke of 0.04 inches over the range of $\Delta P/P$. The measured stroke is 0.016 inches, the reduced range being due to the failure of the receiver to recover the theoretically calculated pressure, (however further experimentation with the nozzle design should result in an optimum configuration). This results in the LVDT output being approximately three times as sensitive to material expansions which cause a displacement of the LVDT core relative to the null point of the coil.

b) The design effort to determine temperature sensitivity was not sufficient in detail to provide for the optimum selection of materials to minimize thermal expansion between the various parts. This results in a temperature change causing a displacement of the stainless steel LVDT core relative to its aluminum housing.

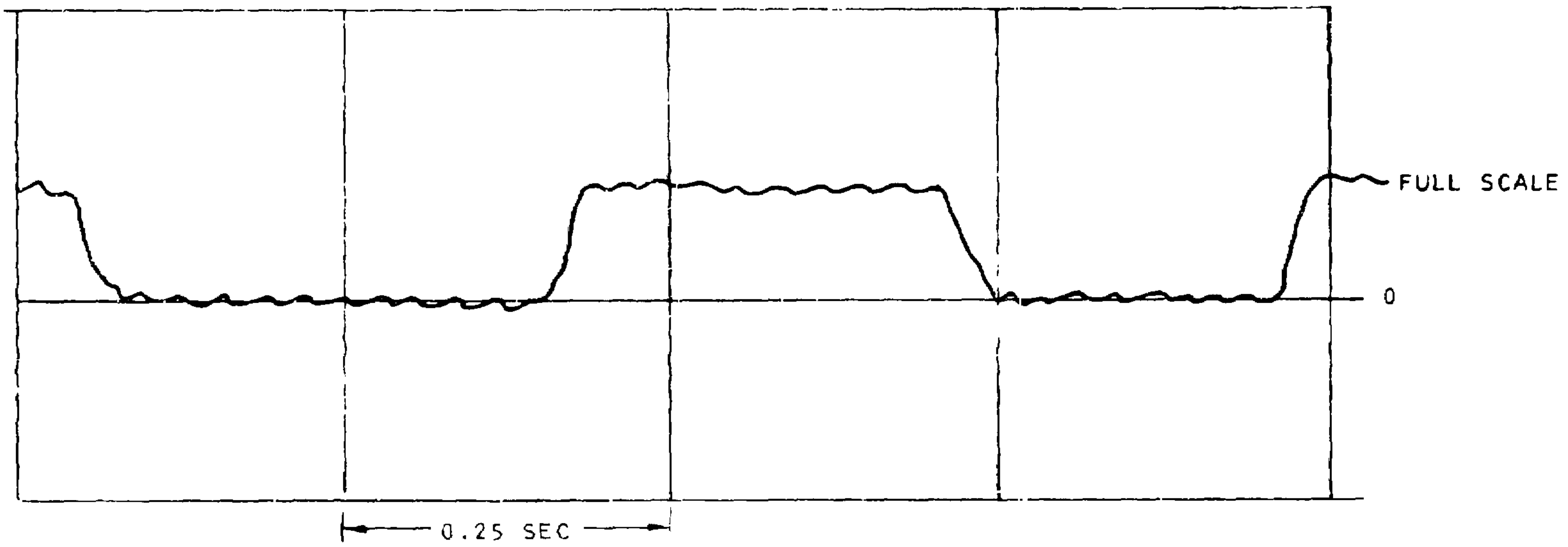

Figure 43. $\Delta P/P$ Sensor Dynamic Response to Step Inputs to P_{s4}.

The present configuration for engine testing is with the LVDT section housed inside the electronic interface box while the fluidic section protrudes outside and is exposed internally to compressor discharge pressure. This means that the two parts are exposed to different temperatures, both of which have not presently been specified. Therefore, as a prerequisite to engine control mode testing, the device should be calibrated at actual operational temperatures on the engine. Future redesigns should allow for material selections to minimize the relative thermal expansion.

Conclusions and Recommendations

The sensor fabricated and tested on this program represented a first cut at a sensor utilizing the principle of momentum summing over a broad range of absolute pressures. The scope of the program did not permit verification of design parameters by segmenting or breadboarding portions of the sensor prior to designing and fabricating the engineering prototype sensor. As a result, several correctible design deficiencies were identified in the sensor test program. Both the analysis of the sensor and results of the test program indicate that the operating principle of the sensor is fundamentally sound and that all of the design goals can be achieved.

As a result of the test program and assembly and check-out experience on the sensor, the following recommendations are made:

1. Redesign of the jet summing nozzles. On the developed sensor the pressure recovered from the primary jet is less than one-half the value predicted from prior experience with fluidic amplifiers. To obtain an adequate supply pressure for the mass-mounted amplifier required a reduction of nozzle-to-receiver spacing to less than one-half of the original design. The maximum travel of the sensor is correspondingly decreased. Another discrepancy with the summing jet, and probably a contributor to the poor recovery, is a skew of the jet axis in a plane perpendicular to the control plane. This characteristic makes assembly and line-up of the jet and receiver axes very difficult. The most probable cause for the skewed jet is considered to be the method of bringing P_{T4} supply air into the primary jet plenum. Redesign of the nozzles will require a program of sufficient scope to experimentally verify several design iterations on the nozzles.

2. Convert the basic sensor from the present four-diaphragm design to a two-diaphragm design. A two-diaphragm design was considered in the early phases of the program, but was abandoned because of a possible pressure reversal and resultant damage to the diaphragm during a rapid P_{T4} transient. The penalties incurred by the four-diaphragm design are significant. All four diaphragms are subjected to differential pressures which can go as high as 250 psi. Heavy diaphragms must be used and rolling friction becomes high. In the two-diaphragm design, the differential pressure is relatively low (less than 40 psi) and lighter diaphragms can be used. In addition, the two-diaphragm design permits a significant reduction in suspended mass and a decrease in overall sensor length. Experimental data verifying the existence or nonexistence of a pressure reversal can be obtained on the present sensor by monitoring the differential pressure between the jet interaction region and the actuators during rapid engine acceleration.

3. Present diaphragms should be replaced with high-temperature silicone diaphragms. Availability of silicone diaphragms was not compatible with the sensor delivery schedule and off-the-shelf Buna-N diaphragms were used. Therefore, engine tests should be performed with sufficiently long input lines to insure gas temperatures less than 200°F.

4. During the redesign, materials should be selected which will minimize relative thermal expansion between the LVDT core and the housing containing the LVDT coil.

The first three of these changes can be incorporated in the present sensors with relatively minor modifications. A nozzle change would be a direct plug-in replacement of the existing nozzles, accompanied by a disassembly and realignment of the sensor.

Conversion of a two-diaphragm design would require removal and replacement of several spacer rings on the sensor mass and body.

The fourth change would require refabricating parts in the selected materials and may also require the parts to be re-sized.

2. RADIATION PYROMETER

The most critically temperature-sensitive section of the gas turbine engine is the first stage turbine which receives the directed gas flow from the high temperature burner section. Slight overtemperatures of the thin, highly stressed turbine blades can result in drastic reductions in their metal creep life. Thus, for advanced turbine engines which push the operating temperature limit of the blade metal, a radiation pyrometer system lends itself ideally to a closed-loop turbine blade temperature limiter.

Based on previous in-house pyrometer designs, it was established that an aperture sensor head, which could negotiate extreme bends and close quarters, was needed for the more difficult installation, on small engines. An aperture assembly was selected because of its installation flexibility and potentially lower cost in production quantities over a lens pyrometer.

Mechanical Design

Photographs of the sensor head assembly and detail parts are shown in Figures 44 and 45; a layout drawing of the pyrometer assembly is included in Figure 46.

The aperture sensor head located within the body of the engine defines the target area on the turbine blade, collects and radiant power emitted by the hot target, and transmits this signal via a flexible fiber optic bundle to a silicon detector located in the electronic interface housing on the outside of the engine. The sensor head is of a four-piece design consisting of two support members permanently welded into the engine bypass casings, the removable aperture probe, and the flexible fiber optic cable. A pyrometer installation drawing is shown in Figure 47.

Vibration induced deflections of the relatively long canti-levered probe are minimized by the stainless steel ribbed sleeve of high moment of inertia but relatively low mass. Calculations show that at the maximum expected level of vibration,

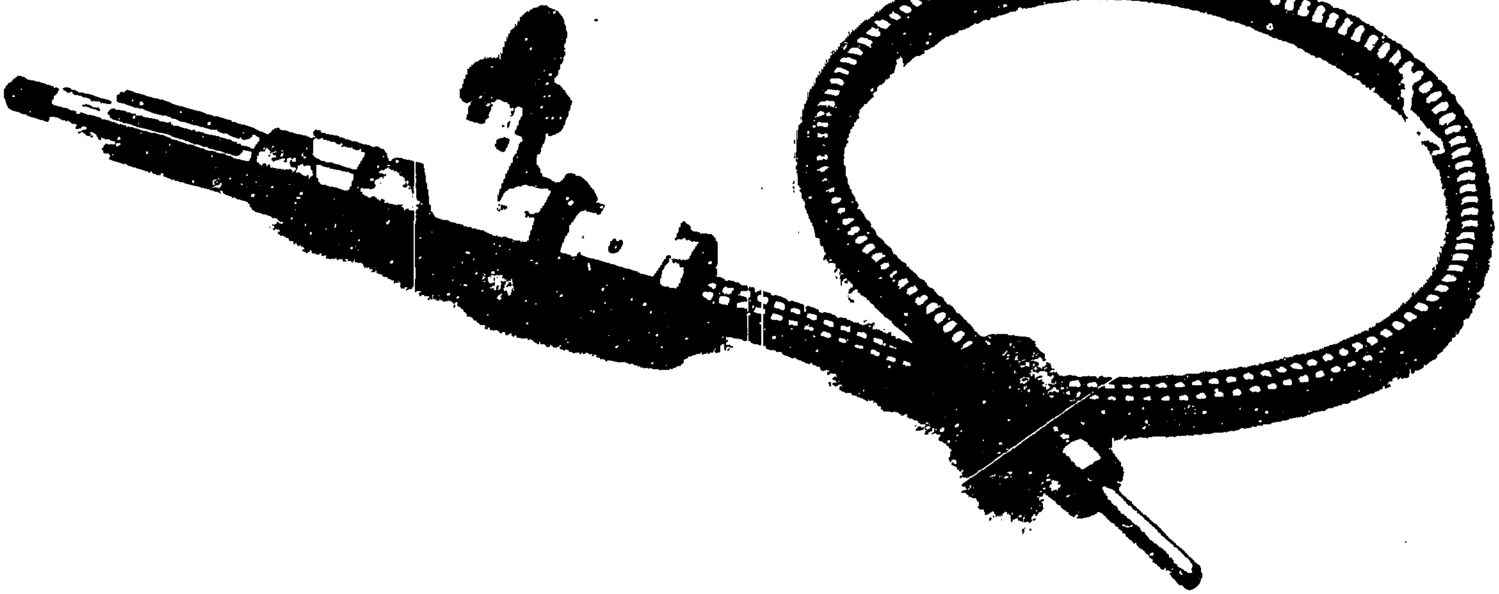

FIGURE 44 RADIATION PYROMETER ASSEMBLY

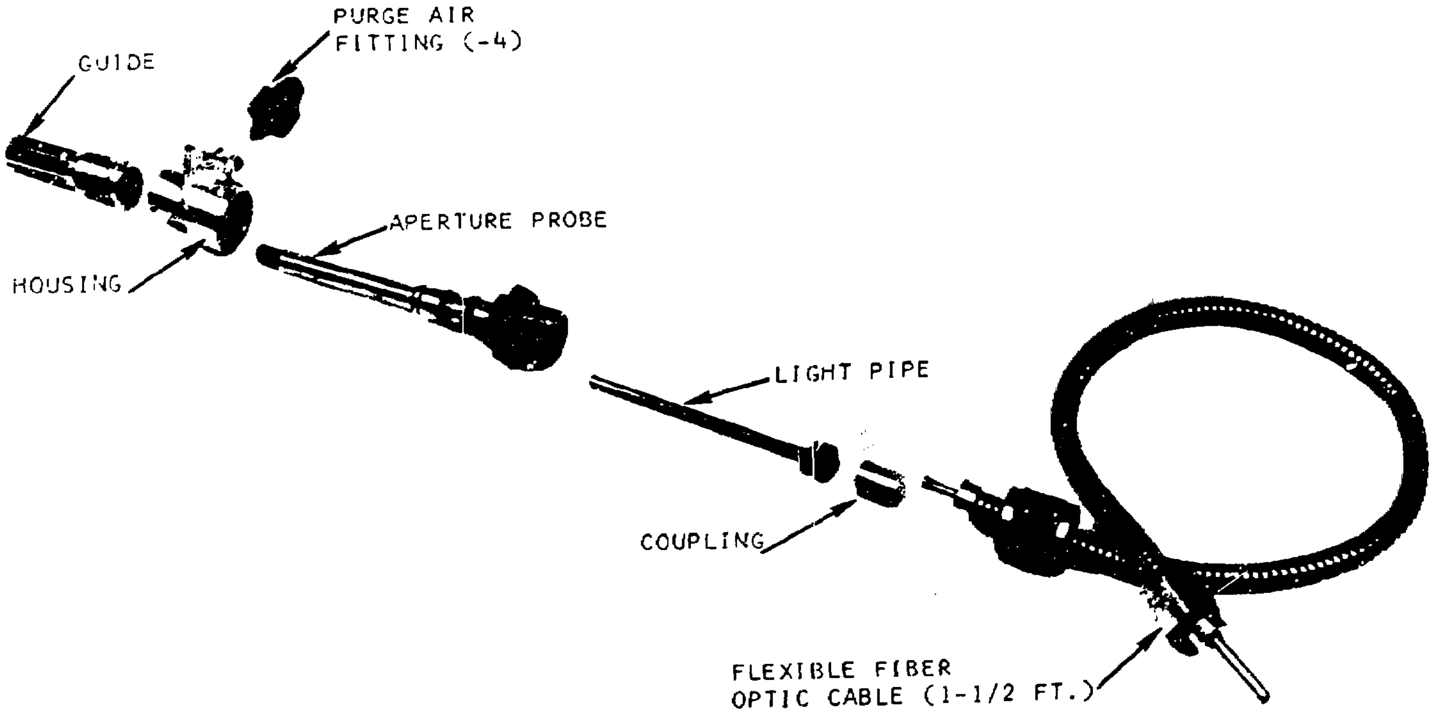

FIGURE 45. RADIATION PYROMETER DISASSEMBLED

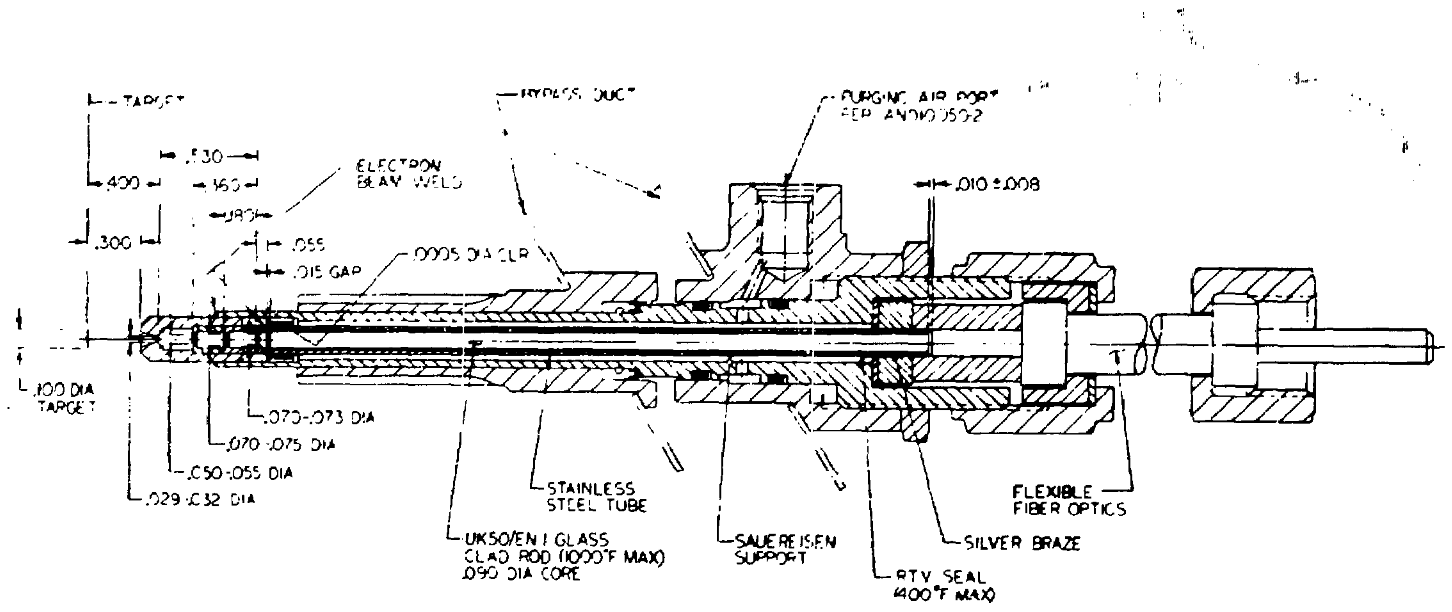

FIGURE 46 RADIATION PYROMETER LAYOUT DRAWING

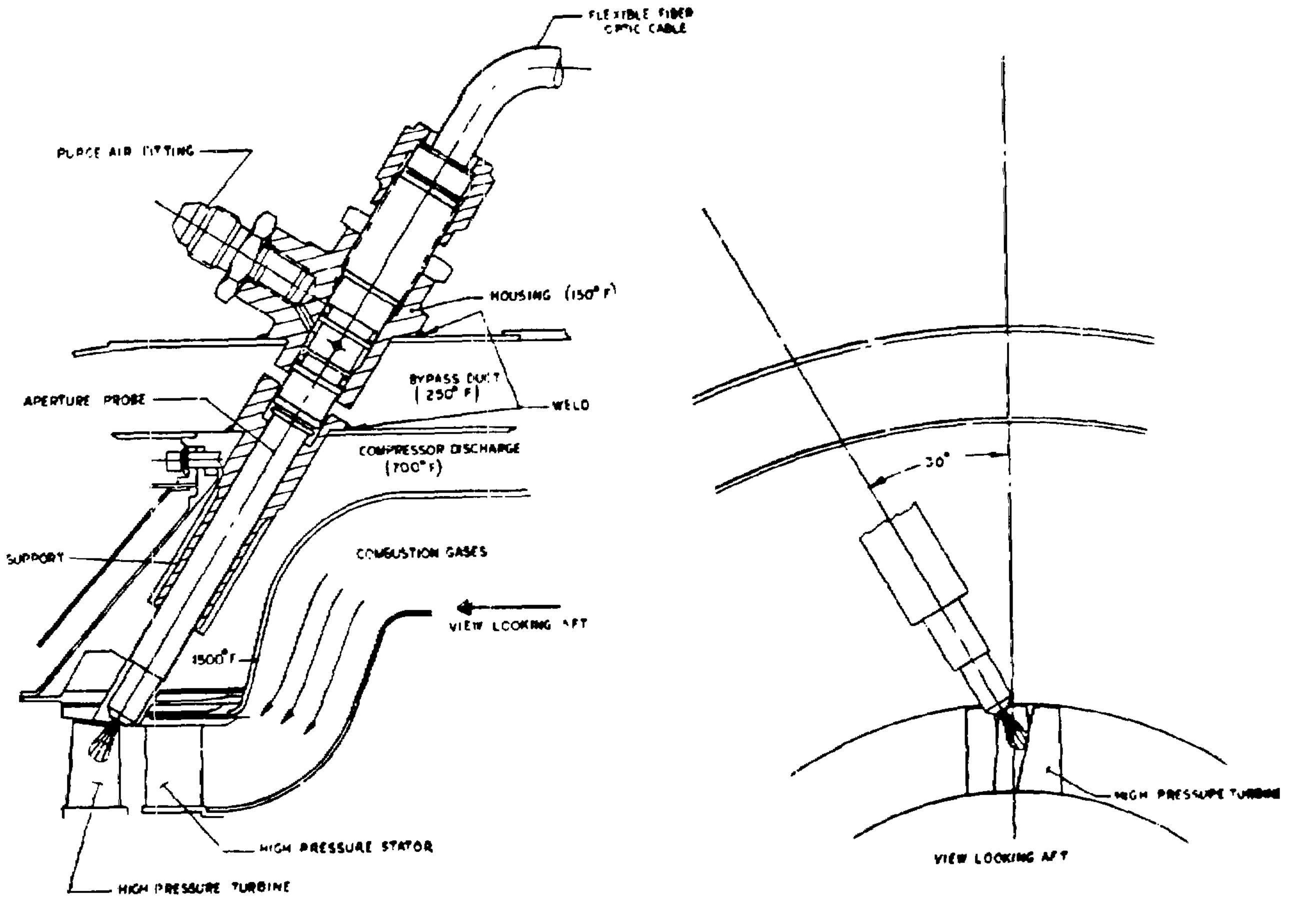

FIGURE 47 RADIATION PYROMETER INSTALLATION

50 g's, the extreme tip of the pyrometer probe should deflect less than .0006 inch. The maximum fiber stress occurring in the sleeve at this condition is well within the structural limits of the material. The glass rod is prevented from knocking about by being bonded into a steel tube. The tube is then supported at each end with a closely fitted bearing in the aperture assembly, and by an essentially rigid compression fit at its outboard, bushing end. The natural frequency of the light pipe supported in this manner computes to be 1400 Hz, approximately 40% greater than the upper limit of the vibration spectrum to be encountered on the engine.

A small amount of air flow for cooling and purging is routed through the pyrometer and into the turbine area. The flow passages are sized to yield an airstream velocity of approximately 20 ft/sec at an air flow of .0025 lb/sec. With an air inlet temperature of 100°F, calculations show that the above flow is sufficient to cool the pyrometer housing which resides in close proximity to the hot combustor and turbine casings (ref. Figure 47) to approximately 500°F. The outboard end of the pyrometer should be much cooler, approaching the ambient temperatures in its vicinity. The pyrometer elements, including the glass light pipe, are capable of withstanding 1000°F temperatures.

In addition to cooling the pyrometer assembly, the other important function of the air flow is to purge the optical elements of engine soot. Sonic flow can be achieved at the outermost orifice by supplying a pressure at the purge inlet port which is twice the pressure in the discharge area. Thus, the products of combustion in the engine gas stream will be prevented from fouling the critical sensor head apertures. Also, the purge air is deflected away from the face of the light pipe, and the light pipe is hermetically sealed to prevent any particles in the airstream from contaminating the glass. Were it not for the 400°F max. operating temperature of the glass to metal seal at the outboard end of the light pipe, the pyrometer could be operated on 700°F compressor discharge air. Development in this area is needed to execute a cost-effective, 1000°F, hermetic glass/metal seal.

Optical Design

The aperture assembly shown in Figure 47 is comprised of two primary orifices, the aperture and field stop, which together define the pyrometer's field of view. Two additional orifices are employed to minimize side wall reflections from off-target radiation. A sketch of this system is shown in Figure 48.

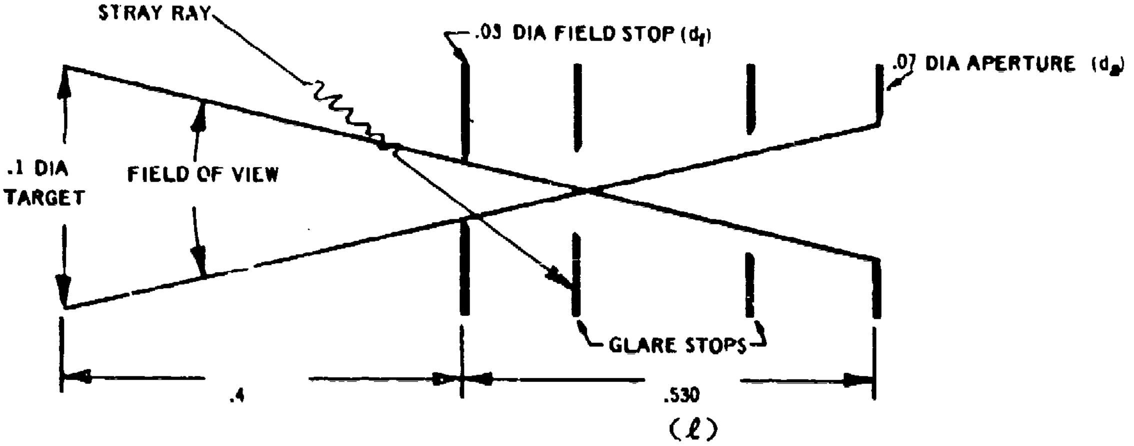

FIGURE 48. OPTICAL SYSTEM DESIGN

The field of view, as defined above, yields a target of .1 inches in diameter at the nominal blade to field stop distance of .4 inches. The bulk of the radiant energy collected by the aperture is contained within this ideal field; however, due to diffraction, internal reflection, etc., the actual field of view is increased over that shown above. Although this larger field of view results in a maximum target of .17 inches in diameter, negligible energy is collected from the outer limits of this increased target. If the side walls of the aperture assembly are cooled below 500°F, then radiation from them is insignificant compared to the radiation from the hot turbine blades.

The total power collected from a target within the field of view of the pyrometer is written as:

$$P = e \frac{W\lambda}{\pi} \left(\frac{\pi d_a^2}{4 \ell^2}\right)\left(\frac{\pi d_f^2}{4}\right)$$

where, P = spectral power collected by aperture, watts

e = emissance of turbine blade

$\frac{W_\lambda}{\pi}$ = spectral radiance of a constant temperature, black body and lambertian surface, watts/in^2/steradian

$\frac{\pi d_f^2}{4}$ = projected target area onto a plane where the solid angle of collected radiation for every point is constant, in^2

$\frac{\pi d_a^2}{4 \ell^2}$ = solid angle of collected radiation, steradian

The above equation is independent of turbine blade to sensor head distance as long as the blade remains within the field of view of the pyrometer. For variations in blade distance, the target diameter changes; however, its projected area onto the plane of the field stop remains constant. Thus, collected power remains unchanged, and consequently, measured blade temperature is not affected by variations in turbine blade to pyrometer distance. Thermal expansion of the components which define the field of view; i.e., field stop, aperture, and separation between the two, have negligible affect on the amount of collected power resulting in less than a 0.5°F error in measured blade temperature.

The radiant power collected by the optical apertures is transmitted through a light guide composed of a solid glass monofiber in series with a flexible fiber bundle. The solid light pipe which can withstand 1000°F temperature is employed in the hot section of the engine; the flexible fiber optic cable is utilized on the outside of the engine where the cooler surroundings are well within its 800°F operating ceiling.

Light transmission through the guide is determined by approximately 5% reflection loss at each glass/air interface, 10% absorption loss per foot, and 30% loss due to the presence of opaque cladding directly in the light stream of the fused fiber bundle. The transmission of the light guide can be totaled as shown below.

$$T = \nu_p \nu_c$$

where, T = transmission ratio of the light guide, watts/watt

ν_p = light pipe transmission, 0.85

ν_c = flex cable transmission, 0.45

Previous in-house testing has demonstrated that the light pipe and flex cable maintain their transmission efficiency after thermal cycling within their operating limits and after vibration to 60g levels.

The radiant energy emanating from the flexible fiber optic cable is displayed onto a silicon, photovoltaic detector. The bandpass characteristics of the silicon are such that radiation energy in the .4 to 1.1 micron wavelength region is accepted. Thus, the useful power incident on the detector may be estimated from the above equations and is tabulated below.

Target Temp. (°F)	Target Spectral Radiance $\left(\frac{\text{Watts}}{\text{In}^2}\right)$	Incident Power at Detector (μ watts)
1300	.02	.023
1600	.21	.24
1800	.73	.84
2000	1.80	2.08

The above power levels are shown to be adequate in the following electronic design section.

Electronic Design - Detector and Current/Voltage Converter

The silicon photovoltaic detector is operated in its short circuit current mode in conjunction with an FET input, high speed (70V/microsecond in the voltage follower mode) LH0062 operational amplifier. A schematic of the detector and converter is shown in Figure 52 . In this mode, the responsivity of the detector (0.3-0.6 amps/watt) yields approximately 10 nanoamperes of current at the minimum blade temperature of interest (1300°F). The input offset and bias currents for the LH0062 amplifier are in the pico-ampere range, thus rendering their drift with ambient temperature, time, etc., insignificant.

The output current of the silicon photovoltaic detector changes with variation in ambient temperature. To counteract this, a thermistor network is bonded to the detector and connected in the feedback path of the amplifier. As the ambient temperature in the vicinity of the detector changes, so does the magnitude of the thermistor resistance and hence, the amplifier gain changes to compensate for the variation in detector current. Over the 0 to 150°F ambient temperature range, the measured blade temperature error is limited to ± 10°F for blade temperatures above 1600°F.

A disadvantage of the low cost approach of combining readily available components in the detector and current to voltage converter was revealed by the variation in detector characteristics, namely the junction resistance and capacitance of the photodiode. The capacitance of the detector played havoc with the stability of the converter, thereby requiring dynamic compensation which lowered the bandwidth of the device below desirable levels. The predicted affect of converter response on the accuracy of the pyrometer is approximately a 2% reduction in measured peak blade temperature at the maximum engine speed of 64,000 RPM. The variation in diode junction resistance with ambient temperature caused the input offset voltage drift of the amplifier to play a larger than expected role at low target temperatures. Thus, a more accurate compensation network was not realizable, resulting in a +40/-20°F error in measured blade temperature at 1300°F.

A total system accuracy of better than ± 1% is the goal of a turbine blade temperature sensing radiation pyrometer. The aperture system developed under the current AFAPL program is capable of meeting this accuracy only in the temperature limiting mode of operation above target temperatures of 1600°F. For better than 1% accurate blade temperature measurement over a wide range of blade temperatures (1300-2000°F), and ambient temperatures (-65-200°F), and turbine speeds in excess of 60,000 RPM, further development of the detector and current to voltage converter is required. The silicon detector must be manufactured to closely controlled specifications and/or an even more sophisticated operational amplifier must be developed.

Test Results

The radiation pyrometer sensor provides the electronic processor with a D.C. voltage level which is proportional to turbine blade temperature. Ideally, this voltage must track a rapidly moving turbine blade; i.e., 14 μseconds to pass the pyrometer's field of view at rated engine speed, and be impervious to sensor head environment and variations in detector ambient temperature. To amplify previous in-house testing on similar components and thereby gain assurance that the hardware is suitable for engine mounting, a series of tests divided into the following categories was performed.

Sensor Head Environment

Optical Performance

Electronic Performance

The results of these tests are summarized in the following sections.

Sensor Head Environment

The potentially most sensitive component to the sensor head environment is the glass light pipe. Thus, vibration, thermal cycling, and high pressure leakage tests were conducted on the light pipe, and the results tabulated in Figure 49 In each configuration, the glass was held firmly within its steel tube and withstood 1000°F temperatures and 50g vibration levels with no visible deterioration and negligible transmission loss. The amount of leakage encountered was negligible compared to engine air flow of approximately 7 lbs/sec; however, any air flow directed past the light pipe could cause contamination to be deposited onto the face and result in a calibration shift. Thus, the final configuration light pipe consists of a combined Sauereisen and RTV bonded rod. The RTV at the cool outboard end of the pipe creates a hermetic seal up to 400°F, while the Sauereisen along the remainder of the tube holds the glass in place at elevated temperatures. Purging with air at approximately 100°F insures that the light pipe in the vicinity of the seal remains below 400°F.

VIBRATION TEST

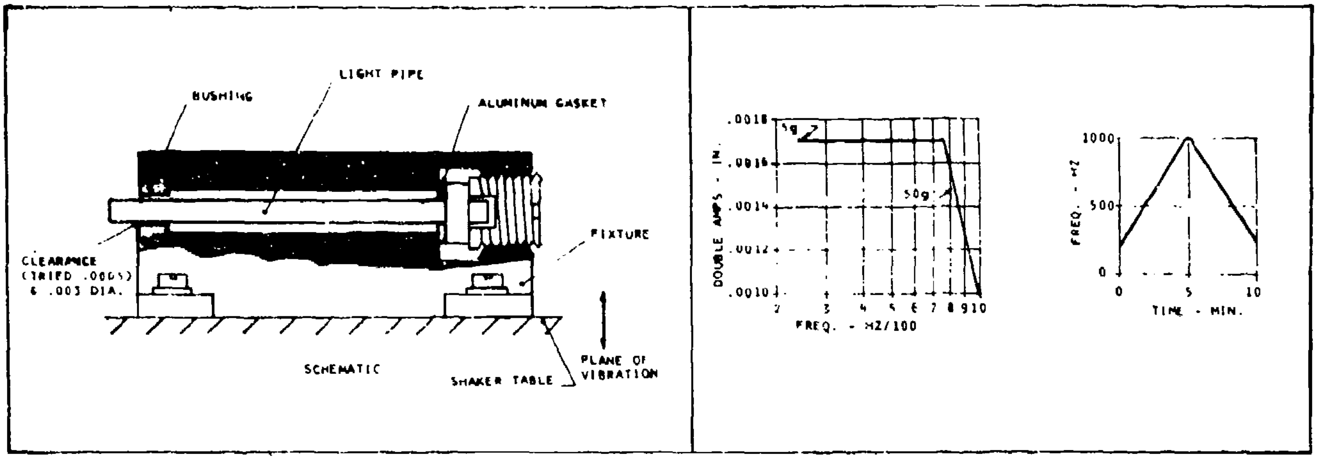

TEMPERATURE TEST

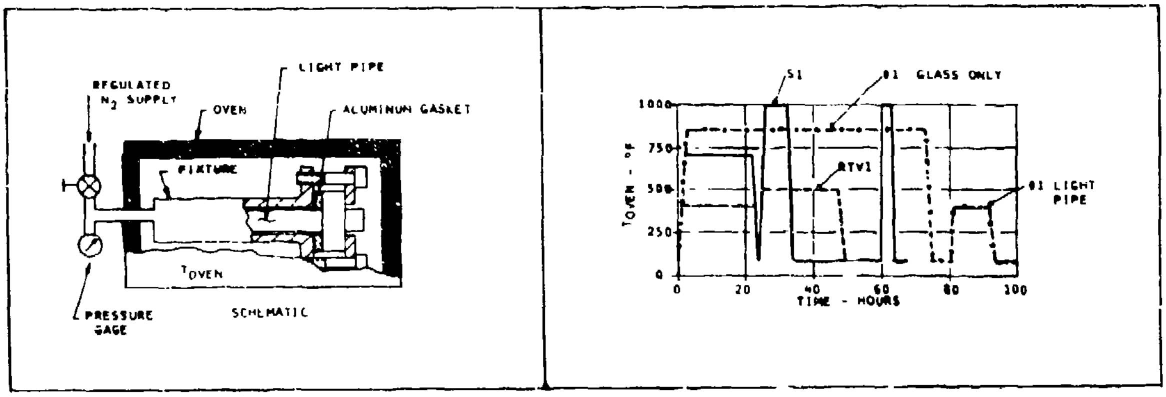

TEST RESULTS

LIGHT PIPE SERIAL NO.	DESCRIPTION	TRANSMISSION		TRANSMISSION		N_2 LEAKAGE AT 250 PSID (LBS/HR)
		BEFORE	AFTER VIBRATION	BEFORE	AFTER THERMAL CYCLES	
S1	SAUEREISEN			115	115	0.2
S2	SAUEREISEN	116	116			0.1
RTV1	RTV BOND			116	116	0 (UP TO 400°F)
RTV2	RTV BOND	116	116			0 (UP TO 400°F)
#1	FINAL CONFIG. SAUEREISEN AND RTV	116	116		116	0 (UP TO 400°F)

FIGURE 49 LIGHT PIPE ENVIRONMENTAL TESTS

The development of a 1000°F hermetic light pipe seal which would have allowed purging with 700°F engine CDP was not successful. However, many promising schemes, including various high temperature cements, were uncovered for future development work. These avenues should be investigated with the goal of developing a cost effective, high temperature, sealed light pipe configuration suitable for production hardware.

The proper amount of purge and cooling air is vital in limiting the temperature of the probe. A flow vs. inlet pressure calibration of the unit was made and is plotted in Figure 50 . A conservative heat transfer analysis shows that a 100°F airstream of .002 lbs/sec and approximately 15 ft/sec is sufficient to cool the hot section of the aperture probe below 500°F at rated engine conditions. For the .025 inch radial clearance between light pipe and probe, the required velocity is exceeded in the operating region shown in Figure 50 . A P_{DIS}/P_{IN} pressure ratio less than .528 and a P_{IN} pressure greater than 200 PSIA is needed to achieve the desired airstream properties and thereby cool and purge the critical optical components of the sensor head.

To qualify as an accurate temperature sensor, the pyrometer's output signal must be insensitive to the variations in sensor head temperature experienced between an engine start-up and rated operation. Differential expansion of the optical orifices and radiation from the internal side walls of the aperture assembly could be a factor at low target and high pyrometer temperatures. A low acceptance angle (± 20°) light pipe and glare stops are employed to minimize the latter effect. The aperture assembly, while viewing a black body radiation standard, was heated locally at its aperture end with a propane torch and its surface temperture monitored with a thermocouple. The results show that at the minimum target temperature of interest, 1300°F, the apertures must be less than approximately 600°F to limit the error in measured blade temperature to less than 10°F. The pyrometer will be cooled to 500°F in this application, at which point the error is less than 2°F at a blade temperature of 1300°F and is negligible at higher blade temperatures.

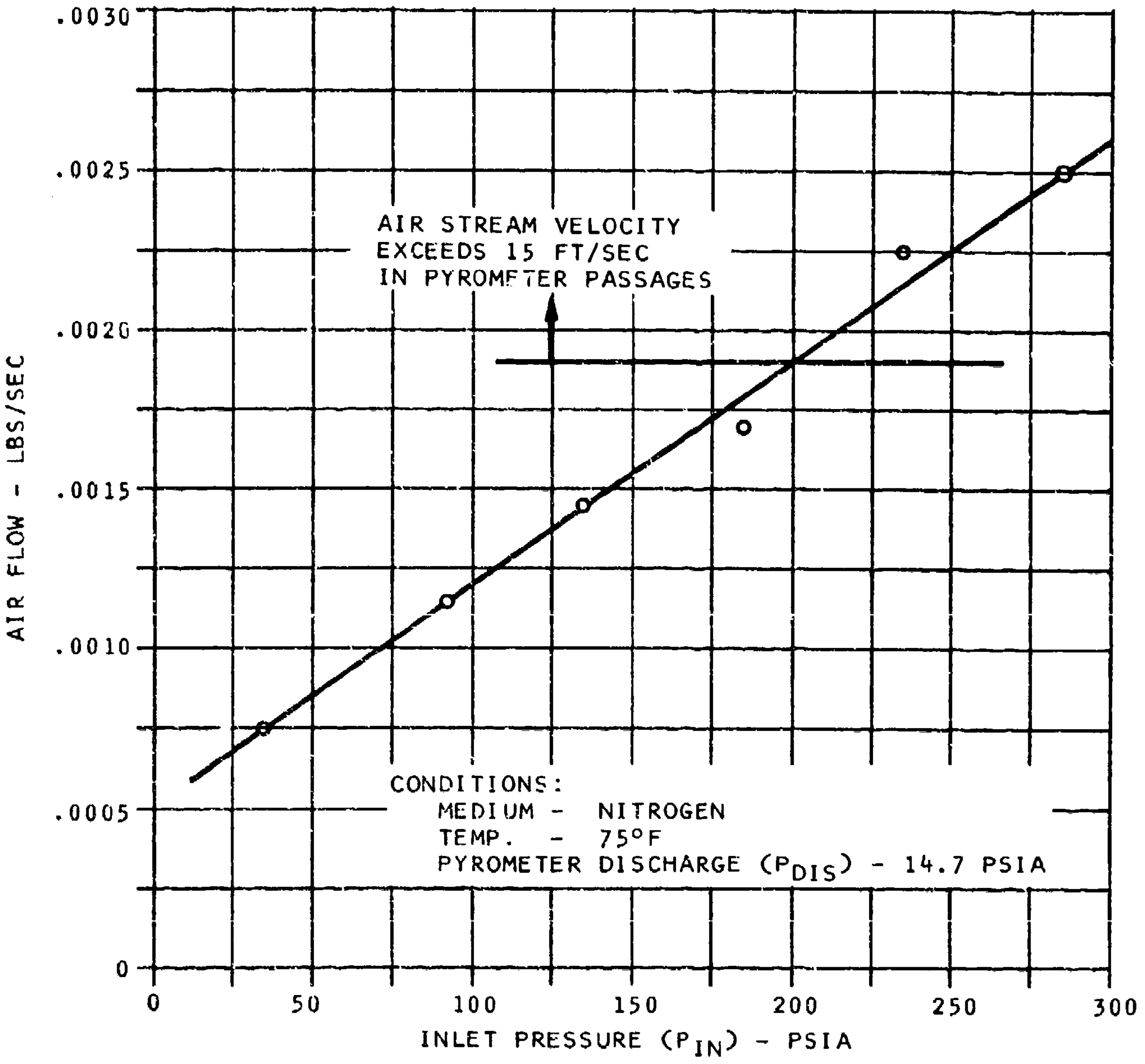

FIGURE 50 PURGING AIR FLOW CALIBRATION

Optical Performance

The function of the aperture assembly is to define the optical field of view of the pyrometer. The manner by which the system performs this task is discussed in the Optical Design section (Page 84). The field of view of the aperture probe was tested by sighting the assembly onto a uniformly intense and diffuse light source in a photographic darkroom. The light pattern emanating from the aperture was displayed onto light sensitive paper which was accurately positioned in relation to the probe. A linear measurement of the developed image yields an indirect reading of target size and thus, the field of view of the instrument. A schematic of the test setup, including a photograph of the target image, is included in Figure 51 . The results show that a large portion of the radiation is collected from a 0.1 diameter target, with a significantly reduced intensity area extending to less than .17 inches diameter. The target size is well within the dimensions of typical turbine blades on small engines and, therefore, is acceptable. For a more precisely defined field of view, the outer fringe region must be reduced with perhaps a more elaborate set of baffles and/or high temperature, unreflective coatings.

Electronic Performance

Steady State

The silicon photovoltaic detector and thermally compensated current/voltage converter were tested over an ambient temperature range from 0-150°F. The aperture sensor head was sighted onto a black body radiation standard and the energy transmitted via the flexible fiber optic cable to the detector and converter which were located in an environmental chamber. A circuit diagram of the electronics and steady state performance at three target temperatures are shown in Figure 52. The variation in output voltage due to a mismatch between the compensating feedback network and detector characteristic can be translated into a measured blade temperature error by comparison with Figure 53 . The latter figure shows a sensor head calibration at a fixed ambient but varying blade temperature. An ambient of 120°F was chosen to average out the effect of the electronic temperature variations at any one target temperature. From the above data, the maximum steady state error due to ambient temperature variations within 0-150°F is tabulated below:

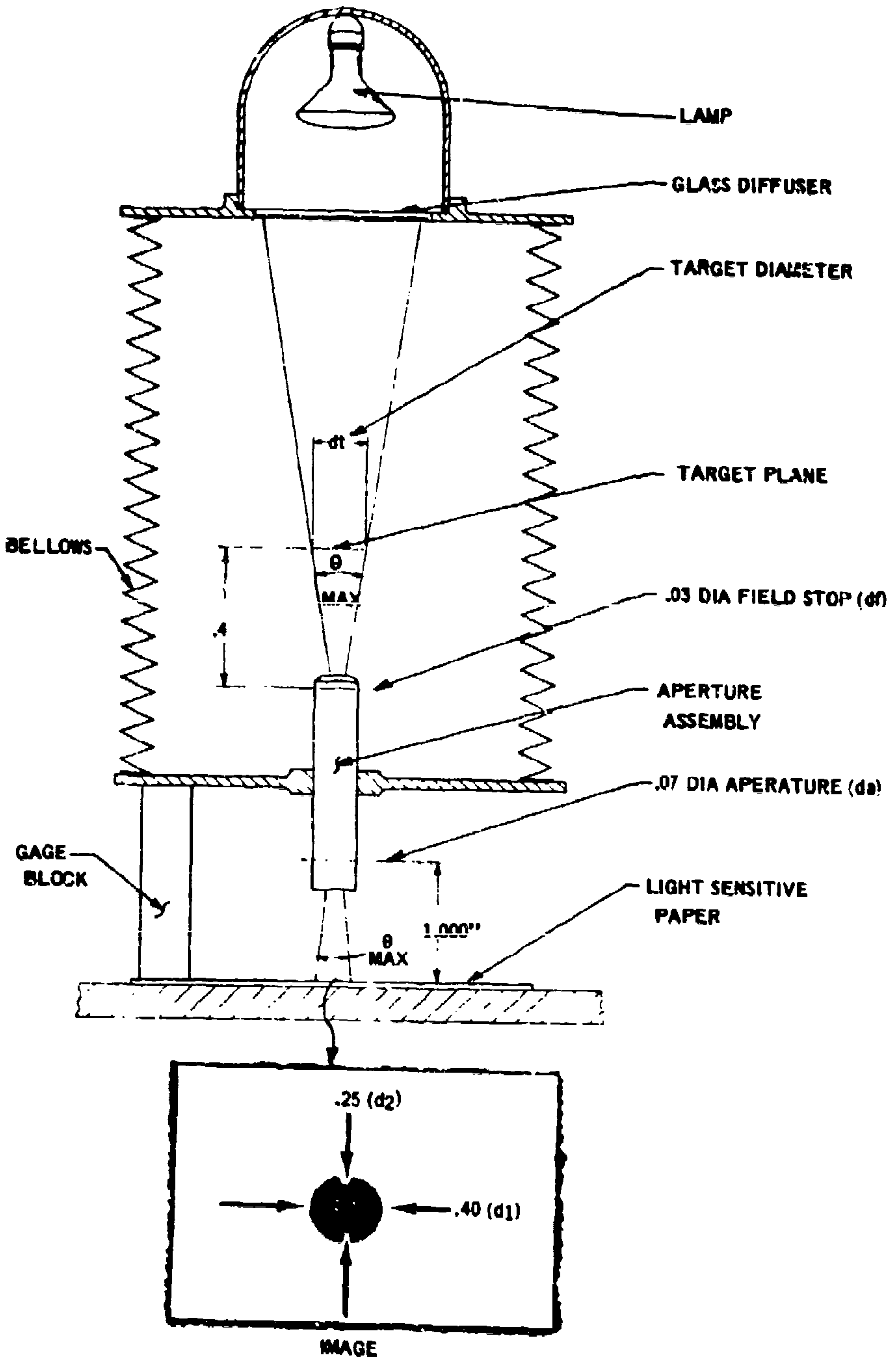

FIELD VIEW, θ_{MAX}

$$\theta_{MAX} = 2\tan^{-1}\left(\frac{d_1 - d_a}{2}\right) = 18.8^\circ$$

$$d_t = 0.8 \tan\left(\frac{\theta_{MAX}}{2}\right) + df = 0.162$$

INNER, INTENSE FIELD OF VIEW

$$\theta_{IN} = 2\tan^{-1}\left(\frac{d_2 - d_a}{2}\right) = 10.3^\circ$$

$$d_{t\,(IN)} = 0.8 \tan\left(\frac{\theta_{IN}}{2}\right) + df = 0.102$$

FIGURE 51 OPTICAL FIELD OF VIEW TEST

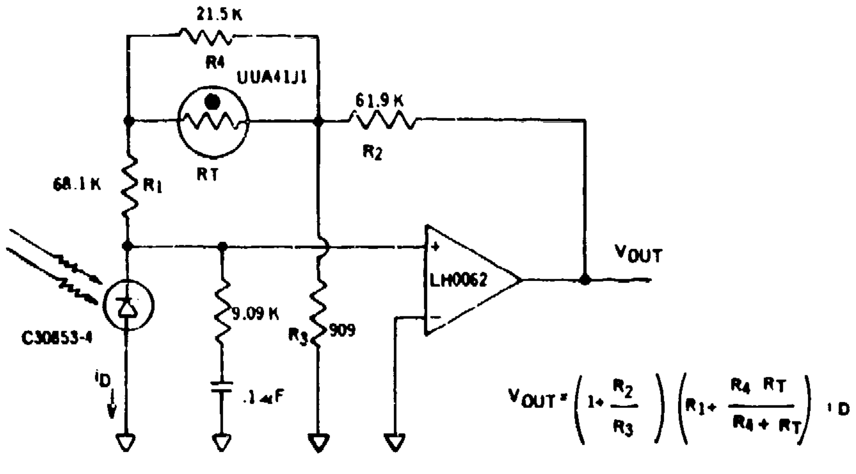

CIRCUIT DIAGRAM

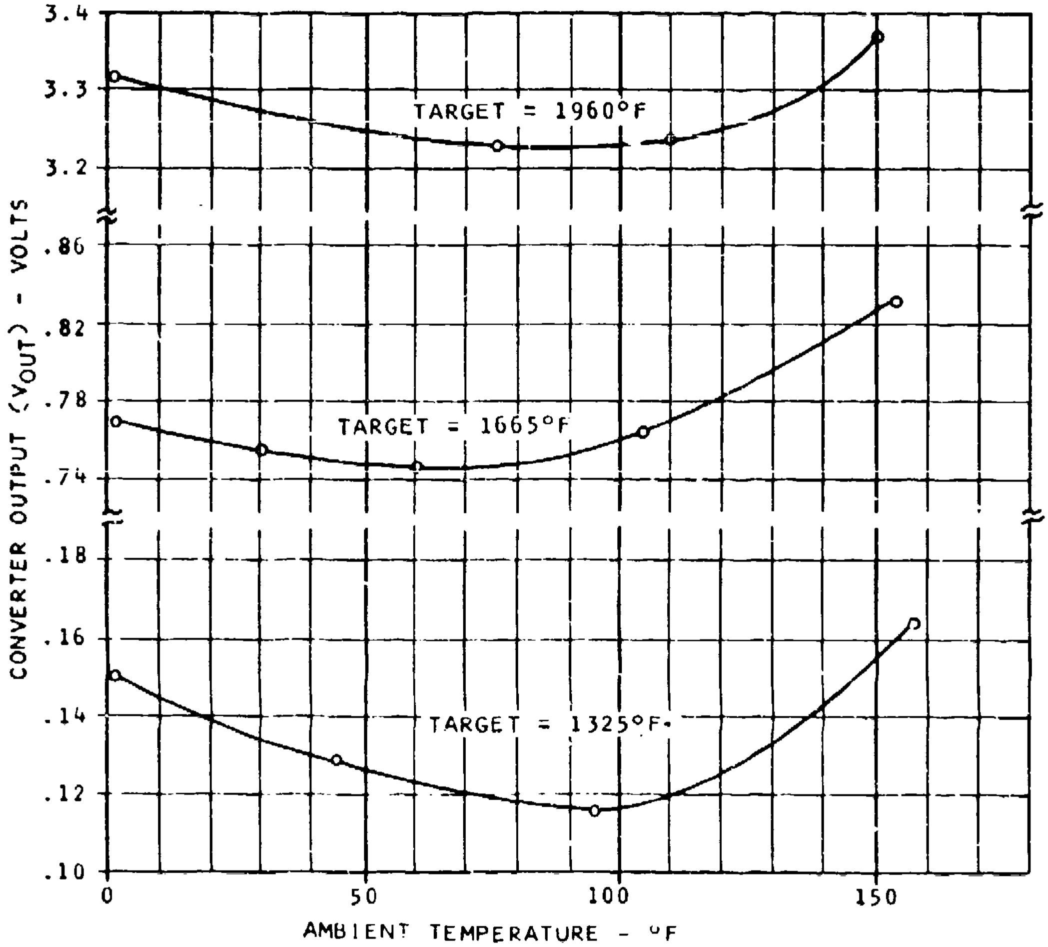

FIGURE 52 DETECTOR AND CURRENT/VOLTAGE CONVERTER STEADY STATE CALIBRATION VS AMBIENT TEMPERATURE

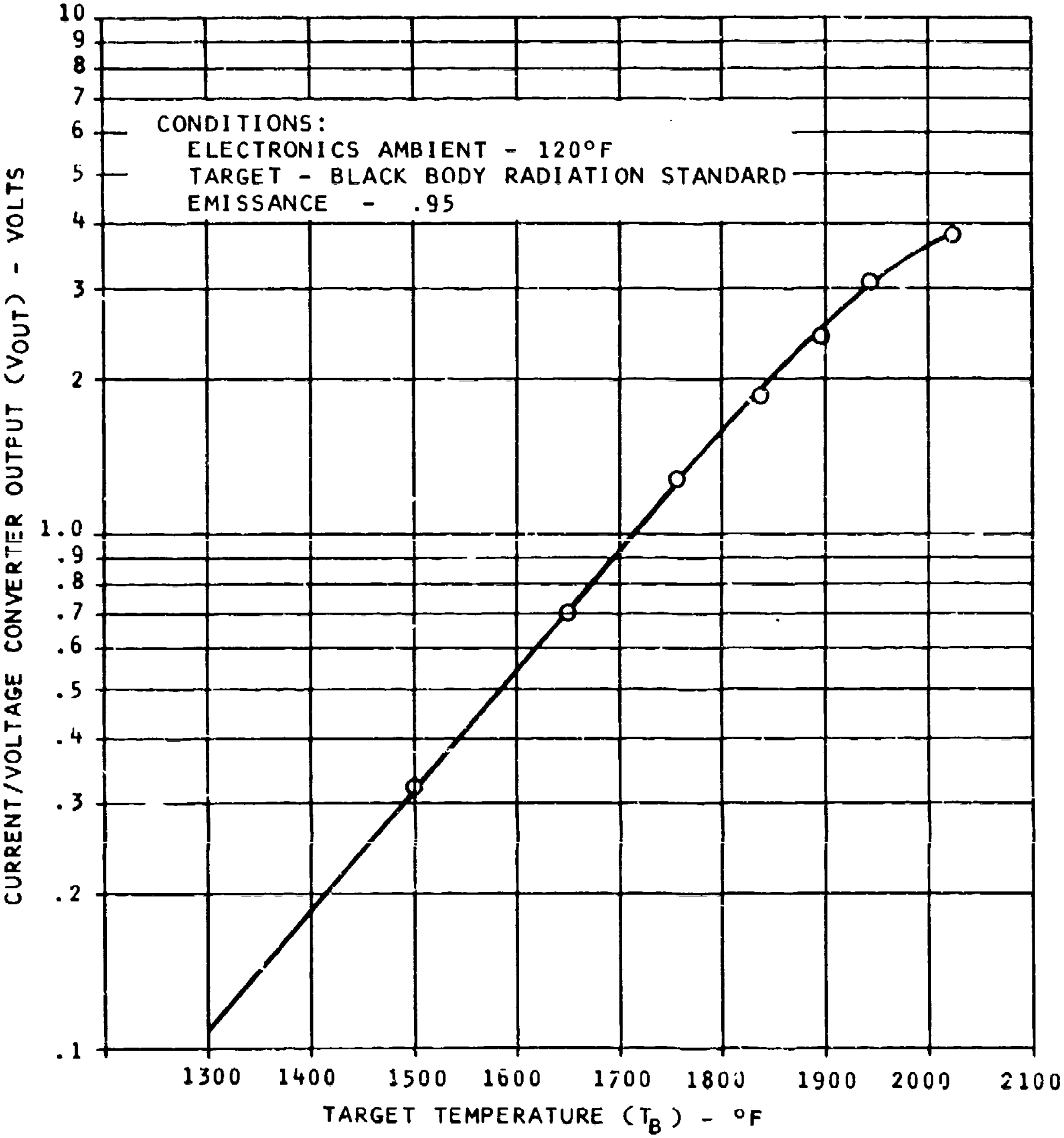

FIGURE 53 DETECTOR AND CURRENT/VOLTAGE CONVERTER STEADY STATE CALIBRATION AT 120°F AMBIENT

Blade Temperature (°F)	Measured Blade Temperature Error (°F)
1325	+40/-20
1665	+10/-10
1960	+ 6/-5

Dynamic

The dynamic response of the detector and current to voltage converter was tested by exciting the aperture sensor head with a function generator driven LED whose light output was monochromatic at 900 nanometers. Since measurement of peak blade temperature is of interest, overshoots in the electronic circuitry prior to the peak detector are not allowable. Dynamic compensation, comprised of a 9.09 K-ohm resistor in series with a blocking capacitor, was used to shunt the photodiode and execute a critically damped system. Step response traces with and without compensation are shown in Figure 54 The time for the output voltage to reach steady state was 20 μ seconds at room temperature and 30 μ seconds at hot and cold ambients.

The period, T, between adjacent blades passing the pyrometer's field of view can be computed as follows:

$$T = \frac{60}{(\#\ \text{Blades}) \times (\text{RPM})}, \ \text{sec.}$$

For 67 blades rotating at 64,000 RPM, the period is 14 μseconds. Since the response time of the pyrometer system exceeds 20 μ-seconds, an error in measured blade temperature could result depending on the input radiation waveform.

Based on the 19° field of view of the pyrometer and its spacial relationship to the first stage turbine as shown in Figure 47 , the radiation input signal can be estimated for two extreme conditions of interest:

a) All blades hot

b) One hot blade

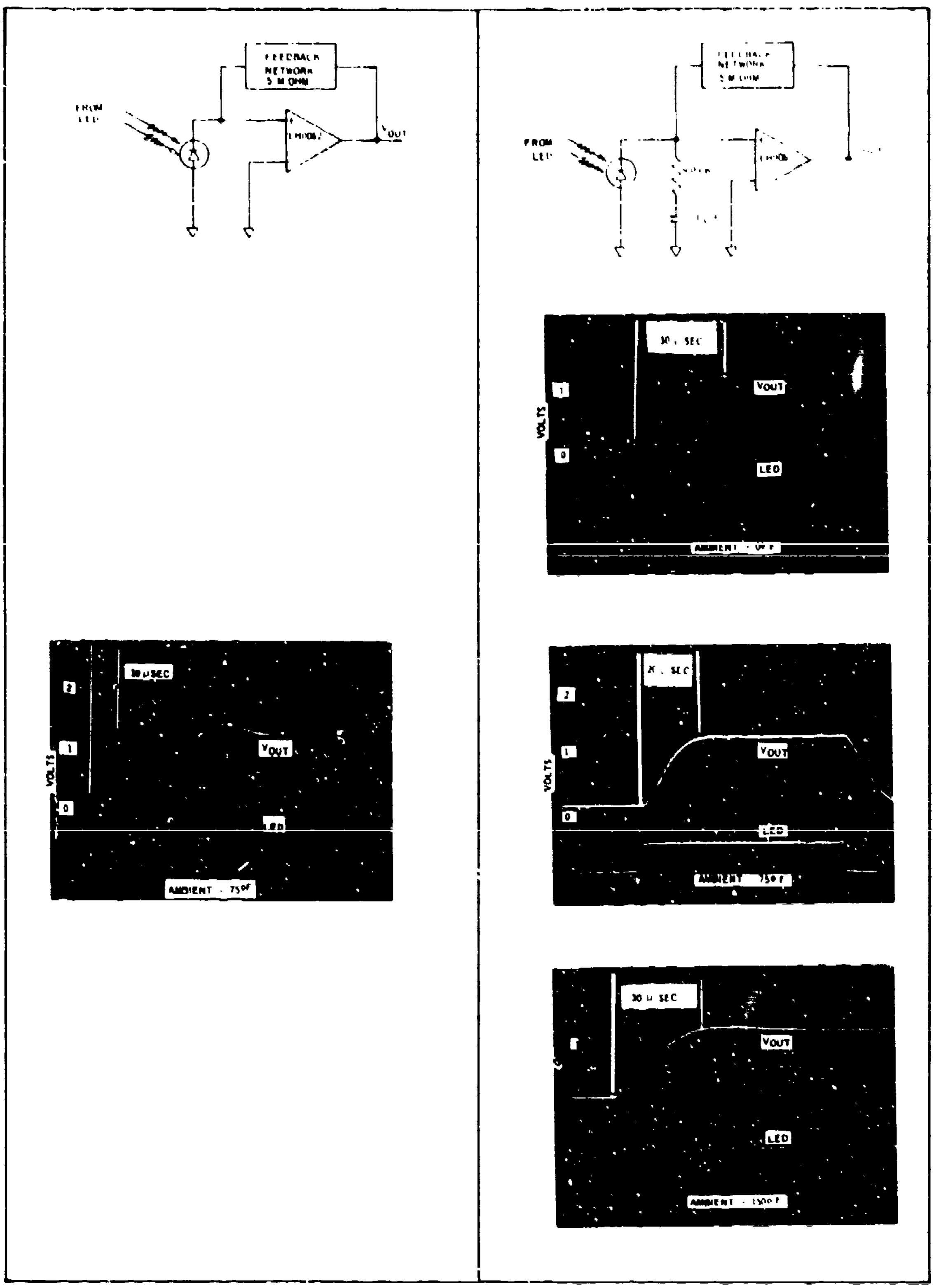

FIGURE 54 PYROMETER RESPONSE TO A STEP RADIATION INPUT

For the condition of all blades at the same temperature, the input waveform is dependent on the portion of the blade which is "seen" by the pyrometer as it sweeps by its field of view. For instance, if the target is always confined to the upper half of all blades where the temperature is uniform, then the radiation input to the pyrometer is essentially a D.C. level. However, if the target sweeps between the blades and views the rotor portion of the turbine then a periodic waveform like the configuration shown in Figure 55 would result.

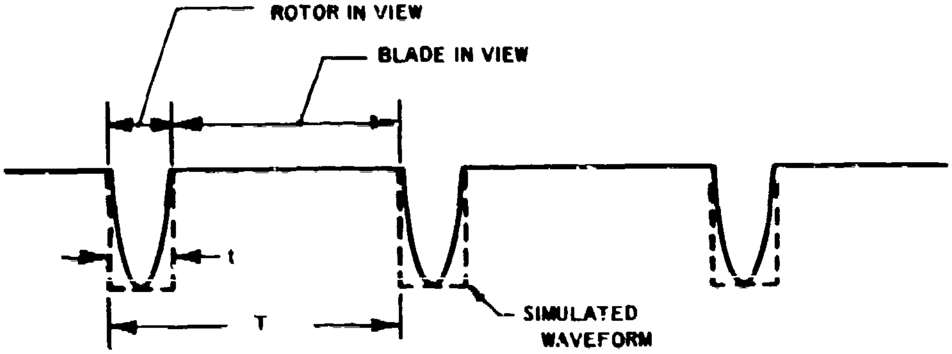

FIGURE 55.TURBINE BLADE RADIATION SIGNAL

The above waveform with an equivalent peak-to-peak temperature variation of approximately 400°F was simulated via the LED and displayed onto the aperture probe. For various t/T-t ratios, the period was varied from 140 to less than 14 μseconds, thereby simulating engine speeds from 10 to over 100%. The peak output voltage of the converter, which attenuates at high engine speeds due to its 20 μsecond response time, was monitored on a wide band oscilloscope. The results of the test are plotted in Figure 56 in terms of measured blade temperature error for a peak blade temperature of 1800°F. For the planned installation shown in Figure 47 , the radiation signal will be defined by the temperature profile of each blade and variations in temperature between adjacent blades since a turbine blade is always in view. Moreover, for a t/T-t viewing ratio of .1, a maximum temperature error of only 10°F will be encountered at rated engine speed of 64,000 RPM.

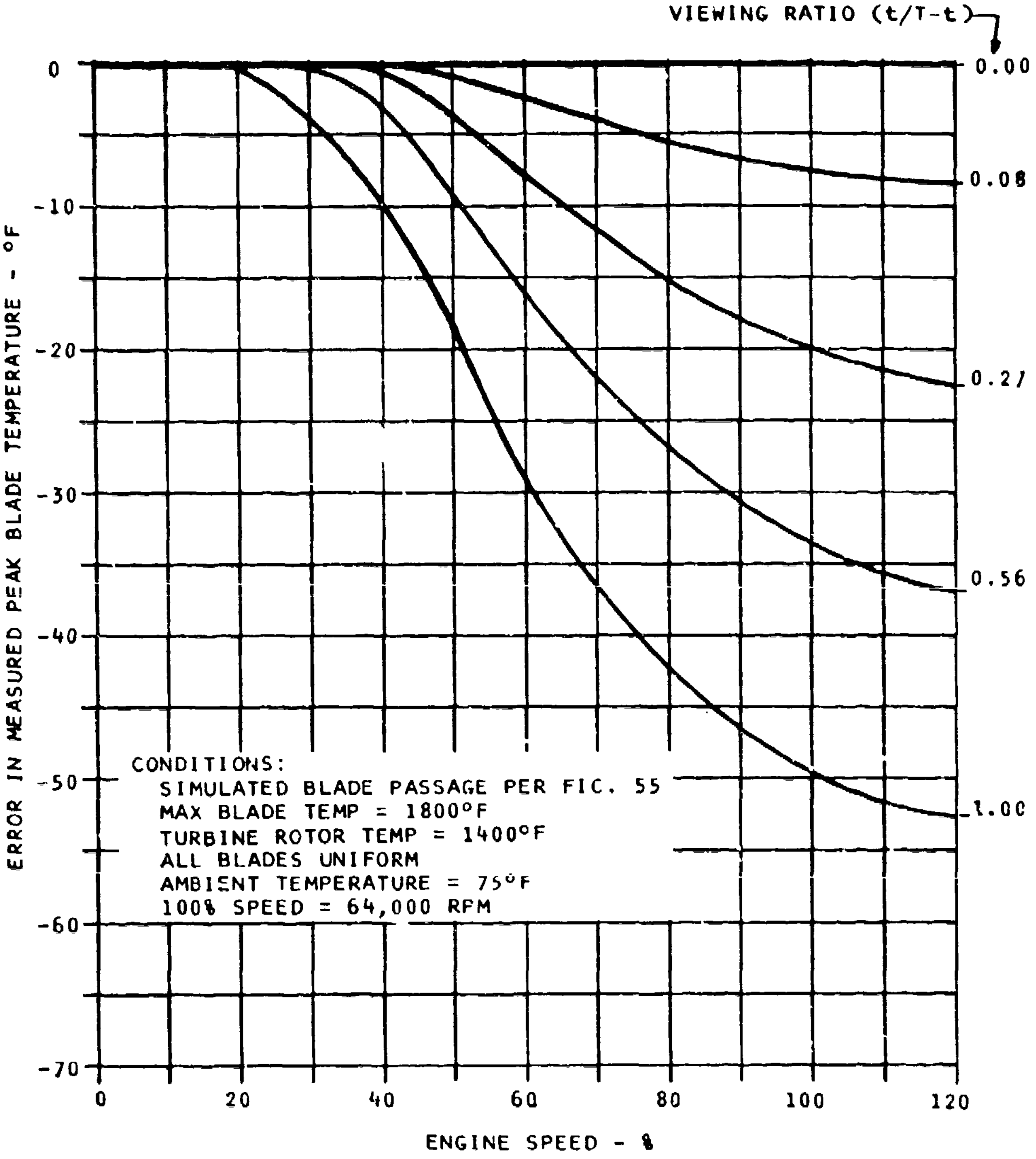

FIGURE 56 PYROMETER RESPONSE TO SIMULATED BLADE PASSAGE AT VARIOUS ENGINE SPEEDS

A more severe input to the current/voltage converter occurs when one blade is significantly hotter than its adjacent blades. Under these conditions, the time during which the hot blade is fully in view is considerably reduced as shown in Figure 57.

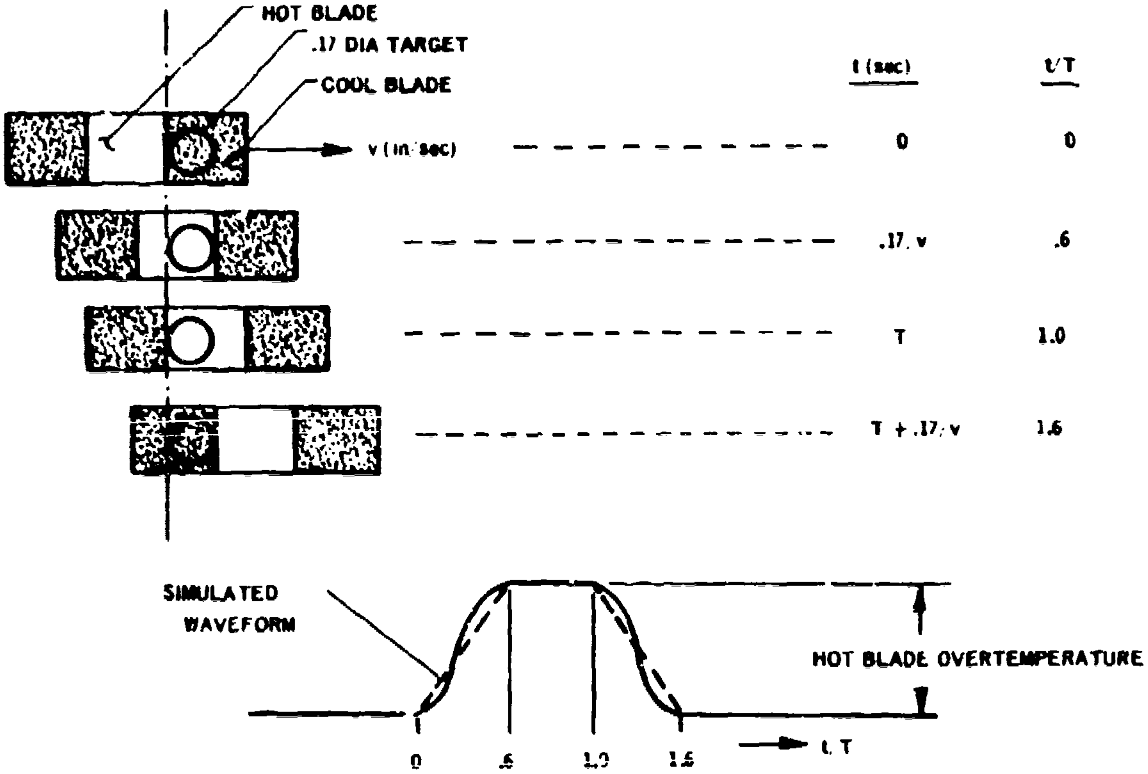

FIGURE 57. SIMULATED HOT BLADE

The target is approximately locaded on a 3-inch radius from the engine centerline, thus the tangential velocity of the turbine blades at this radius may be related to the blade passage period, T, by the following equation:

$$v = \frac{6\pi}{\#\ \text{Blades} \times T}, \ \text{in/sec}$$

For 67 blades, the tangential velocity computes to be .28/T; thus, the input waveform may be plotted relative to the period T as shown above. The time for which the hot blade is fully in view is only 40% of the period. The above waveform for various levels of blade overtemperature and engine speed, was generated via the LED and applied to the aperture sensor head. Photographs of the LED input and current/voltage converter output voltage waveform which were obtained from the oscilloscope are given in Figure 58 . The attentuation in the peak output voltage at 100% speed (T = 14 μ seconds) is expressed in terms of measured blade temperature error in Figure 59 . For a 200°F hot blade overtemperature, the error is less than 40°F for the worst case, 1800°F turbine.

The significant errors in measured blade temperature within the radiation pyrometer sensor head occur in the electronic section consisting of the photodiode and current/voltage converter. Thus, a direct summation of the maximum errors described above will give an indicotion of the expected worst case performance of the pyrometer system.

Blade Temp. (°F)	Steady State Error (°F)	Dynamic Response Error (°F)	Maximum Total Error (°F)
1300	+40/-20	-10	+40/-30
1650	+10/-10	-15	+10/-25
1950	+6/-5	-35	+6/-40

Over the blade temperature range listed above, an electronic ambient temperature range of 0-150°F, and a turbine speed range of 6,400 to 64,000 RPM, the pyrometer sensor head is accurate to within 2% at the high end of its scale, 1.5% at mid-range, and 3% at low turbine blade temperatures.

3. COMPRESSOR DISCHARGE PRESSURE SENSOR

The important requirements for a high performance pressure transducer are as outlined below.

Pressure range	8 to 250 PSIA
Response	10 ms time constant
Accuracy	See Figure 60
Warm-up time	0.5 seconds

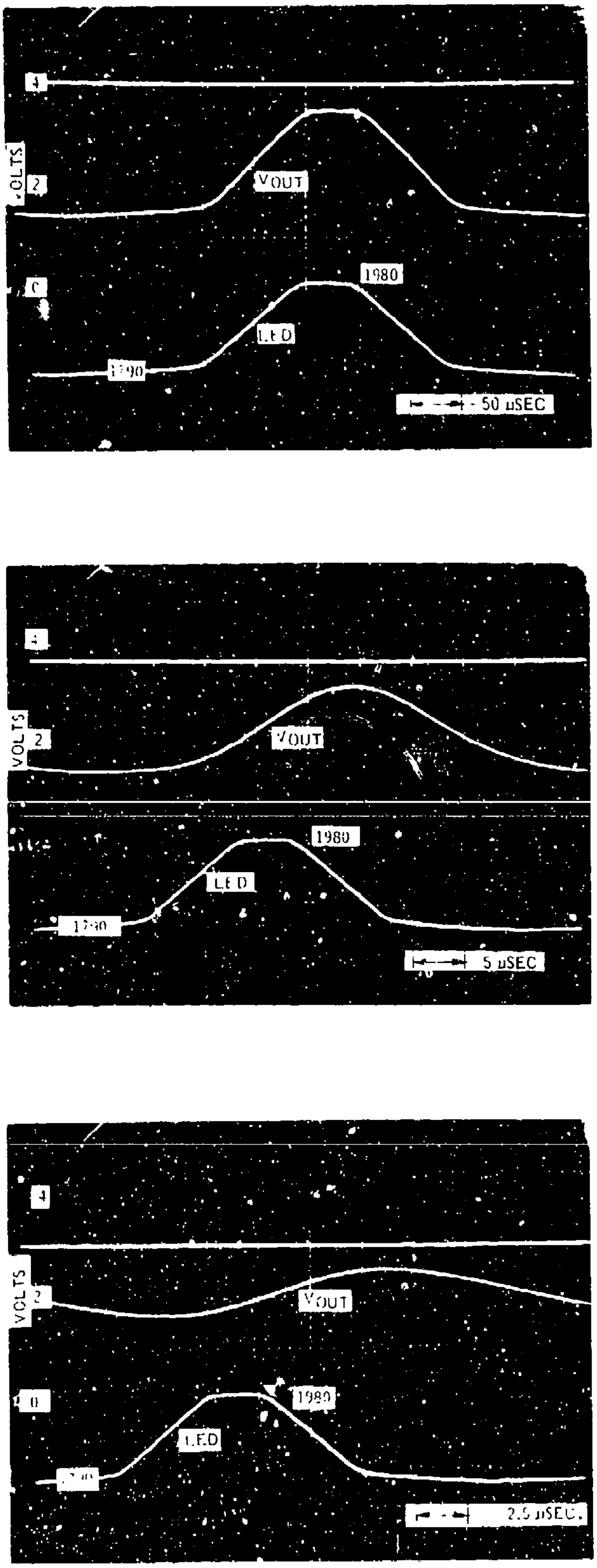

N_1 = 10%

V_{OUT} = 3.5VOLTS (PEAK)

MEASURED T_B = 1980°F

N_1 = 100% (64,0(RPM)

V_{OUT} = 3.1 VOLTS (PEAK)

MEASURED T_B = 1945°F

N_1 = 200%

V_{OUT} = 2.5 VOLTS (PEAK)

MEASURED T_B = 1900°F

FIGURE 58 CURRENT/VOLTAGE CONVERTER WAVEFORMS IN RESPONSE TO A SIMULATED HOT BLADE

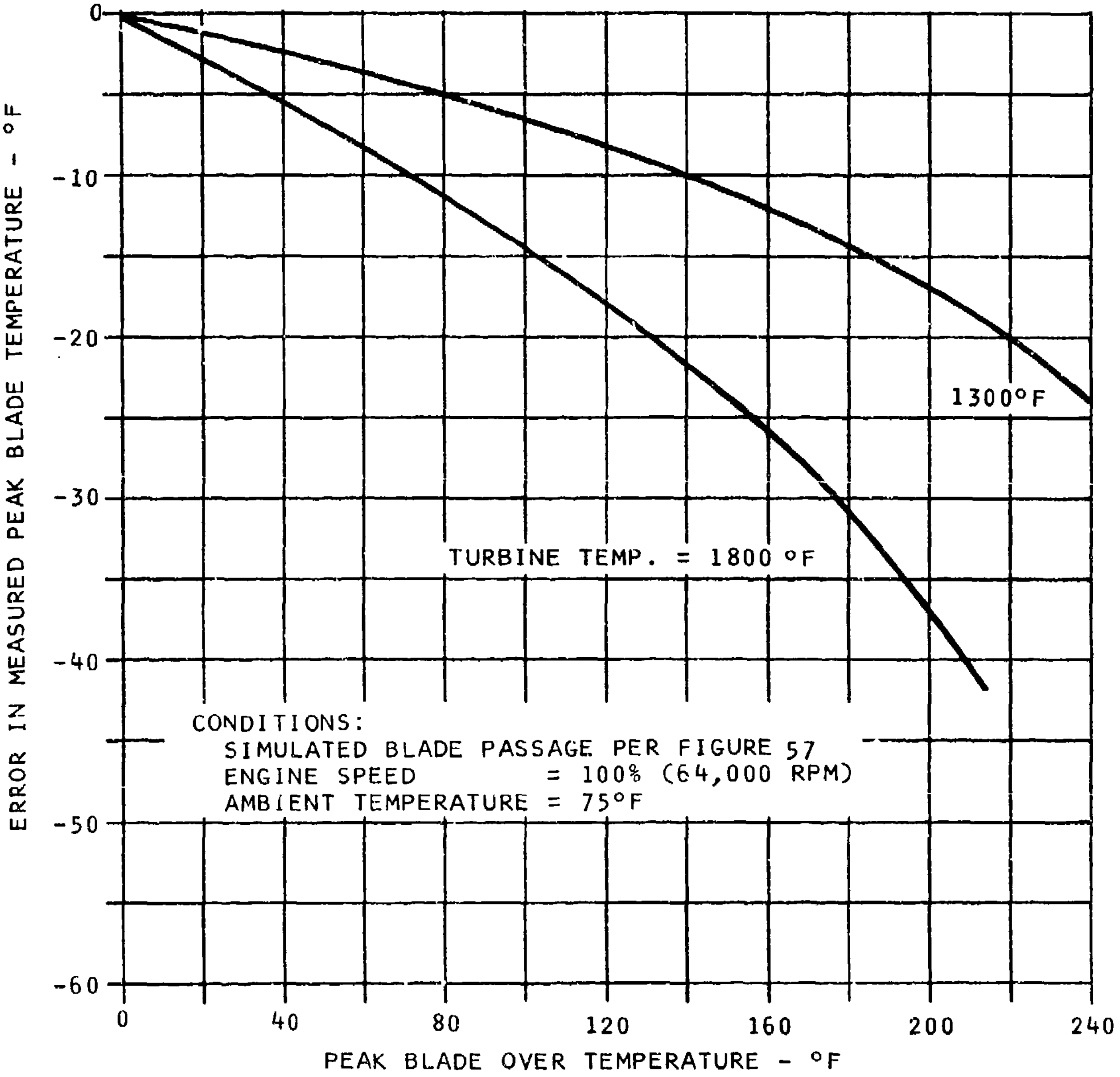

FIGURE 59 PYROMETER RESPONSE TO A SIMULATED HOT BLADE AT 100% ENGINE SPEED

Based on previous work that test evaluated various types of commercially available pressure transducers, it was determined that the variable capacitance type came closest to meeting the performance requirements summarized above. However, there is no known off-the-shelf transducer which can meet the above requirements without special calibration techniques being required.

In consideration of the broad range of control system accuracy that can be required for various applications, it was decided that both a variable capacitance and a potentiometer pressure transducer should be evaluated. Manufacturers whose pressure transducers were previously evaluated were contacted to determine if significant performance improvement had been made. One manufacturer offered an improved strain gage-type transducer that showed considerable potential for this program. As a result, this sensor was also procured for evaluation testing.

Following is a brief description of each type pressure transducer and the results of the bench testing.

Variable Capacitance

This transducer is a Rosemount Model #1331 but specially calibrated to provide full scale accuracy of ± 0.2% to meet specified requirements for this program.

The transducer comprises a pressure sensing capsule that generates a variable capacitance value proportional to pressure. This capacitance change is converted to a d.c. voltage (+5v = full scale) by a signal conditioning electronics circuit located within the transducer. This comprises basically an oscillator that is excited by the pressure varied capacitance. The d.c. output voltage is then derived from the a.c. output from the oscillator.

Test Results

Figure 60 illustrates the performance characteristic of the transducer and integral signal conditioning circuitry when exposed to the temperature which has been specified for test cell conditions. As the figure indicates, only under high temperature and low pressure conditions is there any deviation from the specification limits. However, based on test data taken on other units and the manufacturer's comments, we are confident that this deviation is not indicative of the transducer's true capabilities and that conformance to the specification on a production basis is achievable over the military temperature range -65 to 250°F.

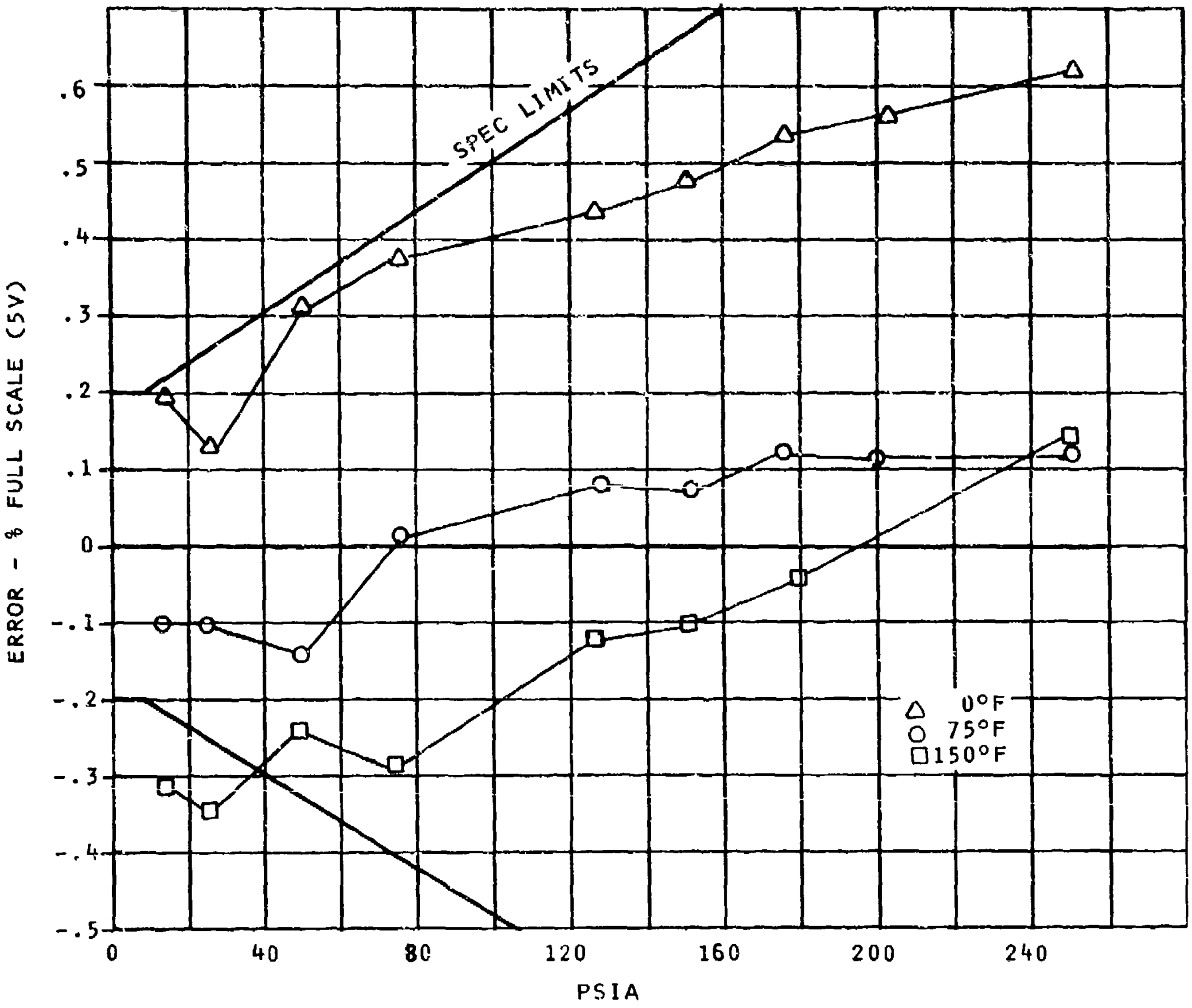

FIGURE 60 CAPACITIVE TYPE PRESSURE TRANSDUCER TEST DATA

Strain Gage

This transducer is a Statham Instruments thin film strain gage transducer. It comprises a beam diaphragm assembly mounted to a thin film vacuum deposited strain gage bridge, via a ceramic substrate. Application of pressure deflects the beam, thereby throwing the bridge out of balance. This change is then detected by external circuitry to provide a +5V output voltage proportional to maximum applied pressure.

The monolithic deposited thin film bridge provides excellent common mode thermal characteristics and with special calibration the overall accuracy is estimated at ± 0.2% full scale.

Test Results

The test results for this transducer, together with its associated signal processing interface, are presented in Figure 61. As this data indicates compliance to the specification requirements is easily met throughout the range. In face, an accuracy of ± 0.2% of full scale is very nearly met throughout the complete pressure and temperature range.

Potentiometric

The potentiometer transducer is a Computer Instrument Company Model 2000. It consists of a bellows acting as a prime mover for positioning a resistor in which the moveable contact (slider) is driven by the motion of the bellows. The elimination of intermediate linkages produces minimum sensitivity to vibration shock and temperature. The resistive element is of a conductive film construction offering infinite resolution and good life and repeatability. The accuracy of the transducer, including errors in the electronic interface, is 1.2% for the pressure range 0-250 psi.

Test Results

Figure 62 presents the test results of this transducer inclusive of its signal processing. Except for one area, the accuracy is well within the specification error bands for the expected test cell temperature extremes. The reason for this deviation has not been defined; however, the most probably cause is the nonlinearity within the pressure transducer itself. However, in reviewing this data, it is interesting to note that the total error band is within ± 1.2% and that compliance could be effected by a mere change of gain within the interface.

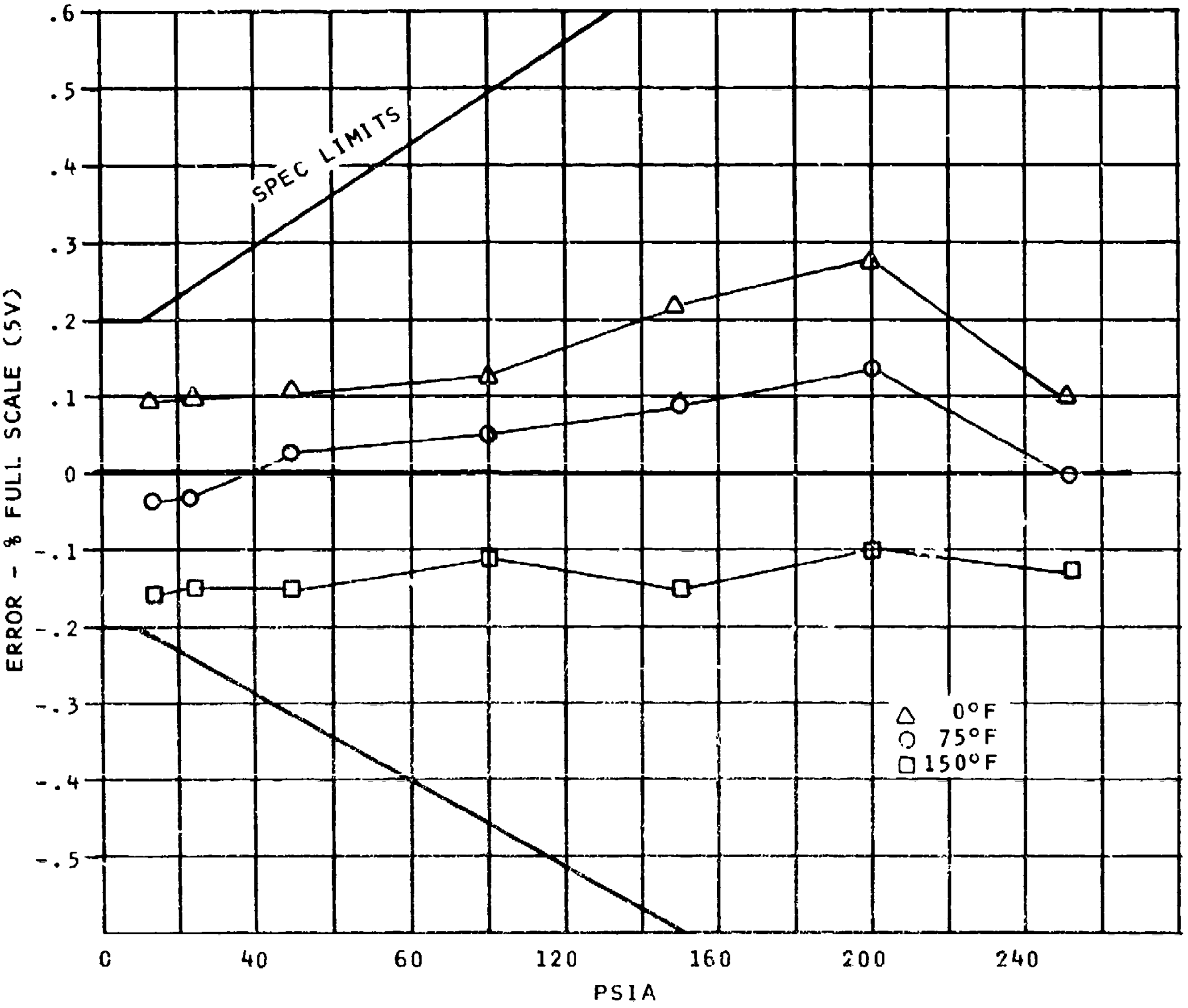

FIGURE 61 STRAIN GAUGE PRESSURE TRANSDUCER TEST DATA

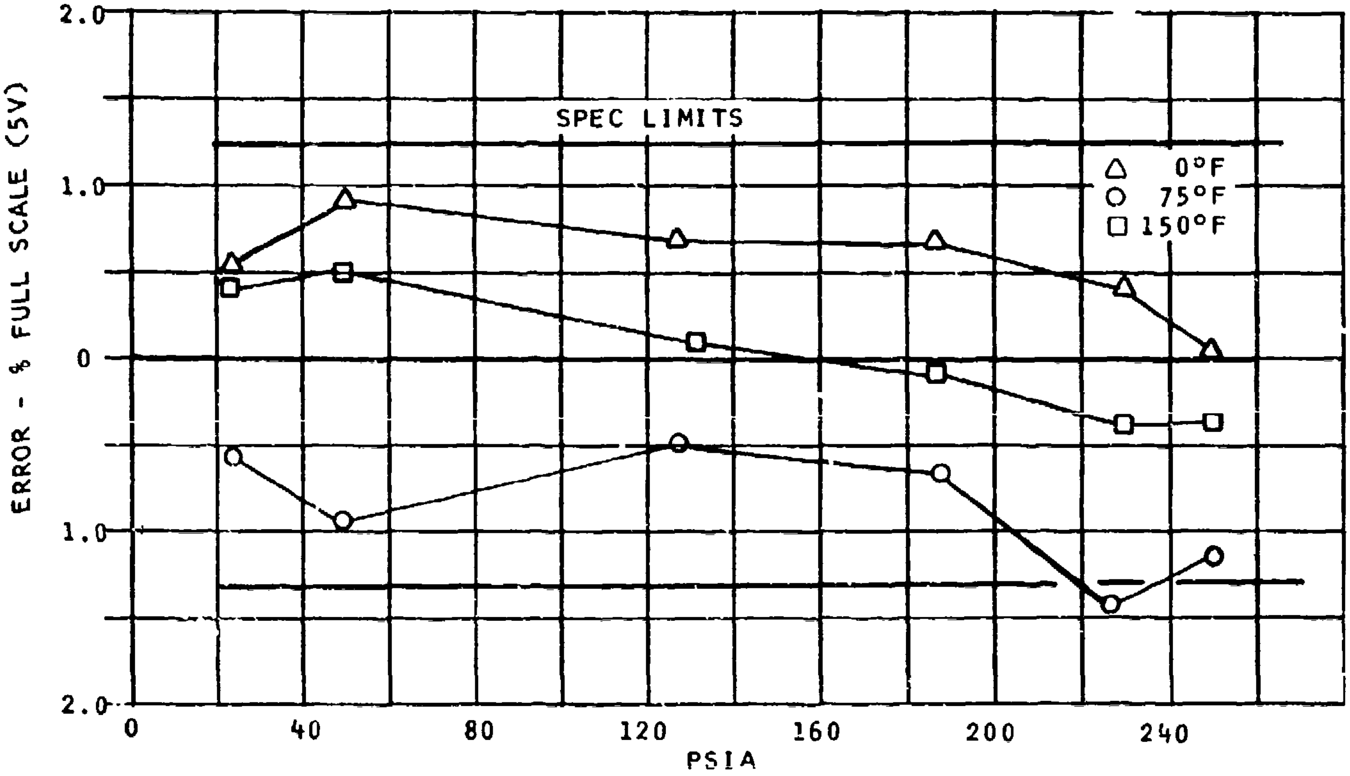

FIGURE 62 POTENTIOMETER PRESSURE TRANSDUCER TEST DATA

4. T_T2 TEMPERATURE SENSOR

For the range of inlet temperature variation of interest (-65°F to +135°F) the thermistor probe, with a consideration for the assessment criteria, previously referenced, is the most attractive sensor for this function.

The probe itself will comprise a simple network of thermistors and resistors, the combinational characteristic of which will provide an output voltage proportional to T_{T2}. However, if it is required to provide a voltage proportional to $\sqrt{\theta}$, the thermistor/resistor network can be easily modified.

As any future engine test program would be conducted in a test cell, variations in actual inlet temperature will be minimal. However, to facilitate experimentation under different inlet temperature conditions, a potentiometer can be substituted for the thermistor probe. Figure 63 presents the potentiometer resistance value to present a given inlet temperature level. Thus, any temperature condition can be set up merely by setting the potentiometer.

5. N_1, N_2 AND PUMP SPEED SENSORS

The magnetic speed pickup has been used extensively for speed measurement. Its frequency output is ideally suited for digital systems and the simplicity of conditioning this frequency to a voltage makes it also suitable for analog systems. Its accuracy, simplicity, reliability, size and cost make it extremely attractive in comparison to alternatives as a means for monitoring shaft speeds.

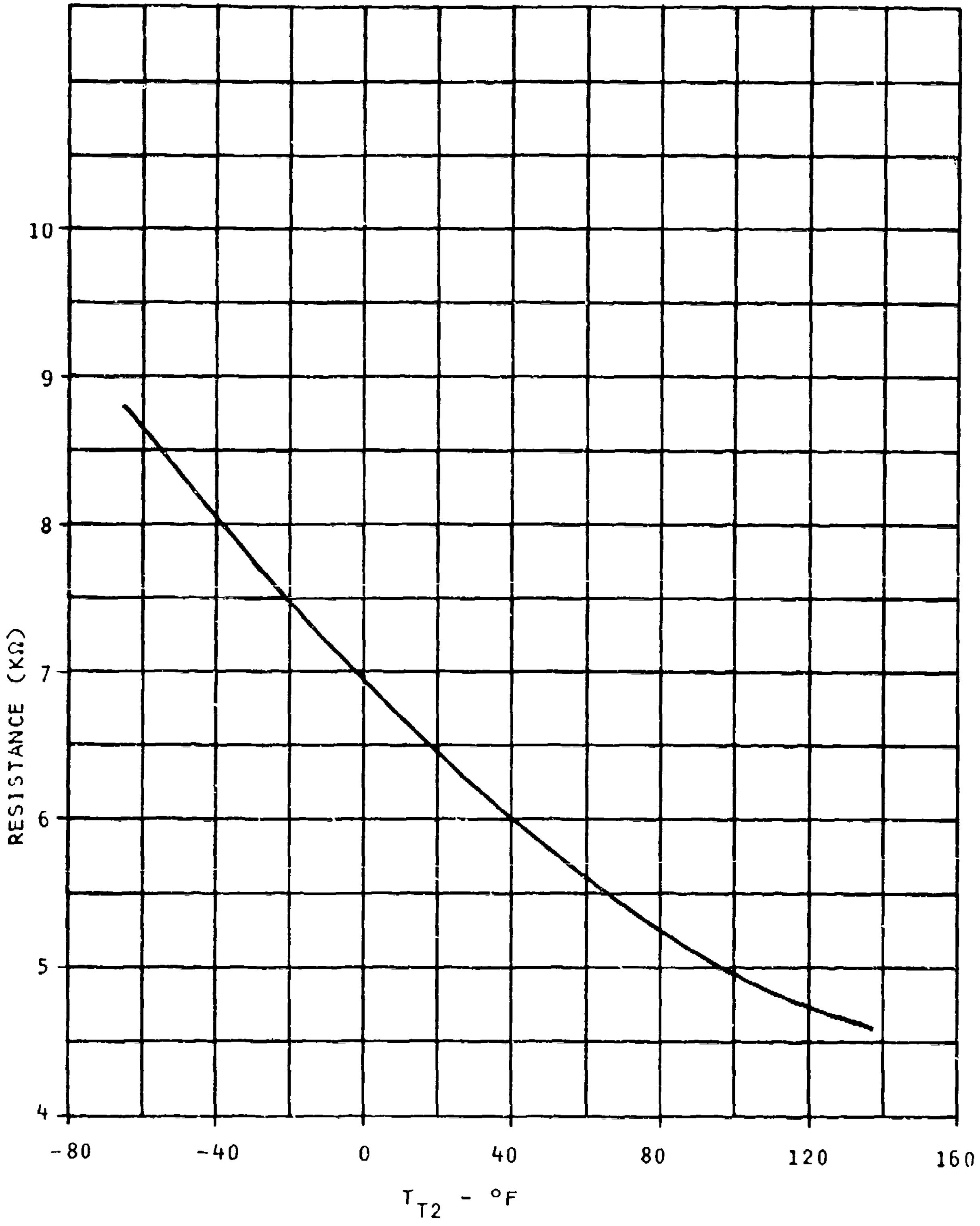

FIGURE 63 T_{t2} PROBE SIMULATOR - RESISTANCE VS TEMPERATURE

4

ELECTRONIC INTERFACE UNIT

1. BACKGROUND

As an integral part of Phase I of this program, (1) various factors that form a part of the process in selecting an electronic engine control system configuration were discussed, and recommendations made as to the optimum solution for a given application. This study was based on the referenced assessment criteria, and included the following aspects dealing with the various applications possible:

a) Control sophistication ranging from a simple single loop, rate controlled, proportional governor to the multi-looped control with such refinements as fault isolation, self-test-and-repair features with the added capability of control and signal exchange with other vehicular systems.

b) Subsonic versus Supersonic applications.

c) Expendable versus Recoverable.

d) Long Range versus Short Range.

e) Multi-mission versus Special Purpose

To facilitate analysis with such a wide range of application requirements possible, three categories were set up - Classes I through III. Class I included the most complex and demanding system, with Class III incorporating the simplest control concepts.

Again, with reference to the aforementioned assessment criteria, the various concepts were analyzed and the optimum control concept selected. The results of this trade-off study appear in Table III, which is a summary of the findings of this phase of the program.

For each of these classes, the following potential configurations were considered:

a) Engine-mounted dedicated control.

b) Engine-mounted sensor interface unit, with control provided by a dedicated airframe-mounted computer.

c) As (b) but with control provided by a segment of the control vehicle computer.

d) Electronic computational concepts including general purpose digital, special purpose digital, and analog functions.

e) Circuitry elements including standard and customized components.

TABLE III CONCEPTUAL DESIGN STUDIES SUMMARY

Control Configuration	Subsonic	Supersonic
Class 1	Engine Mounted I/O Interface Control - Vehicle Central Computer	
Class II	Engine Mounted Dedicated Microprocessor Digital (If Advanced Military Version Available)	
Class III	Engine Mounted Dedicated Analog & Special Purpose Digital Hybrid	

It was our judgment that the capability of electronics to perform the functional and logical requirements of the various engine control concept was in hand and much development activity in the industry was already underway including work on engine mounting, cooling, and vibration isolating electronic systems. Moreover, because of the wide variations in computer requirements and the control modes which were selected for demonstration, it was in the ground rules that a test cell programmable digital computer would be used to provide the required control system functions. This necessitated providing the electronic interface unit to provide for interfacing control system components with the test cell computer.

2. DESIGN DESCRIPTION

The electronic interface unit (EIU) is an engine-mounted electronic accessory designed to provide the interface between the fluid controller and sensors, and the computer system used to provide computation for the control system.

Functional Design

Figure 64 presents a block diagram of the functional interfaces contained within the EIU. In accordance with the specification requirements, signals transmitted to and received from the computer have been scaled within the EIU for a range of 0 to +5v. Further, each input and output signal interfacing with the EIU has been buffered to assure compatability with the cabling connecting the EIU to the computer.

The different elements within the EIU are specifically as follows:

N_1, N_2 and Pump Interface

With all three functions, speed is sensed by a magnetic pick-up viewing a toothed wheel. This oscillating signal, the frequency of which is proportional to speed sensed, is conditioned first to a square wave and then to an output voltage proportional to frequency.

The concept adopted is identical for all three functions (only the frequency to voltage gain is different), and an accuracy of ± 0.3% is typically achievable.

Linear Clutch and Proportional Solenoid Interface

In both cases a controlled output current is provided to the respective load in proportion to the command input voltage signal (0 to +5v).

With both functions, the same concept was adopted (the input voltage to output current gain is different) and based on a simple linear closed-loop regulator, the feedback for which is provided by the voltage drop across a resistor sensing the load current.

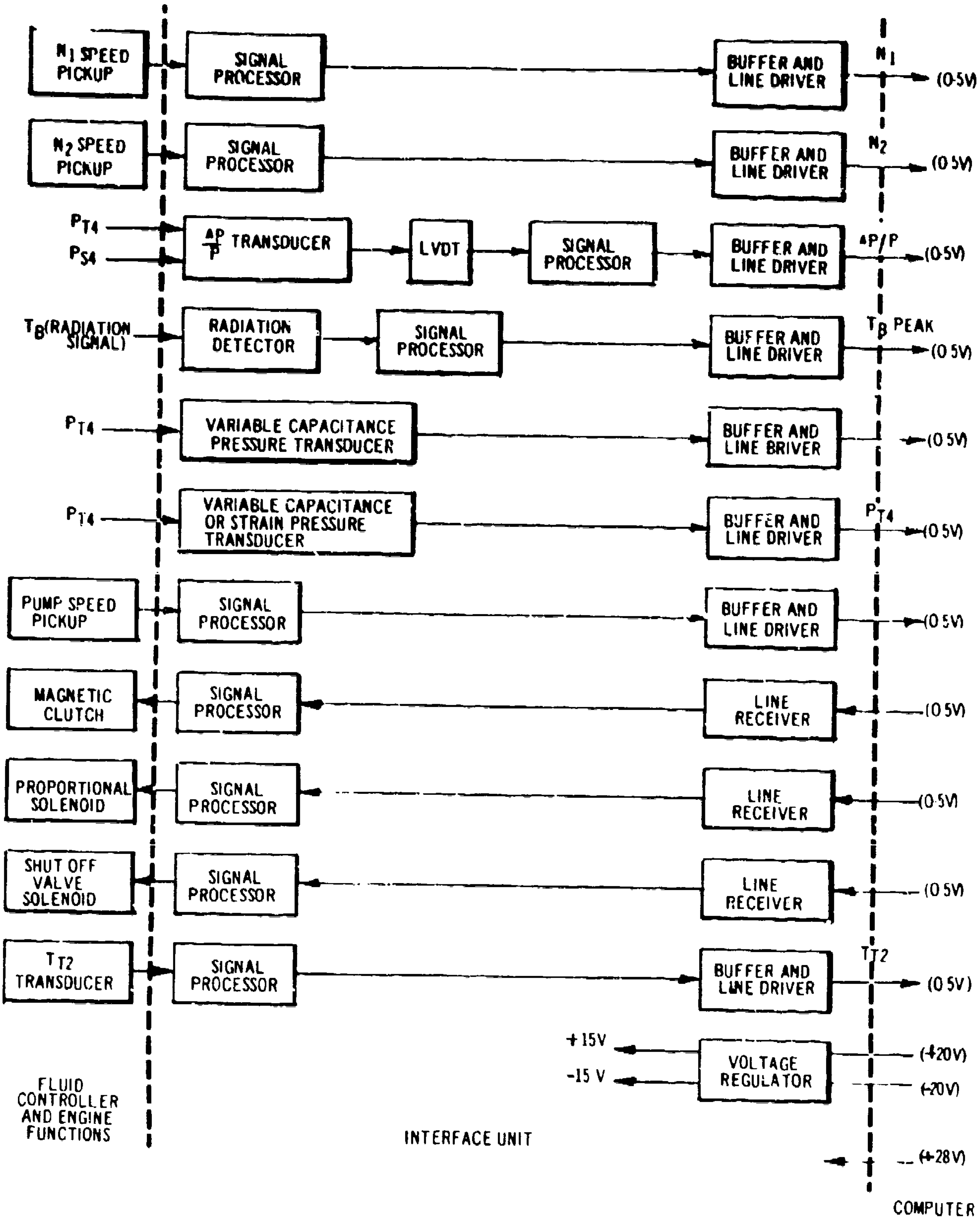

FIGURE 64 ELECTRONIC INTERFACE UNIT FUNCTIONAL BLOCK DIAGRAM

An alternative approach to this concept would have been a switching current regulator. Although this has advantages with regard to power dissipation, it is completely outvoted with considerations for simplicity, reliability and EMI effects.

T_{t2} Transducer Interface

This function comprises a single stage voltage amplifier, the input resistor for which is provided by the transducer resistor/thermistor network. The output voltage is, therefore, a function of this resistance and in turn T_{t2}. Accuracy of the interface is record order in comparison to that of the thermistor network.

Shutoff Valve Solenoid Interface

This element comprises a simple and conventional amplification stage formed by discrete transistors to provide the necessary interface between the 0 to +5v control signal from the computer and the necessary current to operate the 50v solenoid.

T_B Radiation Pyrometer Interface

Figure 65 illustrates a functional block diagram of the radiation pyrometer interface. The basic requirement of this element is to receive a voltage generated by the radiation pyrometer current to voltage converter and to provide an output voltage proportional to the peak blade temperature measured. The concept adopted to achieve this requirement is somewhat complex (as Figure 65 indicates), the cause for which is mainly due to the following:

a) The photovoltaic detector output current is highly nonlinear with respect to measured temperature and in consequence, the output voltage from the current to voltage converter is also nonlinear. It is, therefore, required to provide nonlinear compensation with consideration for the blade temperature range of interest (1300°F to 2000°F).

b) It is required to measure the peak blade temperature over a wide range of engine speed.

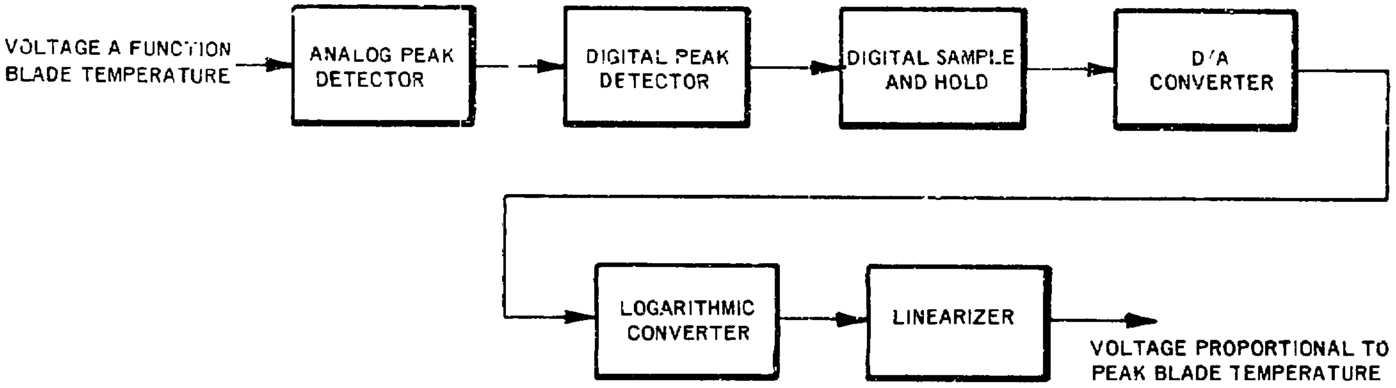

FIGURE 65 RADIATION PYROMETER INTERFACE - FUNCTIONAL BLOCK DIAGRAM

To assure that accuracy is not impaired with this requirement, it is important that the interface has adequate response under maximum speed conditions and yet is capable of retaining data for a period equal to one revolution (i.e., sampling rate) under low speed conditions.

The output voltage from the current to voltage converter (this element covered under the radiation pyrometer section) approximates the form of waveform A, Figure 66. This illustrates the signals generated by the 67 blades passing the pyrometer with, for this example, blade #64 being hotter than the average and blade #9 being the hottest.

To achieve a peak blade temperature measurement, it is necessary to sample with a peak detector over a minimum period covering one engine revolution and to store the accumulated data in a sample-and-hold circuit.

As Figure 66 illustrates, the peak detecting function contains two elements, one analog and the other digital. The reason for this approach is centered around the requirement to achieve an accurate peak blade temperature measurement from light-off to maximum speed.

The analog circuit can be designed to respond to the maximum blade passing frequency and to capture peak blade temperature information at these speeds. However, in doing so, the charge time constant of the memory capacitor circuit has to be extremely fast (approximately 2µS) and in doing so, the discharge time constant or memory drain time inherently becomes short, particularly at elevated ambient temperatures. This situation reflects itself in a circuit capable of accurate data acquisition at maximum engine speed but incapable of accurate data retention at low engine speeds.

On the other hand, digital peak detectors inherently provide data retention over an infinite time period. However, without the incorporation of excessively complex and costly circuitry, and with a consideration for the required resolution (in this case, 8 bit), digital peak detectors cannot respond fast enough to meet the requirements dictated by engine operation at or near maximum speed.

The solution, therefore, is the incorporation of both an analog and a digital peak detector, the former to obtain the data and the latter to retain it.

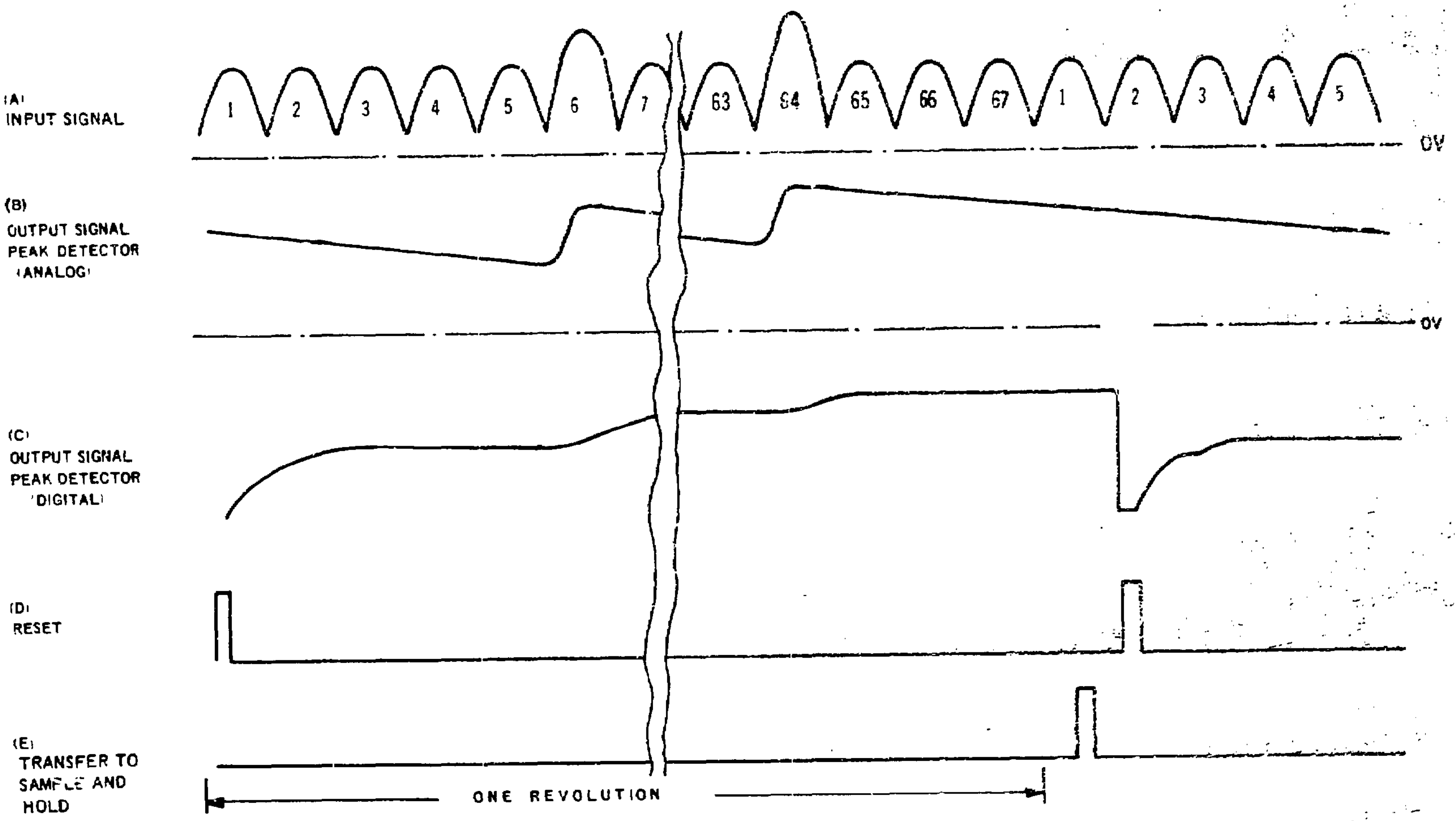

FIGURE 66 WAVE FORMS - RADIATION PYROMETER INTERFACE CIRCUITRY

Figure 66 illustrates typical waveforms of these functions. Waveform B presents the analog peak detector output voltage. As can be seen, the signal level falls away after quickly attaining the desired amplitude. On the other hand, waveform C is the output from the digital peak detector which has a slower response than its analog partner but there is no droop associated with the data contained.

An error exists in the transfer of information between the two peak detectors. This is caused by the droop in the analog output prior to the digital peak detector responding to this signal. The worst case error occurs at maximum speed where the margin between engine speed and the digital peak detector response is the greatest. However, even under these conditions, the maximum error attributed to this aspect is negligible.

Waveforms D and E (Figure 66) present respectively the digital peak detector reset pulse and the pulse to transfer the output from the digital peak detector (8-bit binary) to the sample and hold, which comprises an 8-bit parallel in, parallel out shift register. From here, the signal is processed through an 8-bit D/A converter.

The relationship between the blade target temperature and the photovoltaic detector output current approximates

$$I = KT^{14}$$

where I = detector output current

T = absolute target temperature

K = a constant

The output voltage from the current to voltage converter, therefore, approximates to

$$V_B = K_1 T^{14}$$

where K_1 = a constant

To linearize this voltage, logarithmic conversion is required and as Figure 65 indicates, this element is included as a part of the signal processing network.

In the signal processing chain, the logarithmic converter has been positioned as far downstream as is possible for the following reasons:

a) The elements immediately following the current to voltage converter are required to operate at high speed, whereas downstream, speed requirements are not as severe. The present arrangement is, therefore, advantageous as the problems involved in designing the peak detectors for high speed are second order compared to that for the logarithmic converter.

b) The present configuration minimizes errors, as all circuitry upstream of the logarithmic converter have their errors reduced by a factor of 14 when referenced to target temperature because the output voltage V_B is proportional to temperature to the 14th power.

The logarithmic converter is a relatively conventional design based on the logarithmic relationship between a transistor's collector current and base to emitter voltage. Thermal compensation is included and accuracy of this element has been designed to ± 1.5%, referred to the logarithmic converter input.

As the curves in Figure 67 illustrate, the logarithmic converter does not exactly linearize the signal. It has, therefore, been necessary to include an additional stage of linearization, which utilizes simple straight-line approximation techniques with one breakpoint.

Construction

Figure 68 shows a layout of the EIU. It comprises a bar stock aluminum housing and cover with provisions for mounting to the engine via four elastomer-type vibration isolators. Also included is a heat exchanger cavity formed by the housing base and an internally mounted plate between which metered engine fuel flow or other available fluid can be ported to provide cooling, should the ambient conditions on the engine dictate this requirement.

Functionally, the unit comprises three double-sided printed circuit boards of a glass/epoxy construction suitable for application to engine-mounted electronic controls. Two of the PCB's are 5" x 4" and contain the majority of the electronic functions included in the unit. The third PCB is 1.5" x 1.5", forms part of the T_B detector assembly, and provides the first stage of signal conditioning for the radiation pyrometer function.

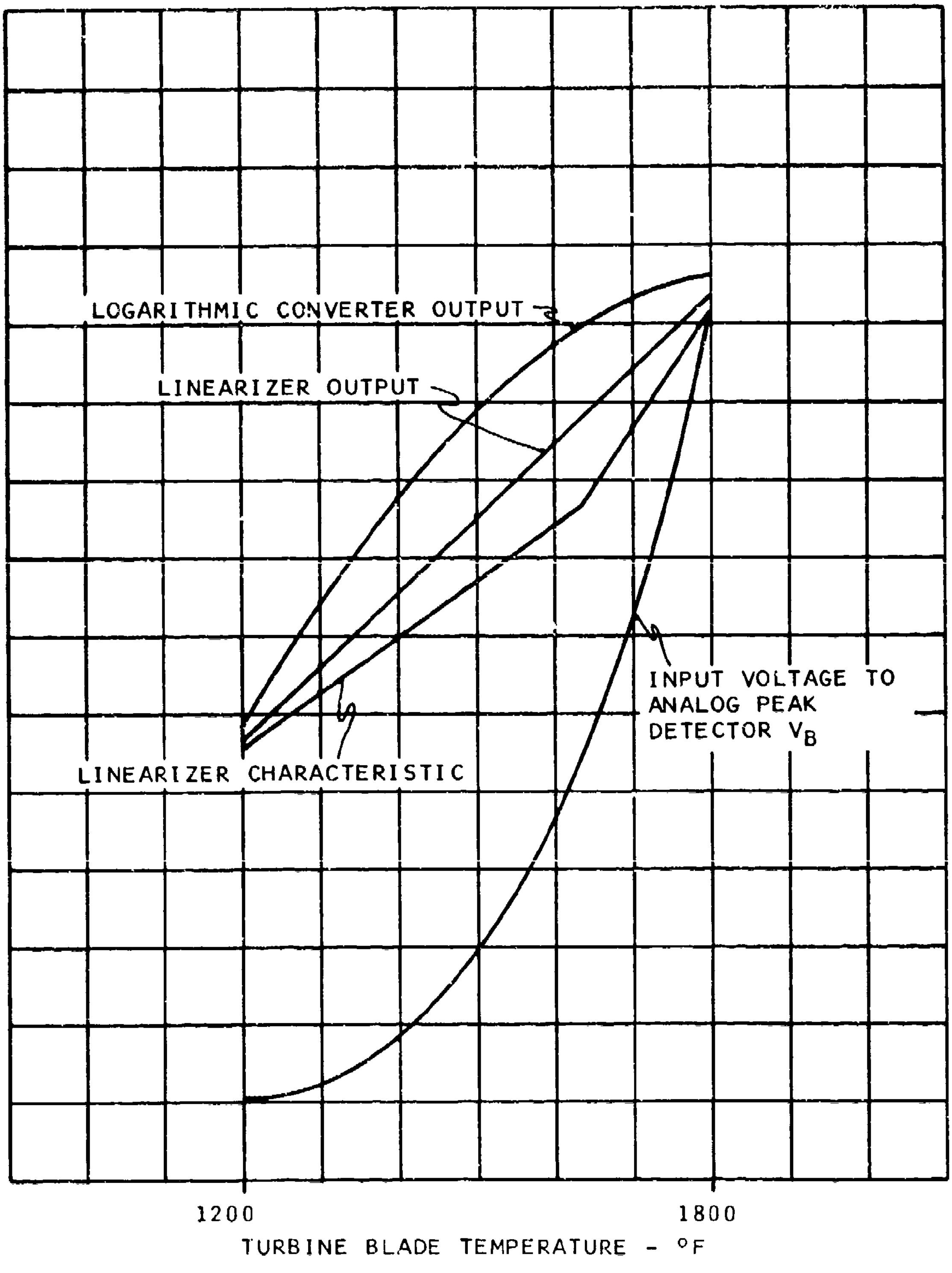

.FIGURE 67 CHARACTERISTICS OF RADIATION PYROMETER INTERFACE

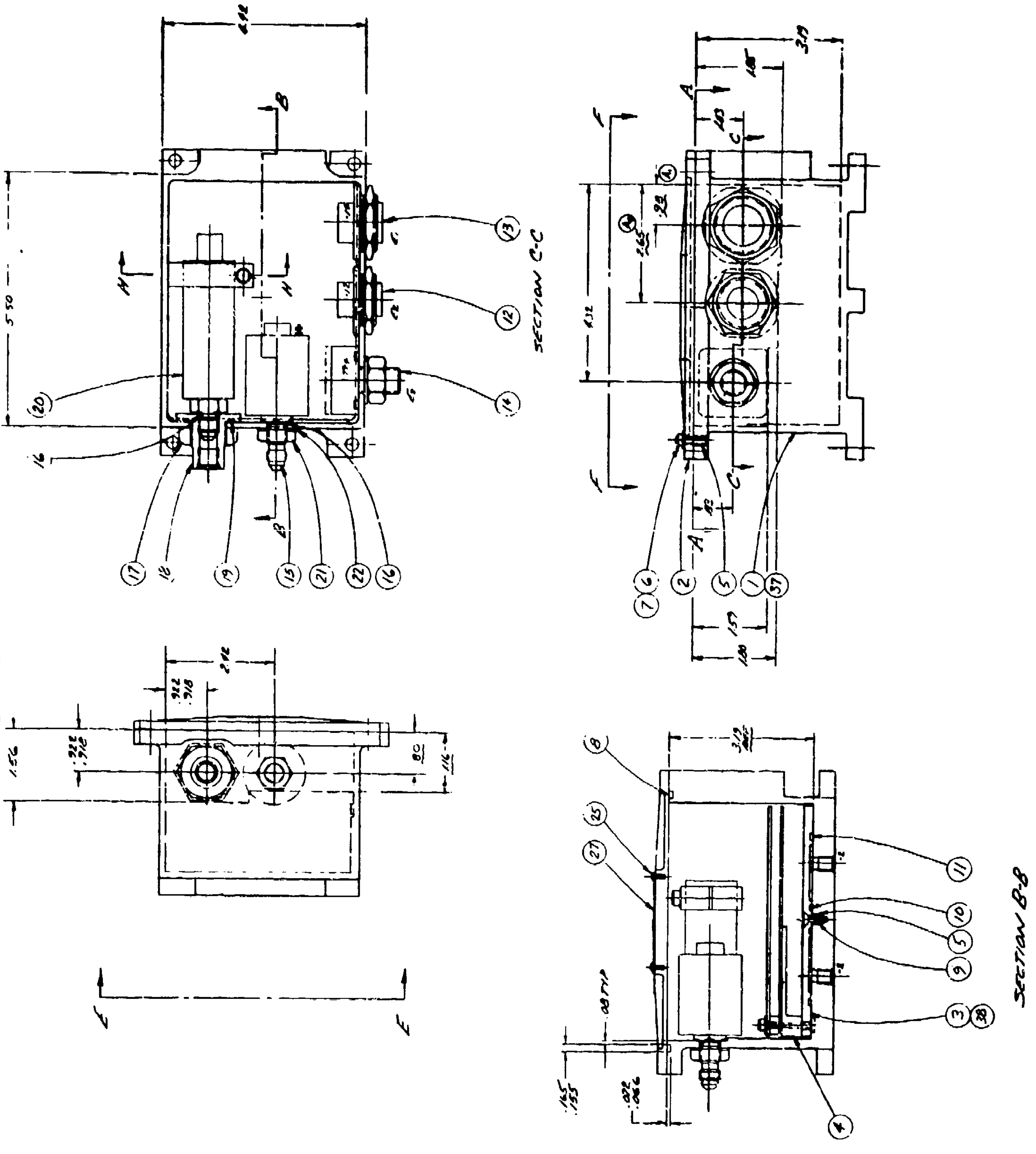

FIGURE 68 ELECTRONIC INTERFACE UNIT LAYOUT

The power transistors that form the drive for the proportional solenoid, magnetic clutch, shutoff valve solenoid, and the -15v and +15v power supplies, are mounted via electrical isolation to a heat sink. This heat sink, which takes the form of a bracket, is thermally connected to the heat exchanger, thereby minimizing the thermal path between the major power dissipating components and the heat exchanger.

Provision has been made within the package to mount the potentiometer and variable capacitance pressure transducers. Evaluation of the strain gage transducer can be done by exchanging it with the variable capacitance unit.

Also included within the package is the radiation pyrometer detector assembly. This includes the silicon photovoltaic detector and the PCB that provides the first stage of signal conditioning mounted directly behind the detector. This arrangement minimizes leakage losses in the transmittal of the low detector output current to the first stage signal processing. A hole is provided in the PCB directly behind the detector, to allow the thermal compensating thermistors to be bonded directly to the base of the detector, thereby optimizing the thermal compensation concept.

Two connectors are provided, one to interface the electronic unit with the fluid controller and engine-mounted sensors, and the other to provide the interface with the control computer. In both cases, the connectors are miniature bayonet conforming to MIL-C-26482. They were specifically chosen because of the availability of pins suitable for interfacing with flexible printed circuit cabling, together with their compliance to military requirements.

Located to the outside of the package is the $\Delta P/P$ fluidic transducer with its LVDT electrical output transducer being located within the package, to again take advantage of the controlled environment.

All elements within the package are interconnected via a flexible printed circuit cable which is constructed using Kapton layers, in between which is bonded the copper conductors.

Vibration and Shock

The maximum vibration levels expected on an engine are shown in Figure 31.

The estimated weight of the electronic interface unit is 4.5 lbs. with the center of gravity being approximately central. The isolators to be used are four elastomer-type manufactured by Lord Kinematics. The characteristic of the isolators when supporting a 4.5 lb. evenly distributed load is approximated by a second order system. Based on the spring rate and damping characteristics of the isolators, the system will behave as tabulated below.

Ambient Temperature (°F)	Resonant Frequency (Hz)	Transmissibility at Resonance
-65	100	
70	50	2.2 - 3.2
200	37	

The actual transmissibility of the isolators at the temperature extremes is not known; however, data provided the manufacturer indicates that as the temperature increases, the resonant frequency drops and the transmissibility increases. Conversely, as the temperature decreases, the resonant frequency increases and the transmissibility decreases. However, the net effect of temperature will be small and at frequencies above the resonant frequency, vibration will be highly attenuated. At 70°F and 238 Hz, the attenuation is less than .01 yielding a transmitted vibration of .01 x 5g = .05g. At higher frequencies, the effects of the isolation will be even more pronounced and should limit the 50g transmittance to .05g or less. The vibration levels at frequencies below 238 Hz are not known, but they correspond to engine speeds below idle where the g level is low and operating is transient.

In the plane, perpendicular to the axis of the isolators, their capability is degraded by a maximum of 20%, but this will not cause a problem. Moreover, the PCBs and components are rated for a minimum of 5 g's and there is adequate reserve available.

The actual shock specification is not known; however, the isolators have been designed to provide protection from a 30 g, 10 mS shock pulse.

Cooling

Although the actual mounting arrangement of the electronic interface unit to the engine has not been firmed up, the EIU would be exposed to between 0°F and 150°F on the engine test bed.

The design of the EIU was conducted with the above temperature range in mind. As an integral part of this design effort, a thermal analysis was conducted based on a model of:

a) Natural convection - PCB and components to air within the EIU.

b) Natural convection - air within the EIU to the top cover.

c) Forced air convection - ambient to top cover and sides.

d) Conduction - top cover and sides to cold plate.

e) Forced fluid convection - cold plate to coolant fuel.

f) Conduction - high power dissipating components to the cold plate.

The results of this thermal analysis can be summarized as follows:

a) The maximum component junction temperature = 202.4°F, which is considerably less than its absolute maximum rating of 300°F.

b) The minimum cooling flow available (50 lb/hr) is more than adequate.

c) An ambient temperature, exceeding 150 F, could be accommodated, although certain aspects of the design would need reviewing if this were a requirement.

3. TEST RESULTS

N_1, N_2 and Pump Speed Interface

As was mentioned, all three speed interfaces utilize the same concept and components. Only their frequency to voltage gain differs. In consequence, as the test results were nearly identical for each system, one set of data, representative of all three will be discussed here.

Figure 69 illustrates the nonlinearity of the output voltage throughout the operating range. As the data indicates, accuracy is well within ± 0.2%.

Figure 70 indicates the temperature characteristic of this function which indicates an approximately ± 0.4% total variation. This level, although adequate for the needs of this program, could be halved by the incorporation of slightly more expensive components such as resistors, with improved thermal characteristics and switches with more stable voltage drops.

T_{T2} Interface

Figure 71 illustrates the characteristic of this interface as a function of ambient temperature change. An accuracy of ± 0.2% is easily met over the full operating range. Again, this performance could be improved by the use of resistors with improved thermal characteristics. However, the referenced temperature error satisfies the requirements of this program.

Proportional Solenoid and Magnetic Clutch Interface

Tables IV and V present the test data for the proportional solenoid and magnetic clutch interface circuit.

With both functions, accuracy of each operating point over the complete temperature range is well within 1% of full scale, thereby providing an accuracy more than adequate for the given application.

As the tables also indicate, linearity is within 1%, thereby again providing an adequate performance characteristic.

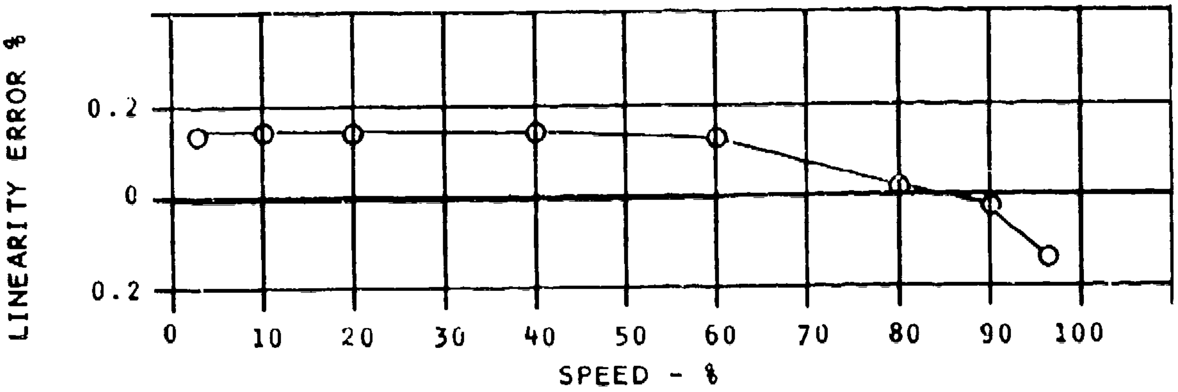

FIGURE 69 SPEED INTERFACE NON-LINEARITY

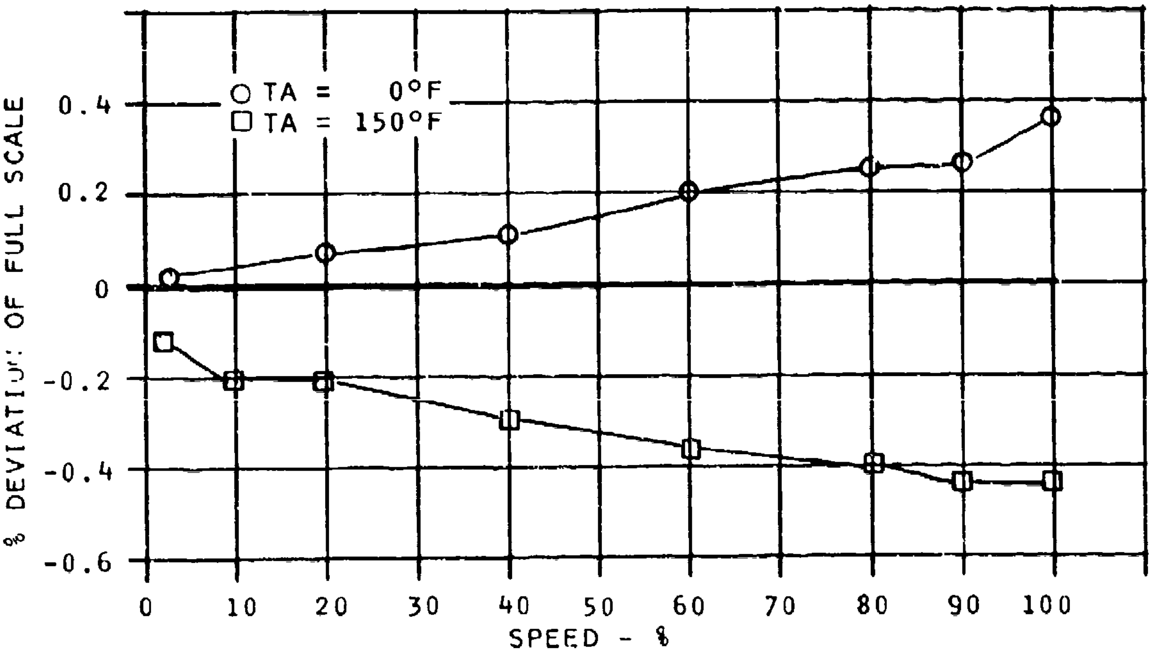

FIGURE 70 SPEED INTERFACE - AMBIENT TEMPERATURE EFFECTS ON CALIBRATION

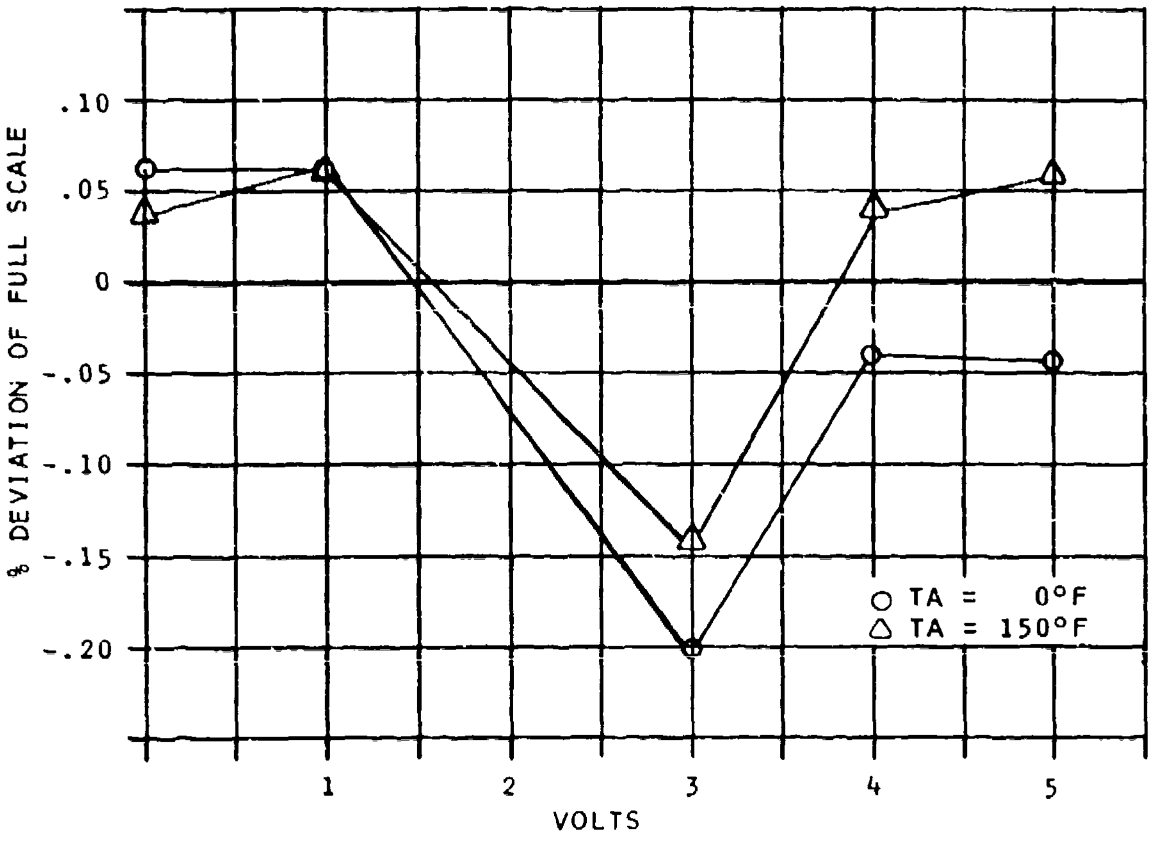

FIGURE 71 T_{t2} INTERFACE - AMBIENT TEMPERATURE EFFECTS ON CALIBRATION

TABLE IV. PROPORTIONAL SOLENOID CIRCUIT EFFECTS OF AMBIENT TEMPERATURE ON DRIVE CURRENT

VOLTAGE INPUT (VOLTS)	CURRENT OUTPUT (MA)		
	TA = 0°F	TA = 70°F	TA = 150°F
0	1.7	1.5	1.4
1	102	100	104
2	204	200	203
3	307	300	300
4	407	400	400
5	500	500	500

TABLE V. MAGNETIC CLUTCH CIRCUIT EFFECT OF AMBIENT TEMPERATURE ON DRIVE CURRENT

VOLTAGE INPUT (VOLTS)	CURRENT OUTPUT (MA)		
	TA = 0°F	TA = 70°F	TA = 150°F
0	.55	.4	.37
1	49	49	49
2	99	99	99
3	147	149	149
4	197	198	197
5	246	248	246

T_B Radiation Pyrometer Interface

A calibration of the complete system from the aperature sensor head thru the electronic interface unit output signal was performed by sighting the pyrometer onto a black body radiation standard. The data, which is included in Figure 72, shows the system to be accurate within ±1.25% at blade temperatures above 1600°F.

Voltage Regulators, ± 15V

With both regulators, testing was conducted for load and line regulation with, in addition, an evaluation of stability with variation in ambient temperature. In all cases, the accuracy was well within the ± 1% requirement yielding deviations in all cases less than ± 0.3%.

Vibration

The electronic package was vibrated in the plane perpendicular to the PCBs (which is the worst case plane) in accordance with the vibration requirements. An accelerometer mounted on the housing monitored output g levels. The output of this accelerometer is shown in Figure and indicates that the vibration isolators provide the required vibration isolation.

Temperature

The electronic package, including the two compressor discharge pressure sensors and the pressure ratio sensors, was subjected to a 150°F ambient temperature. After a two-hour temperature soak, power was applied to the electronics while internal temperatures were recorded from two thermistors located inside the box. One thermistor was located inside the housing in the internal ambient air to give the average internal temperature while the second was located on the proportional solenoid output transistor casing to give the maximum component temperature (the proportional solenoid transistor has the greatest power dissipation of any of the components). The results indicated a 167°F average temperature while the maximum component temperature peaked at 190°F but settled out a few degrees less. These temperatures are well within the operating temperatures of the electronic components and indicate that no further cooling is necessary.

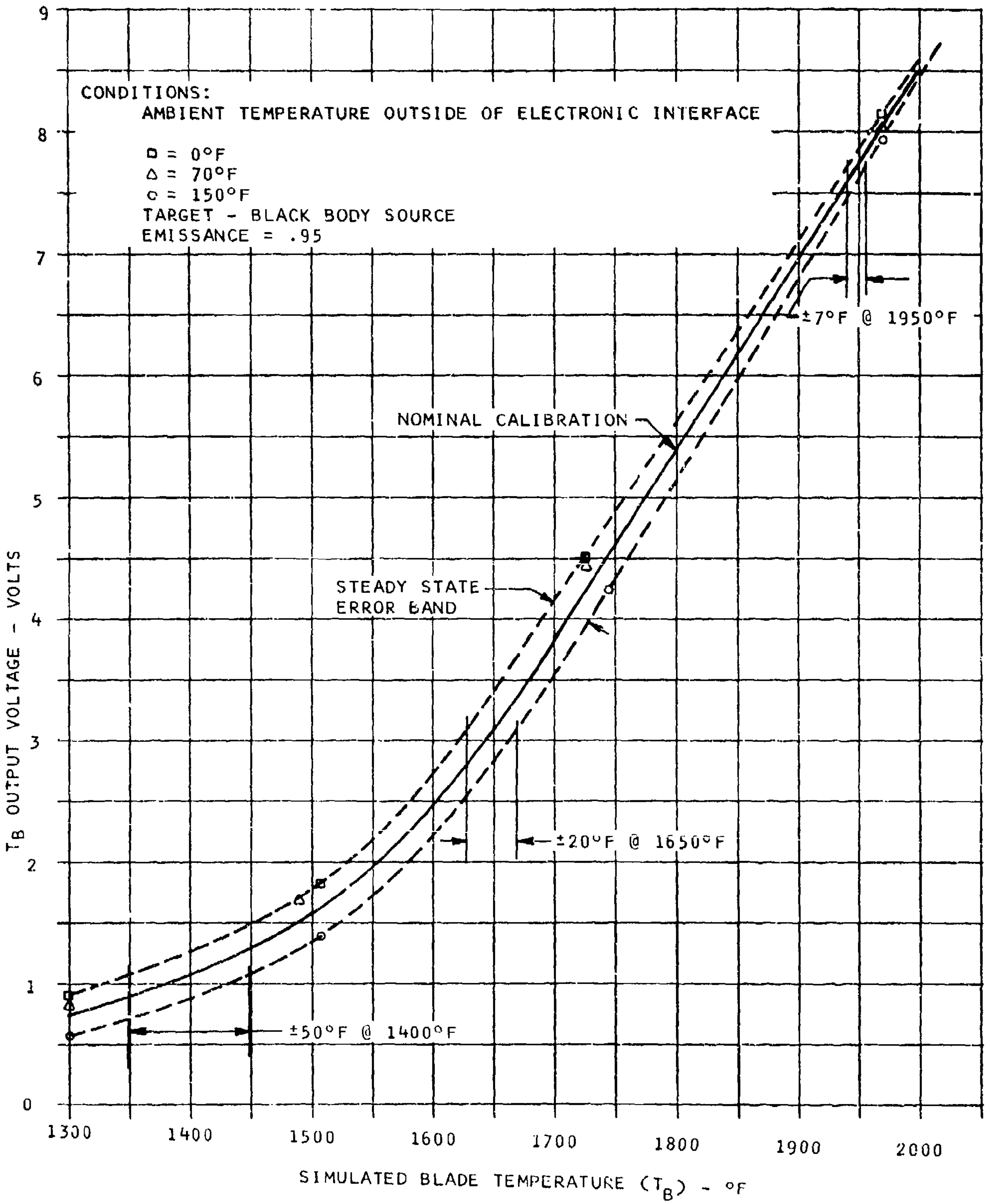

FIGURE 72 T_B RADIATION PYROMETER AND ELECTRONIC INTERFACE CALIBRATION

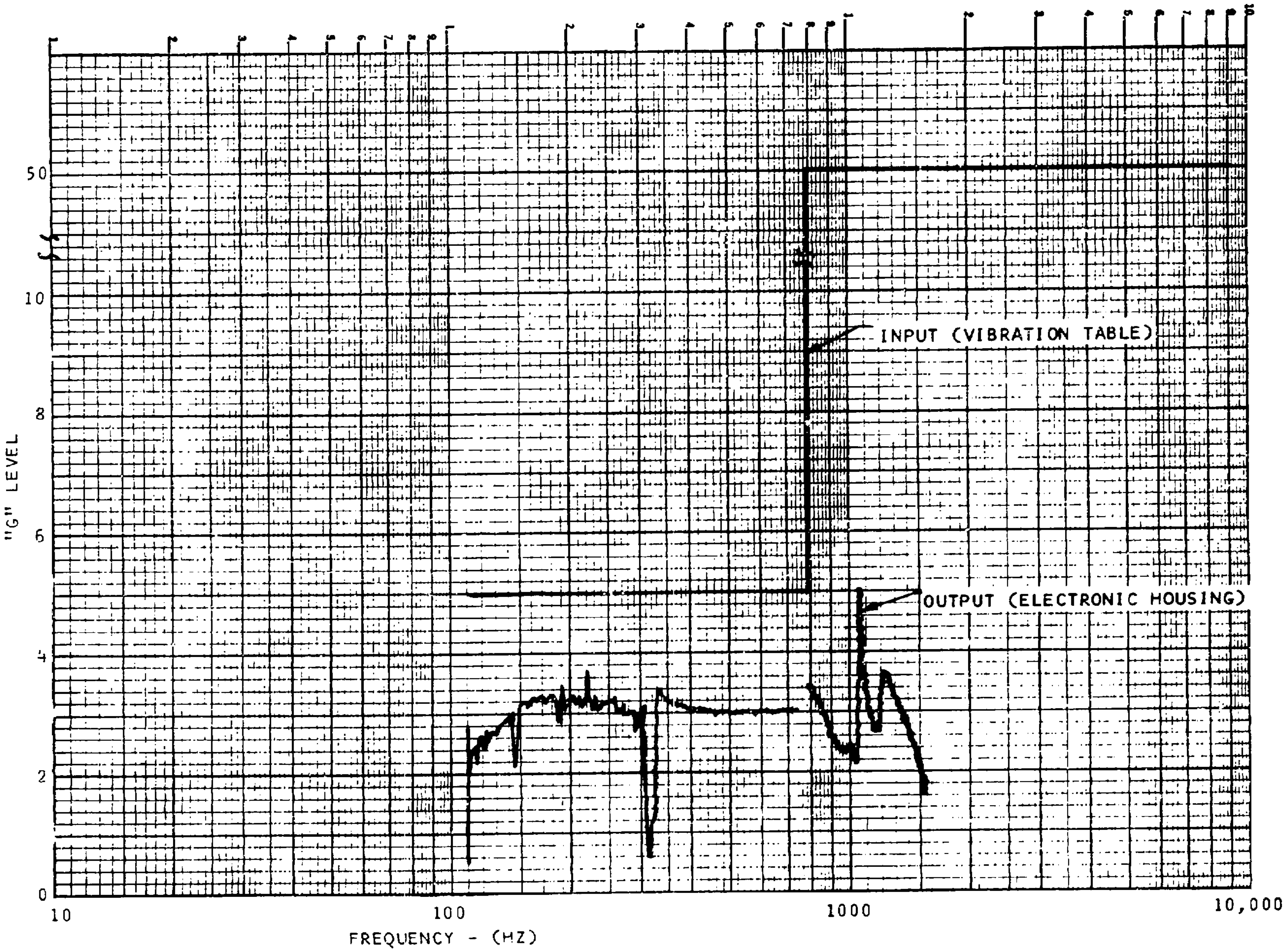

FIGURE 73 VIBRATION TEST OF ELECTRONIC INTERFACE UNIT WITH ISOLATION MOUNTS

5

SIMULATION

1. ENGINE SIMULATION

Work conducted under Phase I of the contract (1) defined the fuel handling and sensing requirements for the family of turbine engines envisaged for future Air Force missile, drone and RPV applications. The present effort (Phases II and III) has been concerned with the design and development of the fuel control components selected as a result of the Phase I study. These components were to be designed for testing on an existing engine. The engine was to be simulated in-house for demonstrating the developed hardware in a closed-loop control configuration. A schematic of the engine is shown in Figure 74.

Description of Model

The engine simulation was based on data taken from a detailed digital computer simulation which had been shown to correlate closely to engine test data. For the purpose of testing fuel control components, a real time simulation of the thermodynamic engine parameters used in computing the fuel flow to the engine was provided. A thermodynamic analog computer model of the engine was prepared, as shown in the block diagram of Figure 75.

Two major simplifications were made to limit the complexity and hence the required computer capacity. Both of these simplifications were done with the knowledge that they would have negligible effect on the validity of the model, and sufficient computer data was generated to substantiate this.

The first simplification was to simulate the fan characteristics as a function of the speed of the high speed compressor. Since there is nothing in the thermodynamics model that would allow

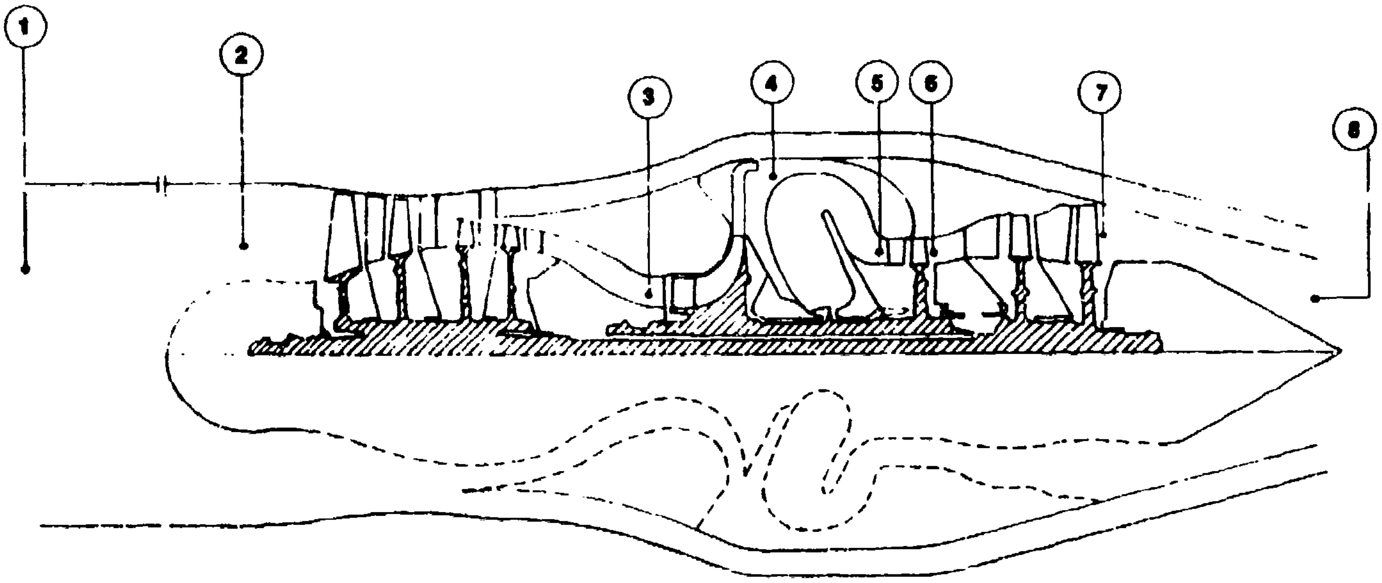

STATION	DEFINITION	PARAMETERS
1	AMBIENT	T_{T1}, P_{T1}
2	FAN INLET	T_{T2}, P_{T2}, W_{At}
3	COMPRESSOR INLET	T_{T3}, P_{T3}, W_A
4	COMPRESSOR DISCHARGE	T_{T4}, P_{T4}
5	HIGH PRESSURE TURBINE INLET	T_{T5}, P_{T5}, T_{5B}, N_2
6	LOW PRESSURE TURBINE INLET	T_{T6}, P_{T6}, N_1
7	EXHAUST NOZZLE	T_{T7}, P_{T7}
8	EXHAUST NOZZLE EXIT	T_{T8}, P_{T1}

FIGURE 74 TYPICAL ENGINE SCHEMATIC

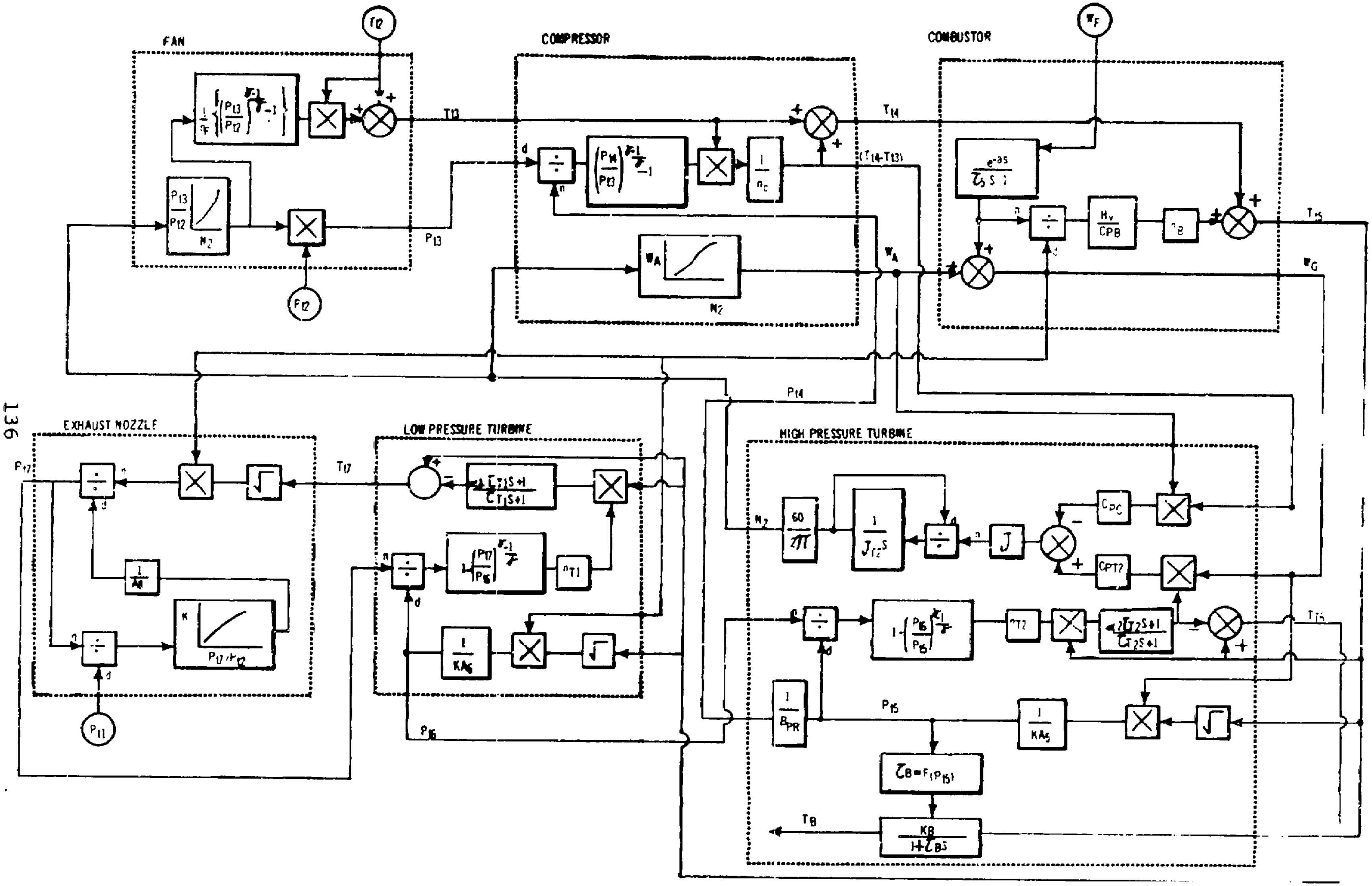

FIGURE 75 ENGINE COMPUTER MODEL BLOCK DIAGRAM

a mismatch between the fan speed and the compressor speed to occur, this change had no effect on the accuracy of the engine model. Moreover, fan speed is not used for a control parameter, and the pressures and temperatures across the fan and the fan turbine are included in the simulation, should they be required.

The other major simplification was to compute the fan turbine back pressure by simulating a variable area exhaust nozzle instead of using the equations describing the airflow mixing from the fan bypass and core at the exhaust nozzle.

Other minor simplifications include using constant efficiencies and perfect gas laws. The acceleration and deceleration limits specified by the engine manufacturer (for a W_f/P mode of control) were used as the reference for the surge, temperature and flameout limits of the engine, as detailed engine data in the form of compressor maps were not available. The simulation of $\Delta P/P$ relates the corrected airflow to the total and static compressor discharge pressures as indicated in the block diagram of Figure 76. A nominal cross-sectional area of 3.38 in^2 was determined for this study. In practice, the cross-sectional area will depend on the location of the sensor probe and must be determined by experimentally probing different areas of the discharge station for an optimum sensitivity point.

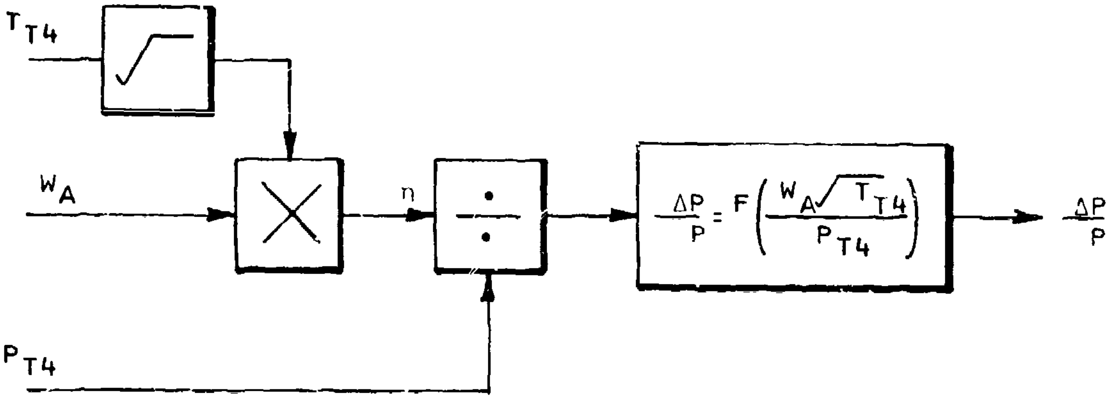

FIGURE 76 $\frac{\Delta P}{P}$ SIMULATION BLOCK DIAGRAM

Computer Data

The validity of the computer model was substantiated by comparing engine data generated at specific steady state operating points between idle and maximum speeds, to the equivalent data taken from the simulation. The curves of Figures 77 and 78 show close agreement between the two models for the steady state engine parameters indicated. The simulation did not include the surge and lean mixture blowout characteristics, as this would be overly complex and not add significantly to the test analysis. Therefore, the acceleration and deceleration schedules were used as the surge, temperature and flameout limits of the engine. During closed-loop testing, the transient performance of the system was based on comparing the defined schedules of specific engine control parameters against the values as recorded from the engine simulator. Figure 80 shows the reference schedules of fuel flow against compressor discharge pressure and inlet temperature. The equivalent schedules in terms of turbine inlet gas temperature and compressor pressure ratio are shown in Figures 81 and 82. One anomoly apparent in this data is that the simulated engine indicates an overtemperature of 100°F when accelerated from idle to max on the reference W_f/P schedule. Since the schedule is chosen to avoid surge and overtemperatures, it must be assumed that the simulated model is in error during large transients. Therefore, during engine testing, the turbine blade temperature schedule should be defined by recording this parameter while accelerating and decelerating the engine on the W_f/P schedules, or by extrapolating the data from the compressor and turbine maps. In the case of the $\Delta P/P$ schedule, a nominal cross-sectional probe area was chosen and this is almost certain to differ from that eventually chosen for maximum sensitivity. This would result in a different $\Delta P/P$ schedule being required.

2. CONTROL SIMULATION

A study to determine the optimum control modes(1) for applications encompassing low thrust missile drones and RPV's analyzed seven potential means of engine and/or vehicle control. The conclusions were that four of these seven modes had potential applications depending on the engine, vehicle and mission requirements. At the same time, the options available in each control mode were virtually unlimited, varying from constant gains and schedules to variable nonlinear gains and transient schedules that are functions of up to three independent variables. Also, complex dynamic compensation may be required to meet certain performance requirements. However, most of the potential applications stress the low cost

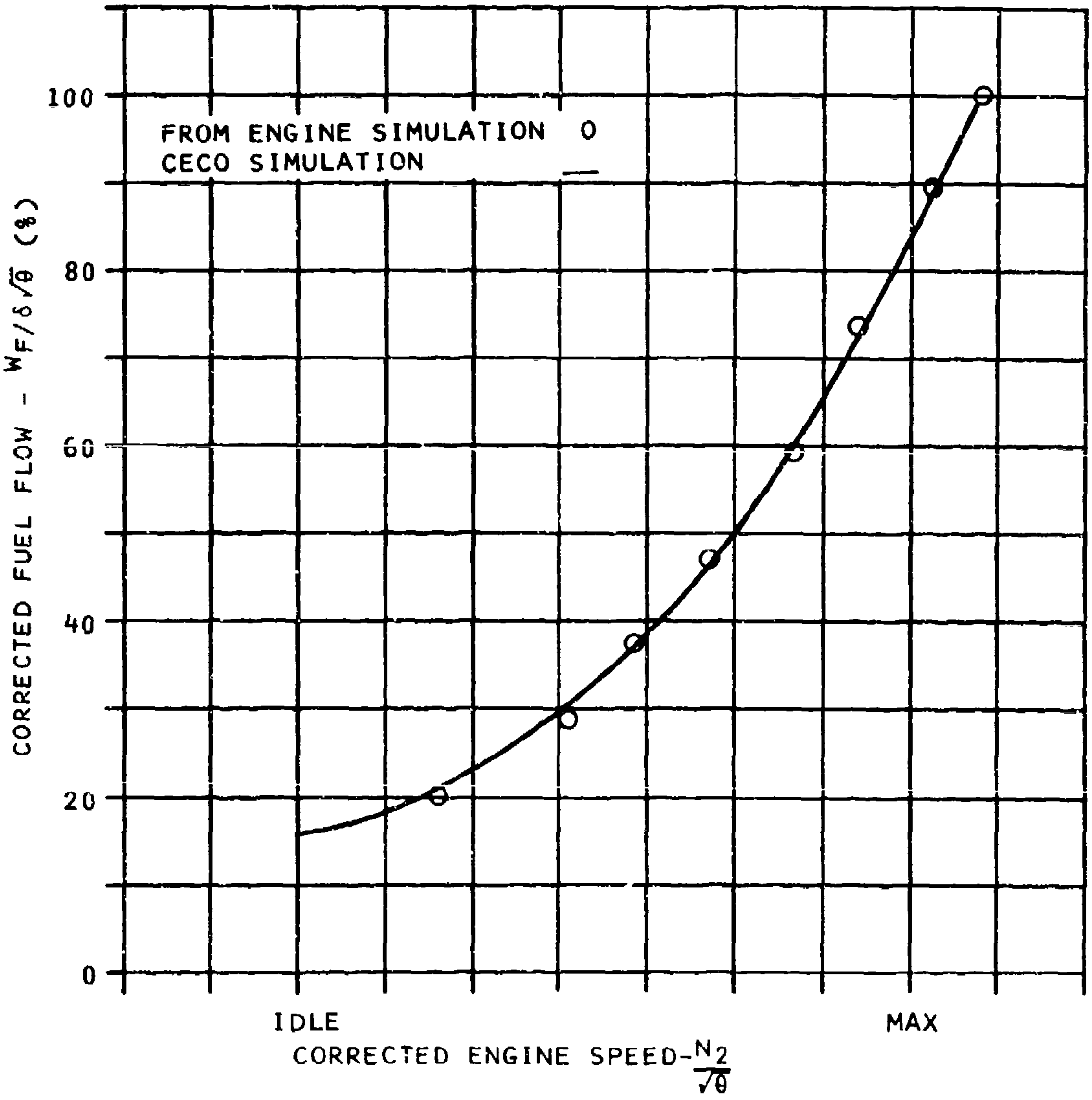

FIGURE 77 SIMULATED VS. ACTUAL STEADY RUNNING FUEL FLOWS

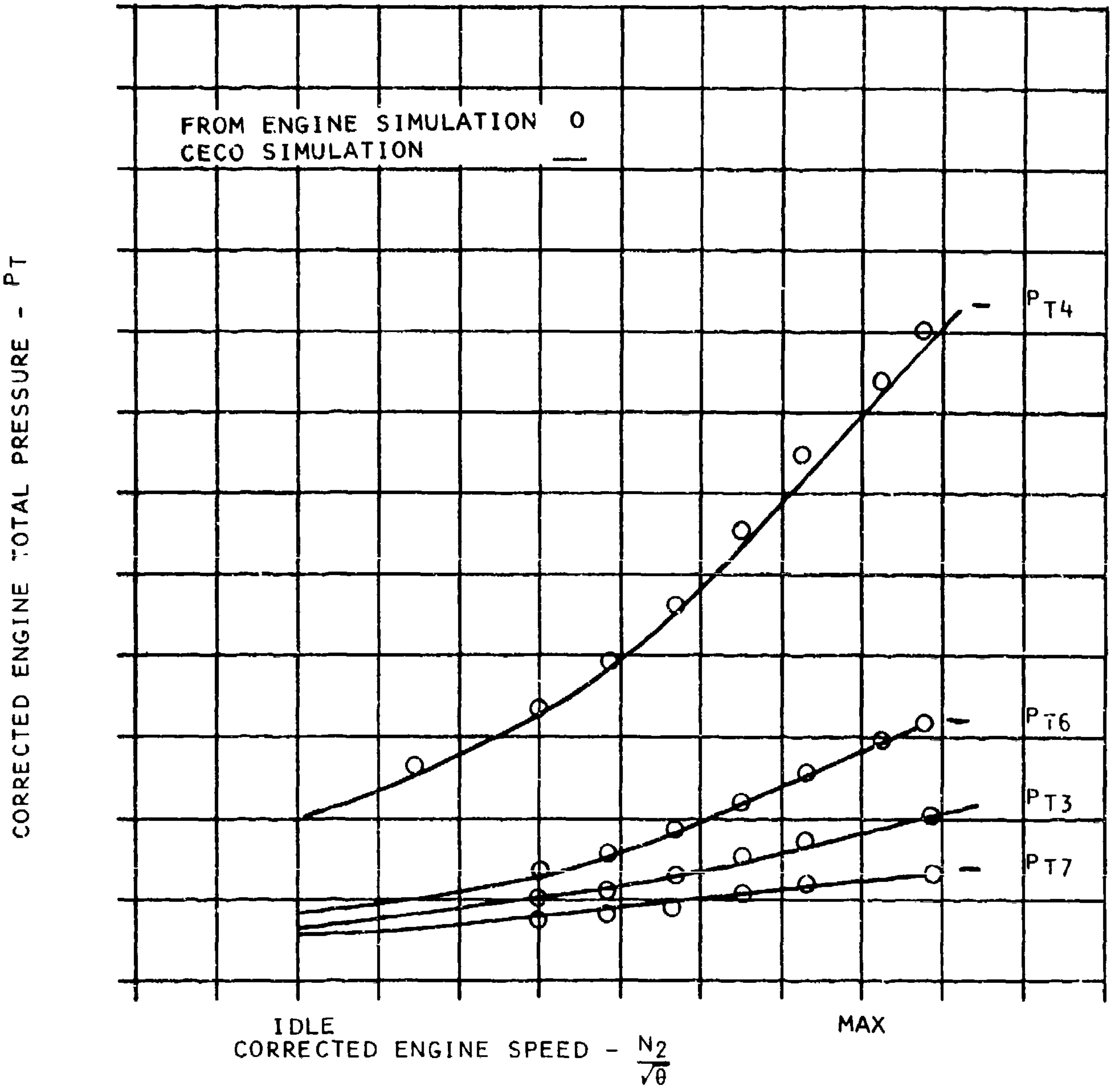

FIGURE 78 SIMULATED VS. ACTUAL STEADY RUNNING PRESSURES

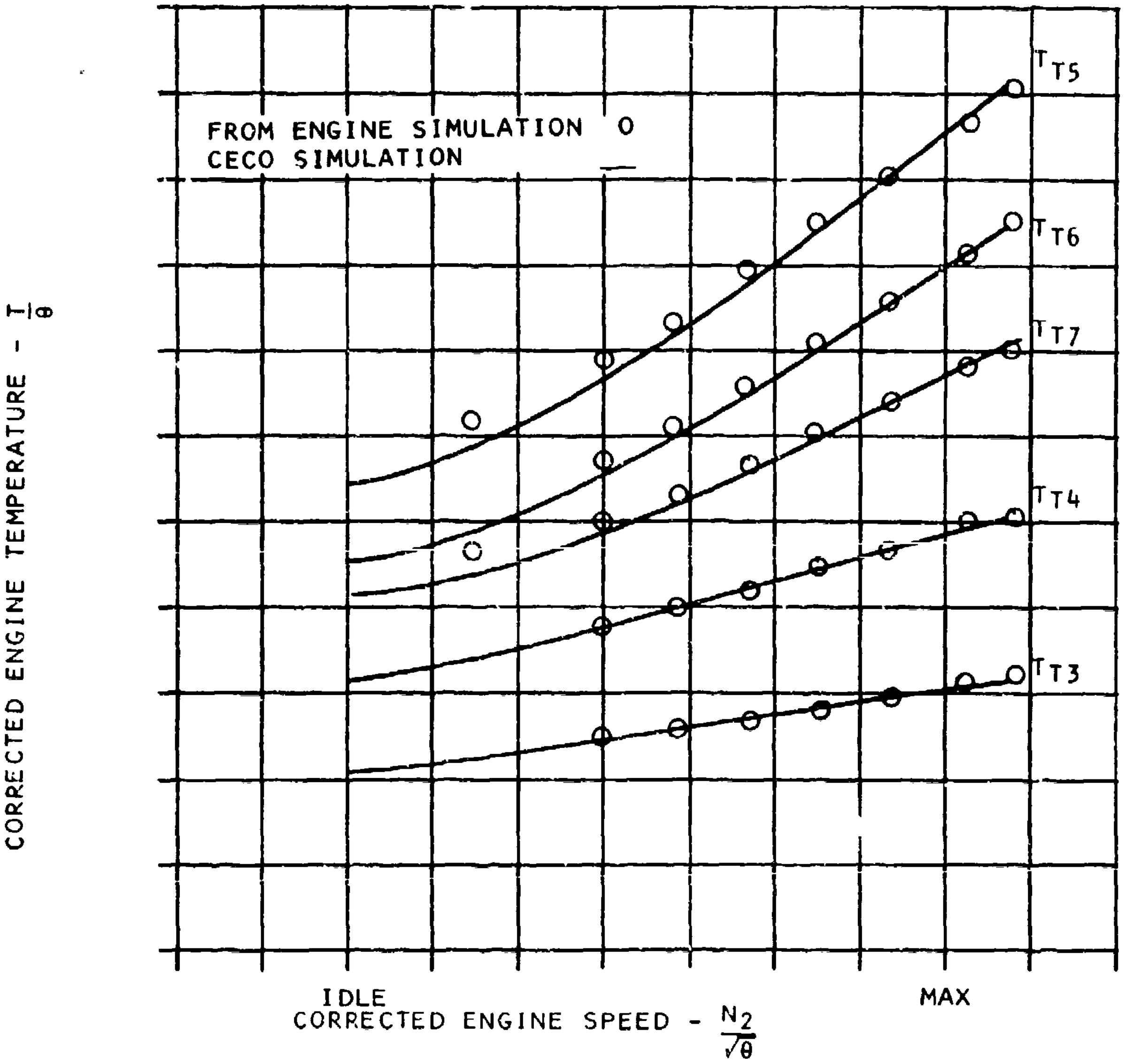

FIGURE 79 SIMULATED VS. ACTUAL STEADY RUNNING TEMPERATURES

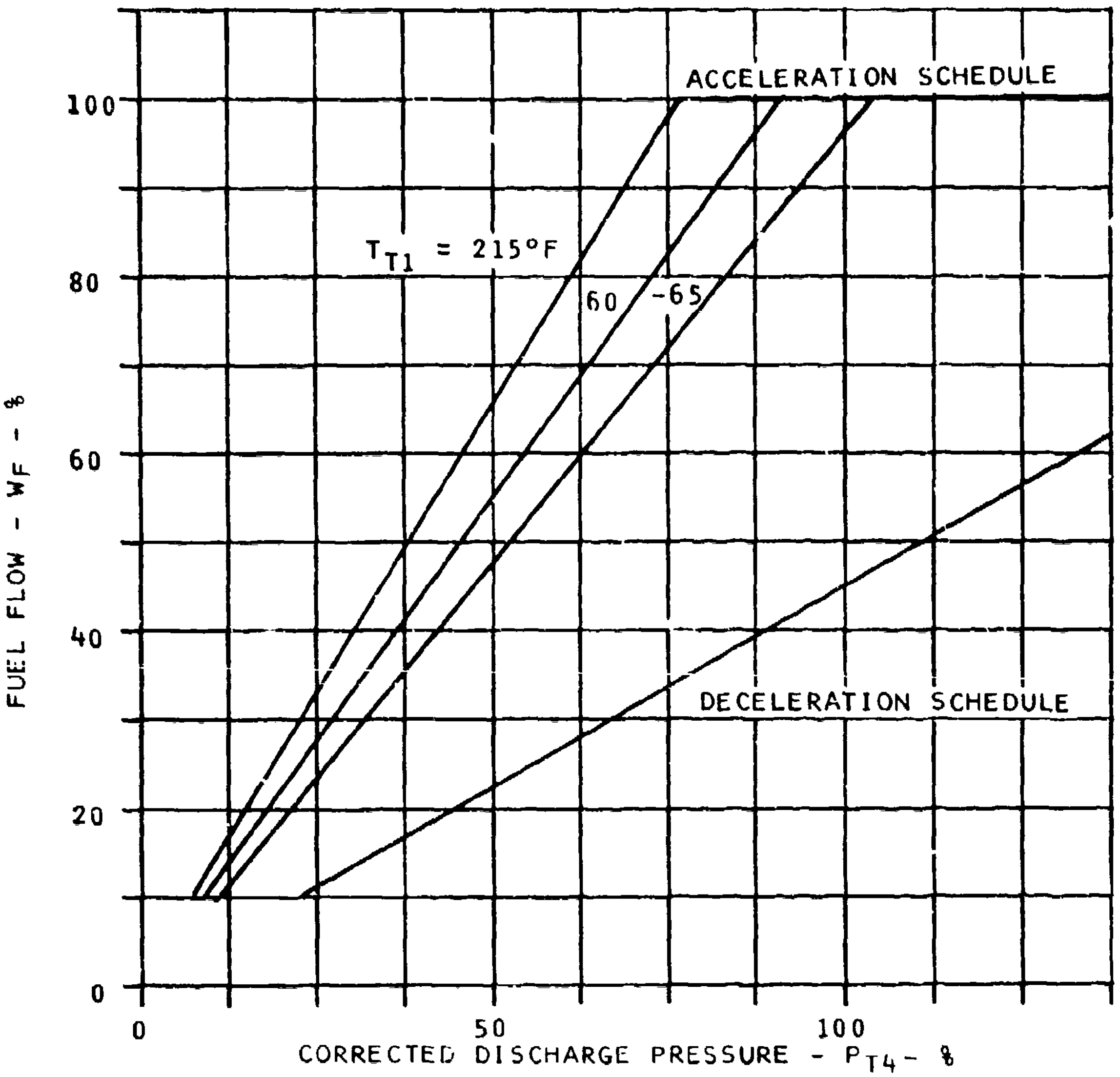

FIGURE 80 W_f/P_{t4} ACCELERATION/DECELERATION SCHEDULES

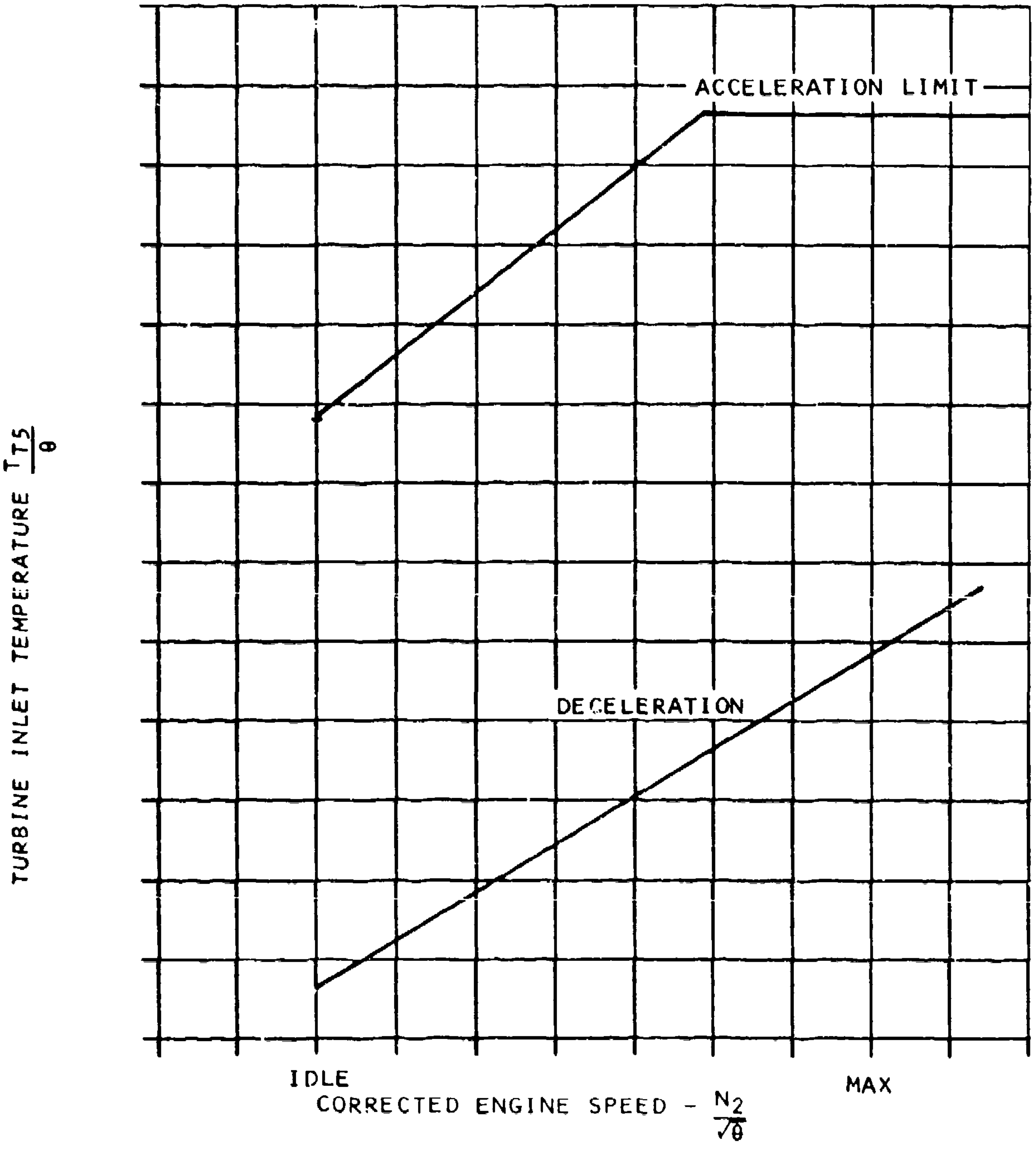

FIGURE 81 T_{t5} ACCELERATION/DECELERATION SCHEDULES

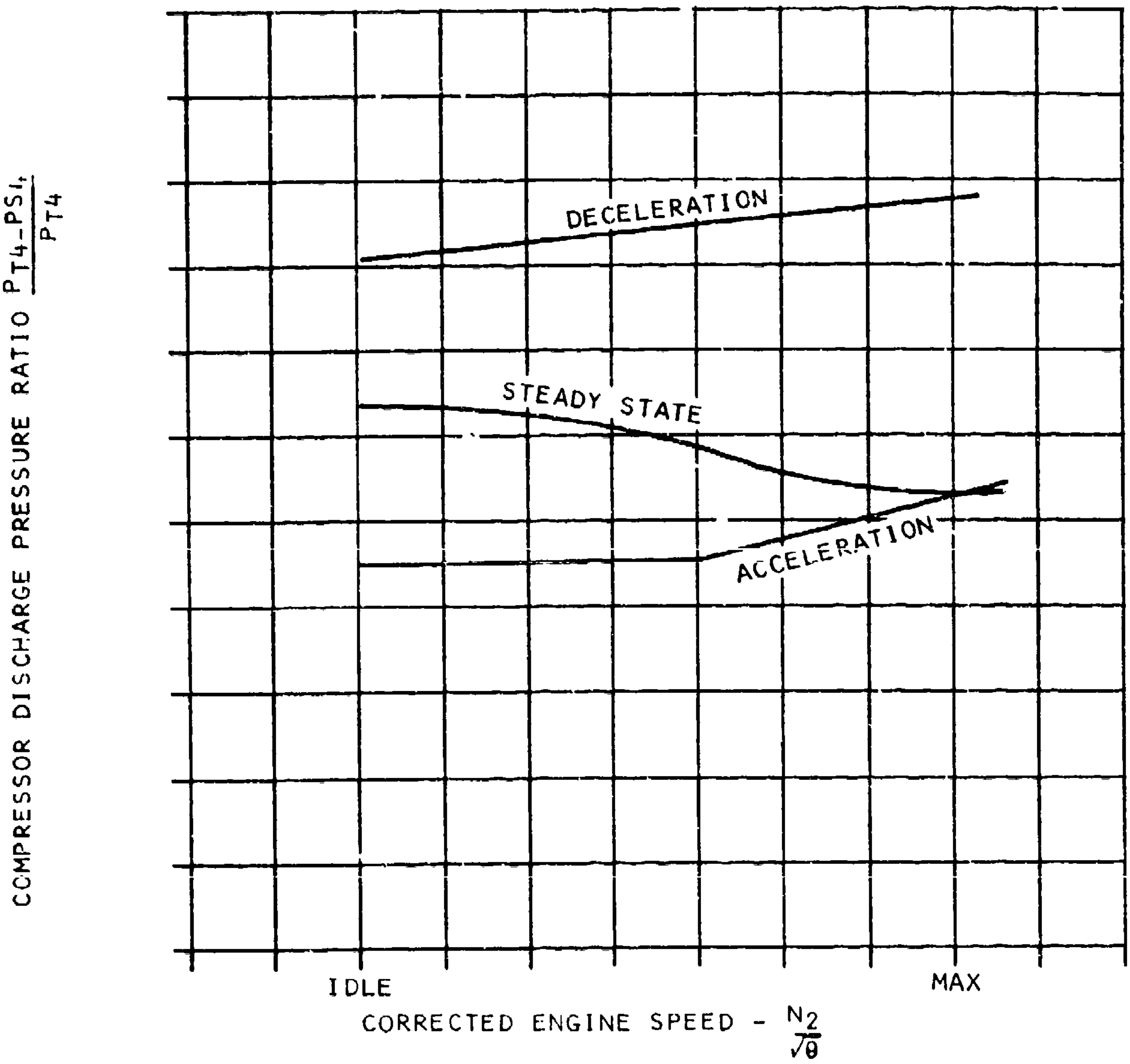

FIGURE 82 ΔP/P ACCELERATION/DECELERATION SCHEDULES

aspect most strongly and, therefore, the present study applies minimum complexity to the four modes selected. Generally, engine control specifications (2) have been used as a guideline for defining the transient and steady state requirements for the control, and the control modes have included sufficient functions to meet these requirements.

Description of Control Modes

1. W_F/P Control (Figure 83)

Fuel flow per engine pressure is scheduled open-loop for acceleration and deceleration. Although the measured pressure is from the compressor discharge station in this configuration (burner pressure) compressor inlet pressure could just as well be used, requiring only changes in the gains and accel/decel schedules. The gas generator speed governor modulates the fuel flow pressure ratio to null the speed error via a proportional plus integral controller. For demonstration purposes, the turbine blade temperature limiting control is included within this control mode configuration. The temperature control can be demonstrated by choosing a set limit below the normal engine limit while the W_F/P control on acceleration will aid as a protective backup mode. When confidence is established in the limiting mode of control the set limit can be increased to the engine temperature limit and the W_F/P scheduled acceleration increased to an overtemperature value. This will demonstrate the limiter in a potential overtemperature condition.

2. $\Delta P/P$ Control (Figure 84)

The $\Delta P/P$ acceleration control is run in conjunction with the reference W_F/P control mode in a similar manner to the turbine blade temperature limiting mode. The engine speed governor and deceleration control are the same W_F/P control modes mentioned previously while the acceleration control is selected from the lowest of the W_F/P and the $\Delta P/P$ controls. When confidence is established in the operation of the $\Delta P/P$ controller, the W_F/P accel schedule can be reprogrammed to a high value. This has the effect of shifting it out of normal operation and gives full authority acceleration control to the $\Delta P/P$ mode.

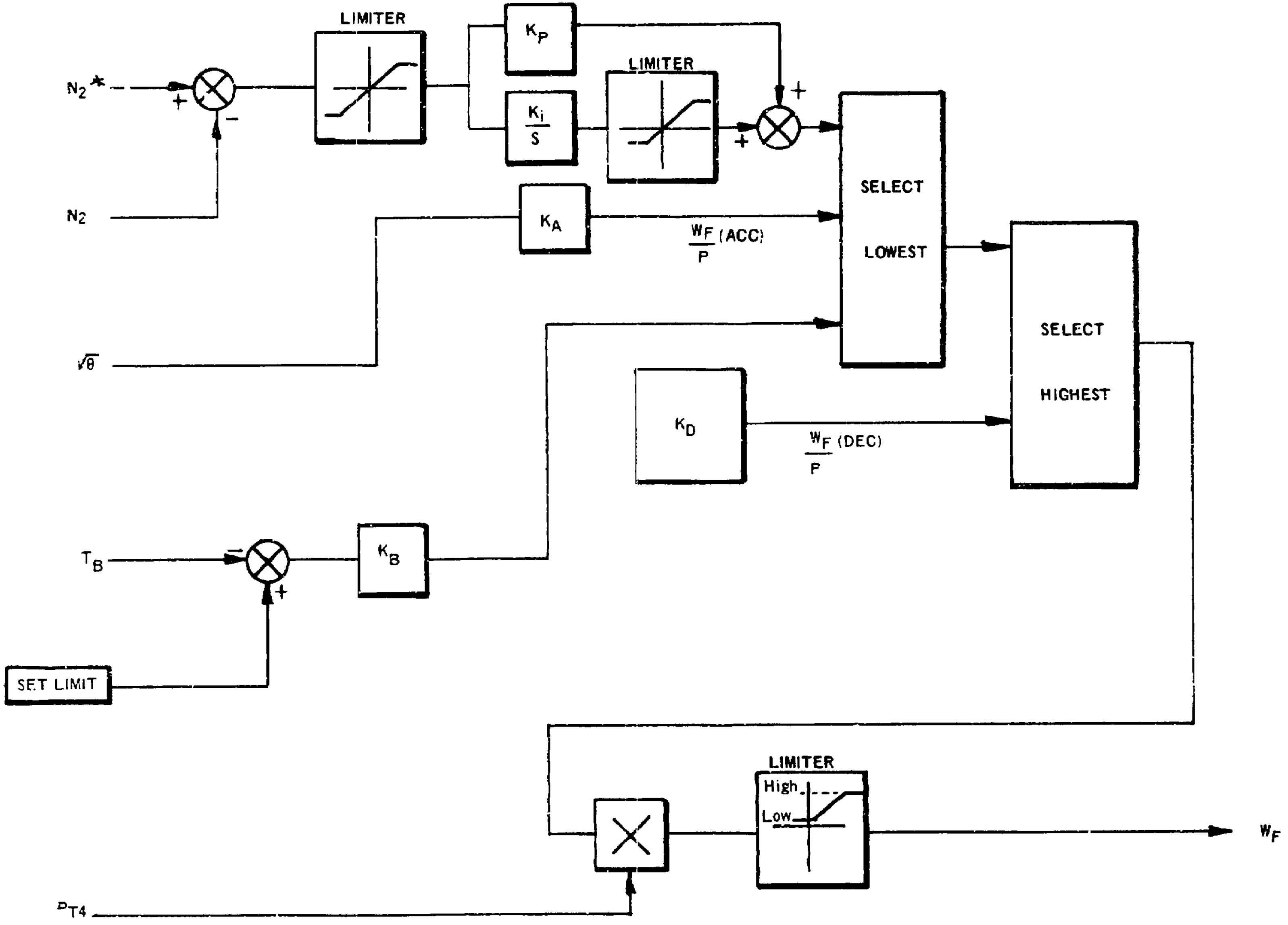

FIGURE 83 W_f/P CONTROL MODE

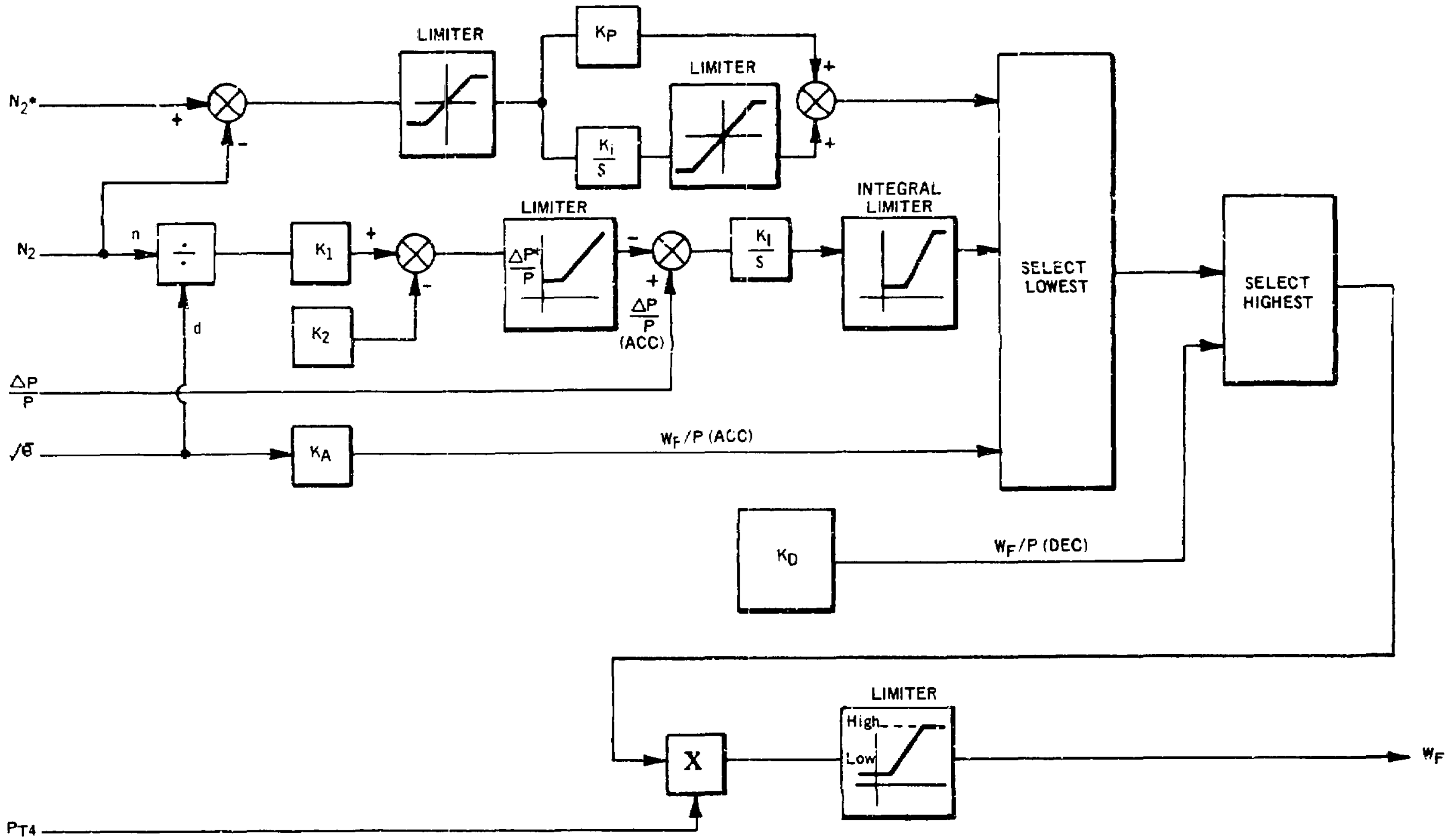

FIGURE 84 $\Delta P/P$ CONTROL MODE

)

3. T_B Mode (Figure 85)

The acceleration and deceleration schedules are computed as linear functions of corrected engine speed, with a limit on the temperature error signal. A lowest and highest wins selects the control signal from the speed governor, acceleration schedule or deceleration schedule respectively. The selected control signal modulates fuel flow through a proportional plus integral error nulling control with a minimum fuel flow limit for starting and a maximum limit for engine protection. As some inaccuracies may exist in the schedules derived from the simulation, they should be redefined from the compressor and turbine maps or from the engine test runs, before operating closed-loop with the test engine.

4. ΔN_2 Control (Figure 86)

This is the simplest of the control configurations relying on only the engine speed signal for both transient and steady state control of the engine. For transients, the throttle input is rate limited while a common proportional plus integral governor serves both for transient and steady state operation. The requirements for starting engines have been specified by engine manufacturers in terms of a W_F/P control. Since the computer model does not simulate engine starting characteristics, starting fuel flow requirements have not been established. If it is later determined that start scheduling is required, then this function can simply be added to the digital computer program. This also applies to the closed-loop temperature control mode where the temperature signal level is unacceptable for starting an engine (see Figure 85).

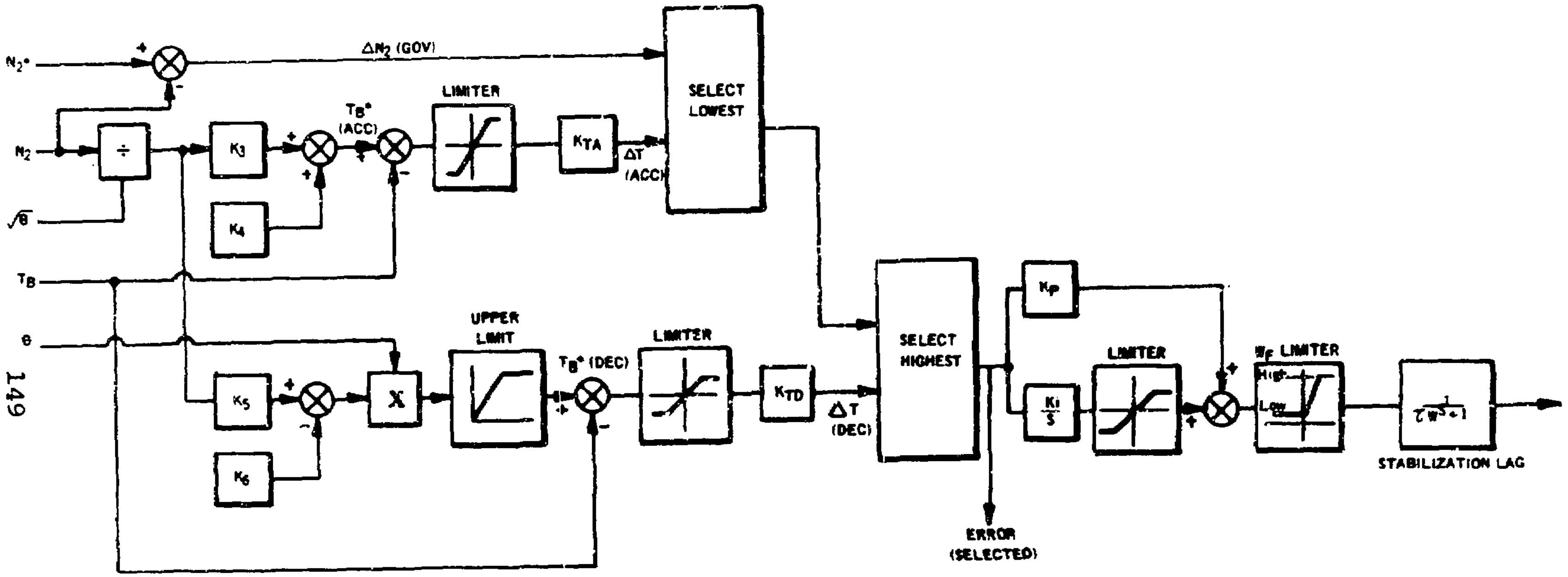

FIGURE 85 CLOSED LOOP TEMPERATURE CONTROL MODE

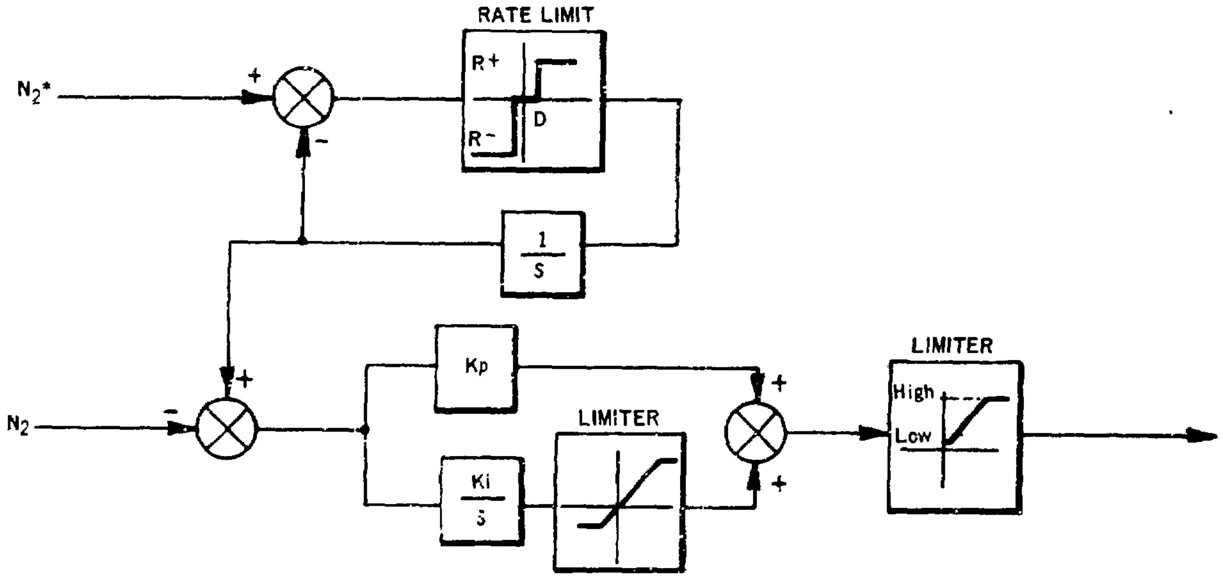

FIGURE 86 ΔN_2 CONTROL MODE

6

CLOSED LOOP TESTING

The developmental sensors, pumps, metering valve, etc., were integrated with the digital fuel control computer and the analog engine simulator for closed-loop evaluation testing. Figure 87 is a block diagram of the test set-up showing the interfacing of the components on the fuel test stand and the simulators in the computer room. All interface signals between the computers and the electronic interface box are low level DC voltages. The engine simulator reference fuel flow signal is measured at the output of the metering system by a turbine flowmeter. A frequency to DC converter with a time constant of 10 to 50 m. seconds was used to supply the required DC level to the analog computer. Figures 6 and 18 are photographs showing the test stand set-up for the magnetic clutch gear pump system and the centrifugal pump proportional solenoid system respectively. The analog computer engine simulator is shown in the photograph of Figure 88.

There is no provision being made for altitude tests with the demonstration engine so that closed-loop tests were limited to standard day sea levels conditions only.

1. MAGNETIC CLUTCH SYSTEM

Pump/Clutch Dynamics

An initial evaluation of the dynamic and static performance of the inner loop of Figure 87 established the clutch, gear pump and pump speed pickup transfer function. The analysis was made by introducing a sine wave input to the speed demand of the proportional pump speed control loop. The results are shown in the bode plots of Figures 12 and 13 indicating a time constant of 50 m secs at low pump speed and 30 m secs at high pump speed. This verifies the theoretical values calculated in Section 2 dealing with the magnetic clutch system design.

A calibration of the loop gain is shown in Table VI. Variations are due to changes in overall efficiency. Preliminary closed-loop testing assumed a linear relationship between the clutch coil

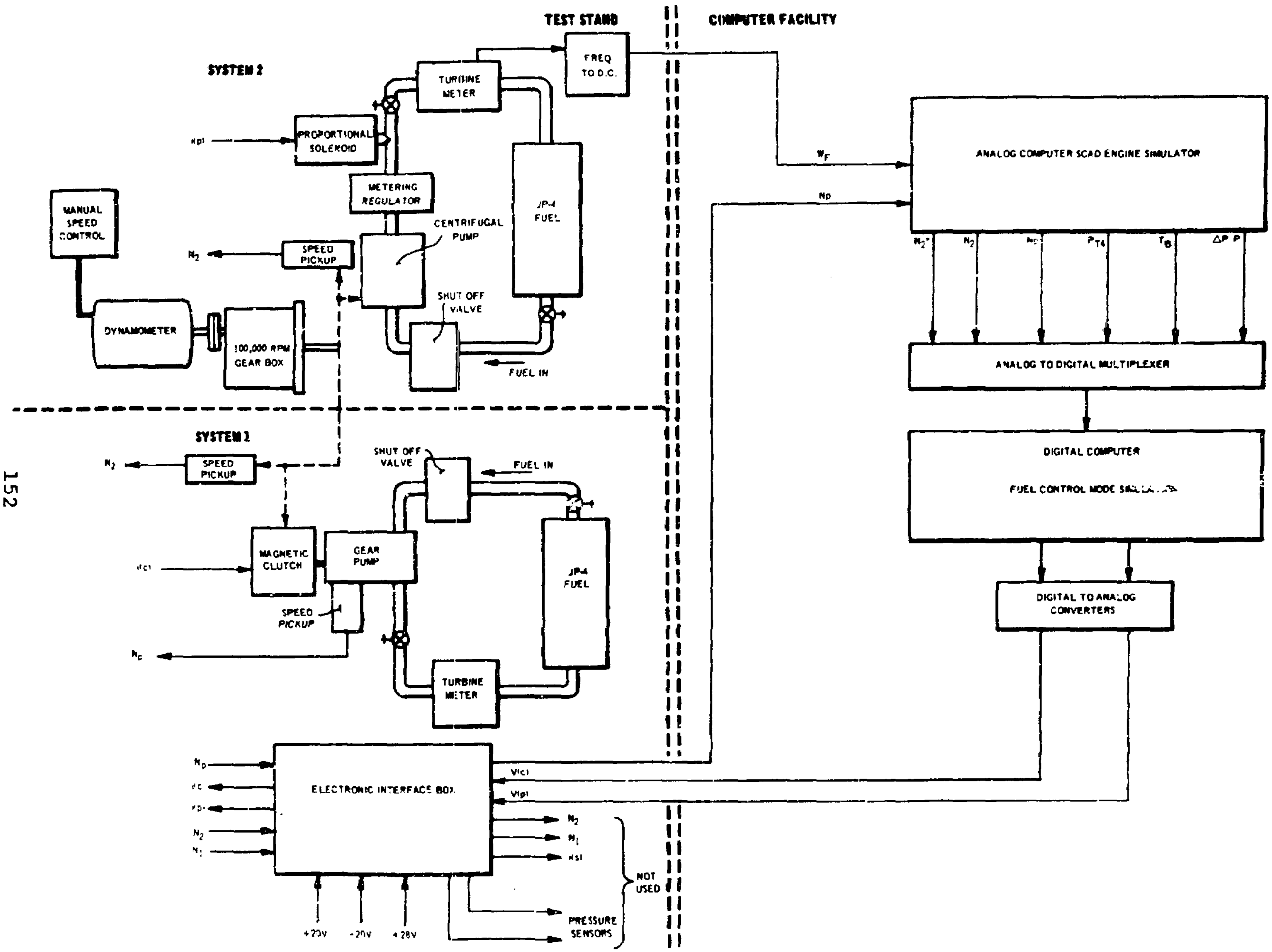

FIGURE 87 CLOSED LOOP TEST SETUP

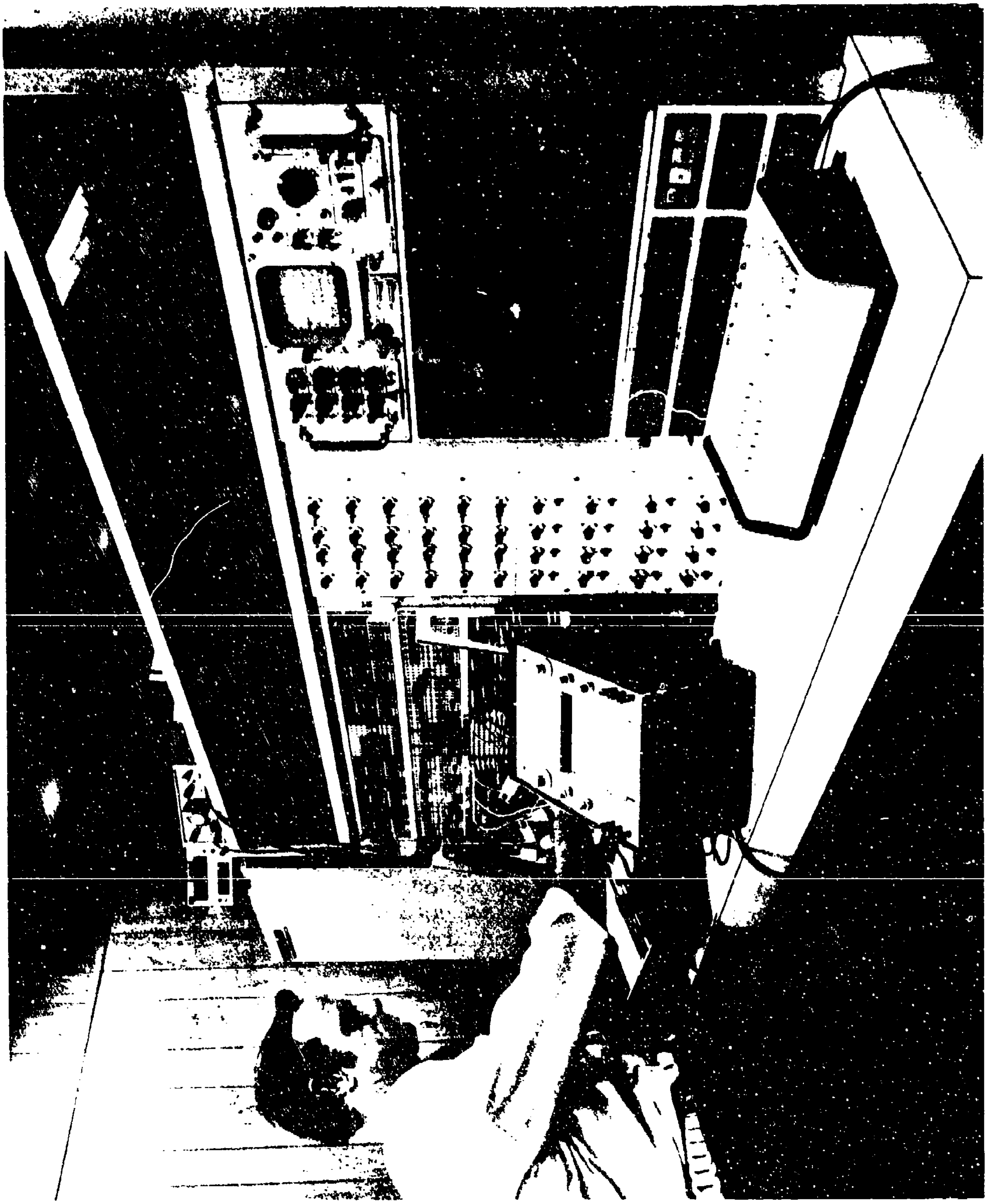

FIGURE 88 ANALOG COMPUTER ENGINE SIMULATOR

TABLE VI. MAGNETIC CLUTCH/GEAR PUMP PROPORTIONAL SPEED CONTROL CALIBRATION

Set Speed N_p* (rpm)	Pump Speed N_p (rpm)	Open Loop Gain G (rpm/rpm)	Closed Loop Gain (G+1)/G (rpm/rpm)
1800	1020	1.3	1.77
3000	2224	2.8	1.35
4800	3888	4.3	1.23
6000	4946	4.7	1.21
7200	5980	5.0	1.20
8400	7000	5.0	1.20
9600	8000	5.0	1.20
10800	9000	5.0	1.20
12000	9947	5.0	1.20
13200	10810	4.5	1.22

excitation current and the pump speed output. This resulted in deceleration transients that exceeded the W_F/P low limit and could result in engine flameouts if not corrected. As a result, a variable gain variation was included in the computer to compensate for this nonlinearity. This is indicated in Figure 89 where, for simplicity, the compensation was approximated as a constant rate from 0 to 4300 rpm and a constant from 4300 rpm to maximum pump speed. The following closed-loop tests were performed with the inclusion of this gain compensation.

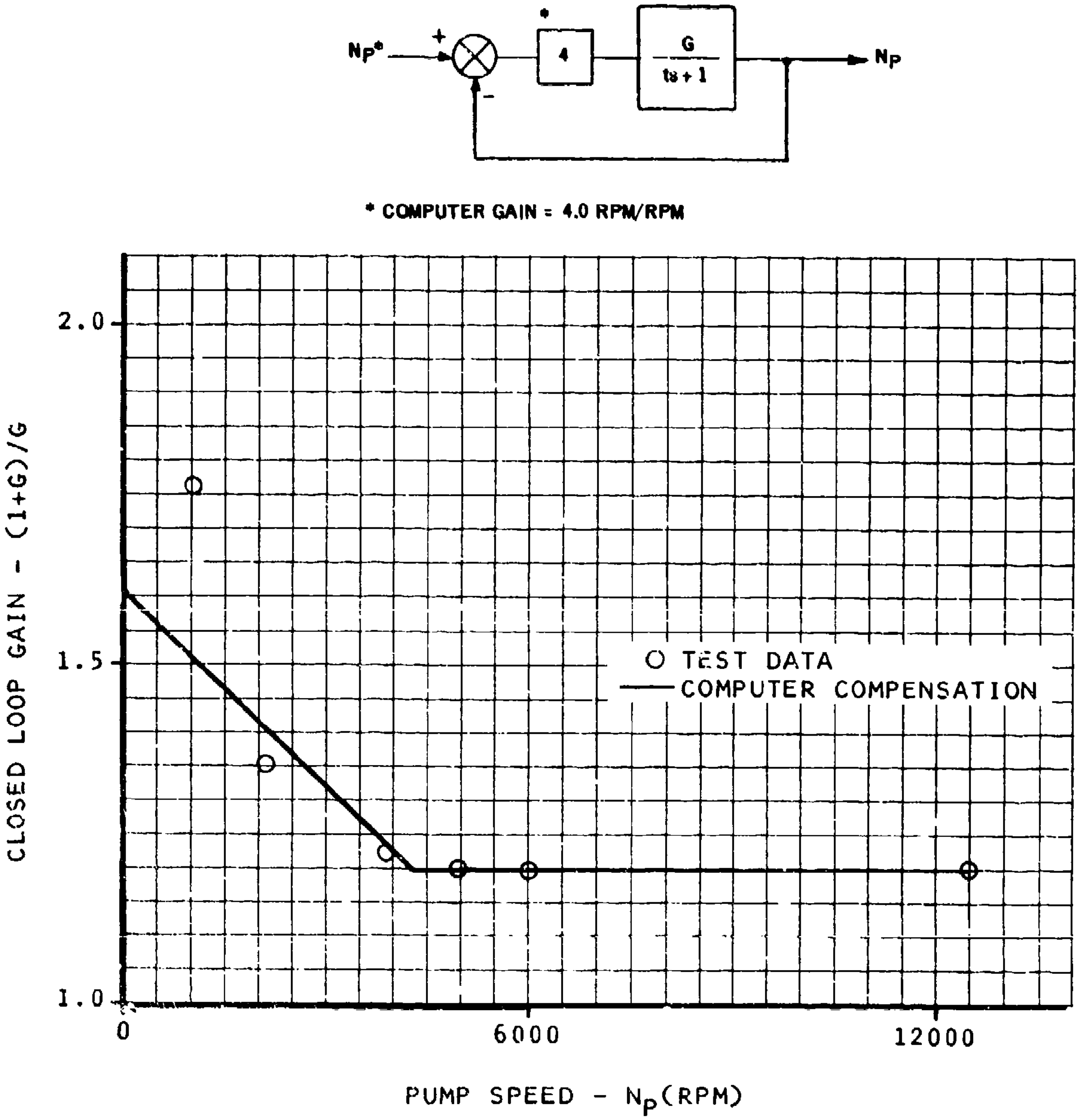

FIGURE 89 MAGNETIC CLUTCH SYSTEM - CLOSED LOOP PUMP SPEED CALIBRATION

Engine Acceleration Control

These tests consisted of accelerating the engine model from idle to maximum speed using each of the four control modes. The recorded engine responses were compared to the reference schedule for performance evaluation, and as indicated in Figure 90, satisfactory acceleration control can be achieved by all of the control modes. The engine speed transient responses for both acceleration and deceleration are shown in Figures 91 and 92. This data is summarized in Table VII. The results show a significant penalty in terms of acceleration performance for the ΔN_2 control mode. This is to be expected from this less sophisticated control mechanization. Of the other three control modes, the open-loop W_F/P scheduled acceleration stands out as the best trade-off between performance and complexity.

TABLE VII. ACCELERATION/DECELERATION PERFORMANCE MAGNETIC CLUTCH SYSTEM

CONTROL MODE	ACCELERATION		DECELERATION	
	t_{90} secs	t_{75} secs	t_{90} secs	t_{75} secs
W_F/P	1.6	0.6	1.5	0.8
$\Delta P/P$ (accel only)	2.2	0.6	---	---
ΔN_2	1.95	0.95	1.4	1.1
T_{5B}	1.2	0.6	1.3	0.95

t_{90} = time to reach 90% of total speed change from idle to max

t_{75} = time to reach 75% of total speed change from idle to max

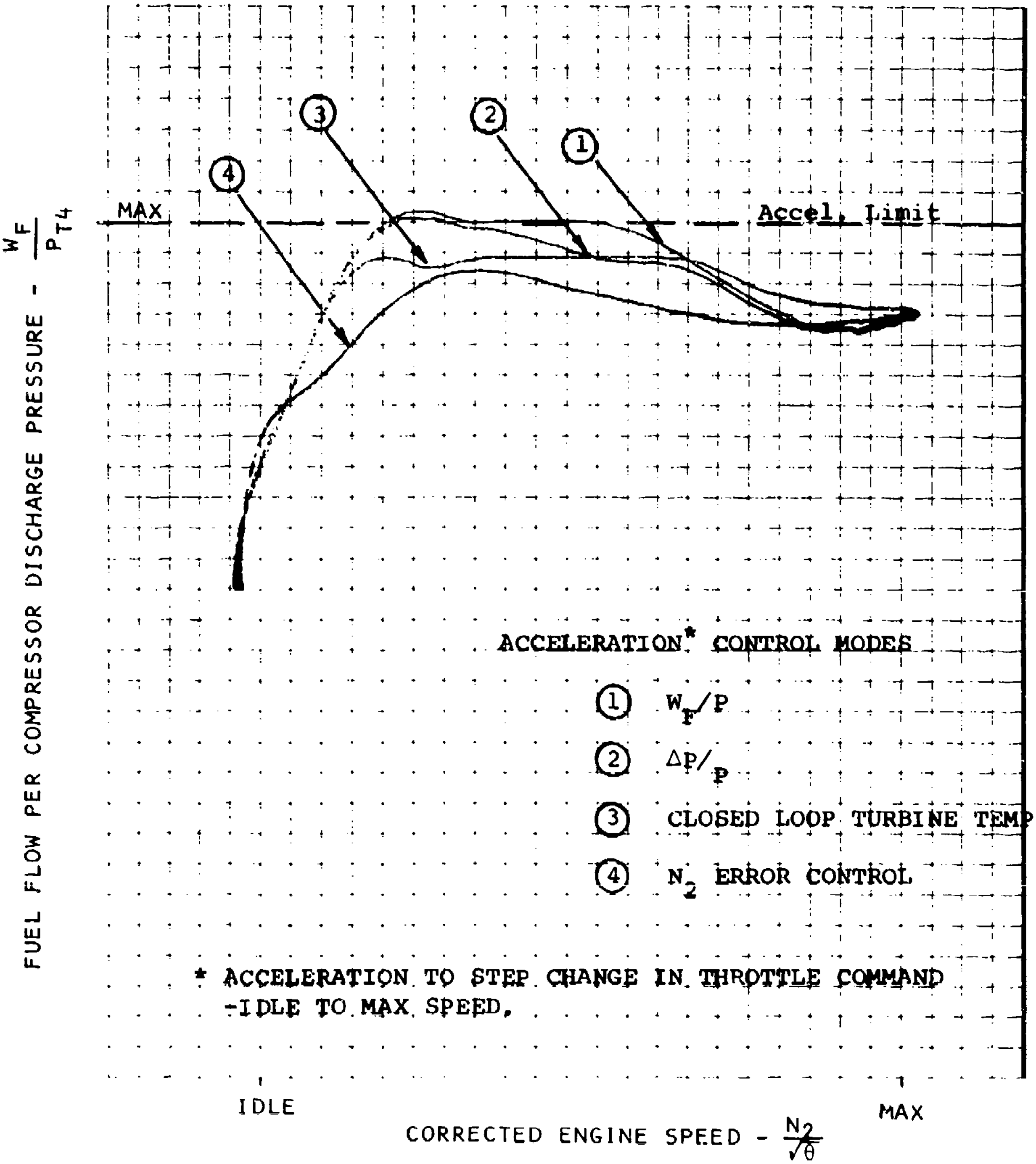

FIGURE 90 MAGNETIC CLUTCH SYSTEM
ACCELERATION PERFORMANCE

W_F/P CONTROL MODE

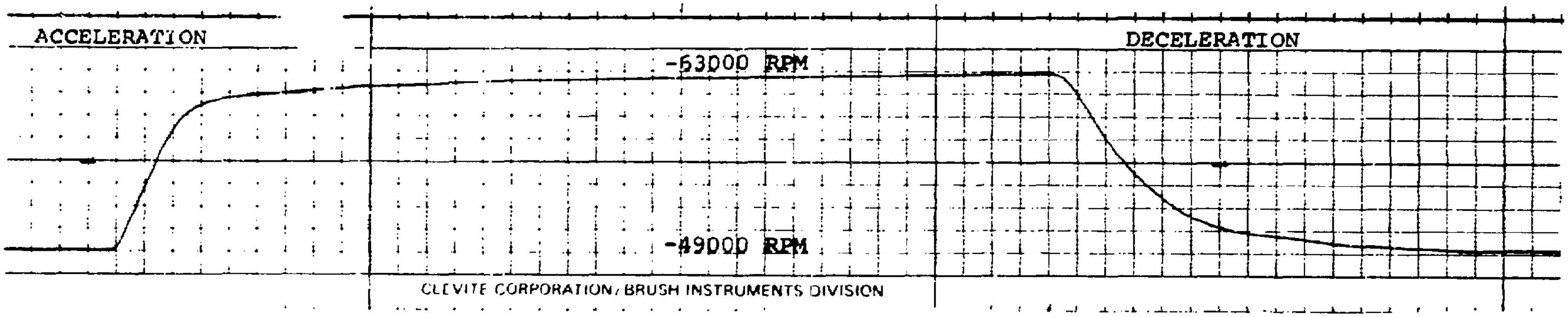

$\Delta P/P$ CONTROL MODE

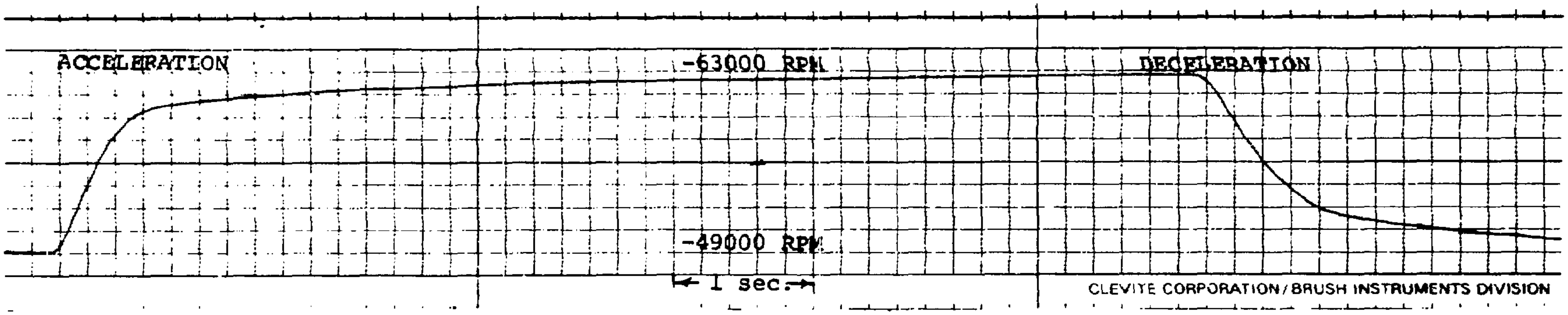

FIGURE 91 MAGNETIC CLUTCH SYSTEM - ACCEL/DECEL PERFORMANCE TRACES

ΔN_2 CONTROL MODE

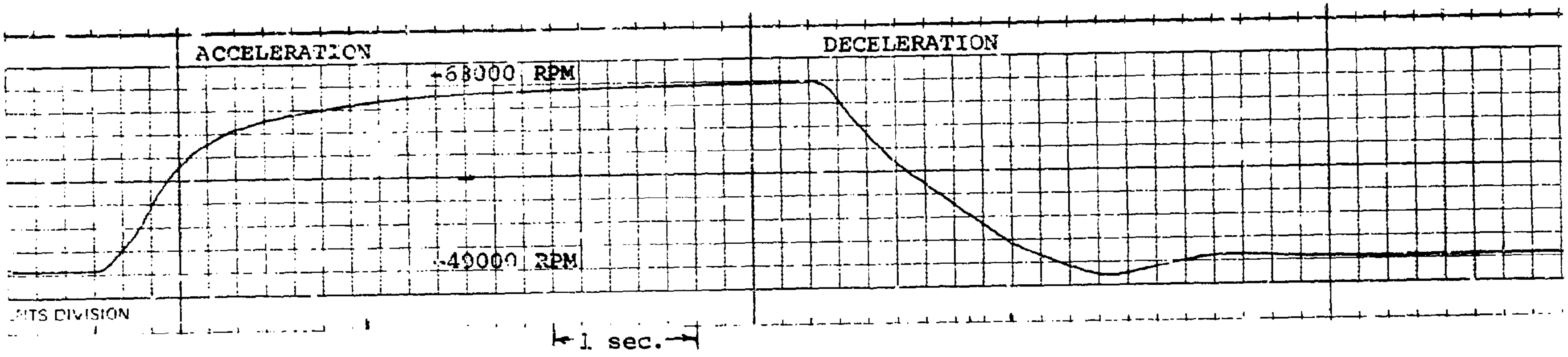

T_B CONTROL MODE

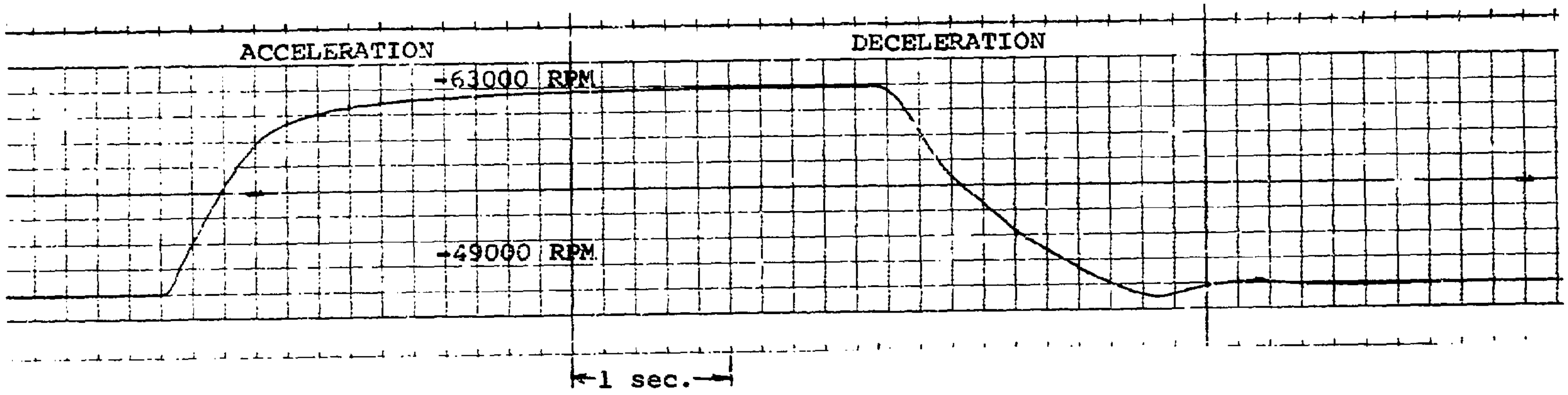

FIGURE 92 MAGNETIC CLUTCH SYSTEM - ACCEL/DECEL PERFORMANCE TRACES

Of the closed-loop controls, $\Delta P/P$ still requires an accelerating schedule* and in addition, requires a high integrator gain which makes it sensitive to lag in the system. The closed-loop temperature control, T_B, requires scheduling acceleration and deceleration gas temperatures. This makes it necessary to have a well-defined turbine blade thermal model in order to relate the measured blade temperature to the scheduled gas temperature. In the case of engines with internally cooled turbine blades, this relationship is such that the control would require the addition of complex compensation for acceptable acceleration performance.

Engine Deceleration Control

Because of the rapid deceleration times resulting from the large margin between the engine steady state running line and the W_F/P decel limit, the deceleration lags the allowable limit during most of the transient. Therefore, providing the low limit is not exceeded, the deceleration performance should be acceptable. Figure 93 indicates the performance of the magnetic clutch system for the deceleration control modes.

The speed error control is the only mode which reaches the limit during the transient, but at the same time there is an approximate 1.5% speed undershoot before idle speed is attained. The deceleration times summarized in Table VII indicate that the magnetic clutch/gear pump system will meet the deceleration requirements of the engine regardless of control mode selection.

---

* Earlier work (3) had indicated that a constant value of $\Delta P/P$ would probably suffice for accelerating most engines over the surge bucket. Also, most advanced engines will operate at higher gas temperatures requiring that the acceleration be not only surge-free but temperature-limited during part of the transient. Therefore, a $\Delta P/P$ control would be required to limit engine temperature as well as prevent surge, and it is unlikely that the simple constant $\Delta P/P$ schedule referred to in the reference will meet these requirements. It is concluded that a closed-loop $\Delta P/P$ control requires some form of scheduling.

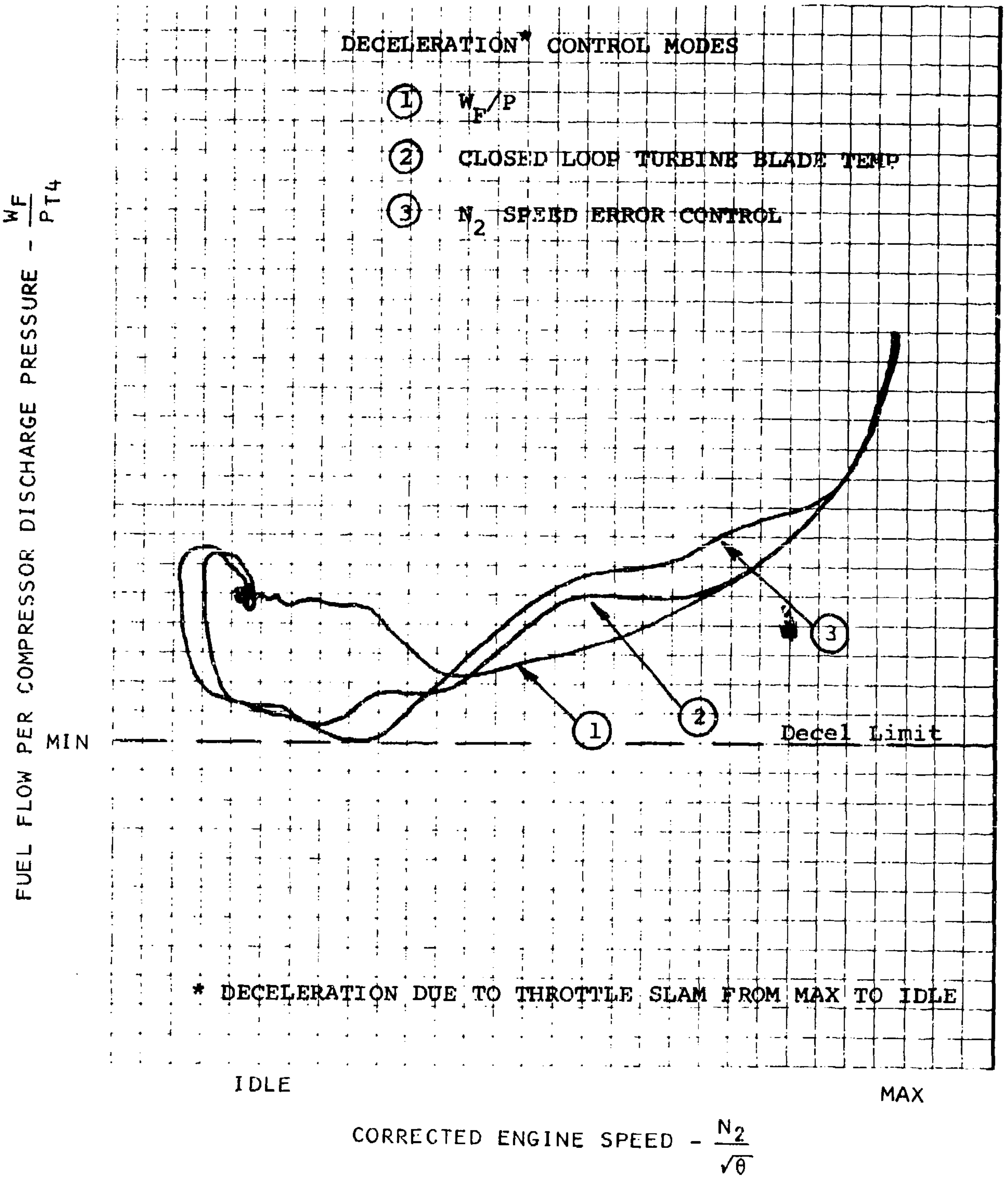

FIGURE 93 MAGNETIC CLUTCH SYSTEM DECELERATION PERFORMANCE

Turbine Blade Temperature Limiting

The development of a radiation pyrometer optical system for indicating the temperature of turbine blades applies to its potential application in the closed-loop control on engine gas temperature. It also applies to a secondary backup mode in which the turbine blade temperature is limited to a value commensurate with efficient engine operation, high performance, and long blade life. Although this latter application was concerned only with the performance at higher engine power levels, protection from potential hot start situations could also be included by adding a variable gain in the control computation.

The lower trace of Figure 94 shows the acceleration response of a W_F/P control when the W_F/P acceleration limit is set higher than the allowable turbine blade temperature upper limit of 2400°R.

The upper trace is the comparable transient when the blade limiter is included and shows that the overtemperature condition has been prevented. The trace does show a tendency for the system to be slightly oscillatory under the blade temperature controller. This results from the high gain that is necessary for limiting overtemperature excursions to less than 30°F. The need for good stability margins may require that some dynamic compensation be included for engine operation. This can quite easily be added to the digital control computer.

Engine Speed Governor

The evaluation of the speed governor modes used an engine speed demand signal as the control input to the governor. This would normally correspond to an external throttle demand from an onboard vehicle control computer. The analysis consisted of inducing small step changes to the set speed input and recording the resulting engine speed transients. This is shown in Figures 95 to 96. The rise time, percent overshoot, and damping (number of overshoots), indicating the relative merits of the governors, is summarized in Table VIII.

The advantage of an inherent gain compensation with engine operating point produced by the P multiplier is apparent in the superior performance of the W_F/P control mode. The closed-loop control has governors which reset fuel flow directly and as a result, gains can not be optimized at both high and low engine pressures. Also, the governor gains were chosen as a compromise

TURBINE BLADE TEMPERATURE WITH LIMITING SET AT 2400°R
Acceleration due to throttle slam from Idle to Max
W_F/P Mode with N_2 and T_B Limiting Governor

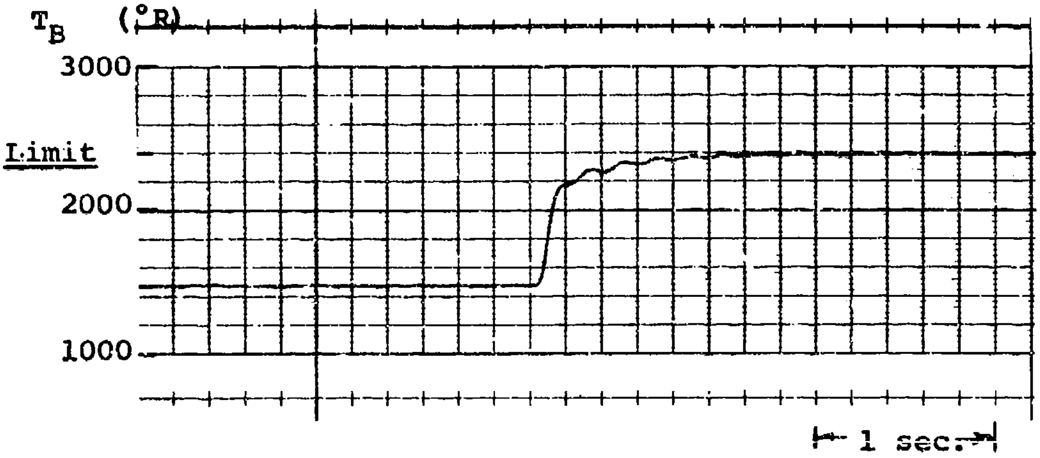

SAME CONDITION WITHOUT TEMPERATURE LIMITING

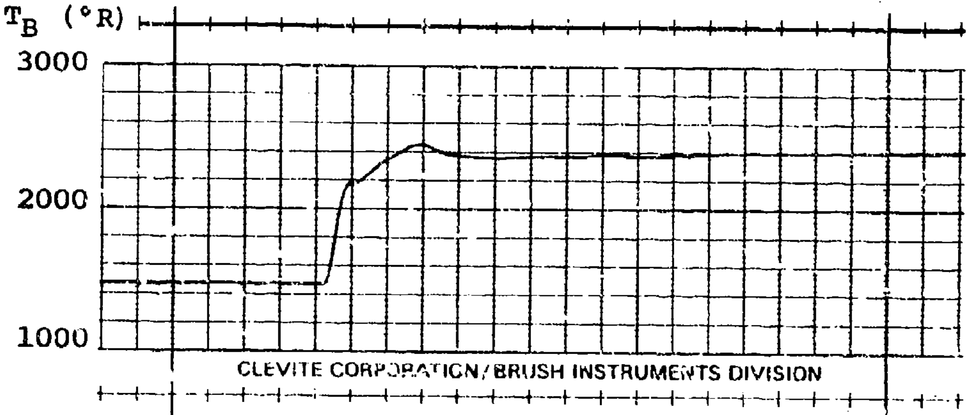

FIGURE 94 MAGNETIC CLUTCH SYSTEM - TURBINE BLADE TEMPERATURE TRACES WITH AND WITHOUT LIMITER

N_2 Speed Error Mode

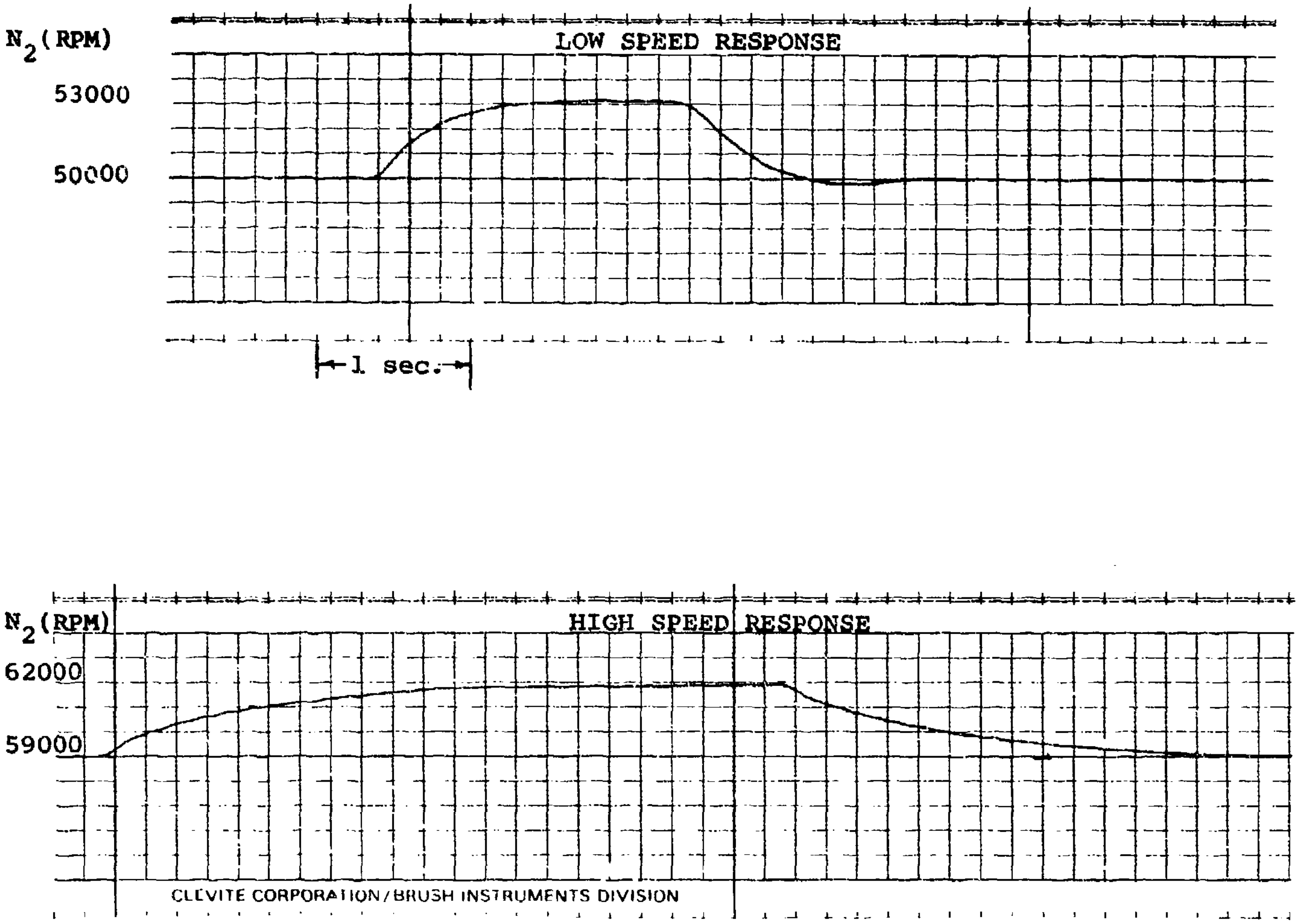

FIGURE 95 MAGNETIC CLUTCH SYSTEM - N_2 GOVERNOR RESPONSE

W_F/P GOVERNOR RESPONSE TO STEP CHANGE INPUT

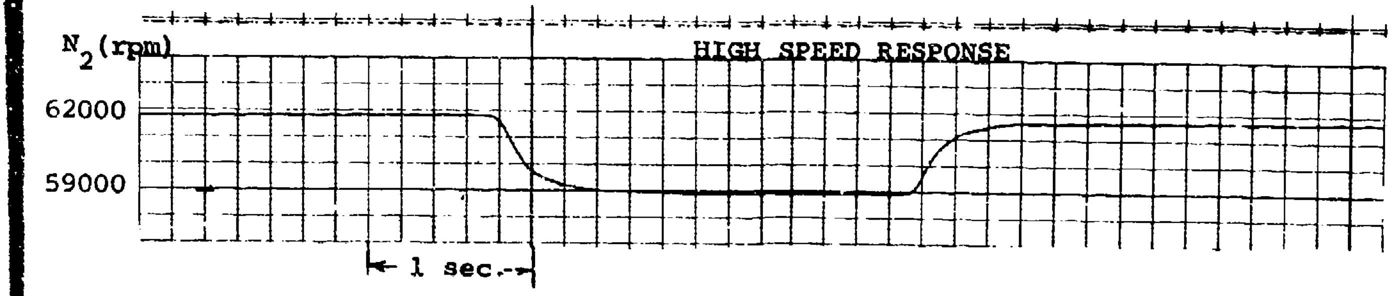

T_{5B} GOVERNOR RESPONSE TO STEP CHANGE INPUT

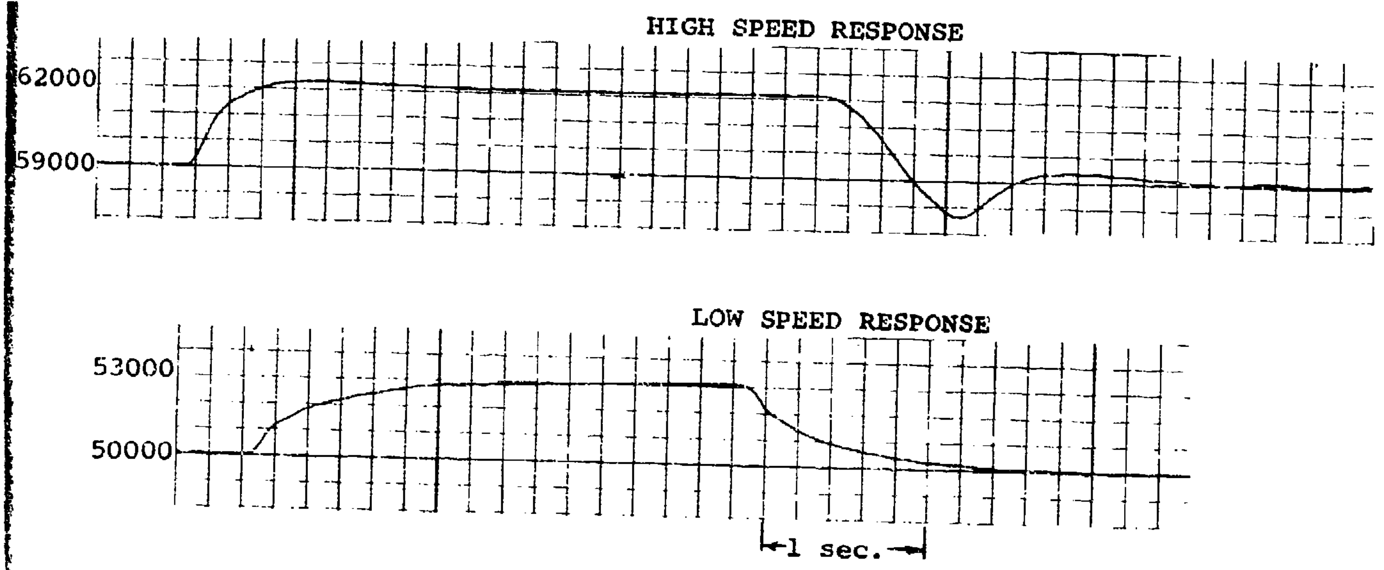

FIGURE 96 MAGNETIC CLUTCH SYSTEM - N_2 GOVERNOR RESPONSE

TABLE VIII. MAGNETIC CLUTCH SYSTEM - SPEED GOVERNOR PERFORMANCE

Mode	Operating Conditions	T_R(secs)	% Overshoot	No Overshoots
W_F/P	100% N_2, pos. step	0.6	0	0
	" , neg. step	0.6	0	0
	80% N_2, pos. step	0.9	0	0
	" , neg. step	0.6	15	1
$\Delta P/P$	Same governor as	-	-	-
	used with the W_F/P	-	-	-
	control	-	-	-
		-	-	-
T_B	100% N_2, pos. step	1.7	0	0
	" , neg. step	1.5	0	0
	80% N_2, pos. step	0.6	6	1
	" , neg. step	0.5	45	2
ΔN_2	100% N_2, pos. step	2.4	0	0
	" , neg. step	1.4	0	0
	80% N_2, pos. step	1.4	0	0
	" , neg. step	0.8	6	1

between acceptable acceleration/deceleration performance and small signal governor performance, since the governor droop determines how long the engine will remain at the transient schedule limits. Figures 90 to 92 in depicting the acceleration and deceleration performance also show the governor performance from the transient control schedules to the steady state operating line.

2. CENTRIFUGAL PUMP SYSTEM

The high speed centrifugal pump system was run closed-loop in a similar manner to the magnetic clutch system. The main difference was that the fuel control computer output sets a proportional current (via the electronic interface voltage to current converter) to the metering valve solenoid while with the clutch system the gear pump speed is read into the computer, compared to the calculated demand speed, and the error signal used to generate a proportional current signal to the clutch. This closes the loop around the pump speed. The test set-up showing both the magnetic clutch system and the centrifugal pump system was shown in Figure 87.

Open Loop System Calibration

An open-loop calibration of measured fuel flow against the control computer voltage to the metering valve solenoid circuit is shown in Figure 97. This also shows the approximation necessary to compensate the nonlinearity and give acceptable transient closed loop performance.

Engine Acceleration Control

Figure 98 is the idle-to-maximum speed traces for the four acceleration control modes analyzed. These traces indicate the performance before gain compensation was added, while the traces of Figure 99 are those taken with the nonlinear gain compensation included in the digital control computer. For these cases, the performance was slightly better without gain compensation as the fuel flow error during the acceleration tended to compensate for the system lag (error tended to overfuel while the lag tended to underfuel). However, the deceleration performances indicated that compensation was necessary to avoid a potential engine flameout condition. The acceleration speed time traces are shown in Figures 100 and 101 and are summarized in Table IX. All responses were initiated by an idle-to-maximum step change in the engine throttle demand. Referring to Table IX, the t_{90} time occurs partly through the accel control and partly through the speed governor control, and gives a better indication of the overall system response. The t_{75} time is mostly under the acceleration control and gives a better indication of the acceleration scheduled portion of the transient.

All of the acceleration performances are considered acceptable for most applications with the temperature control showing a definite advantage for use where higher performance is required.

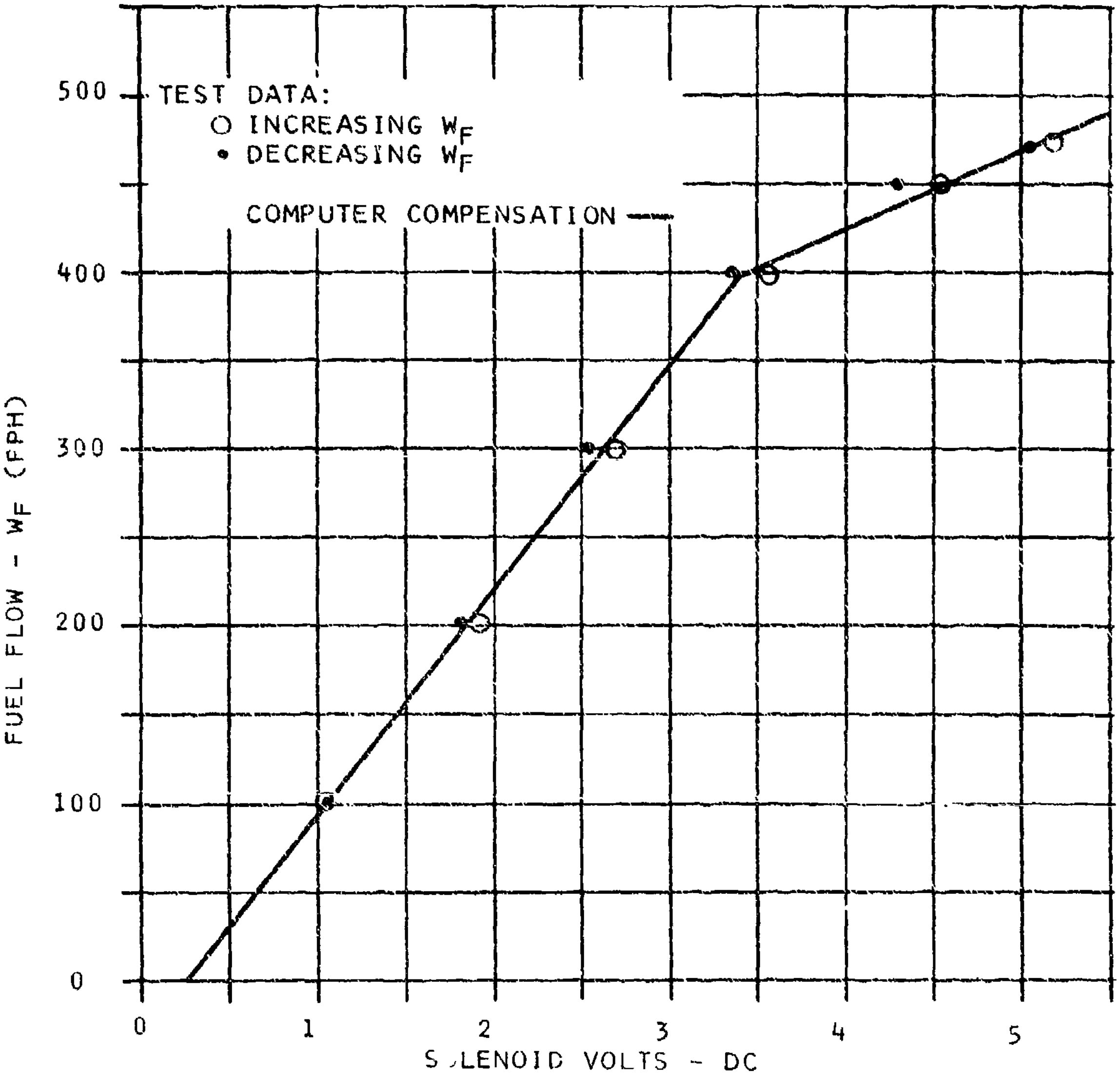

FIGURE 97 CENTRIFUGAL PUMP SYSTEM - FUEL METERING SOLENOID AND CONTROL COMPUTER VOLTAGE CALIBRATION

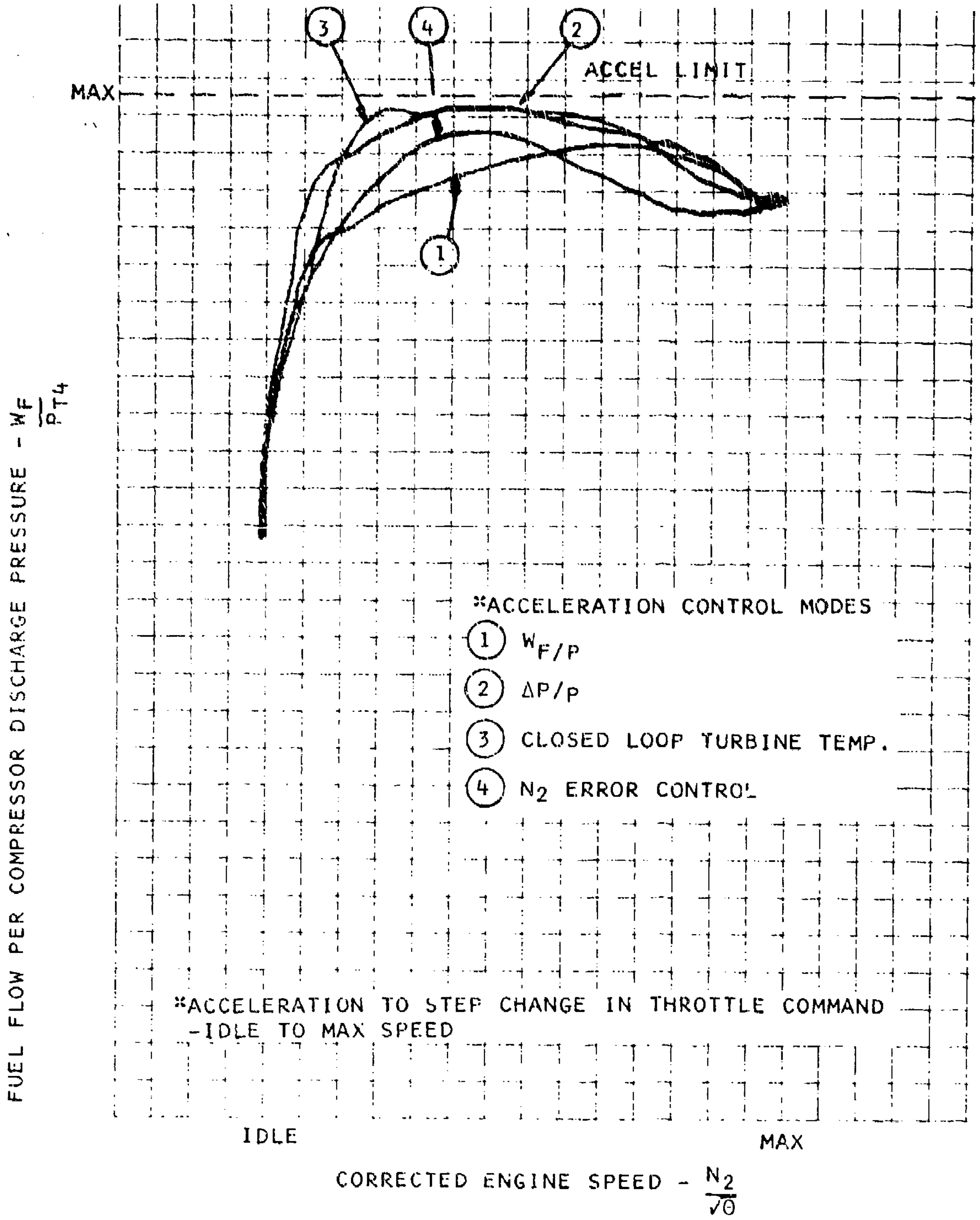

FIGURE 98 CENTRIFUGAL PUMP SYSTEM - ACCELERATION PERFORMANCE W/O GAIN COMPENSATION

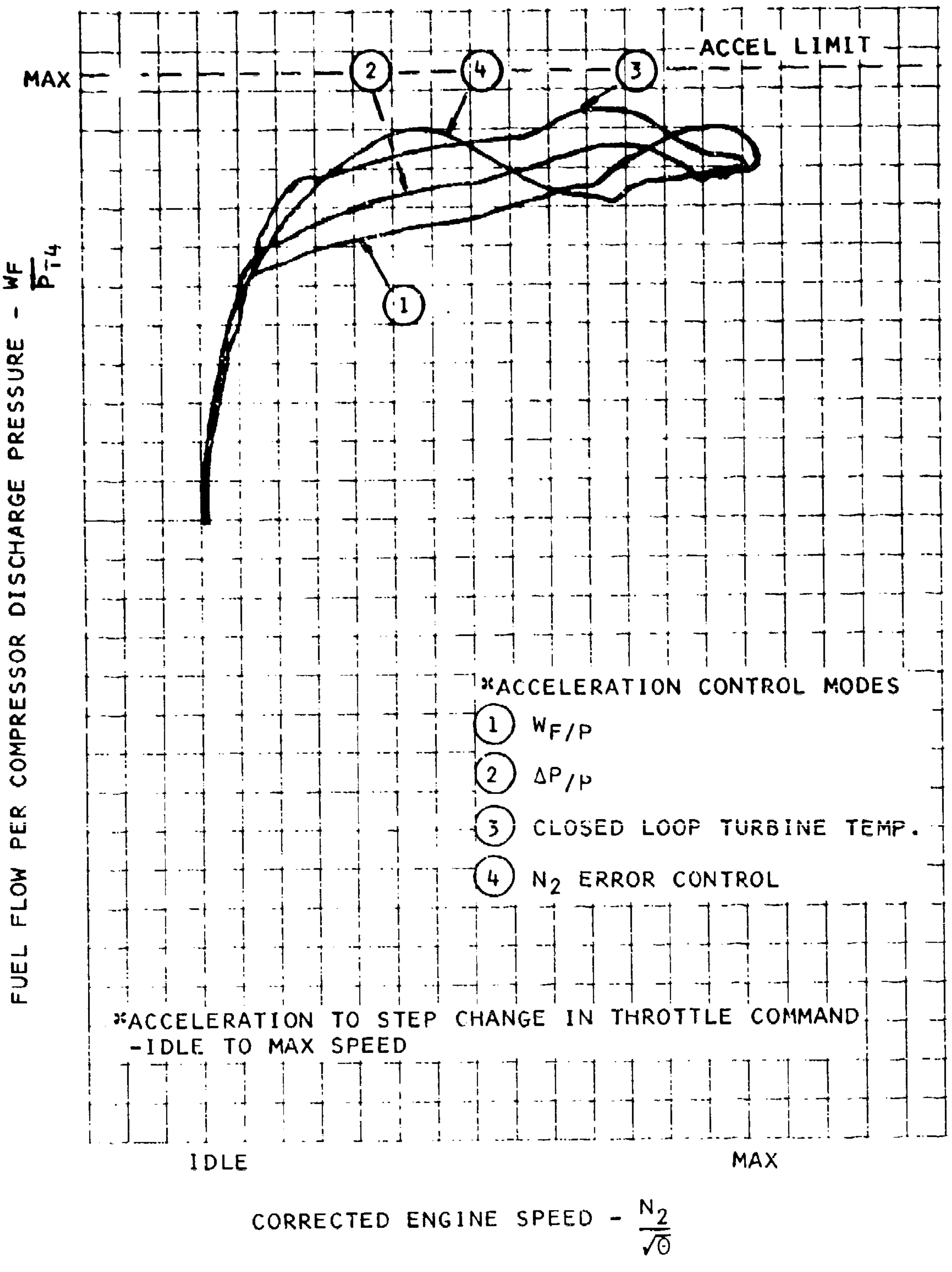

FIGURE 99 CENTRIFUGAL PUMP SYSTEM - ACCELERATION PERFORMANCE WITH GAIN COMPENSATION

W_F/P CONTROL MODE

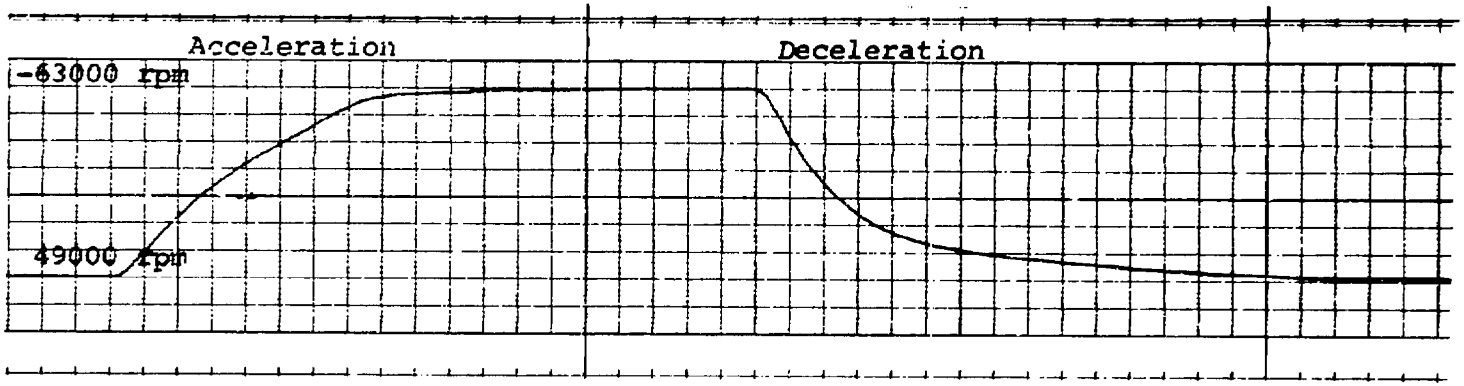

$\Delta P/P$ CONTROL MODE

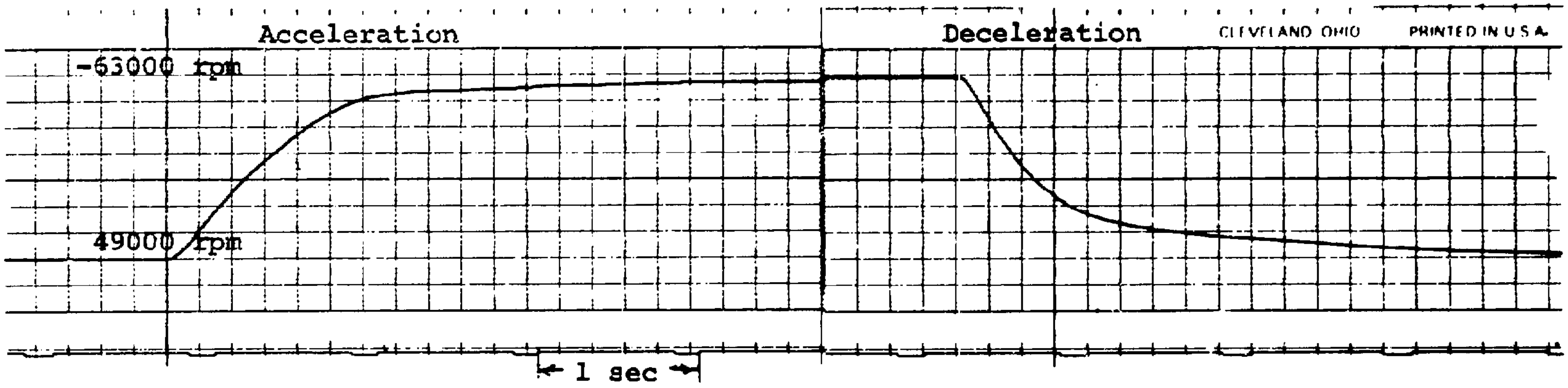

FIGURE 100 CENTRIFUGAL PUMP SYSTEM - ACCEL/DECEL PERFORMANCE TRACES

ΔN_2 CONTROL MODE

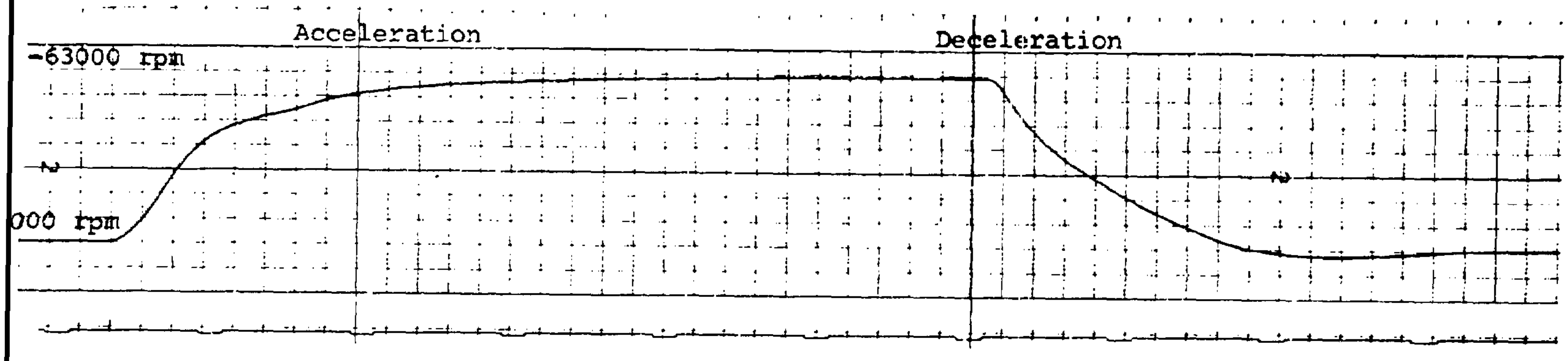

T_3 CONTROL MODE

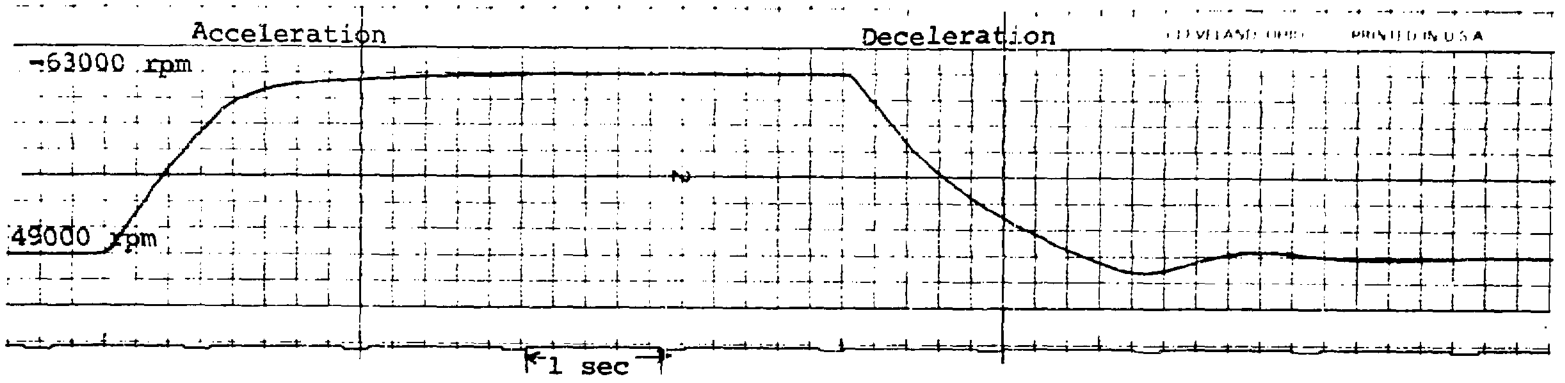

FIGURE 101 CENTRIFUGAL PUMP SYSTEM - ACCEL/DECEL PERFORMANCE TRACES

TABLE IX. ACCELERATION/DECELERATION PERFORMANCE CENTRIFUGAL PUMP SYSTEM

Control Mode	Acceleration		Deceleration	
	t_{90} secs	t_{75} secs	t_{90} secs	t_{75} secs
W_F/P	1.4	1.1	1.6	0.85
$\Delta P/P$ (acc only)	1.35	1.0	---	----
T_B	1.0	0.75	1.6	0.95
ΔN_2	1.75	1.15	1.4	1.1

Engine Deceleration Control

Figure 102 indicates the performance of the centrifugal pumping system in response to a throttle slam from maximum to idle setting. This condition is without the inclusion of compensation for the nonlinearity of the metering valve solenoid and shows undershoot errors up to 17.5% of the scheduled W_F/P deceleration limit. The same transients, but with compensation for the nonlinearity included in the control computer, are shown in Figure 103. As indicated, the system performance with gain compensation does not exceed the scheduled limit.

Speed Governor

The same tests performed with the magnetic clutch system were repeated for the centrifugal pump system. The resulting small signal transients are shown in Figures 104 and 105, and summarized by Table I which indicates the performance in terms of rise time, % overshoot, and damping. The same conclusions are applicable to both systems and have already been summarized in the section dealing with the magnetic clutch system performance.

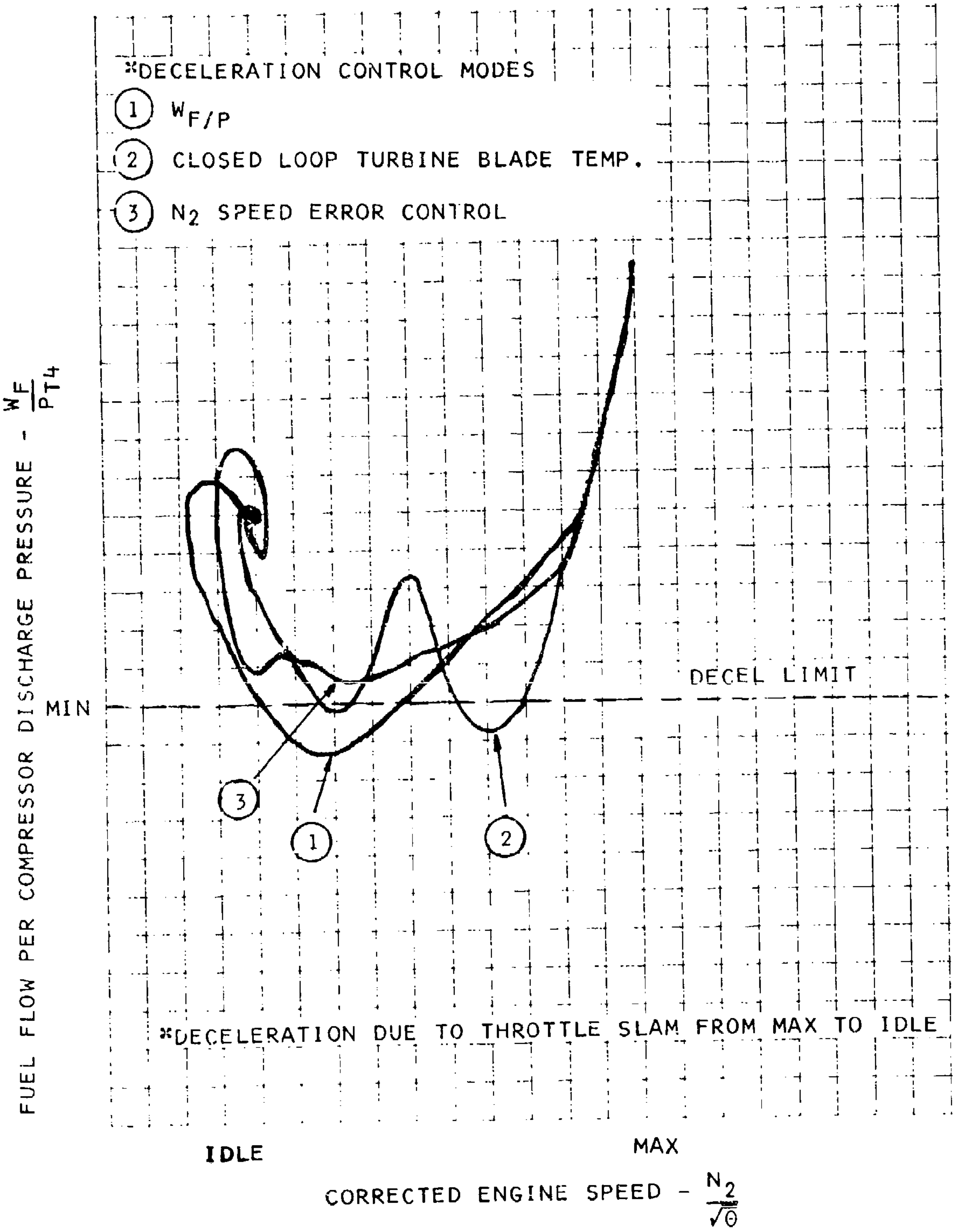

FIGURE 102 CENTRIFUGAL PUMP SYSTEM - DECEL PERFORMANCE W/O GAIN COMPENSATION

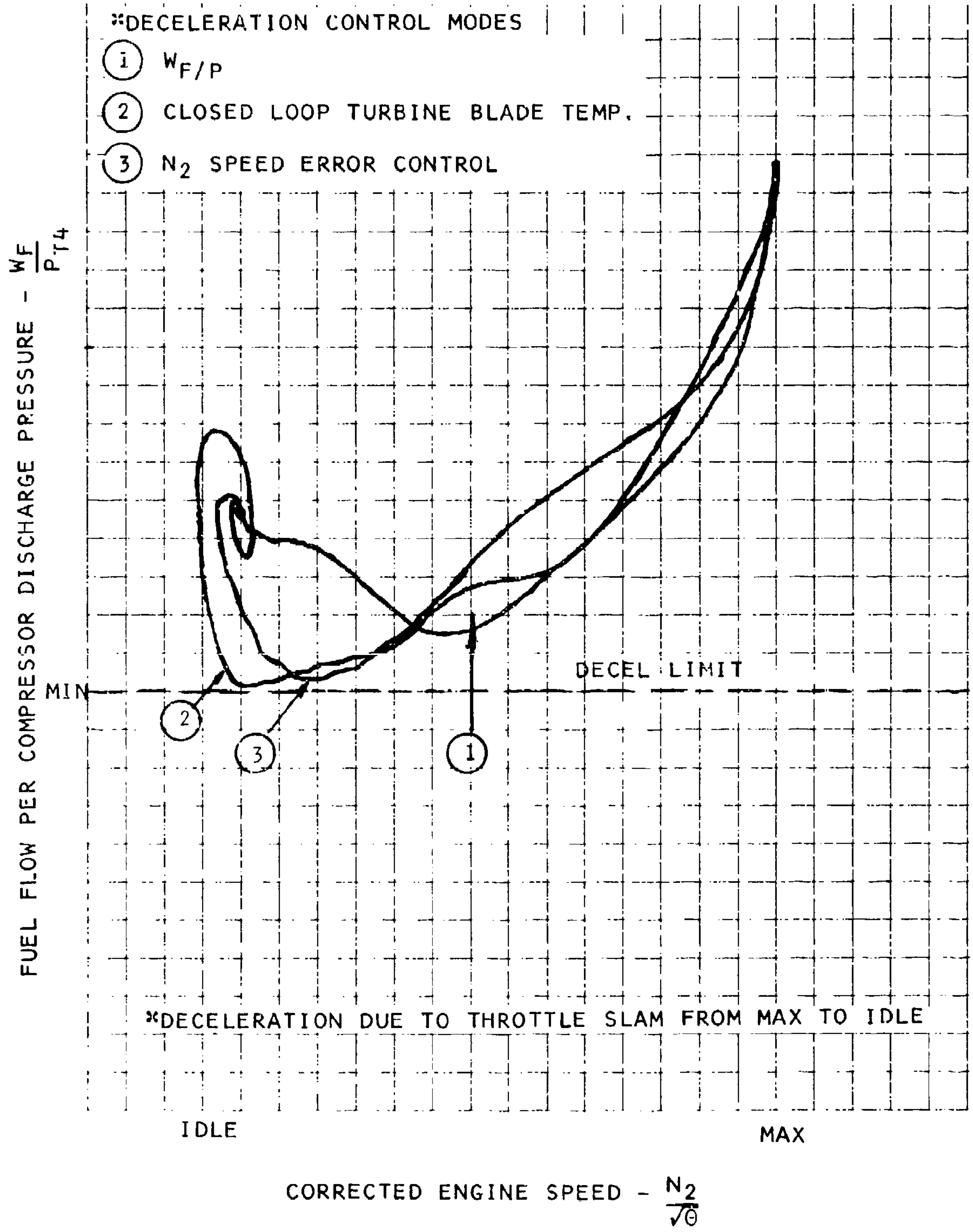

FIGURE 103 CENTRIFUGAL PUMP SYSTEM - DECEL PERFORMANCE WITH GAIN COMPENSATION

W_F/P GOVERNOR RESPONSE TO STEP CHANGE INPUT

Low Speed Response

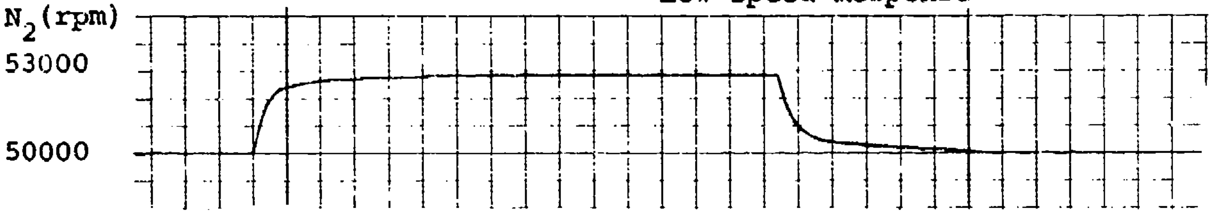

High Speed Response

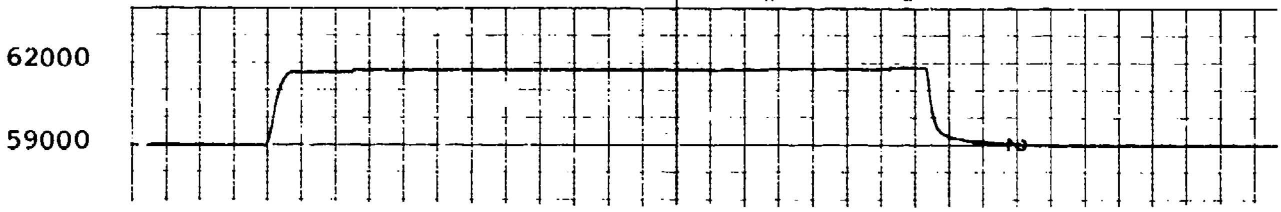

T_B GOVERNOR RESPONSE TO STEP CHANGE INPUT

Low Speed Response

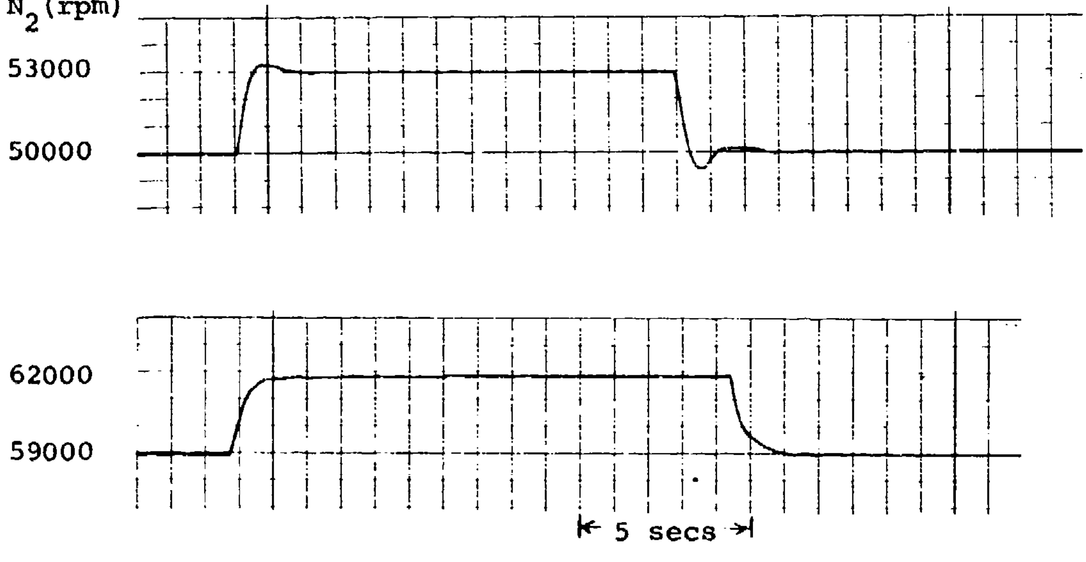

FIGURE 104 CENTRIFUGAL PUMP SYSTEM – N_2 GOVERNOR RESPONSE

N_2 SPEED ERROR MODE

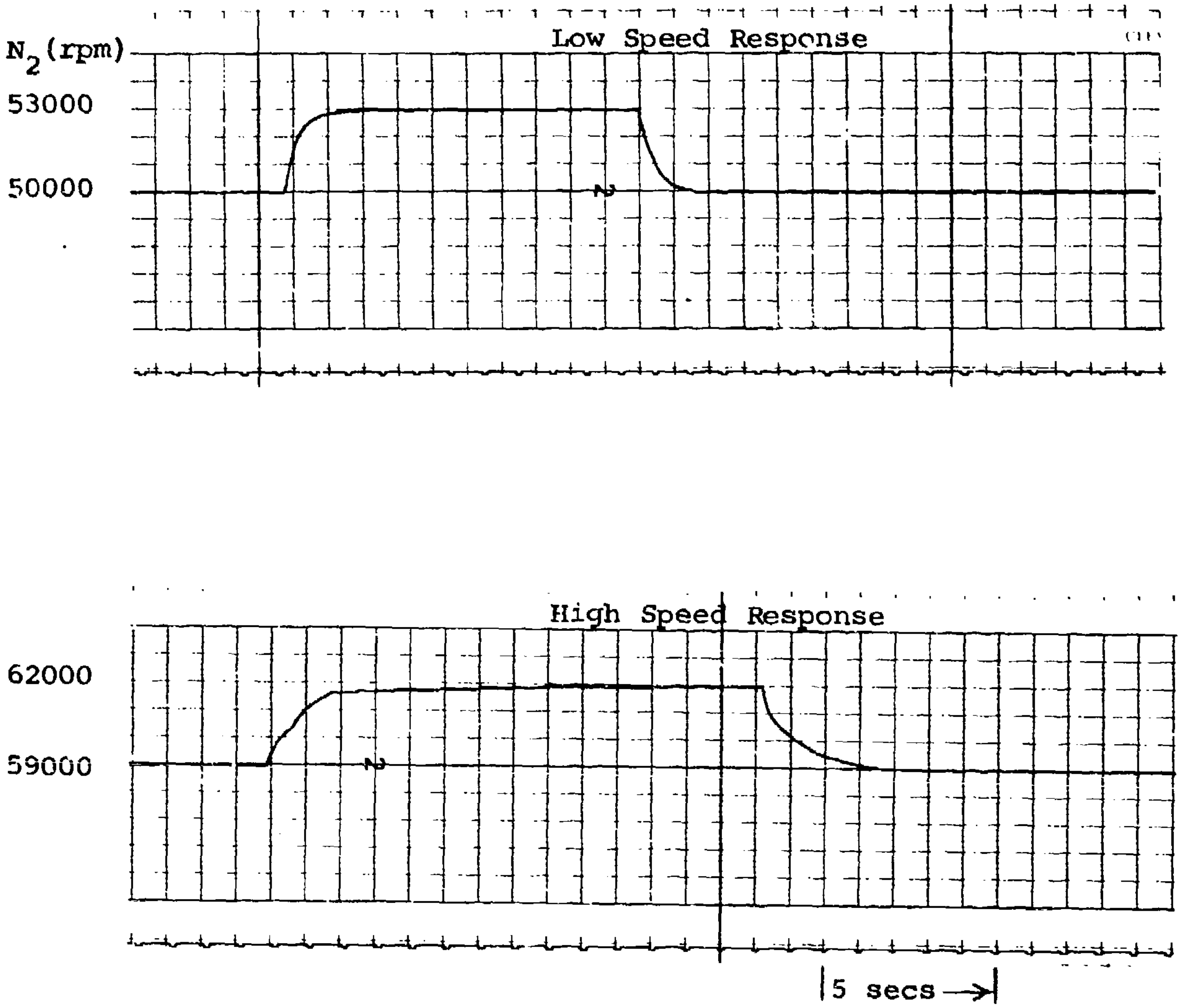

FIGURE 105 CENTRIFUGAL PUMP SYSTEM - N_2 GOVERNOR RESPONSE

TABLE X. CENTRIFUGAL PUMP SYSTEM SPEED GOVERNOR PERFORMANCE

Mode	Operating Conditions	T_R (secs)	% Overshoot	No Overshoots
W_F/P	100% N_2, pos. step	0.5	0	0
	" , neg. step	1.5	0	0
	80% N_2, pos. step	3.0	0	0
	" , neg. step	5.5	0	0
$\Delta P/P$	Same governor as used with the W_F/P control	-	-	-
		-	-	-
		-	-	-
		-	-	-
T_B	100% N_2, pos. step	1.0	0	0
	" , neg. step	1.3	0	0
	80% N_2, pos. step	0.6	7	1
	" , neg. step	0.5	20	1
ΔN_2	100% N_2, pos. step	2.0	0	0
	" , neg. step	3.0	0	0
	80% N_2, pos. step	1.4	0	0
	" , neg. step	1.2	0	0

7

RELIABILITY AND MAINTAINABILITY

1. RELIABILITY

The reliability predictions for the twelve possible control configurations are illustrated in Figure 106. The specific reliability ratings of these components, when considered for a fifty-hour mission, are also tabulated in this figure. The predictions indicate that a centrifugal pumping system with a speed error method of control (System R11) offers the highest reliability with the least amount of maintenance required. This was expected because this is the simplest system.

The electronics considered in the reliability analysis represent only that portion of the electronic unit associated with the speed loops and the solenoids and clutch drive circuits. These circuits are typical of what may be used in a production control, whereas the other portions of the electronic interface unit were designed primarily as breadboard test equipment using shelf components and concepts that would not be used in a production electronic control system.

The following data reflects the failure rates associated with the sensing devices required for each control mode:

Speed Error Control Mode = 22.45 per 10^6 hours

W_f/P Control Mode = 29.11 per 10^6 hours (Strain Gage Sensor)

W_f/P Control Mode = 37.11 per 10^6 hours (Capacitive Sensor)

W_f/P Control Mode = 50.20 per 10^6 hours (Potentiometric Sensor)

$\Delta P/P$ Control Mode = 59.11 per 10^6 hours

Temp. Control Mode = 74.11 per 10^6 hours

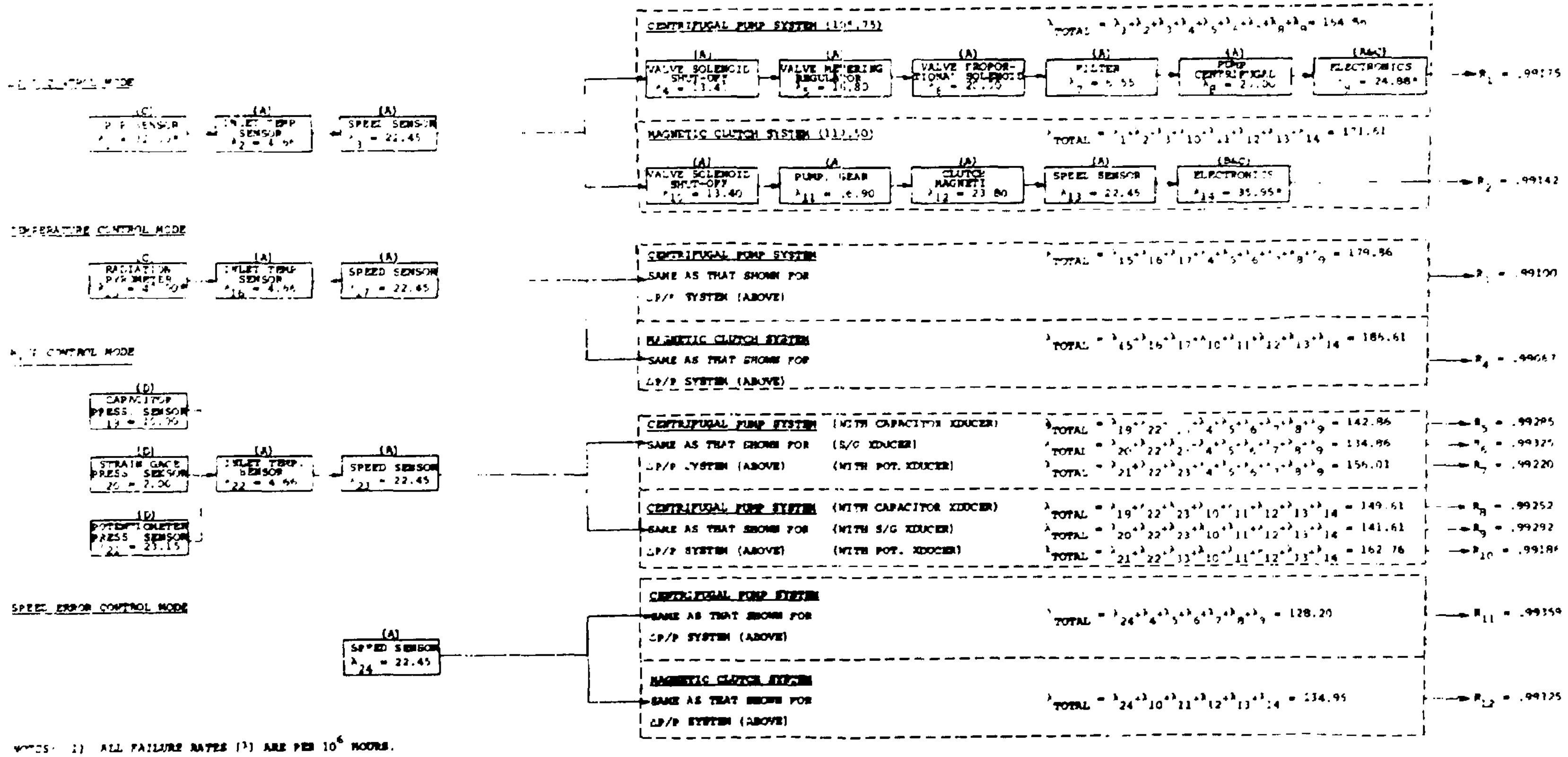

NOTES: 1) ALL FAILURE RATES (λ) ARE PER 10^6 HOURS.

2) R CALCULATIONS ARE FOR A 50-HOUR MISSION.

3) ASTERISKED NUMBERS ARE ESTIMATES ONLY.

SOURCES FOR DATA: A = FALADA

B = MIL-STD-217A

C = ESTIMATE

D = VENDOR

FIGURE 106. Predicted Reliability for Miniature High Speed Engine Controls

Again, due to its simplicity, the speed error control mode system offers the highest reliability in the sensing element area. In addition, there is an obvious cost and maintainability advantage associated with this system.

Of the remaining sensing system configurations, the W_f/P control mode using a strain gage sensor offers the next highest predicted reliability.

It should be noted that the $\Delta P/P$ sensor and the radiation pyrometer sensor are relatively new devices and as such, the predicted reliability has been estimated using piece-part count and engineering judgment as criteria.

2. MAINTAINABILITY

Field maintenance on gas turbine engine fuel controls is limited primarily to remove and replace operations, speed trim, and fuel flow adjustments (metering head, and minimum and maximum flow). The components selected for development in this program were designed for installation on existing accessory pads and therefore, it was not possible to consider quick installation concepts.

In comparing present-day hydromechanical controls with future electronic systems, it is apparent that there will be significant impact on maintenance procedures. What is likely to happen, particularly in sophisticated systems, is that future controls will incorporate provisions for fault isolation to aid maintenance in determining if a control component is malfunctioning. This will be possible and cost effective in future sophisticated electronic controls because the required signals for fault isolating the control are readily available as is the logic and computational capability. These self-check and fault-isolating features will save the maintenance time required to determine if the control system is the cause of the reported problem. Moreover, this capability should eliminate most of the relatively large number and time-consuming occurrences of unjust removals which are made because trouble-shooting maintenance procedures are pretty much limited to remove-and-replace operations.

The goals and nature of the present program precluded detailed considerations of maintenance requirements. This was because a complete control system for a specific application was not being designed. Moreover, each control system installation, depending on the airframe mission, will probably have different control system design criterion which will dictate approaches for maintenance requirements. Moreover, components like the radiation pyrometer for use in temperature limiting will likely reduce overall engine maintenance by eliminating occurrance of engine overtemperature. However, it is not possible to quantitatively evaluate this potential saving.

8

SUMMARY AND CONCLUSIONS

The development effort accomplished during this program has provided new control components and high speed fuel pump technology for interfacing with electronic computer systems for use on future drone, missile, and RPV engines. In addition, the work has provided direction for continuing control technology development. The developed components were designed for installation on an existing engine for control mode evaluation tests. This evaluation testing should provide further visibility for defining future control system requirements. The significant features of each component developed during the program are discussed below.

A miniaturized, low-cost, 70,000 rpm centrifugal pump which is capable of providing fuel flow requirements from light-off to full engine power was successfully developed. The pump is integral with a fuel metering package which includes a low-cost proportional solenoid operated metering valve, a diaphragm operated throttling regulator, and a solenoid shutoff valve. Also, a variable delivery fuel pumping and metering system comprised of a magnetic clutch-driven 12,000 rpm gear pump and solenoid shutoff valve was successfully developed. This system can provide necessary fuel flow without requiring load pressure compensation and with better overall efficiency than a conventional gear pump bypass system. A higher flow turndown unit could be developed for wider flight envelope application by reducing gear pump friction through material selections and surface treatment, and/or by providing a more sophisticated electronic closed-loop speed control than the simple presently used proportional control.

A fluidic $\Delta P/P$ sensor was developed which offers promise for low cost but relatively accurate performance for use in closed loop transient control of the engine. The sensor can also be used in control of engine geometry. Further development should provide for increasing the deflection of the total pressure jet, increasing the pressure gain of the receiver and fluidic amplifier, and miniaturizing the design.

A radiation pyrometer for turbine blade temperature sensing was developed to provide a transducer for demonstrating turbine blade temperature limiting and transient control of the engine. The dynamic response and sensitivity requirements of the system requires detecting the temperature of a .1 inch diameter target on a hot turbine blade that is in view for about 6 microseconds while processing signals as small as 10 nanoamps. These requirements have pushed the state-of-the-art of available operational amplifiers and although the performance of this unit is satisfactory for use in the planned engine control mode evaluation tests, continued development is needed in these areas to improve dynamic performance for future higher speed turbines.

An electronic unit was developed for providing interfacing between the control components and the test cell computer. The electronic package houses a high performance variable capacitance pressure transducer, a low-cost potentiometric pressure transducer and the $\Delta P/P$ sensor. A strain gage-type pressure transducer was also procured for evaluation and it can be mounted in place of the potentiometric pressure sensor.

The bench testing conducted as part of this program included a series of closed-loop tests using an analog computer simulation of an existing engine and a digital computer simulation of the control. Both of the fuel pumping and fuel metering systems were included in the test setup. The testing successfully demonstrated a W_F/P control mode, closed-loop control on turbine blade temperature, closed-loop $\Delta P/P$ control, and time delayed transient control based on speed error. It is significant to note that this series of closed-loop testing uncovered problems in transient fuel flow scheduling that were caused by nonlinearities inherent in both fuel metering systems. These problems were corrected but if not for the closed-loop testing, the nonlinearities would not have been considered a problem area.

The control components developed during this program have successfully completed evaluation testing on the bench. Future testing should encompass engine installation and checkout of the control components and electronic interface unit. Various control mode investigations and evaluations can then be conducted.

REFERENCES

1. Burnell, D. G., Cole, M. A., Morrison, T. B. and White, A. H., Miniaturized High Speed Controls for Turbine Engines, Technical Report AFAPL-TF-73-89, dated 27 August 1973.

2. Williams Research Corporation, Fuel Control, Main Turbine Engine, Code Ident. 24235.

3. Arnett, Samuel E., Turbine Engine Compressor Flow Limiting, Technical Report AFAPL-TR-72-72, dated August 1972.

4. White, A. H., Willis, D. F., Advanced Engine Control Program, USAAMRDL Technical Report 72-59, dated November 1972.

☆U.S.Government Printing Office: 1975 - 657-018/3J6